

Spectroscopic Investigation of Neutral and Impurity Dynamics in the Edge Region of ADITYA-U Tokamak

A Thesis Submitted to
Nirma University
In Partial Fulfilment of the Requirement
For The Degree of

Doctor of Philosophy

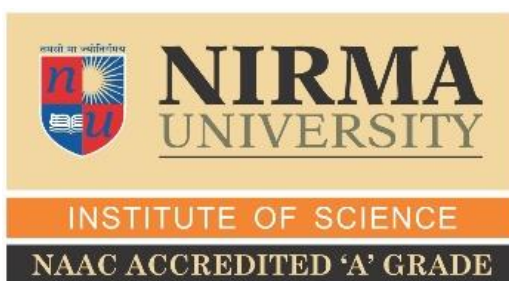
in

Institute of Science

by

NANDINI YADAV

(20PTPHDS77)



Institute of Science, Nirma University
Ahmedabad – 382481, Gujarat, India
May 2023

Nirma University
Institute of Science

Certificate

This is to certify that the thesis entitled "**Spectroscopic Investigation of Neutral and Impurity Dynamics in the Edge Region of ADITYA-U Tokamak**" has been prepared by **Ms. Nandini Yadav** under my supervision and guidance. The thesis is her own original work completed after careful research and investigation. The work of the thesis is of the standard expected of a candidate for Ph.D. Programme in **Science (Physics)** and I recommend that it be sent for evaluation.

Date: 15.05.2023


15.05.'23

Supervisor

(Dr. Ankur Pandya)

Date: 15/05/23



Co-Supervisor

(Joydeep Ghosh)

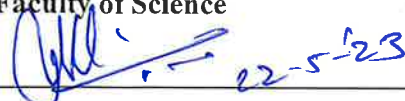
Forwarded Through:



Head of the Department (if any)



Dean Faculty of Science

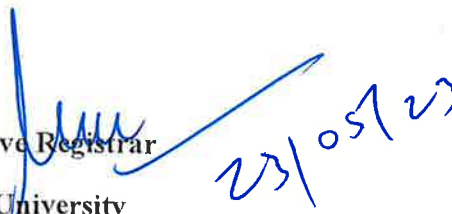

15/05/23

Dean Faculty of Doctoral Studies and Research

To ,

Executive Registrar

Nirma University


23/05/23

Nirma University

Institute of Science

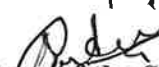
Declaration

I, **Ms. Nandini Yadav**, registered as Research Scholar, bearing Registration No.20PTPHDS77 for Doctoral Programme under the **Faculty of Science** of Nirma University do hereby declare that I have completed the course work, pre-synopsis seminar and my research work as prescribed under R. Ph.D. 3.5.

I do hereby declare that the thesis submitted is original and is the outcome of the independent investigations / research carried out by me and contains no plagiarism. The research is leading to the discovery of new facts / techniques / correlation of scientific facts already known. (Please tick whichever is applicable). This work has not been submitted to any other University or Body in quest of a degree, diploma or any other kind of academic award.

I do hereby further declare that the text, diagrams or any other material taken from other sources (including but not limited to books, journals and web) have been acknowledged, referred and cited to the best of my knowledge and understanding.

Date: 15/05/23


Signature of the Student

I agree with the above declaration made by the student.

Date: 15/05/23


Signature of the Supervisor

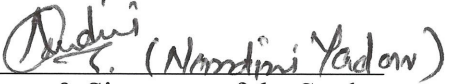
Date: 15/05/23


Signature of the Co-Supervisor
Jaydeep Ghosh

Nirma University
Institute of Science
Certificate

This is to certify that the thesis entitled **Spectroscopic Investigation of Neutral and Impurity Dynamics in the Edge Region of ADITYA-U Tokamak** has been prepared by me, under the supervision and guidance of **Dr. Ankur Pandya (Supervisor)**, Institute of Technology, Nirma University and **Prof. Joydeep Ghosh (Co-supervisor)**, Institute for Plasma Research. The thesis is my own original work completed after careful research and investigation. The work of the thesis is of the standard expected of a candidate for Ph.D. Programme. The final hard bound copy of the thesis is submitted after incorporating all the suggestions / corrections suggested by the referees.

Date: 11/08/2023


Name & Signature of the Student

Date: 11/08/2023


(Dr. Ankur Pandya)
Supervisor



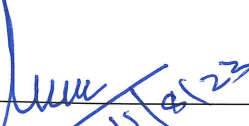
(Prof. Joydeep Ghosh)
Co-supervisor

Forwarded Through:

(i) Dean Faculty of Science


11-8-23

(ii) Dean - Faculty of Doctoral Studies and Research


11-8-23

(iii) Executive Registrar

Nirma University

Dedicated to,

My parents

ACKNOWLEDGEMENTS

The journey to earn my doctorate has been incredible, and I owe it all to the support and advice of countless people. To everyone who have encouraged and helped me along the way to my doctorate and provided me with the wealth of knowledge I need to achieve, I offer my sincerest gratitude.

Nirma University, presented me with an excellent opportunity to uncover my strengths and improve as a researcher. At the outset, I'd want to give my sincere gratitude to Dr. Ankur A. Pandya, my brilliant advisor for all the help he's given me academically and morally throughout my research journey. I am extremely thankful to Prof. Anup K. Singh (Director General), Dr. P. N. Tekwani (Dean, Faculty of Doctoral Studies and Research) and Dr. Sarat Dalai (Dean, Institute of Science) for dealing with any procedural hurdles arises during thesis submission. I would like to express my gratitude towards Ms. A. P. Prashya (Assistant registrar) and other member of Ph.D. section, Mr. Sachin Kikani and Ms. Harvi Suryawala for helping me with my submission process. I also thank Dr. Keyur Sangani for helping me whenever needed at Nirma University. My special acknowledgment to Dr. Kishor Mishra, IPR and Prof. Prafulla Jha, MSU for their fruitful inputs during every review meeting.

Institute for Plasma Research (IPR), gave me a great opportunity to work on tokamak machines and use spectroscopy diagnostic equipment. First and foremost, I am extremely grateful to my co-supervisor Prof. Joydeep Ghosh for his continual guidance at every step of the thesis work and for supporting my ideas with continuous motivation. I would want to express my sincere gratitude to Dr. Malay Bikas Chowdhuri for the valuable time and information that he contributed to make me a capable researcher. He is always there to guide me with spectroscopic techniques as well as to criticize and improve my writing skills. Also, I thank Ms. Ranjana Manchanda for giving me the opportunity in 2015 to work with the spectroscopy group. The words are always less to express my gratitude towards you three mentors. My path to Ph.D. was fraught with setbacks (mainly with my Ph.D. registration). Nevertheless, you three always found solution to every challenge and never made me feel like giving up. You three are my second guardian who always supported me and made me feel like family with a second home at IPR.

I thank Dr. Ashoke De, Dr. Sripathi Punchithaya K., and Dr. Deepti Tripathi. I thank Dr. Amulya Sanyasi for familiarising me with plasma linear devices. I would like to thank Dr. Ritu Dey, Dr. Nilam Ramiya, Dr. Prabhakar Srivastava, Dr. Gaurav Shukla, Dr. Payal Mehta, Dr. Vara Prasad, Sharvil, Aman, Vishal, Manish Rathor, Abhishek, Ketan, Navin, Gayatri, Pradeep Bairagi and Dipexa for working with me in the spectroscopy diagnostic section at IPR. I

appreciate thesis editing help from Ashok, Bharat, Soumitra, Aman, and Vishal. I thank the ADITYA-U tokamak operation and vacuum divisions, Mr. R. Tanna, Mr. K. Jadeja and Mr. K. M. Patel for making every experiment possible and sharing their knowledgebase. Thanks to Ms. Minsha Shah and Mr. E. Praveenlal from the electronics division for helping me with PMT electronics and trigger issues. I thank Makwana Sir and Shivam from APPS division. I thank everyone present during operations and making a friendly atmosphere, including Harshita, Rohit, Tanmay, Devilal, Suman Aich, Kaushal, Suman Dolui, Ankit Kumar, Bharat, Ashok, Ananya, Inzamul, Soumitra, Komal, Kalpesh ji, Laxmikant, Ankit Patel and Kajal. ADITYA-U team has boundless enthusiasm for physics has always given me a boost to work more and more. My immense thanks to the late Shri Vipul Panchal for helping me with the DAQ channel mappings. I also appreciate Varsha madam, Late Shri. Jayesh Sir, Nikita, and Rashmi for celebrating many events in my early career days at lab. I appreciate Asha madam and Zubin's casual talks.

It was the most beautiful year of my life working in the spectroscopic diagnostic division. My special thanks to Abha, Bhoomi, Tanmay, Sharvil, Suman, and Kaushal for more non-technical discussions at the ADITYA-U tokamak control room and for having fun moments at conferences. My special thanks to Aman and Vishal for helping me with the Hindi translation of my thesis abstract. I thank my friends for always being there for me and spreading positive vibes: Neha, Nirali, Deepika, Swati, Shweta, Rini, Madhuri, Dipal, and Rahul.

I want to express my gratitude to my in-law's family for always supporting me and making my life more fun-full: Papa, Vinay bhaiya, Radha didi, Chetan bhaiya, Jyoti didi, Atul bhaiya, Kavita didi, Annu, Anshu, Dushyant, Shrishti, and three kiddos of our family Chikoo, Ipsa and Alina, I also thank my sister-in-law Neeraj didi and her kids Pratik, Tannu, and Kannu. Of course, big heartfelt shout-out to my fantastic husband, Vivek, for tolerating my madness, supporting my passion towards tokamak research, preparing special tea during my thesis writing period and always being with me since 2018.

I thank my Grandparents late Smt. Chandrakala Yadav and late Shri. Girdhar Yadav for their blessings and for transferring knowledge as the legacy of this family. I thank my kaka, Pankaj Yadav, for having endless discussions and helping me with my studies whenever needed. I thank my tau Shashirajan Yadav, Tai Sonal Yadav, and cousin Vidur Yadav. I thank my mother, Shobha Yadav, for bringing me into this beautiful world and constantly boosting my confidence since childhood. I thank my sister, Suhasini Yadav, for sharing her clothes, life stories, stationary everything with me. Lastly, I thank my father, Madhusudan Yadav, for teaching me moral values and supporting my dreams in every possible way.

Table of Contents

ACKNOWLEDGEMENTS.....	XI
LIST OF FIGURES	XIX
LIST OF TABLES	XXVI
ABSTRACT.....	XXIX
CHAPTER 1. INTRODUCTION	35
1.1. FUSION FOR SOCIETY	36
1.2. CONTROLLED NUCLEAR FUSION: BRINGING SUN ONTO EARTH.....	37
1.3. TOKAMAK: ADVANCED MACHINE FOR FUSION	38
1.4. PLASMA-WALL INTERACTION.....	41
1.5. ROLE OF TOKAMAK EDGE REGION FOR BETTER PLASMA CONFINEMENT.....	43
1.6. THE ROLE OF NEUTRALS AND IMPURITY IONS IN EDGE PLASMA	44
1.6.1. <i>Role of neutrals</i>	44
1.6.2. <i>Role of impurity ion</i>	45
1.7. LITERATURE SURVEY ON EDGE PLASMA STUDIES	45
1.7.1. <i>Edge characterization</i>	46
1.7.2. <i>Divertor characterization</i>	51
1.8. MOTIVATION	52
1.9. THESIS OUTLINE.....	54
CHAPTER 2. EXPERIMENTAL SETUP.....	57
2.1. ADITYA-U TOKAMAK	58
2.2. SUBSYSTEMS OF ADITYA-U TOKAMAK.....	60
2.2.1. <i>Vacuum vessel</i>	60
2.2.2. <i>Limiter and divertors</i>	61
2.2.3. <i>Magnets</i>	62
2.2.4. <i>Power supplies</i>	64
2.2.5. <i>Gas fuelling system</i>	64
2.2.6. <i>Wall conditioning</i>	65
2.3. DIAGNOSTICS.....	67
2.3.1. <i>Diagnostics other than spectroscopy</i>	67
2.3.2. <i>Spectroscopy diagnostic</i>	75
CHAPTER 3. INVESTIGATION OF EDGE PLASMA THROUGH THE MODELLING OF SPECTRAL LINE PROFILES	
89	
3.1. ANALYSIS TECHNIQUE FOR SPECTRAL LINE PROFILE MODELLING	89

3.1.1.	<i>Bound-bound transitions</i>	91
3.1.2.	<i>Bound-free transitions</i>	93
3.1.3.	<i>Free-free transitions</i>	93
3.2.	POPULATION KINETIC MODELLING IN PLASMA SPECTROSCOPY	94
3.2.1.	<i>Coronal Equilibrium (CE)</i>	94
3.2.2.	<i>Collisional Radiative (CR) model</i>	94
3.2.3.	<i>Local Thermodynamic Equilibrium (LTE)</i>	94
3.3.	LINE PROFILE DUE TO VARIOUS TYPES OF BROADENING	95
3.3.1.	<i>Natural broadening</i>	95
3.3.2.	<i>Doppler broadening</i>	95
3.3.3.	<i>Pressure broadening/ Stark broadening</i>	96
3.3.4.	<i>Instrumental broadening</i>	97
3.4.	EFFECT OF MAGNETIC FIELD ON LINE PROFILE	97
3.5.	SELF-ABSORPTION AND OPACITY ESTIMATION	98
3.6.	INVESTIGATION OF NEUTRAL AND IMPURITY ION TEMPERATURES AND THEIR RADIAL PROFILES	100
3.6.1.	<i>Spectral line profile modelling for temperature estimation</i>	100
3.6.2.	<i>Experimental arrangements for space-resolved measurements:</i>	102
3.6.3.	<i>Abel-inverted radial profile measurements</i>	103
3.6.4.	<i>Experimental results of ion temperature measurement</i>	104
3.6.5.	<i>Anomaly in C⁺ ion temperature estimation</i>	108
3.6.6.	<i>O⁴⁺ ion temperature</i>	109
3.6.7.	<i>Neutral hydrogen temperature estimation</i>	112
3.6.8.	<i>Two components of neutral temperature (hot & warm)</i>	116
3.6.9.	<i>Neutral temperature Radial profile</i>	117
3.6.10.	<i>Discussion on neutral and ion temperature profiles</i>	118
3.7.	OBSERVATION OF POLOIDAL ASYMMETRY ESTIMATION IN NEUTRAL TEMPERATURE.....	120
3.7.1.	<i>Experimental setup</i>	120
3.7.2.	<i>Experimental Result</i>	122
3.7.3.	<i>Discussion on poloidal asymmetry</i>	125
3.8.	INVESTIGATION OF SELF-ABSORPTION IN SPECTRAL LINE PROFILE FROM TOKAMAK	126
3.8.1.	<i>Li₂TiO₃ pellet injection system</i>	126
3.8.2.	<i>Spectroscopic observation system</i>	129
3.8.3.	<i>Typical plasma discharge parameters</i>	131
3.8.4.	<i>Results and discussion on self-absorption of Li spectral line</i>	132
3.8.5.	<i>Opacity estimation</i>	134
3.9.	SUMMARY.....	136
	CHAPTER 4. INVESTIGATION OF IMPURITY INFUXES AND RECYCLING IN ADITYA-U TOKAMAK.....	139
4.1.	INTRODUCTION.....	139

4.2.	EROSION AND SPUTTERING PROCESSES.....	140
4.3.	BRIEF DESCRIPTION OF RECYCLING.....	142
4.4.	EXPERIMENTAL ARRANGEMENT	143
4.5.	MEASUREMENT TECHNIQUE.....	145
4.6	PLASMA DISCHARGE AND TYPICAL PLASMA PARAMETERS	146
4.8.	BEHAVIOUR OF NEUTRAL AND PARTICLE INFLUXES IN DISCHARGE PRODUCED AFTER GDC	150
4.9.	BEHAVIOUR OF NEUTRAL HYDROGEN AND IMPURITY INFLUXES IN DISCHARGE PRODUCED AFTER GDC WITH LITHIUMIZATION.....	153
4.10.	SUMMARY.....	158
CHAPTER 5. NEUTRAL AND IMPURITY TRANSPORT STUDIES ON ADITYA-U TOKAMAK.....		161
5.1.	THEORY OF PARTICLE TRANSPORT IN TOKAMAK PLASMAS.....	161
5.2.	CLASSICAL, NEOCLASSICAL AND ANOMALOUS DIFFUSION.....	162
5.3.	MASS DEPENDENCY STUDY OF IMPURITY TRANSPORT	165
5.4.	METHODOLOGY FOR STUDYING THE MASS DEPENDENCY OF TRANSPORT IN ADITYA-U TOKAMAK	165
5.5.	INVESTIGATION OF MASS DEPENDENCY STUDY ON IMPURITY TRANSPORT IN TOKAMAK:	169
5.5.1.	<i>Transport of carbon Z=6 (Intrinsic impurity)</i>	169
5.5.2.	<i>Transport of oxygen Z=8 (Intrinsic impurity)</i>	174
5.5.3.	<i>Transport of neon Z=10 (non-intrinsic impurity)</i>	176
5.5.4.	<i>Transport of argon Z=18 (non-Intrinsic impurity)</i>	179
5.5.5.	<i>Transport of iron Z=26 (Intrinsic impurity)</i>	181
5.5.6.	<i>Discussion on the mass dependency on impurity transport:</i>	183
5.6.	MOLECULAR CONTRIBUTION IN PARTICLE INFLUX ESTIMATION:	184
5.6.1.	<i>Theoretical background</i>	184
5.6.2.	<i>Experimental setup</i>	188
5.6.3.	<i>Results about molecular contributions to particle influx</i>	189
5.6.4.	<i>Summary</i>	195
CHAPTER 6. DETERMINATION OF GAS-TEMPERATURE FOR DEVELOPING A TECHNIQUE TO CHARACTERIZE DIVERTOR PLASMA		197
6.1.	LOW-TEMPERATURE PLASMA DISCHARGES	198
6.2.	RELEVANCE OF LOW-TEMPERATURE PLASMA DEVICE TO TOKAMAK.....	199
6.3.	EXPERIMENTAL SETUP.....	202
6.4.	MEASUREMENT TECHNIQUE	203
6.5.	PLASMA NEUTRAL-GAS TEMPERATURE MEASUREMENT USING TWO DIFFERENT APPROACHES.....	206
6.5.1.	<i>Experimental estimation of temperature</i>	206
6.5.2.	<i>Simulated estimation of temperature</i>	213
6.6.	REMOVAL OF AMBIGUITY PRESENT IN GAS TEMPERATURE ESTIMATION	214
CHAPTER 7. CONCLUSION AND FUTURE SCOPE.....		219

7.1. FUTURE SCOPE	225
APPENDIX: A	229
MATHEMATICAL EXPLANATION FOR ZEEMAN POLARIZATION COMPONENTS	229
APPENDIX: B.....	231
LIST OF ABBREVIATES	231
LIST OF STANDARD SYMBOLS USED	234
APPENDIX: C.....	237
LIST OF INDIAN TOKAMAKS DISCUSSED IN THIS THESIS	237
LIST OF WORLDWIDE TOKAMAKS DISCUSSED IN THIS THESIS	237
BIBLIOGRAPHY	241
LIST OF PUBLICATIONS	279

LIST OF FIGURES

FIGURE 1.1. AN ARTISTIC REPRESENTATION OF STARS - GRAVITATIONALLY CONFINED FUSION REACTORS AT THE TOP AND FOSSIL FUEL-GENERATED HUMAN POWER CONSUMPTION AT THE BOTTOM. (FAMOUS ARTWORK- "THE STARRY NIGHT OVER THE RHONE BY VINCENT VAN GOGH. ") (VINCENT VAN GOGH)	35
<i>FIGURE 1.2. WORLDWIDE ENERGY CONSUMPTION TREND (KUMAR)</i>	36
FIGURE 1.3. PICTORIAL REPRESENTATION OF PLASMA MAGNETIC FIELDS AND FLUX SURFACES	39
FIGURE 1.4. PICTORIAL REPRESENTATION OF PLASMA CROSS-SECTION AND DIFFERENT REGIONS. PLASMA CORE WITH HIGH TEMPERATURE AND HIGH DENSITY	41
FIGURE 1.5. LIMITER AND DIVERTOR PLASMA GEOMETRIES	43
FIGURE 2.1. ADITYA-U TOKAMAK	57
FIGURE 2.2. ADITYA-U TOKAMAK VACUUM VESSEL	60
FIGURE 2.3. LIMITER AND DIVERTOR STRUCTURES	61
FIGURE 2.4. ADITYA-U TOKAMAK MAGNETS	63
FIGURE 2.5. LITHIUMIZATION (A), (B) LITHIUM-ROD TECHNIQUE, (C), (D) LITHIUM EVAPORATION TECHNIQUE	65
FIGURE 2.6. MIRNOV COIL DIAGNOSTICS	68
FIGURE 2.7. (A) SEVEN VIEWING CHORDS FOR MICROWAVE INTERFEROMETRY AND (B) SCHEMATIC FOR MICROWAVE INTERFEROMETRY.	69
FIGURE 2.8. LINE OF SIGHT FOR HXR MEASUREMENT	71
FIGURE 2.9. DIFFERENT PROBE DIAGNOSTICS: (A) LANGMUIR PROBE, (B) GARLAND LANGMUIR PROBE, (C) FLUSH LANGMUIR PROBE	73
FIGURE 2.10. PROBE MEASUREMENT CIRCUIT AND ITS CHARACTERISTIC CURVE	74
FIGURE 2.11. SPECTROSCOPICALLY MEASURED PLASMA PROPERTIES	76
FIGURE 2.12. CZERNY-TURNER SPECTROSCOPIC SYSTEM	79
FIGURE 2.13. THE PHOTO-MULTIPLIER TUBE CONTAINS DYNODES FOR SECONDARY ELECTRON MULTIPLICATION ACTION (PHOTONICS HAMAMATSU)	80
FIGURE 2.14. TYPICAL SURVEY LINE EMISSION SPECTRUM ACQUIRED USING AVANTES SPECTROMETER.	82
FIGURE 2.15. ACQUIRED WAVELENGTH-CALIBRATED DATA USING A 0.5 M SPECTROSCOPIC SYSTEM	83
FIGURE 2.16. SPACE RESOLVED HIGH-RESOLUTION SPECTROMETER ENTRANCE: (A) MULTI-FIBER ARRAY ASSEMBLY FC-446-030, (B) THE OPTICAL SCHEMATIC OF MULTI-FIBER ASSEMBLY, (C) ENTRANCE SLIT, (D) ADJUSTING SCREWS OF THE MULTI-FIBER ARRAY, (E) SCHEMATIC OF ADJUSTING SCREW FROM THE DATASHEET	83
FIGURE 2.17. SPACE RESOLVED HIGH-RESOLUTION SPECTROMETER EXIT PLANE: (A) THE EXIT PORT IN OPEN CONDITION, (B) ATTACHED CCD DV440 AT THE EXIT PORT, (C) EIGHT TRACKS OF THE SPECTROMETER ON CCD IMAGE PLANE, (D) MERCURY EMISSION LINE AT 546 NMS	84

LIST OF FIGURES

FIGURE 2.18. SPOT SIZE ESTIMATION OF TOP AND TANGENTIAL PLATES WITH THEIR RESPECTIVE OPTICS ATTACHED: (A) SPOT SIZE OF THE TOP PLATE WITH COLLIMATOR 2 FROM TABLE 2.3, (B) SPOT SIZE OF TANGENTIAL PORT WITH COLLIMATOR 3 FROM TABLE 2.3.	85
FIGURE 2.19. WAVELENGTH CALIBRATION OF SPACE RESOLVED HIGH-RESOLUTION SPECTROMETER: (A) RECIPROCAL LINEAR DISPERSION MEASUREMENT RED DATA POINTS REPRESENT THE EXPERIMENTALLY MEASURED DISPERSION, AND THE SOLID BLACK LINE REPRESENTS THE CALCULATED DISPERSION, (B) 546 NM EMISSION LINE ACQUIRED FOR FWHM ESTIMATION	86
FIGURE 2.20. INTENSITY CALIBRATIONS: (A) RELATIVE INTENSITY CALIBRATION FACTORS, (B) ABSOLUTE INTENSITY CALIBRATION FACTORS	87
FIGURE 3.1 IN PHOTON EMISSION, AN ELECTRON IN EXCITED STATE M DECAYS DOWN TO A LOWER ENERGY STATE N RELEASING A PHOTON WITH ENERGY H_N . ABSORPTION IS THIS PROCESS IN REVERSE; AN ELECTRON IN LOWER STATE N ABSORBS A PHOTON AND ENTERS THE EXCITED STATE M.	90
FIGURE 3.2. SCHEMATIC OF RADIANCE (L) WHICH IS DEFINED BY RADIANT FLUX PER UNIT SOLID ANGLE $d\Omega$ (KUNZE)	91
FIGURE 3.3. (A) BROADENINGS AFFECTING THE SPECTRAL LINE PROFILE DUE TO DIFFERENT FWHM INCLUDING DOPPLER, INSTRUMENTAL AND ZEEMAN (B) MAGNETIC FIELD PROFILE FOR DIFFERENT RADIUS	100
FIGURE 3.4 FLOW CHART OF SIMULATION CUM MODELLING MATLAB CODE FOR ZEEMAN INFLUENCED SPECTRAL LINE PROFILE	101
FIGURE 3.5 SCHEMATIC OF THE VIEWING GEOMETRY USED FOR THE MULTI-TRACK SPECTROMETER. THE LINES OF SIGHT ARE REPRESENTED BY 1 TO 7 FIBER PASSING THROUGH THE PLASMA RADIAL LOCATIONS 0.083, 0.116, 0.149, 0.182, AND 0.215 m	102
FIGURE 3.6. PLASMA PARAMETERS FOR SHOT #33015	105
FIGURE 3.7 SPACE-RESOLVED MEASUREMENT OF ADITYA-U EMISSION SPECTRA FROM MTS SPECTROSCOPIC SYSTEM	106
FIGURE 3.8: WITHOUT ZEEMAN CONSIDERATION: (A) GAUSSIAN FITTED LINE PROFILE ON EXPERIMENTALLY OBSERVED $C +$ SPECTRAL LINE EMISSION FWHM ~ 0.09 NM. WHERE SOLID DATA POINTS REPRESENT THE EXPERIMENTAL DATA AND THE LINE IS THE GAUSSIAN FITTED CURVE. (B) SPATIAL PROFILE OF $C +$ ION TEMPERATURE ESTIMATION WITHOUT CONSIDERATION OF THE ZEEMAN EFFECT	107
FIGURE 3.9. WITH ZEEMAN'S CONSIDERATION: (A) GAUSSIAN FITTED LINE PROFILE ON EXPERIMENTALLY OBSERVED $C +$ SPECTRAL LINE EMISSION WHERE A TOTAL OF SEVEN ZEEMAN LINES ARE REPRESENTED. (B) SPATIAL PROFILE OF $C +$ ION TEMPERATURE ESTIMATION (BLACK-SQUARE DATA) WITH ABEL INVERTED RADIAL ION TEMPERATURE PROFILE (RED-SQUARE DATA) CONSIDERATION OF ZEEMAN EFFECT	110
FIGURE 3.10. WITH ZEEMAN'S CONSIDERATION: (A) GAUSSIAN FITTED LINE PROFILE ON EXPERIMENTALLY OBSERVED $O_4 +$ SPECTRAL LINE EMISSION WHERE A TOTAL OF SEVEN ZEEMAN LINES ARE REPRESENTED. (B) SPATIAL PROFILE OF $O_4 +$ ION TEMPERATURE	

LIST OF FIGURES

ESTIMATION (BLACK-SQUARE DATA) WITH ABEL INVERTED RADIAL ION TEMPERATURE PROFILE (RED-SQUARE DATA) CONSIDERATION OF ZEEMAN EFFECT	111
FIGURE 3.11. SIMULATED ZEEMAN SPECTRA UNDER THE EFFECT OF 1.5 T MAGNETIC FIELD, (A) 48-ZEEMAN COMPONENTS SIMULATED BY CONVOLUTION OF DOPPLER BROADENING AND INSTRUMENTAL WIDTH. (B) RESULTANT OF 48 ZEEMAN COMPONENTS WHEN $T_e = 0.1$ EV.	112
FIGURE 3.12. FITTING OF $H\alpha$ EXPERIMENTAL SPECTRUM WITH SIMULATED SPECTRA BY CONSIDERING ALL 48 ZEEMAN LINES AND SINGLE TEMPERATURE COMPONENT OF THE HYDROGEN ATOM	114
FIGURE 3.13. FITTING OF $H\alpha$ EXPERIMENTAL SPECTRUM WITH CALCULATED SPECTRA BY CONSIDERING ALL THE 48 ZEEMAN COMPONENTS AND TWO NEUTRAL TEMPERATURE COMPONENTS OF THE HYDROGEN ATOM.	114
FIGURE 3.14. WITH ZEEMAN CONSIDERATION: (A) HOT TEMPERATURE COMPONENTS OF $H\alpha$ NEUTRAL (B) WARM TEMPERATURE COMPONENTS (IN BOTH (A) & (B): BLACK DATA POINTS WITHOUT ABEL-INVERSION TEMPERATURE, RED DATA POINTS ARE WITH ABEL-INVERSION TEMPERATURE).	115
FIGURE 3.15. THE RATIO OF IONIZATION AND THERMALIZATION TIMES FOR C^+ AND O_4^+ IONS VERSUS PLASMA RADIAL LOCATION OF ADITYA-U PLASMA	119
FIGURE 3.16. SCHEMATIC OF THE VIEWING GEOMETRY USED FOR THE MULTI-TRACK SPECTROMETER. THE LINE OF SIGHTS IS AT DIFFERENT RADIAL LOCATIONS $R = -0.16$ M AND $R = -0.13$ M ON THE HIGH FIELD SIDE AND $R = 0.11$ M AND 0.14 M ON THE LOW FIELD SIDES.	120
FIGURE 3.17 TEMPORAL PROFILES OF PLASMA PARAMETERS SHOT#32357 EXPERIMENT (A) PLASMA CURRENT AND LOOP VOLTAGE (B) X-RAY (C) $H\alpha$ AND GAS PUFF SIGNALS	121
FIGURE 3.18 (A) SPACE RESOLVED $H\alpha$, C^+ , AND O_4^+ SPECTRA FOR 4 TRACKS CORRESPONDING TO FOUR LOS (B) TEMPORAL EVOLUTION OF $H\alpha$, C^+ , AND O_4^+ SPECTRA FROM A SINGLE TRACK ($R=-0.13$ M) CORRESPONDING TO ONE LOS OF SHOT#32357	122
FIGURE 3.19 NEUTRAL TEMPERATURE MEASUREMENT RESULT FOR SHOTS #32357 AND #32358 IN LOW FIELD SIDE (+VE SIGN, OUTBOARD) AND HIGH FIELD SIDE (-VE SIGN, INBOARD): (A) DURING 0-20 MS (B) DURING 49-69 MS (C) DURING 98-118 MS OF DISCHARGE	124
FIGURE 3.20 PLASMA POSITION MEASUREMENTS AS A FUNCTION OF TIME	125
FIGURE 3.21 SCHEMATIC OF EXPERIMENTAL ELECTROMAGNETICALLY DRIVEN PELLET INJECTION BASED ON THE CONCEPT OF MAGNETIC LINEAR ACCELERATOR	127
FIGURE 3.22. SCHEMATIC OF THE EXPERIMENTAL SETUP (A)TOP VIEW OF THE MACHINE SHOWING PORTS 10, 14, AND 17 FOR IPI AND SPECTROSCOPY SETUP. (B) ALL THE DIAGNOSTICS (0.5 M VISIBLE SPECTROMETER AND 1 M MULTI-TRACK SPECTROMETER) ARE CONSOLIDATED ON THE MACHINE, AND THEIR RESPECTIVE LOS ARE PRESENTED. (C)IPI - Li_2TiO_3 SETUP. (D) 0.5 M SPECTROMETER FOR TIME EVOLUTION MEASUREMENT OF LI SPECTRAL LINE SHAPE PROFILE AND (E) REPRESENTS THE 1 M HIGH-RESOLUTION SPECTROMETER MEASUREMENT OF SPECTRAL LINE SHAPE AND ITS RADIAL PROFILE.	128

LIST OF FIGURES

FIGURE 3.23. SHOT #33317, A TYPICAL IPI DISCHARGE (A) PLASMA CURRENT (SOLID BLACK LINE) AND LOOP VOLTAGE (RED DASH-DOT LINE) (B) FUEL H _A (656.28 NM, SOLID BLACK LINE) AND LITHIUM (670.8 NM, RED DASH-DOT LINE) LINE EMISSION (C) OXYGEN (441.2 NM, SOLID BLACK LINE) AND CARBON (464.7 NM, RED DASH-DOT LINE) EMISSIONS(D) ELECTRON DENSITY (SOLID BLACK LINE)AND SOFT X-RAY SIGNAL (RED DASH-DOT LINE) (E) RADIATIVE POWER, SOLID BLUE LINE REPRESENTS IPI TRIGGER PULSE AT 52-62 MS.	130
FIGURE 3.24. THE EMISSION SPECTRUM WAS ACQUIRED USING A 0.5 M SPECTROGRAPH TO SEE THE TEMPORAL EVOLUTION OF PLASMA DURING THE IPI EXPERIMENT	131
FIGURE 3.25. THE EMISSION SPECTRUM WAS ACQUIRED USING A 1 M SPECTROGRAPH TO SEE THE SPATIAL EVOLUTION OF PLASMA DURING THE IPI EXPERIMENT	132
FIGURE 3.26. ZOOM PART OF SPACE RESOLVED SPECTRA ACQUIRED WITH THE MULTI-TRACK VISIBLE SPECTROMETER	133
FIGURE 3.27. (A) EXPERIMENTAL LINE PROFILE (B) GAUSSIAN FITTED SPECTRA WITHOUT ABSORPTION	134
FIGURE 3.28. (A) GAUSSIAN FITTED EMISSION SPECTRA, (B) MATCHED SELF-ABSORPTION LINE PROFILE	134
FIGURE 4.1. TIME AND SCALE LENGTHS OF DIFFERENT PWI PROCESSES FIGURE TAKEN FROM (HARTWIG)	139
FIGURE 4.2. PHYSICAL AND CHEMICAL PROCESSES OCCURRING DURING PLASMA SURFACE INTERACTION, A FIGURE TAKEN FROM (HARTWIG)	141
FIGURE 4.3. THE PMT-BASED EXPERIMENTAL SETUP CONSISTS OF TWO SETS OF PMT, EACH HAVING THREE SEPARATE PMTS WITH INTERFERENCE FILTERS FOR WAVELENGTH 656.3 NM, 464.7 NM, AND 441.6 NM (TOTAL OF SIX PMT). ONE SET COLLECT EMISSIONS ALONG THE LINES OF SIGHT TERMINATING ON THE BOTTOM WALL, AND ANOTHER SET TERMINATES ON THE INBOARD TOROIDAL BELT LIMITER.	143
FIGURE 4.4. THE S/XB VALUES FOR (A) NEUTRAL HYDROGEN NEUTRAL, (B) O ⁺ , AND (C) C ²⁺ IONS WHEN CORRESPONDING LINE EMISSION MEASURED AT 656.3, 441.6, AND 464.7 NM	144
FIGURE 4.5. TEMPORAL EVOLUTION OF (A) PLASMA CURRENT I _P , (B) H _A AT 656.28 NM, (C) SPECTRAL LINE AT 441.6 NM (MENTIONED AS OII) FROM O ⁺ , AND (D) LINE AT 464.7 NM (MENTIONED AS CIII) FROM C ²⁺ IONS. THE DASHED BLACK AND SOLID RED LINES REPRESENT THE SIGNALS RECORDED FROM TWO DIFFERENT LOS TERMINATING ON THE LIMITER AND BOTTOM WALL, RESPECTIVELY.	147
FIGURE 4.6. CHANGE IN PARTICLE CONFINEMENT TIME, T _P WITH HYDROGEN INFUX (Γ_H)	148
FIGURE 4.7. THE RECYCLING COEFFICIENT, R, WITH RESPECT TO PLASMA SHOTS NUMBER.	149
FIGURE 4.8. PARTICLE INFUXES OF (A) NEUTRAL HYDROGEN, (B) OXYGEN IMPURITY ION, AND (C) CARBON IMPURITY ION. THE RED CIRCLE AND BLACK SQUARE REPRESENT THE INFUXES MEASURED ALONG THE LOS TERMINATING ON THE LIMITER AND BOTTOM WALL, RESPECTIVELY.	150
FIGURE 4.9. THE RATIO OF IMPURITIES INFUXES WITH NEUTRAL HYDROGEN INFUXES FOR THE LOS TERMINATING ON (A) LIMITER (B) BOTTOM WALL	151

FIGURE 4.10. VARIATION IN FLUX OF HYDROGEN NEUTRAL AND CARBON, OXYGEN IMPURITY ION EMISSIONS	153
FIGURE 4.11. RELATIVE CHANGE IN NEUTRAL AND IMPURITY EMISSIONS WITH LITHIUM EMISSION	155
FIGURE 4.12. PARTICLE INFLUXES OF (A) NEUTRAL HYDROGEN, (B) OXYGEN IMPURITY ION, AND (C) CARBON IMPURITY ION. THE RED CIRCLE AND BLACK SQUARE REPRESENT THE INFLUXES MEASURED ALONG THE LOS TERMINATING ON THE LIMITER AND BOTTOM WALL, RESPECTIVELY.	156
FIGURE 4.13. THE RATIO OF IMPURITIES INFLUXES WITH NEUTRAL HYDROGEN INFLUXES FOR THE LOS TERMINATING ON (A) LIMITER (B) BOTTOM WALL	158
FIGURE 5.1. VARIATION IN DIFFUSION COEFFICIENT WITH COLLISION FREQUENCY AND DIFFERENT PLASMA REGIONS	163
FIGURE 5.2. ELECTRON DENSITY AND ELECTRON TEMPERATURE PROFILE USED FOR IMPURITY TRANSPORT STUDY	168
FIGURE 5.3. TEMPORAL EVOLUTION OF TYPICAL PLASMA DISCHARGE SHOT #33880 (A) BLACK SOLID LINE REPRESENTS PLASMA CURRENT I_P , MAXIMUM $\sim 100 \text{ kA}$, RED SOLID LINE REPRESENTS LOOP VOLTAGE; (B) $H\alpha$ EMISSION MEASURED WITH PMT HAVING WAVELENGTH 656.28 nm AND (C) INTRINSIC IMPURITY EMISSIONS AT 464.7 nm C_2^+ (BLACK SMALL DASHED LINE) AND O^+ AT 441 nm MONITORED (RED SOLID LINE) WITH PMT DIAGNOSTIC	170
FIGURE 5.4. SPACE RESOLVED MEASUREMENT OF CARBON EMISSION PRESENT AT 464.7 nm , HAVING IONIZATION STATE C_2^+	171
FIGURE 5.5. IDENTIFICATION OF OTHER NEARBY EMISSION LINES ALONG WITH CARBON EMISSION	171
FIGURE 5.6. EXPERIMENTALLY MEASURED EMISSIVITY PROFILE OF C_2^+ EMISSION LINE AT 464.77 nm	172
FIGURE 5.7. MATCHED EMISSIVITY PROFILE OF C_2^+ IMPURITY ION	173
FIGURE 5.8. DIFFUSIVITY PROFILE FOR C_2^+ EMISSION	173
FIGURE 5.9. IMPURITY DENSITY PROFILE OF SEVERAL CARBON IONS	174
FIGURE 5.10. SPACE RESOLVED MEASUREMENT OF CARBON EMISSION PRESENT AT 650 nm , HAVING IONIZATION STATE O_4^+	175
FIGURE 5.11. DIFFUSIVITY PROFILE FOR MODELLING OF O_4^+ EMISSION	175
FIGURE 5.12. SIMULATED AND EXPERIMENTAL EMISSIVITY PROFILE OF O_4^+ IMPURITY ION	176
FIGURE 5.13. SPACE RESOLVED MEASUREMENT OF NEON EMISSION PRESENT AT 371.8 nm , HAVING IONIZATION STATE N_e	177
FIGURE 5.14. WAVELENGTH RESOLVED SPECTRUM CONTAINS NEON 371.8 nm ALONG WITH OTHER CARBON EMISSION LINES	177
FIGURE 5.15. DIFFUSIVITY PROFILE FOR N_e^+ EMISSION	178
FIGURE 5.16. MATCHED EMISSIVITY PROFILE OF N_e^+ IMPURITY ION	178
FIGURE 5.17. SPACE-RESOLVED MEASUREMENT OF ARGON EMISSION	179
FIGURE 5.18. DIFFUSIVITY AND DRIFT VELOCITY PROFILES FOR Ar EMISSION	180

LIST OF FIGURES

FIGURE 5.19. MATCHED EMISSIVITY PROFILE OF Ar +IMPURITY ION	180
FIGURE 5.20. VUV SURVEY SPECTRUM AND IDENTIFICATION OF IRON EMISSION LINES	181
FIGURE 5.21. DIFFUSIVITY AND DRIFT VELOCITY PROFILES FOR Fe EMISSION	182
FIGURE 5.22. THE EMISSIVITY OF IRON EMISSION LINES SIMULATED BY STRAHL CODE	182
FIGURE 5.23. THE MASS DEPENDENCY (IN TERMS OF Z) ON IMPURITY TRANSPORT DIFFUSIVITY PARAMETER	183
FIGURE 5.24. THE REACTION RATE COEFFICIENTS AS A FUNCTION OF ELECTRON TEMPERATURE ARE USED FOR CALCULATIONS OF S/XB OF H ₂ AND H ₂ ⁺ IONS.	187
FIGURE 5.25. THE S/XB OF ATOMIC H (SOLID LINE) AND H ₂ (DASHED LINE) AND H ₂ ⁺ (DOUBLE DASHED LINE) ION.	188
FIGURE 5.26. SCHEMATIC DIAGRAM OF THE VIEWING GEOMETRY IN ADITYA-U TOKAMAK. ONE LINE OF SIGHT (LOS-1) PASSES THROUGH THE EDGE REGION ONLY. THE OTHER LINE OF SIGHT (LOS-2) PASSES THROUGH THE CENTER OF THE MACHINE.	189
FIGURE 5.27. RADIAL PROFILES OF ELECTRON (A) DENSITY AND (B) TEMPERATURE ARE USED FOR THE SIMULATION. IN THE ZOOM VIEW OF FIGURE (B) THE SOLID, DASHED, AND DASH-DOT CURVES REPRESENT THE EDGE ELECTRON TEMPERATURE (T _{E, A}) OF 5, 7, AND 10 EV, RESPECTIVELY. THE X-AXIS REPRESENTS THE P, WHICH IS THE NORMALIZED RADIAL LOCATION GIVEN BY “R / A”.	190
FIGURE 5.28. (A) SIMULATED DENSITY PROFILES OF H, H ₂ , AND H ₂ ⁺ FOR THE LINE-AVERAGE DENSITY (<N _E >) 1.37X10 ¹⁹ M ⁻³ AND EDGE ELECTRON TEMPERATURE IS FIXED TO 7 EV (THE DASHED CURVE OF FIGURE (4B)). THE SOLID CURVE REPRESENTS TOTAL NEUTRAL HYDROGEN DENSITY, THE DASHED CURVE REPRESENTS THE DENSITY OF H ₂ , AND THE DASH-DOT CURVE REPRESENTS THE DENSITY OF H ₂ ⁺ IONS. (B) THE SIMULATED EMISSION RATE OF H, H ₂ , AND H ₂ ⁺ . THE SOLID CURVE REPRESENTS THE TOTAL EMISSION RATE, THE DOTTED CURVE REPRESENTS THE EMISSION RATE OF H, THE DASHED CURVE REPRESENTS THE EMISSION RATE OF H ₂ AND THE DASH-DOT CURVE REPRESENTS THE EMISSION RATE OF H ₂ ⁺ . THE X-AXIS REPRESENTS THE P, WHICH IS THE NORMALIZED RADIAL LOCATION GIVEN BY “R / A”.	191
FIGURE 5.29. THE SIMULATED EMISSIVITY PROFILE FOR THE LINE-AVERAGED ELECTRON DENSITY IS 1.3× 10 ¹³ CM ⁻³ AND T _{E, A} IS OF 10 EV. THE SOLID CURVE REPRESENTS TOTAL H _A EMISSIVITY AND THE DASHED CURVE REPRESENTS H _A EMISSIVITY EXCLUDING THE CHARGE-EXCHANGE PROCESS.	192
FIGURE 6.1 SCHEMATIC DEPICTION OF THE DIVERTOR PLASMA IN A FUSION DEVICE AND THE AXIAL PROFILES OF NE AND TE AS THEY FORM DURING TRANSPORT INTO THE DIVERTOR PLATE AT HIGH NEUTRAL PRESSURE. ELECTRON (E), ION (I), NEUTRAL (N), AND IMPURITY ARE ALL DENOTED BY THEIR RESPECTIVE LABELS ON THE PERIODIC TABLE. LARGE BUBBLES REPRESENT ATOMS WITH A HIGH LEVEL OF EXCITATION, AS INDICATED BY THEIR COLOUR (HAYASHI ET AL.).	200
FIGURE 6.2. EXPERIMENTAL SETUP ON LINEAR PLASMA DEVICE	202
FIGURE 6.3 IDENTIFIED MOLECULAR BANDS OF NITROGEN ALONG WITH H _A AND H _B LINES	206

LIST OF FIGURES

FIGURE 6.4 EXPERIMENTALLY MEASURED TEMPERATURE WITH BOLTZMANN PLOTS FOR $\Delta N = 4$ BAND (A) EXPERIMENTALLY MEASURED DATA AND GAUSSIAN FITTINGS OF EACH TRANSITION, (B) BOLTZMANN PLOT	210
FIGURE 6.5. EXPERIMENTALLY MEASURED TEMPERATURE WITH BOLTZMANN PLOTS FOR $\Delta N = 3$ BAND (A) EXPERIMENTALLY MEASURED DATA AND GAUSSIAN FITTINGS OF EACH TRANSITION, (B) BOLTZMANN PLOT	211
FIGURE 6.6. EXPERIMENTALLY MEASURED TEMPERATURE WITH BOLTZMANN PLOTS FOR $\Delta N = 2$ BAND (A) EXPERIMENTALLY MEASURED DATA AND GAUSSIAN FITTINGS OF EACH TRANSITION, (B) BOLTZMANN PLOT	212
FIGURE 6.7. SIMULATED SPECTRA FOR BAND (A) $\Delta N = 4$, (B) $\Delta N = 3$ AND (C) $\Delta N = 2$	213
FIGURE 6.8. IDENTIFIED MOLECULAR BANDS OF HYDROGEN	214
FIGURE 6.9. ESTIMATED TEMPERATURE USING BOLTZMANN PLOT METHOD FOR $\Delta v = 4$ band AFTER SUPPRESSING EFFECT OF FULCHER BAND IN MEASUREMENT	215
FIGURE 6.10. SIMULATED SPECTRA FOR BAND $\Delta N = 4$	216
FIGURE 6.11. SIMULATED SPECTRA FOR BAND $\Delta N = 3$	216

LIST OF TABLES

TABLE 1.1. FUSION REACTIONS AND ENERGY PRODUCE.....	37
TABLE 2.1. ADITYA-U TOKAMAK DESIGN PARAMETERS	59
TABLE 2.2. SPECTROSCOPICALLY MEASUREMENT ASPECT AND PLASMA PARAMETERS	76
TABLE 2.3. SEVERAL COLLIMATORS AND THEIR OPTICAL SPECIFICATION	78
TABLE 2.4. LIST OF OBSERVED EMISSIONS WITH PMT/PHOTODIODE	81
TABLE 3.1. THE BASIC ATOMIC PROCESSES IN PLASMA (B-B IS BOUND-BOUND TRANSITIONS, F-F IS FREE-FREE TRANSITIONS, AND B-F IS BOUND-FREEE TRANSITIONS. C IS THE COLLISIONAL PROCESS, AND R REPRESENTS RADIATIVE PROCESS)	90
TABLE 3.2 ATOMIC DATA AND IONIZATION ENERGY FOR ALL THE IONIZATION STAGES OF HYDROGEN (H), CARBON (C), AND OXYGEN (O)	105
TABLE 3.3. ZEEMAN COMPONENTS OF $C1 +\text{ION}$	106
TABLE 3.4. ZEEMAN COMPONENTS OF $O4 +\text{ION}$	109
TABLE 3.5. FINE-STRUCTURE TRANSITIONS OF $H\alpha$	113
TABLE 3.6. THE INTENSITY OF DIFFERENT EMISSIONS FOR $H\alpha$	116
TABLE 3.7 IONIZATION AND THERMALIZATION TIME OF CARBON AND OXYGEN IMPURITY IONS	119
TABLE 4.1 SUMMARY OF MEASURED INFLUXES FROM DIFFERENT LOSS AND INTEGRATED INFLUX PER SEC	153
TABLE 4.2. REDUCTION IN THE EMISSIONS FROM GRAPHITE LIMITER AND SS WALL SURFACES	154
TABLE 4.3. SUMMARY OF MEASURED INFLUXES FROM DIFFERENT LOSS AND INTEGRATED INFLUX PER SEC	157
TABLE 5.1. DIFFERENT CLASSICAL AND NEO-CLASSICAL REGIMES AND THEIR PARTICLE FLUX, DIFFUSIVITY, AND CONVECTIVE TERMS	164
TABLE 5.2. ADITYA-U PLASMA PARAMETERS SET IN THE PROGRAM FOR MODELLING	168
TABLE 5.3. MOLECULAR PROCESSES CONSIDERED FOR INFLUX ESTIMATIONS	187
TABLE 5.4 H_A INTENSITY AND PARTICLE INFLUXES FROM ATOMIC H, MOLECULAR H_2 , AND MOLECULAR H_2^+ ION BASED ON EQUATIONS (4) AND (1), RESPECTIVELY, FOR VARIOUS EDGE ELECTRON TEMPERATURES ($T_{e,a}$). THIS ESTIMATION IS DONE BY CONSIDERING A VIEWING CHORD PASSING THROUGH THE WHOLE PLASMA AND ALONG THE HORIZONTAL MIDPLANE (LOS-2 AS PER FIGURE 5.26).....	192
TABLE 5.5 THE H_A INTENSITY AND PARTICLE INFLUXES FROM ATOMIC H, MOLECULAR H_2 , AND MOLECULAR H_2^+ ION BASED ON EQUATIONS (4) AND (1), RESPECTIVELY, FOR VARIOUS EDGE ELECTRON TEMPERATURES ($T_{e,a}$) ONLY AT THE EDGE REGION. THIS ESTIMATION DONE FOR THE EXPERIMENTAL CONDITION WHEN VIEWING THE CHORD IS PASSING THROUGH THE EDGE PLASMA (LOS-1 AS PER FIGURE 5.26).....	193
TABLE 6.1. WAVELENGTH DATA FOR $\Delta\nu = 4$	208
TABLE 6.2. WAVELENGTH DATA FOR $\Delta\nu = 3$	208

LIST OF FIGURES

TABLE 6.3. WAVELENGTH DATA FOR $\Delta\nu = 2$	209
--	-----

ABSTRACT

The “edge” region of tokamak plasma separates the hot core plasma from the material boundary. The proper understanding of this plasma region is very crucial for maintaining the hot fusion grade core plasma and to provide the adequate gas fuelling. Spectroscopic diagnostics remain the most reliable diagnostic method for diagnosing the edge plasmas. This thesis presents the detailed characterization of ADITYA-U tokamak's edge plasma using various spectroscopic techniques by carrying out experiments, simulations, and modelling. ADITYA-U tokamak has a major/minor radius of 0.75 m/0.25 m respectively with a toroidal magnetic field of $\sim 0.75 - 1.5$ T and plasma currents of $\sim 80 - 250$ kA. The passive spectral emissions from fuel neutrals and impurity-ions are measured using spectrometers and filter-photomultiplier-tube combinations. The collection optics are designed according to the experimental requirements.

The ion/neutral temperatures are estimated from the line shapes of the measured spectra. Estimation of ion/neutral temperatures by supposing the spectral lines are only broadened by the Doppler broadening leads to large temperature values which cannot be explained reasonably. This anomaly in ion/neutral temperature estimation is removed by introducing the broadening by the Zeeman splitting as the emissions are subjected to magnetic fields in tokamaks. This has led to several interesting results such as the existence of a poloidal asymmetry in fuel-neutral temperature obtained from the H_{α} spectra. The fuel neutrals acquire relatively higher temperatures (~ 4 eV) on the high-field side as compared to the low-field side (~ 2 eV). Analysis of H_{α} -spectra also revealed the presence of warm and hot fuel neutrals, originating from different atomic and molecular processes. Using the Zeeman-corrected temperatures, the radial profile of C^+ and O^{4+} ion temperatures reveal higher ion temperatures at the locations of MHD islands which may be related to the transport of ions inside the magnetic islands. Furthermore, Li density and radiative power losses are estimated from the opacity-influenced Li spectral emission in the Li_2TiO_3 particle injection experiments.

The thesis also contributes to the understanding of edge plasma's interaction with the graphite-limiter and the stainless-steel vessel-wall. The spectral intensities of H_{α} , O^+ and C^{2+} emissions are measured from the vessel-wall and limiter. Interestingly, it has been observed that the graphite-limiter and the vessel-wall contribute almost equally to carbon recycling. It has been concluded that the unexposed vessel-wall acts as a sink and becomes a source after several plasma discharges.

ABSTRACT

Furthermore, it has been observed using the DEGAS2 code that the molecular processes cannot be ignored in estimating hydrogen influx using the ionization per photon (S/XB) factor for $T_e < 7$ eV in the edge region. Using the impurity transport code STRAHL, the diffusivities of C, O, Ne, Ar, and Fe impurity species illustrate a clear dependency of impurity-mass on impurity transport.

For establishing the measurements techniques of vibrational temperatures of N₂ molecule in tokamak far-edge/divertor regions, experiments are carried out in radio-frequency produced nitrogen-contaminated hydrogen plasmas. The vibrational temperatures of N₂ molecules are estimated using the Boltzmann method by recording the different N₂ molecular bands. The contribution of hydrogen Fulcher-band contaminating the N₂ 1PS bands are identified and successfully removed using line-shape simulations.

प्राककथन

इस शोध—प्रबंध में आदित्य—यू टोकामक में प्लाज्मा के किनारे के क्षेत्र को विभिन्न स्पेक्ट्रोस्कॉपी पद्धतियों जैसे कि प्रयोग, सिमुलेशन, तथा प्रतिरूपण द्वारा विस्तृत रूप से अध्ययन किया गया है। टोकामक—प्लाज्मा के किनारे का क्षेत्र वह क्षेत्र है, जो कि उच्च तापमान वाले प्लाज्मा के केन्द्रीय मुख्य भाग को टोकामक की वैसेल दीवार की आंतरिक सतह से अलग करता है। इस क्षेत्र का समुचित ज्ञान प्लाज्मा अवस्था की निरंतरता एवं संलयन करने वाली गैसों की पर्याप्त मात्रा में उपलब्धता के निर्धारण के लिए आवश्यक है। आदित्य—यू टोकामक की दीर्घ/लघु त्रिज्या क्रमशः $0.75 / 0.25$ मीटर, टोरॉयडल चुंबकीय क्षेत्र $0.75\text{--}1.5$ टेस्ला एवं प्लाज्मा विद्युत—धारा $80\text{--}250$ किलो—एम्पियर है। उदासीन—ईंधन परमाणुओं एवं अशुद्ध आयनों से प्राप्त उत्सर्जित वर्णक्रम को स्पेक्ट्रोमीटर एवं निस्पंदक फोटॉन गुणित ट्यूब के संयोजन द्वारा मापा गया है। संग्रह प्रकाशिकी का चुनाव विभिन्न प्रायोगिक आवश्यकताओं के अनुसार किया गया है।

टोकामक प्लाज्मा में उपस्थित आयन एवं उदासीन परमाणुओं का तापमान, प्रकाश वर्णक्रम की त्रीवता और तरंगदैध्य के रेखा—आकार से अनुमानित किया गया है। यदि आयन/उदासीन कण के तापमान निर्धारण के दौरान उनके रेखा—आकार में विस्तार होने की प्रक्रिया में केवल डॉप्लर (Doppler) विस्तार को सम्मिलित किया जाए, तो तापमान का मान असंगत प्राप्त होता है, जिसकी यथोचित रूप से व्याख्या कर पाना संभव नहीं है। आयन/उदासीन कण के तापमान अनुमान के दौरान आयी, इस असंगति के निराकरण के लिए ज़ीमान (Zeeman) विभाजन प्रक्रिया द्वारा वर्णक्रम का विस्तार होना शामिल किया गया है, क्योंकि इन विकिरणों का उत्सर्जन टोकामक के चुंबकीय क्षेत्र की उपस्थिति में होता है। इसके परिणामस्वरूप $H\alpha$ वर्णक्रम के द्वारा ईंधनीय—उदासीन कणों के तापमान में पोलोइडल विषमता पायी गयी है। इन कणों का उच्च—चुंबकीय क्षेत्र की ओर अधिक तापमान ($\sim 4\text{eV}$) एवं निम्न—चुंबकीय क्षेत्र की ओर कम तापमान ($\sim 2\text{eV}$) देखा गया है, जो कि इस विषमता को दर्शाता है। $H\alpha$ वर्णक्रम के रेखा—आकार के विश्लेषण द्वारा, विभिन्न परमाणविक एवं आणविक प्रक्रियाओं से उत्पन्न होने वाले उष्ण एवं शीतल ईंधन/उदासीन कणों की उपस्थिति पायी गई है। ज़ीमान (Zeeman) संशोधित तापमान द्वारा, C^+ एवं O^{4+} आयनों के त्रिज्यीय दिशा में बदलाव से यह प्रतीत होता है कि एमएचडी द्वीप की उपस्थिति में इन अणुओं का तापमान का मान बढ़ने लगता है, जो कि चुंबकीय द्वीप में आयनों के परिवहन से संबंधित हो सकता है। Li_2TiO_3 के कण—अन्तक्षेपण: प्रयोग के दौरान अपारदर्शिता से प्रभावित Li^0 के वर्णक्रमीय उत्सर्जन से प्राप्त रेखा—आकार के विश्लेषण द्वारा लीथियम का घनत्व और विकिरण शक्ति का आंकलन किया है।

यह शोध—प्रबंध प्लाज्मा में किनारे के क्षेत्र पर लगे ग्रेफाइट सीमक, जो कि टोकामक के अंदर प्लाज्मा की सीमा का निर्धारण करता है एवं जंगरोधी इस्पात की वैसेल दीवार के मध्य होने वाली क्रियाओं को स्पेक्ट्रोस्कॉपी के माध्यम से समझने में मदद करता है। $H\alpha$, O^+ तथा C^{2+} आयनों की वर्णक्रमीय तीव्रता को वैसेल दीवार और ग्रेफाइट सीमक से प्राप्त वर्णक्रमीय उत्सर्जन द्वारा मापा गया है। यह भी देखा गया है

ABSTRACT

कि कार्बन पुनर्चक्रण में ग्रेफाइट सीमक तथा वेसैल दीवार का समान योगदान होता है। इससे यह निष्कर्ष निकलता है, जब तक वेसैल दीवार का प्लाज्मा के साथ संपर्क कम होता है, तब तक वह अभिगम की तरह कार्य करती है, अन्ततः अनेक प्लाज्मा प्रयोगों के बाद वह स्त्रोत की तरह व्यवहार करने लगती है।

हाइड्रोजन अन्तर्वाह का आंकलन आयनीकरण प्रति फोटॉन कारक का प्रयोग करते हुए, DEGAS2 कोड द्वारा किया गया है। प्लाज्मा के किनारे के क्षेत्र में जहाँ इलेक्ट्रॉन का तापमान 7 eV से कम होता है, वहाँ DEGAS2 कोड द्वारा हाइड्रोजन अन्तर्वाह को ज्ञात करते समय आण्विक प्रक्रियाओं के योगदान को नकारा नहीं जा सकता है। अशुद्धि-परिवहन कोड STRAHL के उपयोग से कार्बन, ऑक्सीजन, नियोन, ऑर्गन तथा आयरन जैसे अशुद्ध आयनों के विसरण द्वारा इनके परिवहन पर आयनों के द्रव्यमान की निर्भरता को दर्शाता है।

इस शोध-प्रबंध में टोकामक के सुदूर किनारा/डाइवर्टर क्षेत्र में नाइट्रोजन अणुओं के कंपन्न-तापमान (Vibrational temperature) के माप विधियों को स्थापित करने के लिए रेडियो आवृत्ति द्वारा बनाए गए नाइट्रोजन युक्त हाइड्रोजन प्लाज्मा में अनेक प्रयोग किए गए हैं। नाइट्रोजन अणुओं के कंपन्न तापमान का आंकलन बोल्ट्जमान (Boltzmann) पद्धति द्वारा नाइट्रोजन के विभिन्न आण्विक बैंडों द्वारा किया गया है। इन प्रयोगों द्वारा पाया गया है कि यह हाइड्रोजन के फलचर बैंड नाइट्रोजन के 1PS बैंड को दूषित करते हैं, जिनको रेखा-आकार सिमुलेशन द्वारा सफलतापूर्वक पृथक करने के पश्चात् नाइट्रोजन अणुओं का उचित कंपन्न-तापमान का निर्धारण किया गया है।

Chapter 1. Introduction

If you want to shine like a sun, first burn like a sun.

— Dr. A. P. J. Abdul Kalam



Figure 1.1. An artistic representation of stars - gravitationally confined fusion reactors at the top and fossil fuel-generated human power consumption at the bottom. (Famous artwork - "The Starry Night Over the Rhone by Vincent Van Gogh. ") (Vincent van Gogh)

The *fusion* reaction between two light nuclei ($Z < Z_{Fe} = 26$) produces heavy nuclei and releases enormous energy. The painting by *Vincent Van Gogh* Figure 1.1, “a starry night” represents a very nice artistic scenic view of myriad tiny stars in the sky, each of them producing

a fusion reaction inside them. The enormous amount of energy released by our star “Sun” nurture human existence on earth. However, over the centuries (since 1880 (Williams et al.)), humankind has been using fossil fuels as a source of energy to generate electricity. The fossil fuel-generated electricity power lightens the street lights in Figure 1.1.

1.1. Fusion for society

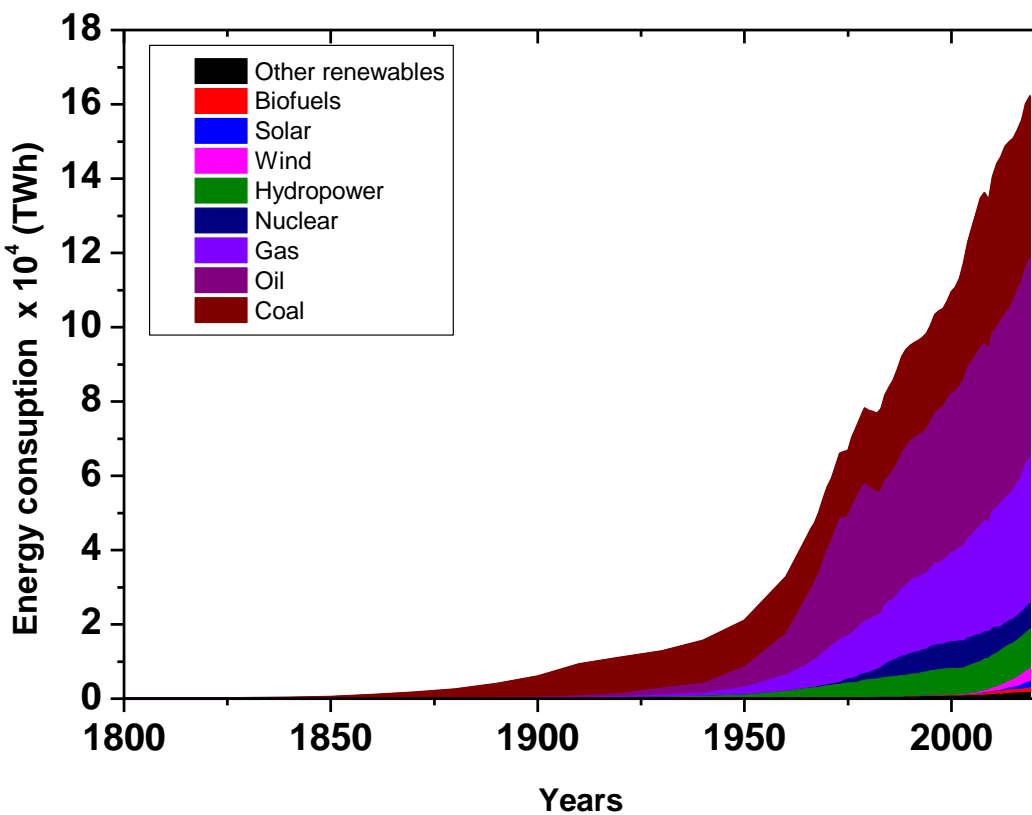


Figure 1.2. Worldwide energy consumption trend (Kumar)

Energy demands, which started with lighting the streets, are increasing exponentially due to the growing population and industrialization all over the world. These large-scale energy necessities have been fulfilled since the 18th century mainly by fossil fuel supplies: coal, oil, and natural gases, as seen with data statistics in Figure 1.2 (Kumar). Other fuels, including nuclear fission, hydroelectricity, wind, and solar, contribute only 14.5% of global energy utilization. However, the utilization of fossil fuels further results in carbon dioxide (CO_2) emissions into the earth's periphery (Kumar); this gas is mainly responsible for the global warming phenomena witnessed by the world (Freidberg). There has been a drastic increase in CO_2 emission since the mid-20^s due to subsequent energy consumption (Boehm and Schumer; Zhang and Trygve Magne Eikevik). A rapid reduction in fossil fuel supplies due to limited resources is suspected. Due to this, humans can rely on fossil fuels until the end of the 20th

century at the cost of increasing carbon emissions, pollution, and human health-related issues. For the future survival of humankind, a sustainable, abundant, and carbon-free long-term energy source from nuclear fusion power is needed urgently (<http://www.ITER.org/sci/fusion>).

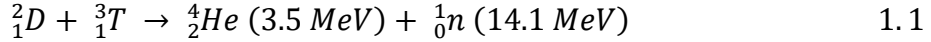
1.2. Controlled Nuclear Fusion: bringing Sun onto Earth

Fusion research aims to harness the energy generated by the controlled nuclear fusion reaction on the earth, which is considered as an artificial Sun on the Earth, the fusion of hydrogen nuclei produces about 600 million tonnes of helium every second, along with an enormous amount of energy (McCracken and Stott). For two nuclei to fuse, a strong-nuclear binding force should be dominant to overcome the Coulomb repulsion of two nuclei. The hydrogen isotope requires less binding energy than any other periodic table element (Loudon). There is a variety of possible candidates for fusion reaction which are generally considered. They are listed in Table 1.1. For facilitating fusion reactions on the earth, the gravitational force present on the sun should be compensated (Eni Staff).

Table 1.1. Fusion reactions and energy produce

Reaction	Threshold energy (MeV)	Maximum plasma temperature	Maximum energy gain (keV)
$D + T \rightarrow {}^4He + n$	17.6	4	1800
$D + D \rightarrow {}^3He + p$	3.2	50	70
$D + D \rightarrow T + p$	4.0	50	80
$D + {}^3He \rightarrow {}^4He + p$	18.3	100	180
${}^6Li + P \rightarrow {}^4He + {}^3He$	4.0	900	6
${}^6Li + D \rightarrow {}^7Li + p$	5.0	>900	6
${}^6Li + D \rightarrow T$ + ${}^4He + p$	2.6	>900	3
${}^6Li + D \rightarrow 2({}^4He)$	11.0	>900	22
${}^7Li + p \rightarrow 2({}^4He)$	177.5	>900	18
${}^{11}B + p \rightarrow 3({}^4He)$	8.7	300	30

A considerable amount of external energy is required to energize the fusing nuclei. This energy is equivalent to a temperature of $\sim 150,000,000^\circ$ C. However, one of the favorable reactions is that concerning the hydrogen isotopes Deuterium and Tritium (D-T) since it has a higher cross-section as compared to other reactions (Bosch and Hale):



This fusion reaction produces α -particle of energy 3.5 MeV and the 14.1 MeV neutron. The deuterium isotope is stable and naturally occurring in a fraction of 0.0156% of seawater hydrogen atoms. On the other side, tritium has a half-life of 12.32 years. In the current scenario, the power plants will be designed in which an energetic neutron will interact with lithium and produce tritium, i.e., the tritium breeding incorporated in the current fusion reactors. The D and T get confined and heated to a specific high temperature inside the vacuum chamber. This high-temperature requirement brings the gas into a 'plasma' state; species get ionized and retain the charge state.

The necessary condition for the self-sustained fusion called ignition should satisfy the "Lawson criteria" (Lawson). Lawson criteria state the relationship of the triple product of plasma density (n_e), temperature (T_e), and confinement time (τ_e) by the equation must satisfy the following inequality $n_e T_e \tau_e > 3 \times 10^{21} \text{ keV} \cdot \text{s} \cdot \text{m}^{-3}$. This describes the quality of plasma in any fusion reactor. Attaining this condition makes the plasma self-sustaining to have the fusion reaction take place with high-confinement time. The maximum cross-section of the D-T reaction is at 40 keV. This reaction requires $T_e \sim 1 - 10 \text{ keV}$ for fusion plasma to happen (Chen; Miyamoto). For the controlled nuclear fusion on earth without strong gravitational forces as in the Sun, two approaches are followed: (a) ICF: Inertial Confinement Fusion, (b) MCF: Magnetic Confinement Fusion. In ICF, plasma production and confinement with the laser. The National Ignition Facility (NIF), USA, has established the production of 1.37 MJ of fusion energy through ICF; the same is named "burning plasma" (Zylstra et al.). More recently, on 5th December 2022, Lawrence Livermore National Laboratory facility in Northern California achieved the milestone of net energy gain through 2.05 MJ of input laser power giving an output power of 3.05 MJ (Achenbach and Halper).

1.3. Tokamak: Advanced machine for fusion

In the MCF approach, plasma gets confined through magnetic fields by restricting particle motion in a perpendicular direction. The primary MCF devices with this configuration are the

'tokamak' and 'stellarator.' In 1950 Russian scientists projected the design for an MCF device, the tokamak (Wesson and Campbell). Later in 1951, the stellarator concept was introduced (Herman). In the stellarators, the helical-shaped magnetic field is designed from the outside. However, in the tokamak, the poloidal magnetic field is generated by plasma current, and the toroidal field is produced externally through electromagnets. As research progressed, it was found that the tokamak concept is more promising and efficient than the stellarator.

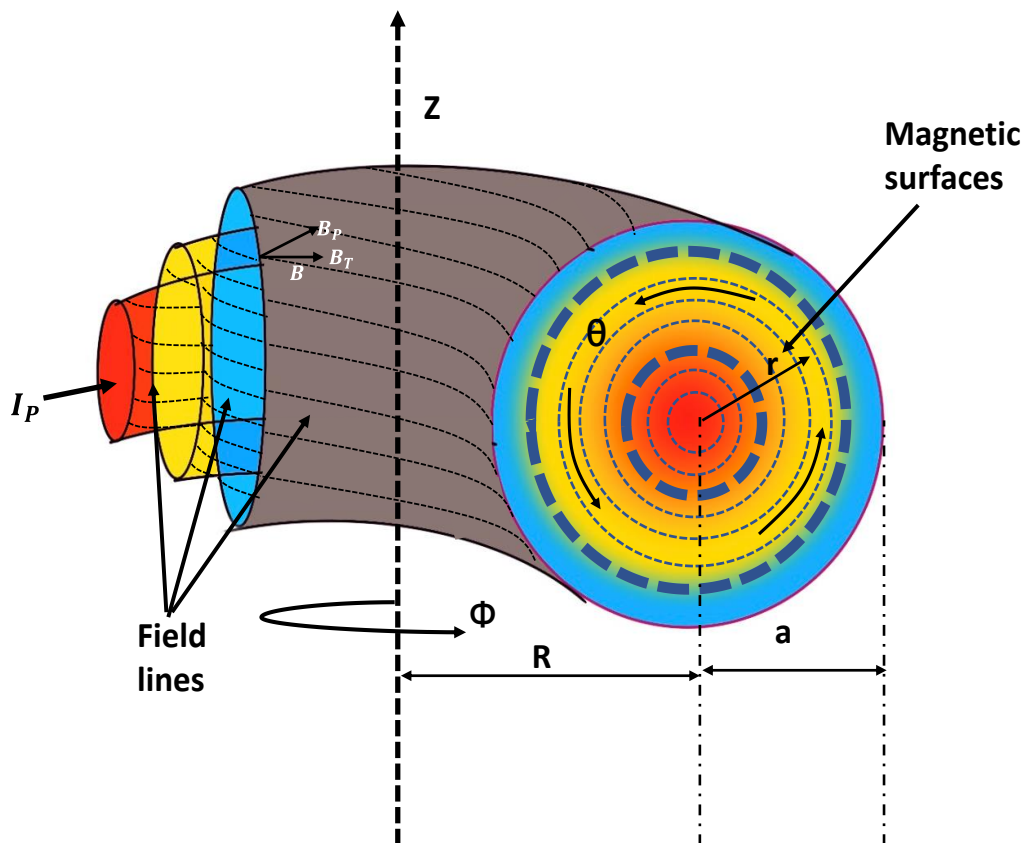


Figure 1.3. Pictorial representation of plasma magnetic fields and flux surfaces

The tokamak conceptualizes as a doughnut-shaped vacuum vessel surrounded by the magnetic field generated through the transformer action of conducting loop voltage; the magnetic field is in the toroidal direction. The pre-filled fuel gas becomes ionized by the toroidal electric field generated by the central solenoid and reaches the plasma state. The plasma conducts fluid that flows in a toroidal direction confined by a toroidal magnetic field. The motion of the plasma electron in the toroidal direction generates plasma current in the toroidal direction which produces a magnetic field in the poloidal direction. Therefore, the combination of the externally applied toroidal magnetic field and the plasma generated poloidal magnetic field, makes the total magnetic field helical in nature. It drives the plasma current in the toroidal path. The particle has a gyrating motion with a gyro radius $\rho_L = v_\perp/\omega_c$ (Larmor radius) in the

perpendicular direction to the magnetic field lines with a frequency $\omega_c = |q|B/m$ (cyclotron frequency). Where q is the particle's charge, m is the particle's mass, B is the magnetic field strength, and v_\perp is the particle's velocity in the perpendicular direction. It is evident that in the ideal scenario, increasing B will increase ω_c . Subsequently, a reduction in ρ_L means the charged particle's motion is minimized in the perpendicular direction and becomes confined in a magnetic field. Figure 1.3 shows the toroidal and poloidal directions represented by ϕ and θ , respectively. R and a are the major and minor plasma radii, respectively, with marked helical magnetic field B , which creates the flux surfaces, as shown in Figure 1.3. However, due to the geometry of the tokamak, various drift motion of the particle comes into the picture, and perpendicular transport becomes higher, as was thought in an ideal scenario. Due to non-uniform E and B fields, there is particle drift. Due to curvature drifts, asymmetries in plasma particles are present; along with this, the magnetic field lines break up, and reconnection gives rise to magneto-hydrodynamic (MHD) instabilities and hence radial losses of plasma. The particle motion has remained parallel to the magnetic field and radially outward perpendicular to the field. Hence, the particle diffuses radially outward to the field lines. Together limits the achievement of plasma confinement. Not only that, it is found that the edge plasma is interlinked with core plasma, where the maximum number of fusion reactions occur. As the edge plasma is connected to the first wall of the tokamak, the plasma-wall interaction is an essential aspect of the tokamak research.

Still, the tokamak is the leading candidate for fusion reactor-based experiments. In the past 60 years, R&D related to the tokamak has been intensively performed. The highest value of fusion triple product is $1.1 \pm 0.3 \times 10^{21} \text{ m}^{-3} \cdot \text{s} \cdot \text{keV}$ reached by JT-60 tokamak in Japan in 1994 (Mori et al. 6). It has given thrust to initiate the International Thermonuclear Experimental Reactor (ITER) megaproject with the contribution of more than seven countries, including developed and developing countries. This project was started officially in 1988. One of the objectives of the ITER project is to achieve the Q-value 10 ((producing 500 MW of fusion power for 50 MW consumed by the heating systems). The Q-value is the plasma gain factor, defined by the ratio of power generated by fusion to the power input for fusion $P_{\text{fusion}}/P_{\text{aux}}$. The Maximum achieved Q-value is claimed 0.67 with 24 MW of P_{aux} and 16 MW of P_{fusion} in Joint European Torus (JET) in 1997 (EUROfusion). However, JET recently produced 59 MW of power in 2022, smashing all the past energy production records (Gibney). In 2004 the Tore Supra tokamak in France set the record for the most prolonged plasma discharge of 390 seconds (Houtte et al.). Also, there is outstanding progress in theory and technology related to tokamak research (Furth; Artsimovich).

1.4. Plasma-wall interaction

The highly energetic particles from the plasma interior encroach on the walls and generates heat and particle loads. The particle and energy transport occurs across the magnetic field lines. The surface in contact with plasma acts as the continuous source and sink of fuel (hydrogen neutrals) and non-fuel (impurity ions) particles. During this process, the particle undergoes interaction with other electrons leaving the former at excited state and subsequently radiating before reaching to the material surface. The total power loss in the form of electromagnetic radiation, which occurs through line radiation from atomic transitions and recombination of ions, and synchrotron radiation/bremsstrahlung in the plasma is known as radiations loss and defined as a product of charge ion density, electron density and radiative cooling factor (Glöggler). It leads to power loss from the central plasma. The particles transfer their kinetic energy to the wall surface, also charged particles are neutralized by interacting with the wall. The neutral particle is generated in front of the wall, and they interact with the central plasma. Through the charge-exchange process, the neutrals gain energy and again go back to the wall and contribute to wall loading. The neutrals re-ionize through the ionization process and again return to the charged state; this is the particle recycling process. In an ideal condition, during steady-state plasma operation, the flux of neutral and charged particles must be equal.

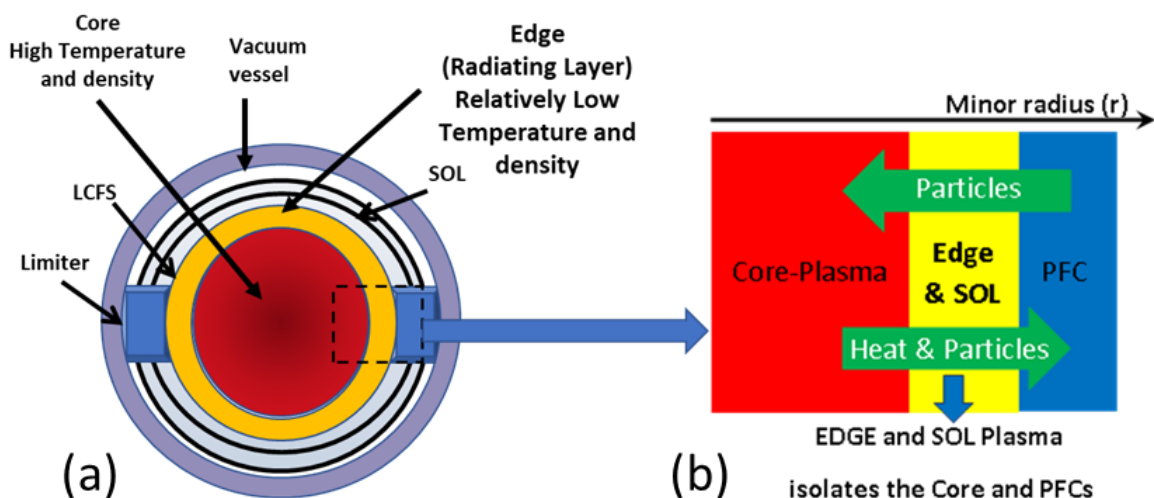


Figure 1.4. Pictorial representation of plasma cross-section and different regions. Plasma core with high temperature and high density

For better plasma confinement, plasma-wall contact must be minimized and controlled. The limiter surface concept has been introduced to restrict the central plasma's volume from the vessel-wall. Here the field lines break, and particles are scrapped out of plasma with low energy.

On the other hand, the positive side of plasma-wall interaction is that the "ash product" generated in the fusion reactor can easily migrate to the edge and be further removed through the advanced diverter concept (Loarte). The tokamak cross-section, including plasma and vessel-walls, can be distributed mainly in two regions, as shown in Figure 1.4 (Strangeby and McCracken):

- (a) Core region: This represents the central zone of the plasma where plasma density and temperatures are relatively higher and their gradients are shallower. The eventual goal of tokamak research is to improvise the plasma core condition in terms of achieving the triple product for nuclear fusion.
- (b) Boundary plasma (edge and scrap off layer): Here, the temperature and density (~ 1 to 40 eV and $\sim 1 - 3.5 \times 10^{18} \text{ m}^{-3}$ respectively in the case of ADITYA – U) are relatively much lesser than the core region of the plasma where the temperature and density ($\sim 250 - 500$ eV and $\sim 1 - 4 \times 10^{19} \text{ m}^{-3}$ respectively for ADITYA-U). The edge plasma region meets the material surfaces, and the gradient in plasma parameters are much steeper in this region. The boundary layer inside the last closed flux surface (LCFS) is known as the edge layer, where particles follow the magnetic field line. The layer outside the LCFS is known as the scrape-off layer (SOL), the collision processes dominated in this region. This region is having even lower temperatures than the edge region, and particle motion is generally in a radially outward direction.

In other words, edge plasma is described as a region of the plasma periphery surrounding the gradient in the neighborhood of LCFS. As described in Figure 1.4 and Figure 1.5 (a), a limiter can define the surface. In limiter tokamaks, the edge plasma remains close to the main chamber. Hence the plasma-wall interactions can more prominently affect the central plasma by introducing impurities into the plasma core. Also, the SOL region remains hot due to neutral recycling, and the wall continues to release impurities. As a result, the divertor concept is more beneficial than the limiter concept; most tokamaks are moving towards the divertor through its upgrade. It allows the open field lines to divert from the main chamber onto the divertor plates. It is done with externally applied divertor magnetic fields. The plasma-wall interaction becomes localized onto the divertor plate (Figure 1.5(b)). A small amount of magnetic field lines is present in the X-point region. Also, field lines are needed to follow the long path to reach the target plates (from central plasma to SOL to target plates). The particle density is high to collide with themselves several times. It produces parallel temperature gradients. The temperature in the divertor region falls less (< 5 eV), and the neutrals cannot get re-ionize. Neutrals accumulate

and produce a sharp pressure gradient. The temperatures can also fall below 1 eV in a specific condition of H-mode plasma, such as in detached plasma. In this condition, the plasma becomes detached from the target plates. Here, electron-ion recombination becomes very important to understand. The future fusion reactor, ITER, is based on the divertor concept for its power exhaust management. Another benefit of this configuration is that the H-mode can quickly achieve, as reported by ASDEX tokamak (ASDEX Team).

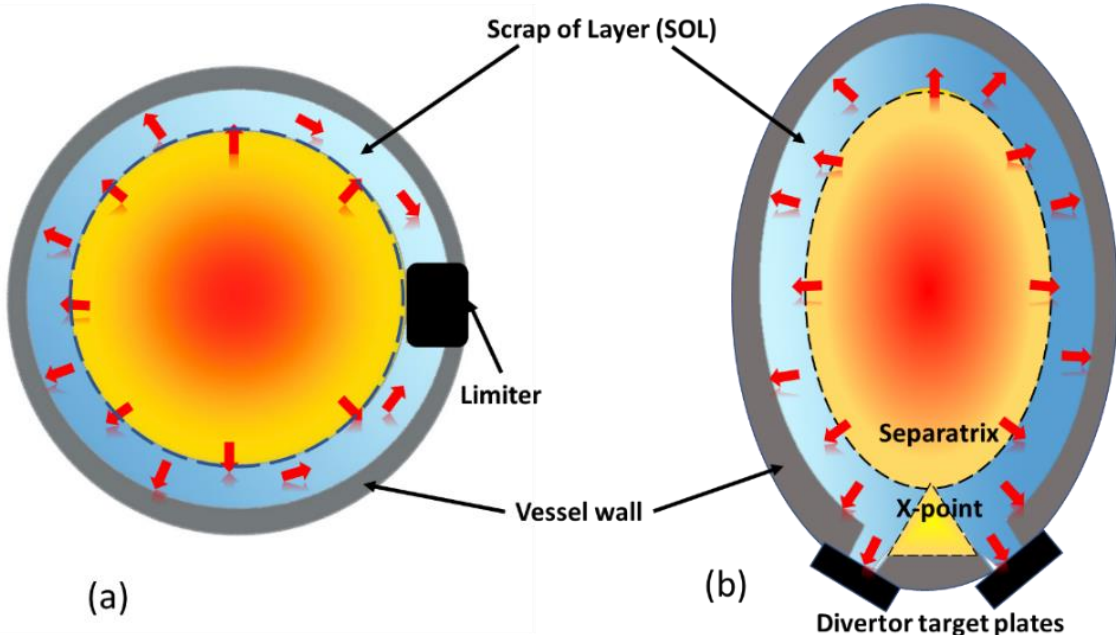


Figure 1.5. Limiter and divertor plasma geometries

1.5. Role of tokamak edge region for better plasma confinement

The principal task of tokamak research is to have a better-confined plasma. To obtain this, the edge plasma conditions should be optimized to achieve better core confinement, fulfilling the Lawson criterion. The primary constraint is the sparse knowledge of the relationship between the core and edge plasma. Through the edge region of the tokamak, the plasma directly interacts with plasma-facing components (PFCs). The unwanted ions enter the central plasma and modify the plasma conditions. Through the edge region, the high heat loads of the main plasma are transferred to the PFC via particles, which may damage the surface. In other words, the edge plasma region is the isolation layer (junction) between core plasma (hotter) and PFCs (cooler). Optimizing the edge plasma conditions is essential to have the desired core plasma conditions. The edge plasma controls many parameters, such as particle confinement, the plasma neutral, and impurity ion densities (Lipschultz et al.). The edge plasma condition plays a vital role in the H-mode plasma operations, whereas neutral play a crucial role in the pedestal

formation at the edge requires the high confinement of the core plasma. Overall, the edge also plays a vital role in achieving better confinement via IOC (Improved Ohmic confinement) and superhot plasma mode (Ongena and Messiaen; Rice et al.; McCormick et al.). However, understanding the tokamak edge still requires lots of effort as it involves complicated physical geometry and atomic and molecular processes. Considering that lots of efforts have been devoted to experimental and theoretical studies related to plasma boundary physics (Stangeby and McCracken). These edge studies are mainly on the plasma-wall interactions (PWI), characterization of the edge plasma, impurity productions, and their transport, neutral recycling and particle balance, and neutral transport.

1.6. The role of neutrals and impurity ions in edge plasma

Because of PWI in the edge, the neutral atoms and charged particles continuously bombard the material surface, such as on the wall and limiter/divertor plates producing particles and impurities. These particles re-enter into the edge plasma and participate in the edge plasma dynamics.

1.6.1. *Role of neutrals*

The fuel neutrals are mainly present in the edge region of plasma due to their lower temperature than the bulk plasma. They act as a refuelling source as they get ionized and gains temperature. The neutral particles are important in modifying the plasma edge dynamics and play an active role in high confinement (H-mode) plasma operation by participating in the pedestal formation in the edge (Groebner et al.; Wolf et al.). Particles interact with the first wall, which can cause the sputtering of wall material. The neutrals can retain in the wall for milliseconds to years. They can also get high energy through the charge exchange with ions, and these hot neutrals can bring high Z material into the plasma through interaction with the wall. These high Z materials known as impurities cause radiation losses, which may lead to lowering the plasma thermal stored energy. Not only that, several atomic and molecular pathways, such as charge exchange, ionization, and recombination, are available to produce neutral emissions. Then these processes play an essential role in establishing edge plasma dynamics (Janev, Post, et al.; Čadež et al.). Subsequently, neutrals particle penetration studies are essential to understand the neural dynamics in the plasma. It is done mainly by modelling the experimental measurement using the neutral transport codes.

1.6.2. Role of impurity ion

The continuous bombardment of the wall and limiter/divertor plates by particles leads to the desorption of impurities such as oxygen and carbon. These impurity ions diffuse into plasma depending upon their ionization state. Also, they ionize, they enter deeper into the core plasma. The presence of impurities inside the core leads to fuel dilution as the plasma is in a charge-neutral state. Not only that, as these particles can penetrate deep into the plasma, there is possibly the migration of these particles and gets redeposited to some other location of the vessel, causing the property degradation of the original material exposed to the plasma (Brooks et al.). The radiation from impurities is emitted as lines and ions except those completely stripped, leading to power loss from the plasma. The fully ionized ions can also produce power loss through bremsstrahlung. In addition to those significant consequences, impurities inside the central plasma region cause micro-instabilities (Brunner et al.; Tang et al.). The impurities are classified as low-Z ($Z < 10$), medium-Z ($Z=10-30$), and high-Z ($Z>30$), depending upon their mass number. The power loss for high-Z impurity ions is higher as they have many electrons compared to medium-Z and low-Z impurities. Then, the maximum permissible impurity concentration is required to be inversely proportional to the Z number for a stable and highly confined plasma operation.

Occasionally impurities are intentionally injected into the plasma for diagnostic or operational purposes, which has certain benefits. Edge plasma cooling is advantageous by spreading radiation losses and lowering the plasma-facing component's heat load. The reduced power exhaust via PWI is necessary to increase the lifetime of PFC in a fusion reactor environment (Hirai et al.). Impurity injection in the plasma edge can produce better-confined plasmas such as improved Ohmic confinement mode and improved radiative mode (McCracken et al.; Jackson et al.), which reduces the plasma-wall interaction by increasing core plasma properties (Malay Bikas Chowdhuri et al.). In addition, different non-fuel ions are used for wall cleaning and coating purposes. Considering that, the characterization and investigation of the edge plasma is still a research area for developing a tokamak-based fusion reactor.

1.7. Literature survey on edge plasma studies

To understand the tokamak edge for better plasma properties, estimating the plasma parameters at the plasma edge region becomes essential. Moreover, modelling or computational techniques are used to understand the experimental results of various parameters. The studies here focus on the line shape profile modelling for neutral and ion temperature measurements,

investigation of neutral and particle influxes, neutral recycling, and neutral and impurity transport in the edge. The investigation of these topics almost started from the beginning of the tokamak history; the literature survey is paramount to explore the impending measurement and physics issues in the plasma edge.

1.7.1. Edge characterization

Here, the ion temperature measurement is still an open area as the ion, especially hydrogen ion produced through many atomic and molecular processes that acquire various energies. Not only that, the measurements through Doppler broadening require including Zeeman Effect due to the presence of magnetic fields in tokamaks.

Studies on Zeeman Effect in tokamaks

Tokamaks are usually operated with high magnetic fields. The Zeeman Effect influences the spectral line broadening. The Zeeman splitting is taken into account in many tokamaks for corrected neutral and ions temperature measurements. Studies on neutral atoms including the Strong field Zeeman components are done in many tokamaks. In TEXTOR (Tokamak-Experiment for Technology Oriented Research) (J. D. Hey, M. Korten, Lie, Pospieszczyk, et al.; J. D. Hey, Chu, Mertens, et al.; J. D. Hey, Chu, and Hintz; J D Hey et al.). The extensive study on the line shape of neutral and impurity ions, influenced by the Zeeman Effect, is carried out by J. D. Hey et al. In one of the papers, through line shape modelling of $D_\alpha(H_\alpha)$, $D_\beta(H_\beta)$, and $D_\gamma(H_\gamma)$, it is found that the continuous production of very low-energy $T_H \leq 0.5$ eV are found in SOL layer of TEXTOR tokamak (J. D. Hey, M. Korten, Lie, Pospieszczyk, et al.). These components are a primary indication of electron impact processes on the molecular hydrogen/deuterium. In TEXTOR, the hydrogen atom attains the "cold" temperature depending upon different atomic processes (J. D. Hey, Chu, and Hintz). However, the "lukewarm" component was found at a temperature ~ 3 eV. This component is the responsible collision between ions and excited atoms(J. D. Hey, Chu, Mertens, et al.). In the same literature cold temperature component is < 1 eV and two hot temperature components are described, in which one hot components less than 100 eV and another is greater than 100 eV (J. D. Hey, Chu, Mertens, et al.).

Along with neutral studies, the temperature of impurity ions was also measured by including Zeeman components in C II (16 eV), C III (79 eV), C IV ($\sim 70 - 135$ eV), Si II (10 – 11 eV) and Si III (24 eV) spectral lines emissions (J. D. Hey, Y. T. Lie, Rusbüldt, and Hintz). The CIII/OII

multiplet lines are present around 464.7 nm, and they were not entirely resolved in many cases due to the instrument's limitation. The Zeeman components of these lines are derived through modelling and matched with the experimentally measured data at different field strengths (J D Hey et al.). In the JT-60U (Japan atomic energy research institute Tokamak-60 Upgraded) (Kubo et al.; Kumagai et al.), the divertor region of the D_α spectral line shape is measured to investigate the emission and recycling process of deuterium atoms, and here combined three Zeeman components are included for modelling the Lorentzian triplet of the Balmer line (Kubo et al.). In the extended work, the spatial profile of the divertor region is studied (Kumagai et al.). Isler et al. combined the Zeeman and translation Stark effects to take into account in profiles of the Balmer- α line. The maximum difference was found at the core of the plasma (Isler). In DIII-D tokamak, the CII-doublet (657.80 nm and 658.02 nm) and CIII (464.9 nm) are measured along different vertical viewing chords, and the evaluated temperatures are less than 20 eV after including the Zeeman components (R. C. Isler, Brooks, et al.; R. C. Isler, Wood, et al.; R. C. Isler, McKee, et al.). In Alcator C-Mod tokamak, several studies are carried out on the Zeeman broadening. The Zeeman studies have been included in neutral emission line measurement with two different lines of sight: normal to the mid-plane and tangential (Weaver et al.). The neutral flows have been estimated by the inclusion of Zeeman broadening in the spectral line profile (Welch et al.). The toroidal flow velocities have been estimated using HeI at 468.6 nm or 656.1 nm deuterium emissions, and this study also includes Zeeman components (Joydeep Ghosh, Griem, et al.). In Tore Supra (Escarguel, Guirlet, et al.; Escarguel, Pégourié, et al.) tokamak, the D_α density in the edge has been estimated through the same modelling technique (Escarguel, Guirlet, et al.). Extension of this work at the mid-plane neutralizer plate of ergodic divertor includes the study of the cold atom through the D_α spectral line shape after the inclusion of the Zeeman and Doppler broadening taken into account (Escarguel, Pégourié, et al.). In TRIAM-1M tokamak, Shikama et al. conducted multiple studies on line shape and relevant plasma parameter measurements. The Doppler broadening separated from the measured spectra. The local profile values of neutral emission position, temperature, and flow velocities are estimated through high-resolution spectroscopic measurement in the visible range (Shikama, Kado, Zushi, Sakamoto, et al.). However, as the higher ionization of oxygen ions is more prominent in the ultraviolet or near-ultraviolet region of the electromagnetic spectrum, the OV spectral line emission at 279 nm having ionization energy ~114 eV is countered for Zeeman measurement of line shape in TRIAM-1M tokamak (Shikama, Kado, Zushi, Iwamae, et al.). In LHD (Large Helical Device) stellarator, three HeII lines are measured and introduced to the Zeeman effect to measure the inward neutral fluxes (Motoshi Goto and Morita). The line

emission locations were also identified for the same plasma (M. Goto and Morita). In TJ-II Stellarator the C⁺, C²⁺ and Li ion temperatures are investigated using passive spectroscopy (Peláez et al.)

Similarly, for neutral hydrogen, Iwamae et al. measured the temperature, emission location, and inward flux(Iwamae et al.). Gao et al. used the same technique for the measurement of D _{α} in EAST tokamak (Gao, Huang, Wu, et al.; Gao, Huang, Su, et al.). These studies show that the Zeeman and Doppler broadened line shape effectively estimates the neutral and impurity ion dynamics in the edge region of the tokamak plasmas.

Studies on recycling and particle balance

As discussed earlier, due to PWI, the particles radiate energy and modify the plasma properties. The plasma density control is a significant issue and it is highly modified through recycling, the process of exchange of neutrals between plasma and material surface. The recycling coefficient is defined as the ratio of incoming neutrals to the plasma (influx) to the total number of outgoing neutrals to the wall (out-flow). The knowledge of particle behaviour at the plasma edge would be helpful for achieving better density control and better plasma confinement. The particle behaviour is studied in many tokamaks through particle balance and recycling studies, as discussed here.

In TEXTOR tokamak, the first wall characterization by hydrogen recycling was done (Winter, Waelbroeck, et al.) through the estimation of the recycling constant (R_c). It was found that the recycling coefficient reduces at the beginning of the experimental campaign, and then the reduced values are maintained for ~ 5000 tokamak discharges. It is also proved that oxygen contamination on the liner increases as the recycling increases and carbon deposition on the liner decreases (Wienhold et al.). The energy and particle confinement time induced by electric fields are studied in L-mode and H-mode discharges. Particle confinement is less than 1.2 s for L-mode plasma and varies between 1.2 to 4 s for H-mode plasma discharges (Weynants et al.). The low recycling condition is also established through boronization (Winter, Esser, et al.). The impurity ion CI and OI fluxes are also measured (Samm et al.). The global particle balance is studied at JT-60 tokamak (Yamada et al.), and particle confinement time is ~ 0.5 to 5 s in Ohmically confined plasma and ~10 to 150 ms in the neutral beam heating plasma. The recycling coefficient is between 0.9 to 1. In ASDEX tokamak, the experiments were carried out in a limiter configuration, and different material surfaces (Stainless steel, graphite, and SiC) were studied (Wagner). It is found that the wall acted as a source during the steady state phase

of discharge, and the recycling at limiter retains value 1. The particle recycling is studied with the gas puff, and particle confinement time is measured at $\sim 30 - 80$ ms (Haas et al.). At TRIAM-1M tokamak, recycling is studied for high and low-density long-duration discharges (Sakamoto et al.). Here, the wall acts as a sink and source depending upon wall loading conditions, and in high power and high-density discharges, wall saturation is dominated. The steady-state global particle balance is modelled and compared with experimental data (Yoshi Hirooka et al.). In HL-7 tokamak with long-duration discharges, the recycling coefficient of every discharge increase with time. In a very distinctive way, the electron density is increased by hydrogen, and impurity originates from the limiter surface (Wan et al.; Juan et al.). In DIII-D tokamak, the particle confinement time modification is studied with recycling and the measured particle confinement time was 0.2 to 1 s (Unterberg et al.). Asymmetry in divertor impurity influx is measured in a toroidal direction. It was noted that integrated flux measurement inaccuracies are due to a single line of sight measurement (Bedoya et al.). Much work has been done on TEXTOR-94 tokamak to understand the behaviour of low-Z and high-Z material exposed to plasma (V. Philipps et al.). The experimental review of particle confinement in tokamaks is presented in (Shunji Tsuji). The extensive measurement of impurity influxes and their concentration with beryllium rail limiter is carried out at ISX-B tokamak (R.C. Isler et al.). At QUEST spherical tokamak, the particle balance is investigated by combining some modelling techniques (Hanada et al.).

Neutral particle and impurity transport

The fundamental theory of plasma transport is derived from the continuity equation with plasma neutrals and ions as a source and sink term. The theory of plasma transport in a toroidal confinement system was reviewed by Hinton et al. in 1976 (Hinton and Hazeltine). Since then, there has been much progress in this field of tokamak research. The impurity transport study requires knowledge of diffusion and convection. For different charge states, these quantities vary (Angioni et al.). The kinetic treatment of the neutral particles in the plasma is helpful for neutral transport studies via the Monte-Carlo method, and several neutral codes are developed based on it (Stotler, Scotti, et al.; Sakharov).

The transport is studied through global calculation of neoclassical impurity transport and experiment and then modelling the experimental data in terms of their diffusivity and convective velocities (Fujita et al.; Sudo). The transport does not mostly follow the neoclassical theory and is mainly dominated by fluctuation in the plasma. In LHD, the Ar ($Z = 18$), V ($Z = 23$), Mn ($Z = 25$), and Co ($Z = 27$) are studied to understand the transport of these

impurities (Sudo, Tamura, Muto, et al.; Sudo, Tamura, Suzuki, et al.). In MAST tokamak, the He ($Z=2$) transport (Henderson et al.), C ($Z=6$) transport (Mccone et al.) and Sn ($Z = 50$) transport (Foster et al.) are reported. The B ($Z = 5$) transport is studied at ASDEX tokamak (Bruhn et al.). Impurity production and transport in the divertor region are reviewed in ASDEX-U (Roth and Janeschitz). At ASDEX-U tokamak impurity transport of Ne ($Z = 10$), C ($Z = 6$), and O ($Z = 8$) us studied (Nishizawa et al.).The core transport for the JET and ASDEX-U plasma is studied with tungsten W ($Z = 74$) (V. Philipps et al.). The mass dependency in diffusion coefficient is studied in ASDEX-U tokamak with impurity ions Ne ($Z = 10$), Ar ($Z = 18$), Kr ($Z = 36$), and Xe ($Z = 54$), the diffusion coefficient (D) within the center is $D \leq 6 \times 10^{-2} \text{ m}^{-2}/\text{s}$ and rises with the radial distance towards the core. It was found that with increasing Z number, the transport becomes strongly convective with inward-directed drift velocities that produce very peaked impurity densities for high Z (Dux et al.). At TEXTOR-94 tokamak, Ar ($Z = 18$) impurity transport is investigated with anomalous and neoclassical transport for different plasma conditions (W Biel et al.). Ne ($Z = 10$) impurity transport in Tore Supra tokamak is studied for different ionization stages of neon ion, Ne^{7+} , Ne^{6+} and Ne^{5+} (Mattioli, Fournier, et al.). The Ni ($Z = 28$) is studied in the same tokamak . In LHD To analyze impurity behaviour in a magnetically confined plasma, a new diagnostic approach uses tracer-encapsulated solid pellet (TESPEL) injection with several tracers impurities is used (Sudo, Tamura, Suzuki, et al.). The investigation of impurity transport for C ($Z = 6$), Al ($Z = 13$), and Fe ($Z = 26$) has been carried out at DIII-D tokamak (Sciortino et al.).

The study of the neutral density distribution of H_α emissions in PLT tokamak has been done, and it was found that the neutral density changes by four times towards the edge, with electron density (n_e) and electron temperature (T_e) is $0.1 - 0.5 \times 10^{19} \text{ m}^{-3}$ and 25 to 100 eV, respectively (McNeill). In NSTX tokamak, the DEGAS 2 code is used to understand atomic physics with gas puff imaging (Maqueda et al.). In Alcator C-Mod tokamak, the quantitative study of gas-puff imaging is done by considering the density and temperature dependencies (Stotler, LaBombard, et al.). The neutral gas transport code EIRENE was developed initially for TEXTOR tokamak in the 1980s (Reiter et al.). The code was validated with TEXTOR edge plasma parameters $n_e < 1 \times 10^{19} \text{ m}^{-3}$ and $T_e < 100 \text{ eV}$ and is being used in many tokamaks. In JT60-U tokamak, the recycling studies for the first wall are evaluated through the distribution of D_α calculated by transport code DEGAS 2 (Takenaga et al.). Here the background plasma parameters are evaluated by UEDGE code (Rognlien et al.).

These studies show that the Zeeman broadened line profile studies, along with the study of neutral and impurity transport, is an effective way for estimating the neutral and impurity ion dynamics in the edge region of the tokamak plasmas.

1.7.2. Divertor characterization

Studies on molecular emissions

As seen in sections 1.4 to 1.6, the role of PWI is very much apparent in modifying the central plasma. In divertor plasmas, the magnetic field line terminates on divertor plates with magnetic null at separatrix. The plasma generated with this configuration is separated from the central plasma. To understand the PWI mechanism at divertor regions and further reduce the damage to the material surfaces, it is imperative to understand the local plasma parameters. The divertor detachment is characterized by low temperature and low-density plasmas at divertor plates (Leonard). In this plasma condition, more atomic and molecular processes occur, and using the emission from the atomic and molecular species, the spectroscopy diagnostic can be used in the divertor region.

Due to the low temperature of plasma at the divertor, recombination is critical in detachment. The volume recombination of ions and electrons can have multiple paths: radiative recombination, three-body recombination, and Molecular Activated Recombination (MAR) (Terry et al.; Janev, Post, et al.; Post). There have been several studies related to exploring electron-ion recombination using high-n Balmer emission lines (R. C. Isler, Wood, et al.; Terry et al.; Wenzel et al.). Krasheninnikov et al. explained the physics of MAR, and it is more critical than electron-ion recombination (EIR) (Krasheninnikov and Kukushkin). The plasma molecules' interactions can impact power, particle, and momentum losses. These collisions can excite the rovibronic interaction in the molecule, leading to Fulcher molecular band emission (Hollmann, Brezinsek, et al.; Fantz et al.; Park et al.). The reaction between molecules and electrons can produce H_2^+ –ions, it again interacts with plasma and contributes to MAR or MAI (Hollmann, Brezinsek, et al.; Fantz et al.; Groth et al.). While investigating molecular contribution in S/XB for influx measurement, it recently received renewed attention (Kremeyer et al.). In TEXTOR tokamak, the effect of MAR on influx measurement is studied through the measurement of D_α and D_2 Fulcher bands in front of graphite limiters (Brezinsek et al.). In DIII-D tokamak, the D_2 molecular flux with Fulcher bands at edge/ SOL is measured (Hollmann, Brezinsek, et al.). The experimental observation of D_α/H_α and D_2 Fulcher bands are challenging due to small rovibronic excited population densities. However, the molecular

Fulcher band can affect other measurements of plasma. The modelling is required to have the correct S/XB estimations. The complementary laboratory techniques in linear divertor simulator plasmas can be used to analyze plasma parameters and the behaviour of atoms and molecules in chambers that are more easily accessible and on a smaller scale. Such devices are, NAGDIS-II, PISCES-B, GAMMA-10, and MAGNUM PSI (Ohno; Y. Hirooka et al.; Nakashima et al.; Hayashi et al.). The experimental observation of D_α/H_α and D_2 Fulcher bands are challenging due to small rovibronic excited population densities. However, the molecular Fulcher band can affect other measurements of plasma. The modelling is required to have the correct S/XB ratio estimations. The complementary laboratory techniques in linear discharge plasmas can be used to analyze plasma parameters and the behaviour of atoms and molecules in chambers that are more easily accessible and on a smaller scale.

1.8. Motivation

The small and medium-sized tokamaks have contributed immensely towards fusion science research, from developing techniques to identify and minimize destructive physical phenomena to establishing diagnostics and to several tokamak physics studies. While the tokamak research has progressed resolutely towards building a fusion power plant, the role of edge/SOL plasma in influencing the core plasma confinement properties as well as on the material structures of the machine remains to be understood in totality and is an important area which requires to be addressed urgently. This thesis work is motivated by dedicated experiments, careful analysis and focused simulations for enhancing the understanding of predominant physical processes occurring in the edge/SOL plasma regions of a tokamak and their influence on the core-plasma.

In the edge/SOL regions, the neutral and impurity ions play a significant role through PWI. This study is done mainly through the combination of profile measurement of various parameters and edge transport modelling. Hence, the characterization of plasma parameters in this region is essential. In this aspect, the radial profile of ion temperature estimation in the edge plasma region and its investigation is crucial as ion temperature is often assumed to be equal to electron temperature during the investigation and modelling of the edge plasma region. However, it is found that the ion temperature mostly differs from the electron temperature, and sometimes ion temperature shows poloidal asymmetry (Chen et al.). In this thesis, to understand the neutral and impurity ion dynamics via estimating neutral and ions temperatures, a line profile modelling technique has been developed to produce synthetic spectra including all possible broadening mechanisms. This can be used on future fusion devices like ITER to predict the spectra by knowing specific plasma parameters. The radial profile of neutral and impurity

ion temperatures are thus estimated in the ADITYA-U tokamak, and their behaviors are investigated experimentally by focussing the emissions from the neutral hydrogen, low ionized carbon, and oxygen as the ADITYA-U tokamak is suitable for recording H_{α} and C^+ and O^{4+} emissions due to its lower temperatures in the plasma edge region.

In general, the divertor concept of tokamak has led to lowering the impurity content in the core plasma as in this case the plasma-PFC interaction happens far away from the core plasma. This has led to several advanced operational scenarios, like H-mode and detached plasmas. However, the wall still plays a vital role in recycling and particle balance even after the introduction of the divertor, as the surface-area of the vessel-wall is quite large compared to the divertor. The role of the wall in plasma production as well as in the core plasma confinement remains one of the major issues for a giant machine like ITER. To understand the importance of neutral and several impurities ions in the plasma, the particle influxes from different material surfaces have been targeted in this thesis. This has been carried out with various wall conditioning to understand the role of wall-conditioning such as Lithiumization etc. In this aspect, the ADITYA-U tokamak highly benefited from the availability and accessibility of view-ports, which are challenging to get in a large machine. Particle and impurity influxes may have a direct contribution from molecular processes in the divertor and SOL plasmas due to their low T_e . This situation is a reality in a detached divertor condition, in which the plasma temperature may decrease below 5 eV. However, the large machines may not be suitable to understand this due to various above-stated and other economic reasons. Considering ADITYA-U's edge plasma having T_e of ~ 7 to 15 eV, the effect of molecular emission on the influx emissions has been explored in this thesis by estimating molecular contribution via neutral particle transport modeling.

As noted earlier, the tokamak edge plays an essential role in the core properties alternation. The impurity concentration in the core plasma depends on the PWI and their transport in the plasma edge. Many studies have been done on core and edge transports of impurities. Also, the physics behind the impurity accumulation in the plasma is well studied. Not only that, the way to minimize the impurity accumulation in the core has been investigated thoroughly. However, not much research has been done on the mass dependency of impurity transport as it has become more crucial considering the high Z material being explored for the PFC. Also, krypton and xenon gases are proposed to be used in fusion-grade large machines like ITER for core diagnostic purposes. However, studies of mass dependency of impurity transport even in the plasma edge require monitoring the VUV and X-ray emissions due to those machines' large

edge electron temperature. It can be done efficiently in small and medium-sized tokamaks, like ADITYA-U, where visible emissions from different impurities come from the edge plasma regions. The radial profile of these emissions can be measured using the fiber optics-based light collection system. In ADITYA-U tokamak, the emission profile is used to determine the diffusion coefficient profile and its dependence on Z species.

Additionally, considering the importance of detached H mode plasma operation in large fusion grade tokamak, the divertor area will have low T_e and high n_e . Then, it is crucial to develop the characterization technique for its various plasma parameter, including neutral gas temperature present in this region, as it plays an essential role in the divertor region plasma dynamic by participating in various atomic and molecular processes. Then, as proof of principle, a gas temperature estimation procedure has been established in this thesis using a low-temperature RF plasma device. This technique will be helpful for the future operation of the ADITYA-U tokamak as it has the capability of shaped plasma operation.

1.9. Thesis outline

The thesis is arranged as follows:

Chapter 2: It describes the setting up of a high-resolution spectroscopic diagnostic through the development of a front-end light collection system using available spectroscopic systems on ADITYA-U tokamak. It also describes the other diagnostics available on ADITYA-U tokamak. As the wavelength and absolute intensity calibration are very much crucial for quantitative analysis. The details of it are also described in this chapter.

Chapter 3: It consists of the measurement of spatially resolved high-resolution spectral line profile and estimation of neutral and ion temperatures by including apparent broadening due to the Zeeman Effect. This is done through the development of code for spectral line profile simulation. This chapter also deals with investigating radial profiles of neutral and ion temperatures of ADITYA-U tokamak. Along with this, the self-absorption spectrum has been analyzed, and the opacity of plasma has been estimated.

Chapter 4: It focuses on the plasma-wall interaction through the analysis of the recycling by measuring the influx from various first wall components and the plasma outflow. This chapter details the investigation of the influxes from various surfaces and the changes in particle influxes with plasma wall coatings. The finding of these results is discussed to identify the importance of walls in recycling and particle balance.

Chapter 5: The neutral and impurity transports have been studied with the neutral transport code, DEGAS2, and the impurity transport code, STRAHL. The role of molecular contribution in the particle influxes is also explored in this chapter through quantifying molecular contribution in the H α intensity due to molecular pathways using neutral transport code DEGAS2. In this chapter, the impurity transport study finds Z's dependency on impurity transport using experimentally obtained radial profiles of visible emissions from various impurities.

Chapter 6: It deals with the development of a technique for estimating the neutral gas temperature relevant to the plasma in the divertor region. It is done by modelling the line profile of the molecular spectral band emitted from a low-temperature device. Here, the importance of including spectral bands from other species present in the low-temperature plasma during line profile modelling is discussed while developing the technique.

Chapter 7: The results are discussed and summarized here, along with the future scope of this thesis.

Chapter 2. Experimental setup



Figure 2.1. ADITYA-U tokamak

This thesis focuses on neutral and impurity ion dynamics in the edge region of ADITYA-U tokamak. A spectroscopic diagnostic is a crucial tool for understanding the tokamak edge plasma via measuring edge parameters. The neutral and impurity ion line profile is modelled

by including the Zeeman Effect to find the neutral and ion temperature. This helps to understand the neutral and impurity ion behaviour in the edge. Further, the plasma wall interactions are impacts the edge plasma properties. Here the particle influxes are measured for different wall conditioning and material surfaces. Using these, recycling and particle confinement times are estimated and analyzed. The role of molecular processes in the influx measurement is also explored by quantifying the direct molecular contribution to the influxes. In plasma, several species having different Z are released owing to the plasma-wall interactions, and the dependency of mass in the impurity transport is presented. For developing a technique for divertor characterization, the divertor plasma condition is produced on a linear plasma device. The gas temperature is estimated and the effect of H₂ Fulcher bands on it are investigated. The setup based on a linear plasma device will be discussed in Chapter 6 of this thesis. All these have been mostly done on ADITYA-U tokamak by employing the spectroscopic technique.

Here we present the experimental setup, including the description of the ADITYA-U tokamak device. The spectroscopy diagnostic systems are used here, with different detectors and optics setups. Along with this, gas-puff, pellet injection, and wall conditioning are described here. Further, other diagnostic systems are used to study physics phenomena and briefed. Chapter 6 of this thesis explains the setup of the linear device to simulate the divertor-like environment and to characterize the divertor.

2.1. ADITYA-U tokamak

In India, theoretical and experimental plasma physics studies, specifically linear and toroidal devices, began during the early 1970s at Physical Research Laboratory (PRL), Ahmedabad, Gujarat. To make further progress in research, in 1982, the Department of Science (DOS) launched Plasma Physics Program (PPP). After several years of research in PRL itself, the PPP program transformed into a major program in 1986. The program is then shifted to the Department of Science and Technology (DST) – Institute for Plasma Research (IPR) at Gandhinagar, Gujarat. Later IPR became part of the Department of Atomic energy. The major project of IPR was to build ADITYA tokamak, which was commissioned in 1989 (S B Bhatt et al.). The ADITYA tokamak has a major radius of 0.75 m and a minor radius of 0.25 m with a magnetic field of 0.75 to 1.5 T. The vacuum vessel of the ADITYA tokamak was rectangular with a limiter configuration (Kaw). It has contributed immensely to fusion science research (H. K. B. Pandya et al.; Banerjee, Kumar, et al.; Ambulkar et al.; R. Manchanda, Ghosh, et al.; Rathi et al.; Paradkar et al.; Prakash et al.; Banerjee, GHOSH, et al.; Mishra et al.; Shukla, D

Bora, et al.; Bisai, Singh, et al.; S. B. Bhatt et al.; S. P. Pandya, Pandya, et al.; Suratia et al.; N. Patel et al.; Jadeja and Bhatt; R L Tanna, Jadeja, et al.; Kodarkar et al.; S. P. Pandya, Ajay, et al.; Roseline; M. B. Chowdhuri, Manchanda, Ghosh, Bhatt, et al.; Makwana et al.; R Manchanda et al.; Sangwan, Jha, Brotankova, and Gopalakrishna; Sharma et al.; S. S. Kumar, Jayaraj, Kumar, et al.; Goswami; Tahiliani, Jha, and Kumar; Sangwan, Jha, Brotankova, and Gopalakrishna; Dhyani, J. Ghosh, et al.; Dhyani, Joydeep Ghosh, et al.; Goswami et al.; Bisai, Jha, et al.; R. L. Tanna, Ghosh, Chattopadhyay, et al.; Eidietis et al.; Sahoo et al.; Chattopadhyay et al.; Sangwan, Jha, and Tanna; Shukla, D. Bora, et al.; J. J. Patel et al.; K. Patel, Pillai, et al.; Gupta et al.; Arambhadiya et al.; Goswami and Artaud; Purohit et al.). It continued its operation till 2014.

Table 2.1. ADITYA-U tokamak design parameters

Fuel gas	Hydrogen, Deuterium
Duration of plasma discharge	250 – 300 ms
Plasma current (I_P)	~150 – 250 kA (in limiter operations) ~100 – 150 kA (in divertor operations)
Loop voltage (V_{loop})	~ 1.5 – 2 V
Toroidal magnetic field (B_T)	~0.75 – 1.5 T
Plasma density (n_e)	~1 – 4 × 10 ¹⁹ m ⁻³
Plasma temperature (T_e)	~500 – 1 keV
Elongation (k)	~1.1– 1.2
Triangularity	~0.45
Vacuum vessel volume (m³)	~1.6
Vacuum vessel surface area (m²)	~16

Nowadays, the main attention in tokamaks research is towards the divertor geometry and tungsten (W) wall to get an ITER-like environment for engineering and physics studies. Several of them are JET (JET Team), DIII-D (Luxon), ALCATOR C-MOD (Greenwald et al.), TCV

(Coda et al.), ASDEX-U (Schweinzer et al.), and EAST (Wu). However, the small/ medium-sized tokamak help to study the different physics phenomena and engineering challenges with reasonably fewer complications and damages. This will further be utilized for construction and studying the large-size tokamaks. With this, the ADITYA tokamak is upgraded to ADITYA-U tokamak to have the open divertor configuration with limiters (J Ghosh et al.). Here, the vacuum vessel is mainly replaced by a circular-shaped vessel to find the space for the divertor coil. Magnets and other assemblies remained the same. The ADITYA-U is accomplished to have the shaped plasma operations. The upgradation of ADITYA-U is dedicated to facilitating experiments related to plasma disruption, runaway mitigations, studies related to edge and divertor regions, plasma-wall interactions, plasma transport, and particle balance in tokamaks. The ADITYA-U tokamak provides an excellent environment for developing new diagnostics, which can be further conceptually utilized on large tokamaks. The machine is integrated with a gas fuelling system, wall conditioning systems (glow discharge cleaning and pulse discharge cleaning), pellet injection system, pulsed power systems for ohmic heating, position control system, toroidal magnetic field, vertical field, and many diagnostics for physics studies. The ADITYA-U tokamak progress is presented yearly by Tanna et al. (R. L. Tanna, Ghosh, Raj, et al.; R L Tanna, Raj, et al.; R. L. Tanna, Macwan, Ghosh, et al.). The designed machine plasma parameters are given in Table 2.1, and Figure 2.1 represents standard plasma parameters.

2.2. Subsystems of ADITYA-U tokamak

2.2.1. Vacuum vessel

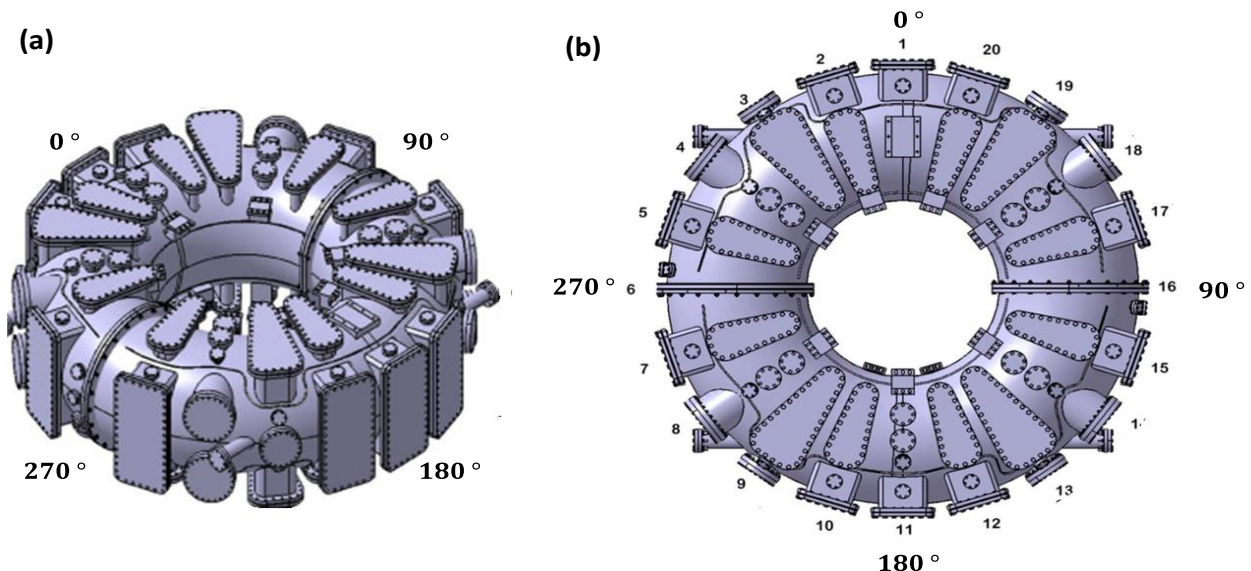


Figure 2.2. ADITYA-U tokamak vacuum vessel
 (a) 3D view of the vessel, (b) top-view of the vessel

The ADITYA-U tokamak has a circular vacuum vessel made of SS304L nonmagnetic stainless-steel material connected as two semi-tori electrically isolated with Viton O-ring. The minor and major radii of the torus vessel are 305 mm and 750 mm, respectively. The wall thickness of the vessel is 10 mm with a vessel volume of 1.6 m^3 . The two torus sections are made (semi-torus) and connected at 180° . The machine is equipped with a total of 111 viewports, including ten rectangular, four tangential, 24 triangular, 35CF, 150CF, 63CF, and 200 CF ports. The vessel's ultra-high vacuum (UHV) pressure is maintained at $\sim 2 - 5 \times 10^{-8}$ Torr with the help of two turbomolecular pumps of capacity $1900 \text{ Ls}^{-1} \text{ N}_2$ and two cryogenic pumps of capacity $9500 \text{ Ls}^{-1} \text{ H}_2\text{O}$. The pumps are being supported by rotary pumps of speed $\sim 60 \text{ m}^3/\text{h}$. The machine can be baked up to 150°C with current filaments wrapped all over the vessel (K. Jadeja et al.). The 3D and top view of the vacuum vessel are given in Figure 2.2 (a and b).

2.2.2. Limiter and divertors

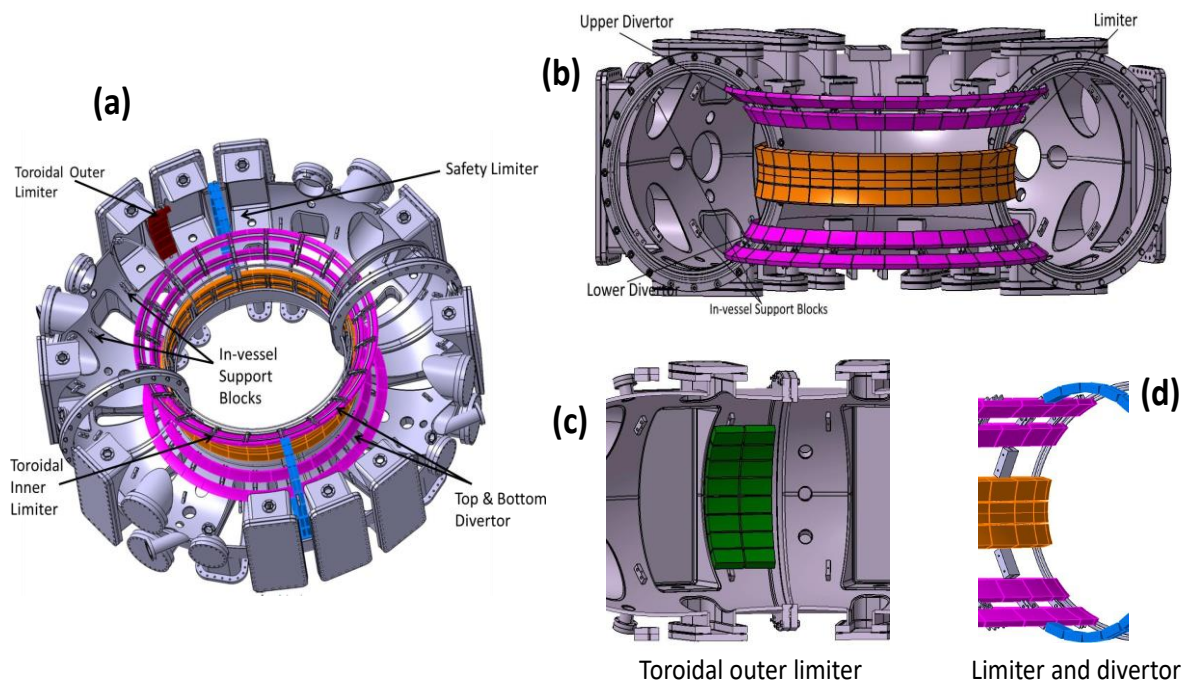


Figure 2.3. Limiter and divertor structures

Limiter and divertor assemblies are a significant part of the tokamak machine to limit the plasma boundary and constraint the high-temperature plasma to interact with the main vessel-wall. Earlier ADITYA tokamak had a limiter configuration. It has been upgraded to a divertor tokamak by adding divertor coils and plates during upgradation. Currently, the machine is designed to be equipped with three different configurations of limiter with divertor assemblies,

as shown in Figure 2.3. One is the toroidal continuous belt limiter, placed at the inner periphery of the vessel, as shown in Figure 2.3 (b). Another is a toroidal outer limiter at the outboard side of the vessel, and safety ring limiters are placed at two toroidally symmetric locations (Figure 2.3). The top and bottom two divertor belts are placed at the inner periphery of the vacuum vessel at symmetrically top and bottom locations, as shown in Figure 2.3 (b). All the limiter and divertor tile surfaces are made-up of fusion-grade graphite IG-430. The tiles are designed to sustain heat loads of $\sim 0.5 \text{ MW/m}^2$ (K. M. Patel et al.).

2.2.3. Magnets

ADITYA-U tokamak uses electromagnetic coils to generate the magnetic field. The magnets in ADITYA-U are made with OFHC (oxygen-free high conductivity) copper.

The primary coil TR-1 (central solenoid coil) is placed at the central axis of the torus in ADITYA-U tokamak. The toroidal vacuum vessel acts as a secondary of the transformer. The TR coil acts as a primary transformer. This produces the electric field inside the vacuum vessel. Ohmic transformer induces the peak loop voltage (V_{loop}) of $\sim 15 - 25 \text{ V}$ during plasma discharge and $\sim 1 - 2 \text{ V}$ during the plasma flat-top phase. The induced magnetic field from TR acts as an error field for the plasma cross-section region. For minimizing the error field within the vessel, four pair of compensating poloidal magnetic field coils, TR-2, TR-3, TR-4, and TR-5, at the upper and lower side of the machine is present, as seen in Figure 2.4.

A total of 20 toroidal fields (TF) magnetic coils of rectangular-shaped magnets are present and arranged in the closed loop on a torus-shaped vacuum vessel. The shape of each coil is a rectangle with $0.78 \text{ m} \times 0.9 \text{ m}$ and an outer dimension of $1.03 \text{ m} \times 1.26 \text{ m}$, with the weight of each coil being $\sim 500 \text{ kg}$. The toroidal gap between each coil is 18° . It is getting heated by I^2R heating is known as joule heating or ohmic heating. The demineralized (D.M.) chilled water passes through cooling tubes entrenched inside each turn's inner surface to cool the coils. The TF coil can produce a magnetic field strength of 0.75 to 1.5 T.

Hoop forces and the shafranov shift are displacing the plasma. The vertical field (VF) coil is also present to maintain the force equilibrium in the horizontal direction. With the following equation, the adequate magnetic field to maintain the equilibrium is estimated (Mukhovatov and Shafranov):

$$B_v = -\frac{\mu_0 I_p}{4\pi R} \left(\ln \frac{8R}{a} - \Lambda - \frac{1}{2} \right) \quad 2.1$$

Here $\Lambda = \beta_P + \frac{l_i}{2} - 1$, and l_i is the internal inductance of plasma current. The estimated $B_v = 4$ G/kA is enough to maintain the plasma equilibrium.

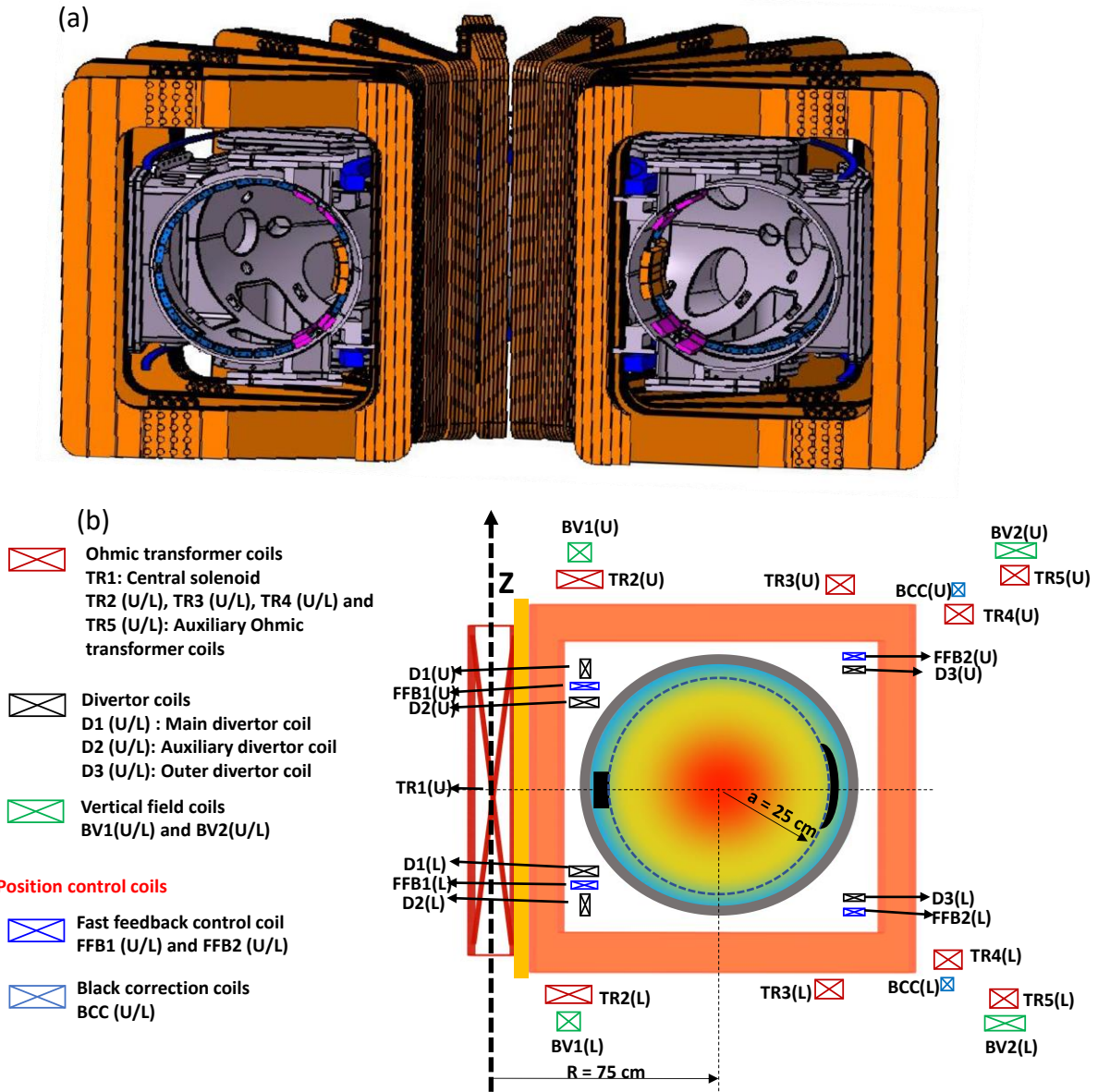


Figure 2.4. ADITYA-U tokamak magnets

During plasma operations, the plasma position only sometimes remains at the core due to drift forces and several plasma phenomena. Two sets of fast feedback coils (FFB) with horizontal position control and a set of black correction coils (BCC) for vertical position control are installed for real-time position control.

For divertor plasma operations, the three sets of divertor coils are placed for diverter-shaped plasma operations in single and double null configurations. All the coils are placed outside of the vacuum vessel. The primary and auxiliary divertor coils are situated at the high field side

of the machine. The outer divertor coil is placed at the low field side of the vessel, as shown in Figure 2.4. Single lower null, single upper null, and double null divertor configurations are modelled to produce shaped plasma.

2.2.4. Power supplies

ADITYA-U has dedicated power supplies for TR, TF, and VF magnetic field coils. The computer-controlled converter-based power supply of 2 kV with ± 20 kA of current is powering the primary TR (Ohmic) coil. The power supply is dedicated as ADITYA pulsed power system (APPS). It also involves the wave-shaping unit with a VCB (Vacuum Circuit Breaker), a capacitor of 1200 μ F, 22 kV, switches, and resistors of 1.8Ω , 36 MJ. With this, the three-step switching is achieved to regulate the loop voltage–temporal evolution.

TF coil consists of two resistances of ~ 6 m Ω , getting power through a power supply of 400 V, 50 kA. For vertical field (VF) coils, the power supply of 2.2 kV, 12.5 kA is used. The mutual coupling between TR and BV coils is nullified through the anti-transformer. According to the experimental needs, the current waveform's magnitude, shape, and duration are pre-programmed before each experiment. The analog controllers, logic cards, and interlocks through Computer/VME interfaces are utilized to have the desired waveforms. The air-cooled thyristor-based converters are used to convert AC to DC signals. During conversion, $\sim 6\%$ noise voltage is observed in loop voltage with a constant frequency of 600 Hz. It is low in magnitude but still affects the observed other diagnostic channels.

2.2.5. Gas fuelling system

The ADITYA-U tokamak is operated with hydrogen and deuterium fuel gases. The gas is filled in the vessel before activating the loop voltage with pre-fill pressure of $\sim 10^{-4} - 10^{-5}$ Torr. After the plasma build-up to maintain the plasma density control, the periodic H₂ gas puff is injected into the vessel through the bottom port of the machine at a single toroidal location through a constant pressure reservoir via a fast response piezoelectric valve. With a programmable pulse generator. It controls the duration and number of fuel particles per experimental requirements. Each gas puff introduces $\sim 1 - 10 \times 10^{17}$ atoms into the vessel. Several gas injections are done from the port at 0.1 m radially via a Piezoelectric valve (500 sccm at 100 V). more details are given in ref. (N. Patel et al.).

2.2.6. Wall conditioning

With the given operational plasma vacuum conditions, some intrinsic impurities exist, i.e., carbon from limiter and oxygen from trapped particles in the form of water vapor. However, it is an unavoidable part of plasma operations, though it can be controlled or reduced through baking, wall coating, and wall conditioning through glow discharge cleanings. Also, the neutral particle recycling through the wall and limiter surface of the vessel can be controlled.

2.2.6.1. Glow Discharge Cleaning (GDC)

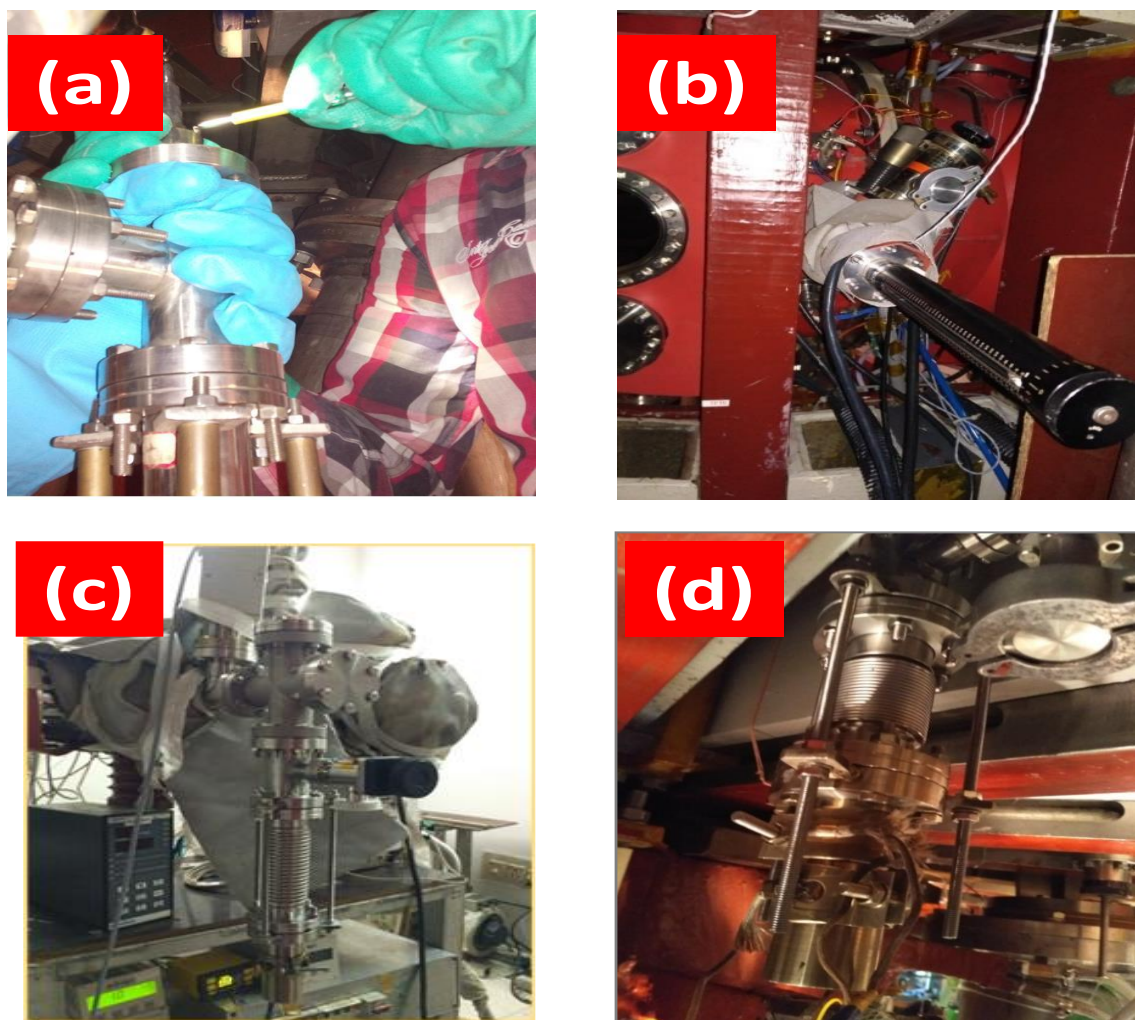


Figure 2.5. Lithiumization (a), (b) Lithium-rod technique, (c), (d) Lithium evaporation technique

ADITYA-U tokamak is equipped with Glow Discharge Cleaning (GDC) system with H₂ or a mixture of gases H₂ – Ar and H₂ – He. With hydrogen gas at pressure $\sim 10^{-2}$ Torr and $\sim 400 - 600$ V electrode bias voltages. After the generation of GDC plasma, the working pressure is reduced to $\sim 10^{-4}$ Torr. The Pulse Discharge Cleaning (PDC) system can also have

intense short plasma pulses with Electron Cyclotron Resonance (ECR) cleaning. It can be used in only PDC mode with a pulse duration of ~ 4 ms and a pulse rate of ~ 900 . When PDC is done with ECR, the ECR frequency is 2.45 GHz, and ECR power is ~ 2 kW. Working pressure in both the cleaning kept $\sim 10^{-4} - 10^{-5}$ Torr. Every day the GDC and ECR-PDC are carried out for better impurity control during experiments. Through a Residual gas Analyzer (RGA), the reduction in each impurity content is monitored during wall conditioning. It is an effective technique for reducing carbon and oxygen impurities. The long hours of wall cleaning with H₂ gas results in fuel retention at first wall surfaces (any surface that comes first in contact with plasma: limiter, wall, or in-vessel diagnostics). Hydrogen removal requires a long duration and it affects plasma density control during plasma operations.

2.2.6.2. A new concept of pulsed discharge cleaning (P-GDC)

A new concept of pulsed discharge cleaning (P-GDC) has been established to address the above-described limitations (K.A. Jadeja et al.). The free electrons are produced with a pre-ionization filament to assist the initiation of each GDC pulse. The maintained working pressure during GDC/PDC/P-GDC $\sim 10^{-4}$ Torr. Active feedback control helps to achieve controlled gas fuelling (Edappala et al.). The usual On and Off time of P-GDC is 2 minutes and 3 minutes, respectively. To have a similar effect as GDC, ~ 2.5 times less fuel gas is required. It is found that, on average, $\sim 2 - 4$ times better results in terms of removal of impurities (H₂O, CO₂, CO and CH₄) can achieve in P-GDC than GDC of 25 minutes. Also, fuel recycling substantially reduces with P-GDC.

2.2.6.3. Wall coatings-Lithiumization

Wall coatings of low-Z impurities play a vital role in impurity control and better plasma performance (Winter). Generally, Lithium, Silicon, and Boron are used for coating in several tokamaks. Due to wall coatings, the plasma will not come in direct contact with the first wall components. In other words, it protects the plasma from radiation losses due to the minimization of particles entering the plasma from wall surfaces. This eventually improves the overall plasma performance. In ADITYA-U, Lithium coating is done using two different techniques (K. A. Jadeja et al.).

- (a) Li rod sputtering technique: Li – a rod of diameter ~ 12.5 mm and length ~ 60 mm is inserted in the vessel and heated to a fixed temperature ~ 120 °C constantly during H₂ GDC plasma with linear motion feedthrough mounted on 35CF port at radial mid-plane.

The sputtering occurs in this technique due to the bombardment of ions present in H₂ plasma on Li rod. The rod is heated via conduction through the silicon-wrapped heater. Earlier in ADITYA tokamak, the Li rod need not be heated due to its lower graphite surface area. Here Li-rod is heated to 120° C to increase the Li sputtering yield to produce sufficient coating in ADITYA-U tokamak walls. Figure 2.5 (a) and (b) represent the installation of Li – rod on the machine port.

(b) Li -Evaporator technique: The Li – evaporator is built in-house to bring the Li vapor into the vacuum vessel of ADITYA-U tokamak through the stainless-steel delivery tube and Li-crucible. The setup is present at the bottom 63 CF port of the machine. The setup consists of ~10 g lithium powder heated at ~ 450 °C to 600 °C. During H₂ GDC, the delivery tube is inserted and retracted by the flexible bellow. The clamp heaters of 150 W are used to control the heating temperature. In this, the high-temperature Li evaporator is used, and due to the vaporization of Li, the uniform coating in the vessel-wall is produced. The significantly improved plasma parameter is achieved when Lithiumization is done in proper sequence, and Li – evaporation technique is found to be more effective than Li – rod technique. Figure 2.5 (c) and Figure 2.5 (d) show the lab testing and the Li evaporator machine.

2.3. Diagnostics

The plasma is generated and confined, as discussed in the previous section. The role of neutral and impurity ions becomes essential to study in the plasma edge region, which influences the core plasma parameters. Further, to study the plasma-wall interaction, plasma diagnostics have been necessary from the beginning of tokamak research (Eubank and Sindoni; W. Biel et al.; Equipe TFR; Huddlestone and Leonard). Then, several diagnostics are installed and discussed in this section of the thesis to understand the physical processes prevailing inside the ADITYA-U tokamak plasma.

2.3.1. Diagnostics other than spectroscopy

2.3.1.1 Magnetic diagnostics

The Rogowski coils are wound poloidally around the vacuum vessel to measure the Plasma Current (I_P). The loop voltage measurement is done through a two-single-turn toroidal pickup coil located at the high field side and low field side of the tokamak. The diamagnetic flux is

essential to estimate the total stored energy. It is the deviation of the total toroidal flux in the absence and presence of plasma. This is measured using a pickup loop called a diamagnetic loop placed poloidally enclosing tokamak plasma and a compensating loop of six turns made of polyimide-insulated wire. This provides the poloidal beta (β_P). Further, the β_P is obtained from the formula given in (S. Kumar, Jha, Lal, et al.).

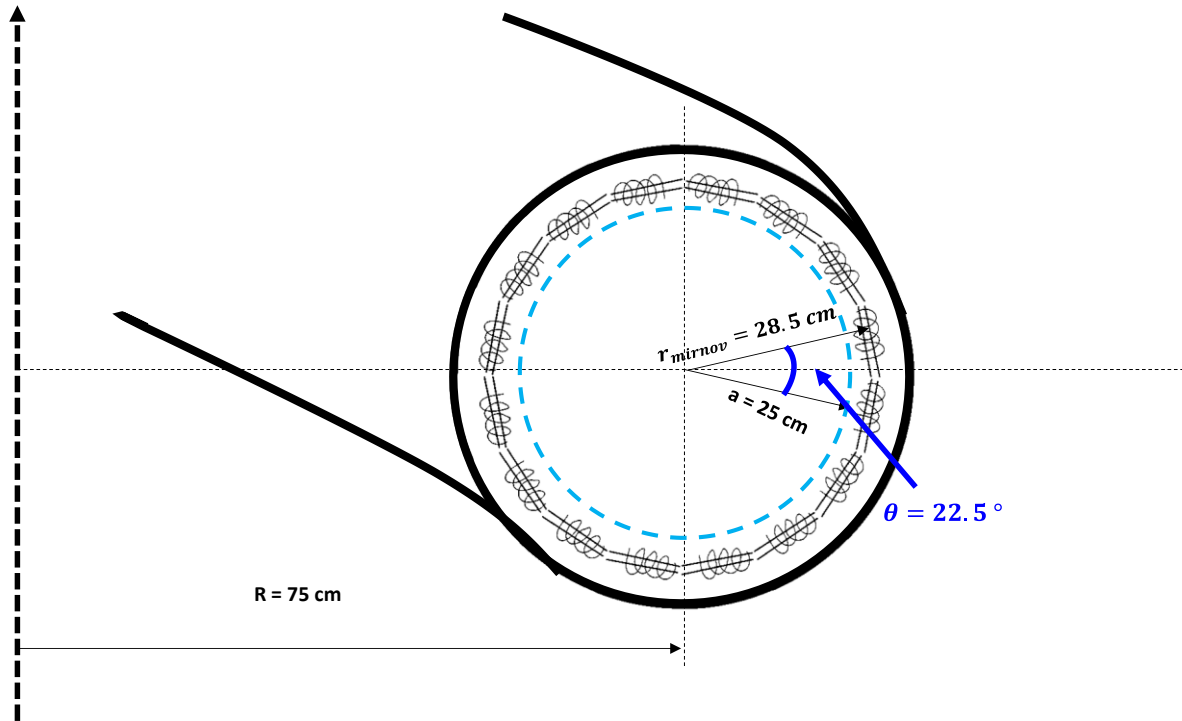


Figure 2.6. Mirnov coil diagnostics

Mirnov coils

Two sets of Mirnov garlands are present in ADITYA-U tokamak. Sixteen magnetic probes are distributed equally in the poloidal periphery with a separation of 22.5° of each Mirnov garland, as shown in Figure 2.6. The single magnetic probe has a rectangular cross-section of $35 \times 15 \text{ mm}^2$ with the copper wire of diameter $d = 0.6 \text{ mm}$ is insulated through 176 turns of Kapton. The response time of the probe is $\sim 20 \mu\text{s}$ determined as L/R with resistance $R \sim 3 \Omega$ and inductance $L \sim 60 \mu\text{H}$. The coils are placed at $r \sim 28.5 \text{ cm}$ within the stainless-steel casing, and the toroidal separation between coils is 180° . The coils are calibrated in situ by passing current in the conductors placed within the vessel at several vertical locations $r = 0, 0.2, 0.4, 0.8, 1.0 \text{ m}$ and $z = 0, 0.4, 0.8 \text{ m}$. The voltage induced in each Mirnov coil by current conductors is measured. More details on this diagnostic are present in the ref (R. Kumar, Ghosh, et al.; R. Kumar, Aich, et al.).

2.3.1.2. Microwave interferometer

The line averaged electron density, and their radial profiles can be inferred through the Microwave interferometer technique. The basic principle behind this measurement is that due to the change in the plasma medium's refractive index, the electromagnetic wave traveling through the plasma experiences the phase difference(Φ). The refractive index of plasma varies in proportion to the plasma density n_e . Hence the measurement of phase difference gives the line-averaged measurement of plasma density with the following equation (Heald and Wharton):

$$n_e = \frac{2\epsilon_0 m_e c \omega \Phi}{e^2 L} \quad 2.2$$

The L is the path length of the cord. There are two techniques to have the measurement

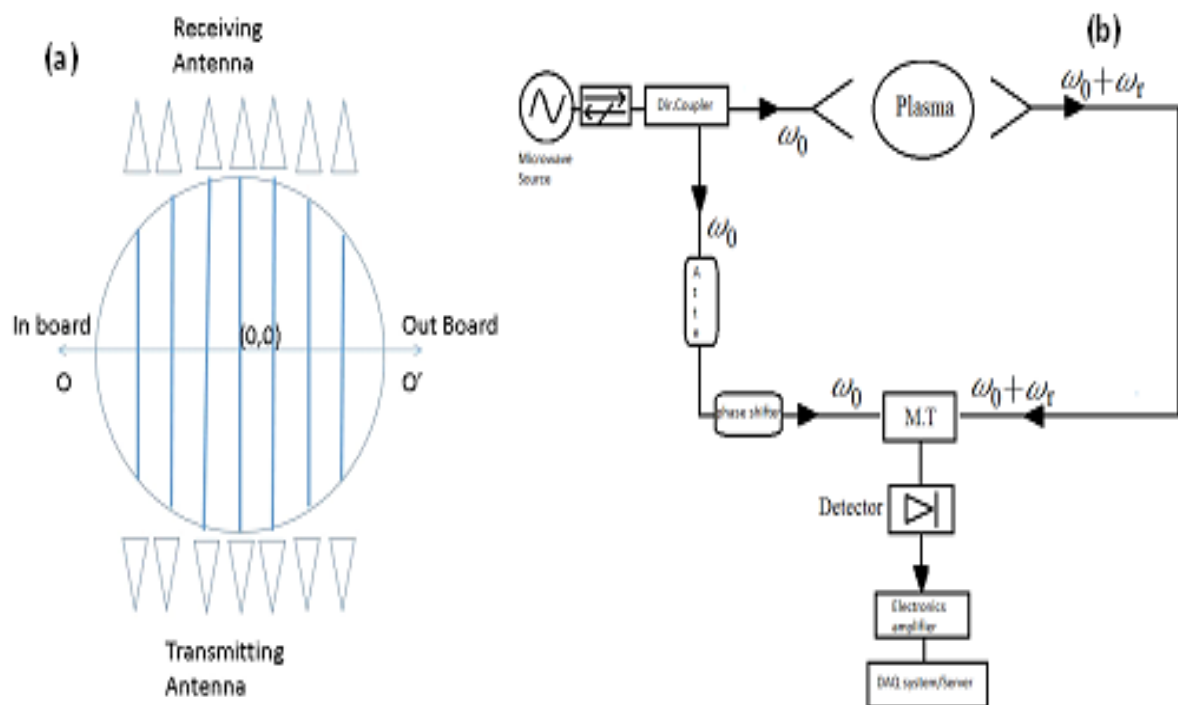


Figure 2.7. (a) Seven viewing chords for microwave interferometry and (b) Schematic for microwave interferometry.

(a) Homodyne (Atrey et al.)

The Homodyne Microwave measurement can provide line integrated measurement on a total of seven viewing chords with position $r = -0.21, -0.14, -0.07, 0, +0.07, +0.14$ and $+0.21$ m, as shown in Figure 2.7. This consists 100 GHz Gunn oscillator to generate the EM

wave, then through the directional coupler, the EM is diverted to one transmitting and one reference wave. Further, an attenuator is used as a phase shifter, which can adjust both signals without the plasma. Through the inversion technique, the radial profile of density is achieved.

(b) Heterodyne (Nagora et al.)

For radio frequency (RF) and local oscillator (LO), the Gunn Oscillator (Quinstar) mechanically tuned with frequencies 100 GHz and 100.85 GHz, respectively. 90 % of power is launched to the plasma through 10 – dB DC (directional coupler). From remaining 3 – dB is used as a reference signal (K. Patel, Nagora, et al.). The 1-radian minimum phase shift can be measured through a heterodyne system. The minimum measured cord-averaged density is $\sim 2 \times 10^{17} \text{ m}^{-3}$. In plasma with the cord averaged density $\sim 1 \times 10^{19} \text{ m}^{-3}$ measurement, the fluctuation of $\sim 2\%$ can be captured through the discussed diagnostic.

2.3.1.3. Soft X-ray (SXR)

The electron temperature (T_e) is an equally important parameter to understanding tokamak plasma. The cord-averaged temperature measurement is measured through soft X-ray (SXR) diagnostics. The SXR diagnostic uses the absorption foil technique (Wesson and Campbell; Hutchinson). The AXUV detector array can capture energy from 100 eV to 10 keV in ADITYA-U tokamak. These particles can come mainly from the core of the plasma. The radiations reach the diagnostic through a pinhole arrangement covered by Beryllium (Be) foil of a very small thickness of 25 μm . SXR intensity depends on the density (n_e), temperature (T_e), and the effective charge (Z_{eff}) of plasma. The cut-off energy (E) of SXR is proportional to measured power $\exp(-E/T_e)$. Cut-off energy is a function of Be- thickness. F. C. Jahoda et al. proposed a technique for the measurement of T_e in 1960 by using the ratio method (Jahoda et al.). Here the plasma volume of the n_e , T_e and Z_{eff} should remain the same. The SXR intensity is then measured through two detectors and the ratio gives the T_e through the following equation:

$$R = \frac{I_1}{I_2} = \exp\left(\frac{E_1 - E_2}{T_e}\right) \quad 2.3$$

Where R is the ratio of the intensities measured with two SXR detectors. E_1 and E_2 stand for the cut-off energy of the two metallic foils having different thicknesses. ADITYA-U tokamak equipped with AXUV photodiode detectors. The resolutions are 0.2 m for space-resolved measurement and 10 μs for time-resolved measurement.

2.3.1.4. Hard X-ray (HXR)

The runaway electrons (RE) emissions are detected through the Hard X-ray (HXR) detectors. To study the RE dynamics, the 3 – inch NaI (TI) scintillator detector coupled with photomultipliers is used (R. L. Tanna, Ghosh, Chattopadhyay, et al.). The detector is kept inside the lead shield and is located at the equatorial plane 5 m away from the ADITYA-U tokamak vessel. It is collimated to see the limiter cross-section as shown in Figure 2.8. The calibration of this detector is done through the standard HXR source cesium-137 and cobalt. Due to the high density of the graphite limiter, the HXR contribution of the main plasma volume can be neglected in comparison to the HXR from the limiter surface. The total HXR intensity observed is proportional to lost runaway electron populations.

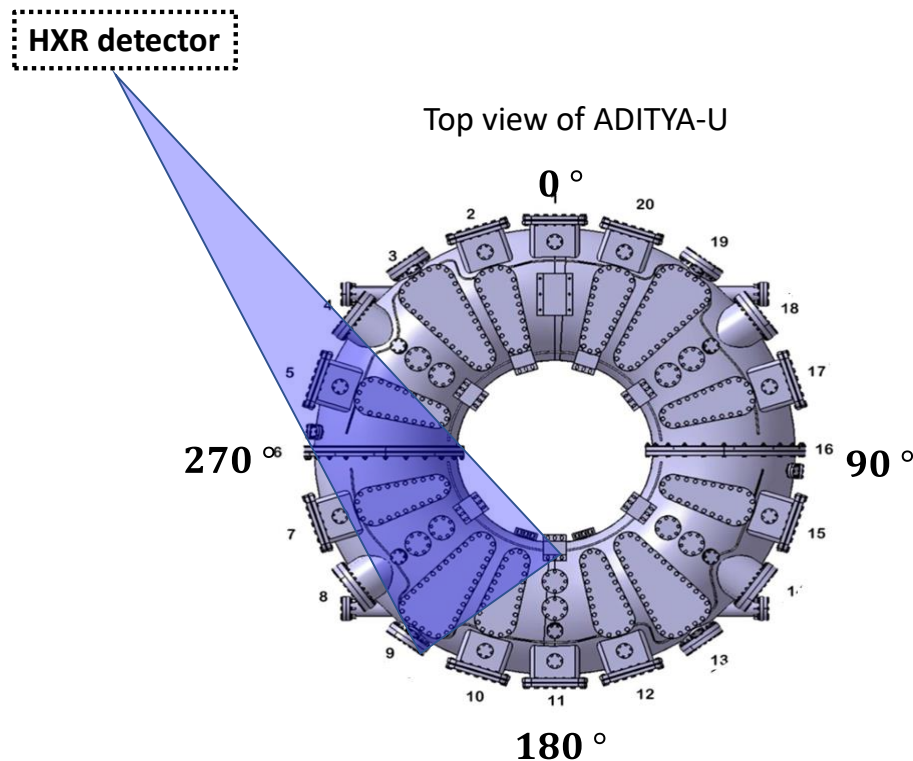


Figure 2.8. Line of sight for HXR measurement

2.3.1.5. Bolometer array diagnostics

The total power loss from fuel and impurity radiations is estimated using a bolometer diagnostic. Usually, metal foil resistors and silicon photodiodes are used in tokamaks. The basic concept of metal foil is to measure detector resistance change with the variation of radiation. However, silicon photodiodes have been commonly used in recent years. The AXUV photodiodes are used due to their excellent response time in $\sim \mu\text{s}$ order. Whereas the metal foil

detectors have a time response of \sim ms order. The detectors used in ADITYA-U tokamak are the AXUV photodiodes. Two cameras are installed on the top and bottom ports of the machine at a toroidal location for the emission of radiation power loss and radiation emission distribution (Tahiliani, Jha, Gopalkrishana, et al.). It consists of 16 detector channels to see the plasma in a poloidal cross-section through the pinhole arrangement. The spatial resolution of this detector is 4 cm at mid-plane with a time resolution of 0.2 ms. The channels are directly coupled to the tokamak vessel, and the electronics are kept in a compact housing mounted on the machine port directly. The electronics include the IV converter, amplifier, high-frequency cut-off filter, and drivers. It is typically seen in the ADITYA-U tokamak that 20 – 40 % of total input power loss occurs due to radiation.

2.3.1.6. Probe diagnostics

Probes are widely used diagnostics for low-temperature and density plasmas. The fundamental plasma parameter in the tokamak edge region, such as electron temperature, density, and plasma potentials, and their fluctuations, can be determined through probe measurements. This is only immersing a simple electrode (metal/wire) inside the plasma and studying the change in its I-V characteristics. The probes are designed for edge plasma parameters $T_e = 50$ eV with $n_e = 10^{19}$ m $^{-3}$ for a plasma duration of 500 ms, which is much higher than the predicted ADITYA-U design parameters.

Langmuir probe (LP)

The molybdenum material is used for making a cylindrical probe, which has a length of 4 mm and a diameter of 4 mm, shown in Figure 2.9 (a). The radial array of 7 such probes was installed on the top and bottom port of the machine at 160 ° toroidally apart. The probes are further kept inside the glass ceramic (MACOR). This setup is connected to the assembly containing SS below for radial movements through the mechanical action. Electrical feedthrough is used to have the probe output signals.

Garland Langmuir probe (GLP)

A matrix of 15 such Langmuir probes was placed to get the measurement in the edge and SoL region at several radials, poloidal, and toroidal locations, as shown in Figure 2.9 (b). These probes have a mushroom-shaped tip with a diameter of \sim 4 mm, and the tip is placed inside the non-machinable ceramic bushes (alumina, Al₂O₃) of different radial lengths. The ceramic

bushes are further bolted to SS support consisting of two SS plates each of thickness 3 mm at $r \sim 0.28$ m. This assembly is mounted on the vessel. Figure 2.9 (b) shows how the probes are mounted on the SS plate. It is seen clearly how the Kapton-coated copper wire is connected to the probe through the check nut and secured via ceramic beads till it gets connected to the feedthrough assembly. Two such plates are fabricated, one consisting of 6 probes on the bottom port and another consisting of 9 probes located on the radial. This can measure plasma density, temperature, plasma potential, and its fluctuations.

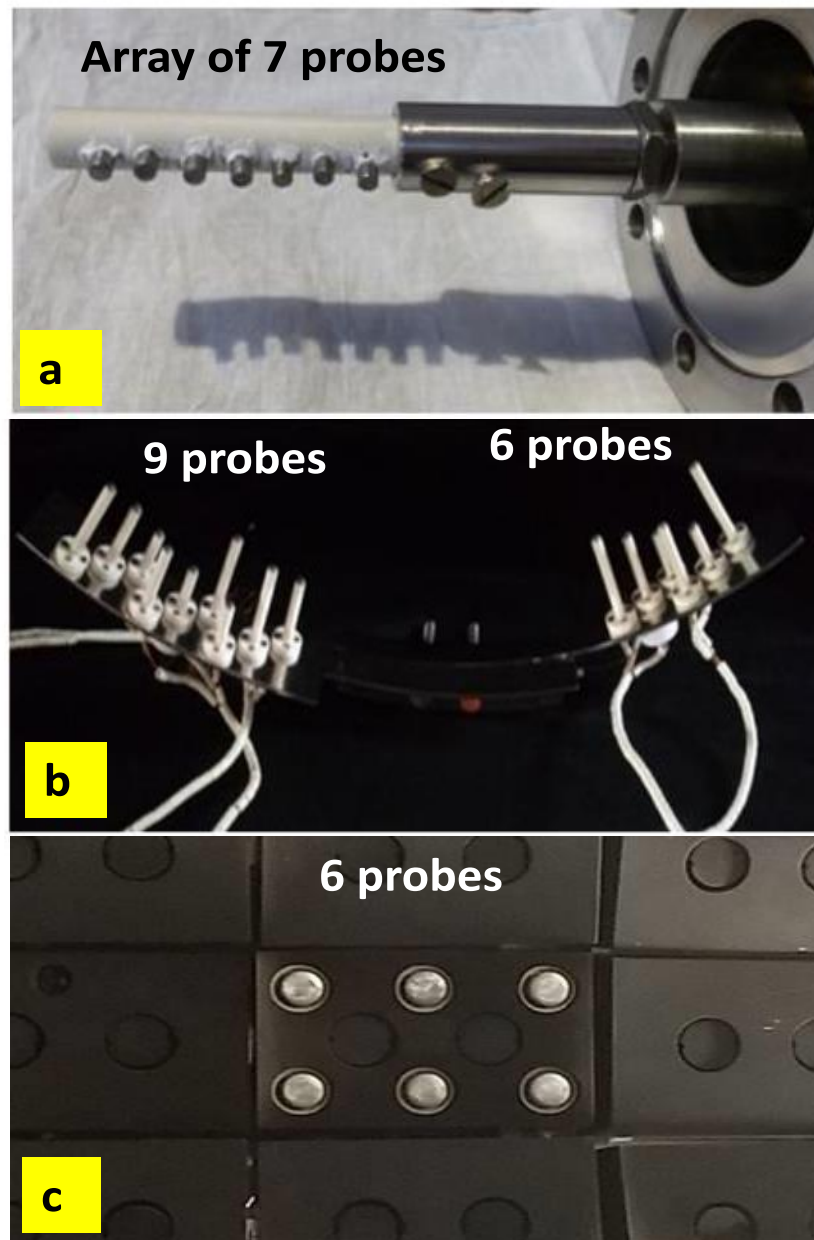


Figure 2.9. Different probe diagnostics: (a) Langmuir probe, (b) Garland Langmuir probe, (c) Flush Langmuir probe

Flush Langmuir probe (FLP)

The six flush Langmuir probes are present in the limiter tile of ADITYA-U tokamak. The flush Langmuir probes help measure the vertical flux falling on its surface (limiter tile). Figure 2.9 (c) shows the six probes having a 5 mm diameter FLP placed inside the limiter surface. The gas puff-induced detachment can be studied using these flush probes.

Triple Langmuir Probe (TLP)

The TLP is advantageous in sweep voltage generation and signal data analyzed and compared to data acquired by single and double Langmuir probes. Details on data acquisition are found in ref. (Rajpal et al.; Raulji et al.). The instantaneous plasma density and temperature measurement are possible through three identical probes. More details on this are described in ref. (S. Ghosh et al.)

Laser-heated emissive probe (LHEP)

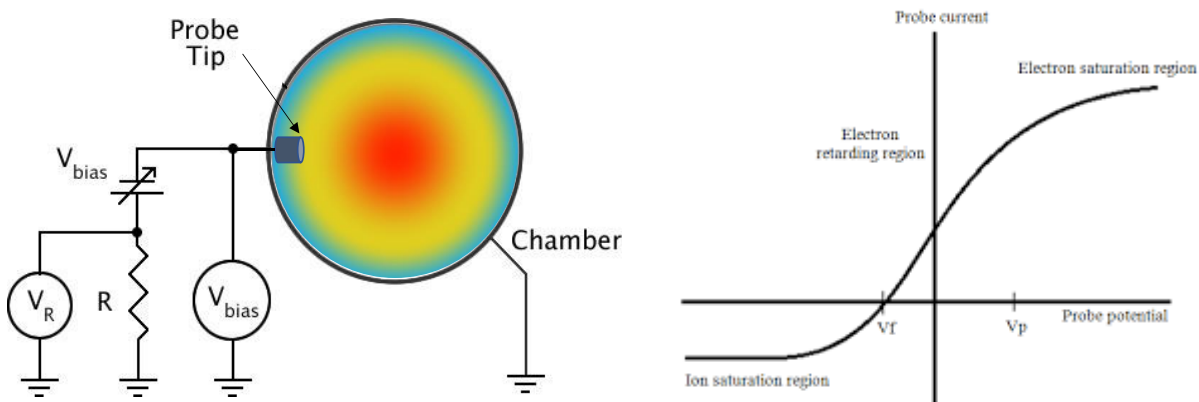


Figure 2.10. Probe measurement circuit and its characteristic curve

Two probes of 6 mm diameters of graphite material are installed on the radial port of the machine. The probes are radially movable. LHEP system is designed to measure plasma potential and its fluctuations in the SOL region considering the experimental and technical parameters of ADITYA-U. The probe surface is heated by continuously focusing CO₂ laser at 10.6 μm, 55 W. The laser is focused on the probe tip through optical arrangements.

The probe theories are well described in ref. (Pitts and Stangeby; Sudit and Woods). The probe circuit consists of the applied bias voltage and resistor through ion current flow. The probe is biased to a sufficient negative voltage such that only ions get collected through the probe. The circuit of the probe is shown in Figure 2.10 with its characteristic curve. The

saturated ion current represents the total current flow into the $I_{sat} = 0.5en_iA\nu_B$. where A is area of probe tip, ν_B is Bohm velocity ($\nu_B = \sqrt{(kT_e/m_i)}$), n_i is density of ions and m_i is the ion mass. Here for density measurement, the edge electron temperature of ADITYA-U is taken as 5 to 25 eV. The following equation relates the ion current and ion density,

$$n_i = \frac{2I_{sat}}{eA} \sqrt{\frac{m_i}{T_e(eV)}} \quad 2.4$$

Probe measurements can also determine floating plasma potential, edge electron temperature, and density.

2.3.2. Spectroscopy diagnostic

The selection of a spectroscopic system depends on the wavelength region of interest, the required spectral and time resolution, and the system's overall efficiency(Griem; Kunze; Sawyer). The visible spectroscopic system consists of dispersing elements to get the spectrally dispersed image and the mirror or optical arrangement for focussing the spectrally dispersed image on the detector. The primary example of dispersing element is the prism. The prism converts the white light into a spectrum of different colors. Another widely used dispersing element is gratings. The diffraction grating is used to have the higher resolving power in extensive wavelength coverage (Stroke; Zhuravlev). The transmission gratings can cover the infrared and short wavelengths in soft X-ray regions other than the visible range. Reflection grating is commonly used and is constructed by having identical structures (grooves) on a plane or concave surface. There are different methods to construct grooves on surfaces. The metals have decreased refractivity at lower wavelengths; hence the refractive grating reduces the efficiency. Then to reduce the number of elements in the spectrometer, the concave grating is used in this case (Namioka). Several other types of gratings include toroidal and varied line spacing gratings. The interferometer can also use as dispersing element with high dispersing power. Wide variants in optics, filters, and windows are available, and the glass material and the coating are changed depending on the studies. The spectrometer can have different mounting setups: Litrow (prism/grating), Ebert-Fastie (grating), and Czerny-Turner (grating). When the grating is concave, then eagle mounting, seya-namioka type, and grazing incidence mount can be used (Kunze). Various detectors are available, e.g., photodiode, photomultipliers tube (PMT), PMT array, Photodiode array, CCD (charge-coupled device), and CMOS (complementary metal-oxide-semiconductors) detectors.

Table 2.2. spectroscopically measurement aspect and plasma parameters

Spectroscopic aspect	Measurement of plasma parameter
Doppler broadening	Neutral and ion temperatures
Line intensity	Particle fluxes, density, and transport
The intensity of the line at different radial locations	ion density distribution and transport
Zeeman splitting	Local magnetic field
Molecular band structures	Vibrational and rotational temperatures
Line intensity ratio	Electron temperature or density measurement
Stark broadening	Electron density
Doppler shift due to moving ion	Rotation velocity

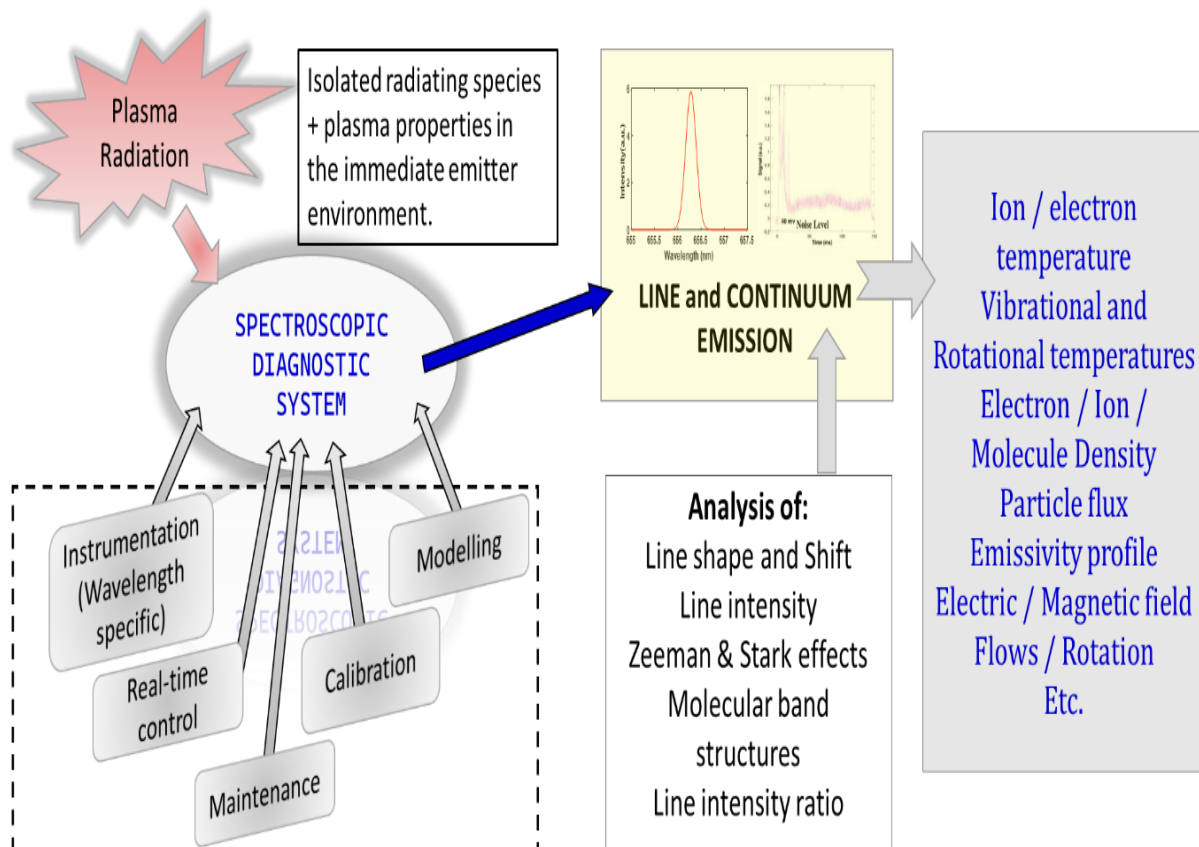


Figure 2.11. Spectroscopically measured plasma properties

However, selecting a spectrometer depends on the required spectral and time resolutions. The spectral resolution is a function of the grating properties (groove density, grating angle), the slit width of the entrance, focal length, and detection system alignment. The spectral line profile tells us the spectral resolution at different slit widths, and time resolution depends on the grating reflectivity and the detector quantum efficiency. The CCD-based cameras are slower than PMT detectors. The spectrometer is called a “spectrograph” when mounted with the 2D detector.

Spectroscopy diagnostics on ADITYA-U tokamak

The lines and continuum emissions from plasmas are spread over extended wavelength ranges. It involves X-ray to NIR wavelength regions. Spectroscopy plasma diagnostic is rich in providing plasma parameter information and its characterization at ADITYA-U tokamak. The spectroscopy studies in ADITYA-U tokamak are in several wavelengths ranging from X-ray at 0.3 nm, extreme ultraviolet EUV at 3 to 30 nm, vacuum ultra-violet (VUV) at 30 to 200 nm, UV 200 to 350 nm, Visible 350 to 750 nm, and NIR 750 to 1800 nm. The overview of physics studies on ADITYA and ADITYA-U tokamak can be found in (R. Manchanda, Chowdhuri, et al.)

2.3.2.1. Visible spectroscopy

Visible spectroscopy is an essential diagnostic to understand the edge plasma. Not only that, unlike probe diagnostics, it is a passive diagnostic tool since it does not perturb the plasma. Visible light emission covers the 350 – 750 nm wavelength range. The human eye is a detector that sends a visible signal to the brain. The brain act as an analyzer; it identifies the object through its captured image eyes. Hence, we use our eyes and brain as diagnostic to understand the world around us. In a similar way to understanding the plasma, the visible light radiations are captured using an optical setup, and it is recorded in a detector. The recorded data in the form of a spectrum is then analyzed. Figure 2.11 shows how the plasma radiations are captured through the spectroscopic diagnostic system, and the captured data can be line or continuum emission or absorption spectrums depending upon plasma properties. The captured spectra are analyzed for different spectroscopic aspects to measure relevant plasma parameters, as shown in Figure 2.11, and tabulated parameters in Table 2.2. The investigation and analysis require knowledge of the atomic molecular structure of different atoms, ions, and molecules. The well-known databases corresponding to that are NIST and ADAS (Summers; Kramida and Ralchenko). The modelling of the fundamental atomic and molecular processes is central to the analysis techniques.

Many optical viewports having circular and rectangular shapes with UHV compatibility have been chosen to get the single chord and space resolved measurement. In ADITYA-U tokamak, many lines of sight (LOS) crisscross the plasma using many radial top, bottom, and tangential ports of the machine to view the plasma. The radial viewports are standard the 63 and 100 CF glass windows. The tangential viewport is a re-entrant type and is customized in nature. It has a clear aperture of ~ 40 mm with a depth of ~ 146 mm and an inner diameter of ~ 48 mm. To have the space resolved profile measurements, two indigenously made long rectangular viewports having a length of 0.44 m and a width of 0.2 m are installed on the top and bottom port of the machine on the same toroidal locations. This port was developed using an O-ring, double V-groove technique, and ultraviolet (UV) grade fused silica glass. The viewport covers the entire low field side of the plasma poloidal cross-section and up to radius $r = 0.18$ m (minor radius $a = 0.25$ m) toward the high field side from the core of the plasma. Figure 2.2 shows several viewports available on ADITYA-U tokamak. All the visible systems have plano-convex lens-based light collection optics and optical fiber to transfer the light to the visible/NIR spectrometer. The lens-based light collection optics is known as a collimating beam probe. Here the tip of the SubMiniature A (SMA) connector coupled with optical fiber is placed at the lens's focal point, and thus a chord having almost parallel light is collected. Several combinations of collimating beam probes are present with different core diameter optical fibers having a diameter of 400 μm , 600 μm , and 1 mm in visible/NIR ranges. These are tabulated in Table 2.3.

Table 2.3. Several collimators and their optical specification

	Aperture (mm)	Focal length (mm)	Fiber used(mm)
Collimator 1	11	19	1
Collimator 2	6	8.7	0.4
Collimator 3	4	10	0.4

The visible spectroscopic systems are categorized into CCD and spectrometer-based detection systems and PMT-based detection systems. PMTs have a fast response compared to CCD detectors and are used to capture temporal profile measurements. The spectrometers used

here have a Czerny-turner configuration, an entrance slit followed by a collimating mirror for parallel light, and dispersing elements further. The light falls on the focusing mirror, which focuses the light at the exit port on the detector plane. The Czerny-turner spectroscopic configuration is displayed in Figure 2.12.

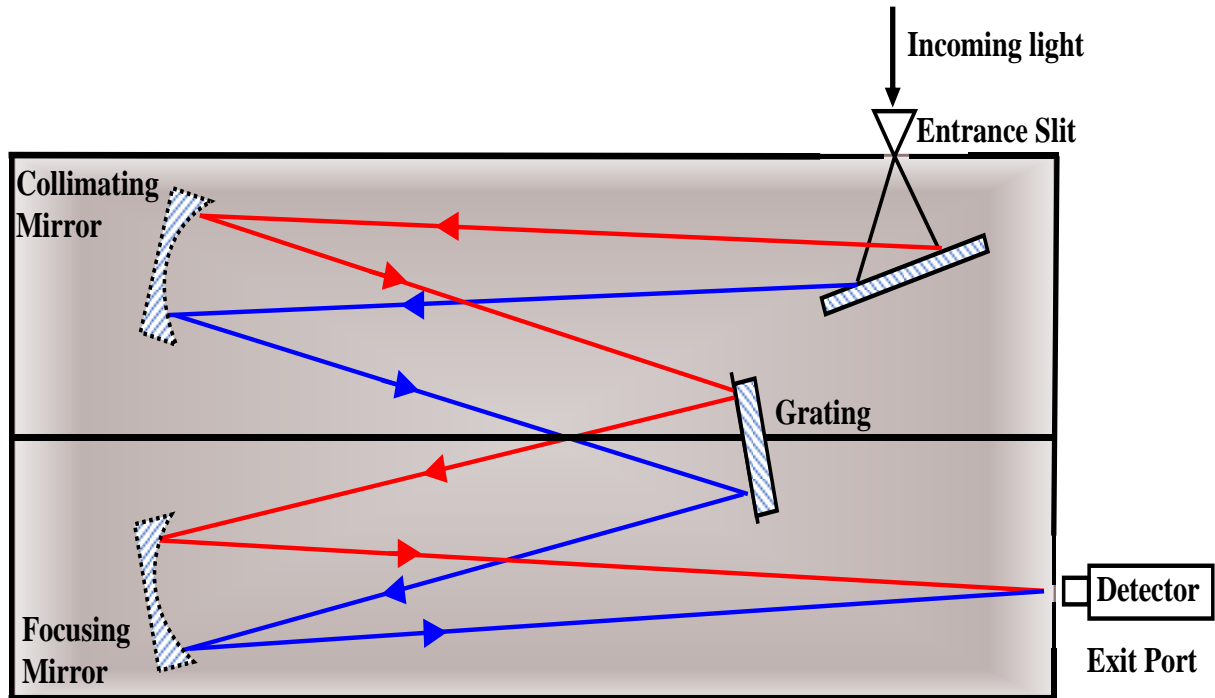


Figure 2.12. Czerny-turner Spectroscopic system

2.3.2.2. PMT and photo-diode-based spectroscopic system

The semiconductor-based PN junction photo-diodes are used to detect light and produce an electric current. The PMT uses the concept of multiplication of electrons through secondary electron emission for the low light measurements with fast time response, as shown in Figure 2.13. PMT-based diagnostics are used with an interference filter (IF) for wavelength selection and it is having 3 nm / 1 nm bandwidth and a diameter of 0.05 cm / 0.025 cm. Using this, the routine observation of H_α , O^+ , C^{2+} and viscount at 536 nm from the radial and top port of the machine is measured. Along with this, the PMTs are also used for H_β , H_γ , and neutral helium line emissions. The wavelength of the respective emission lines measured is given in Table 2.4.

The PMT array-based space-resolved measurement system has been developed to measure the H_α and visible continuum radiations from ADITYA-U tokamak plasma (M. B. Chowdhuri, Manchanda, Ghosh, Yadava, et al.). The system has a multi-channel wavelength selection system, PMT modules, and high voltage units. The data with this system is acquired in a

poloidal cross-section from the bottom port of the machine. The wavelength selection system is developed indigenously. It is an optical set-up made of fiber, lenses, and IF and has 16 channels. The aim of having 16 channels in the system is to record the radiation from both in and outboard sides of the plasma simultaneously. However, eight channels out of sixteen ones of the wavelength selection system have been utilized for measuring the spatial profile of the visible continuum. In this set-up, one end of the 1.5 m long 16 fibers has been arranged in the form of a 4×4 matrix type fiber packing having the size of 15×15 mm and held by the fiber locking cube. A combination of two broadband anti-reflection coated plano-convex lenses has been used to convert the light into a parallel beam before passing through the IF. The IF holder can be quickly taken out to change the IF depending on the wavelength selection.

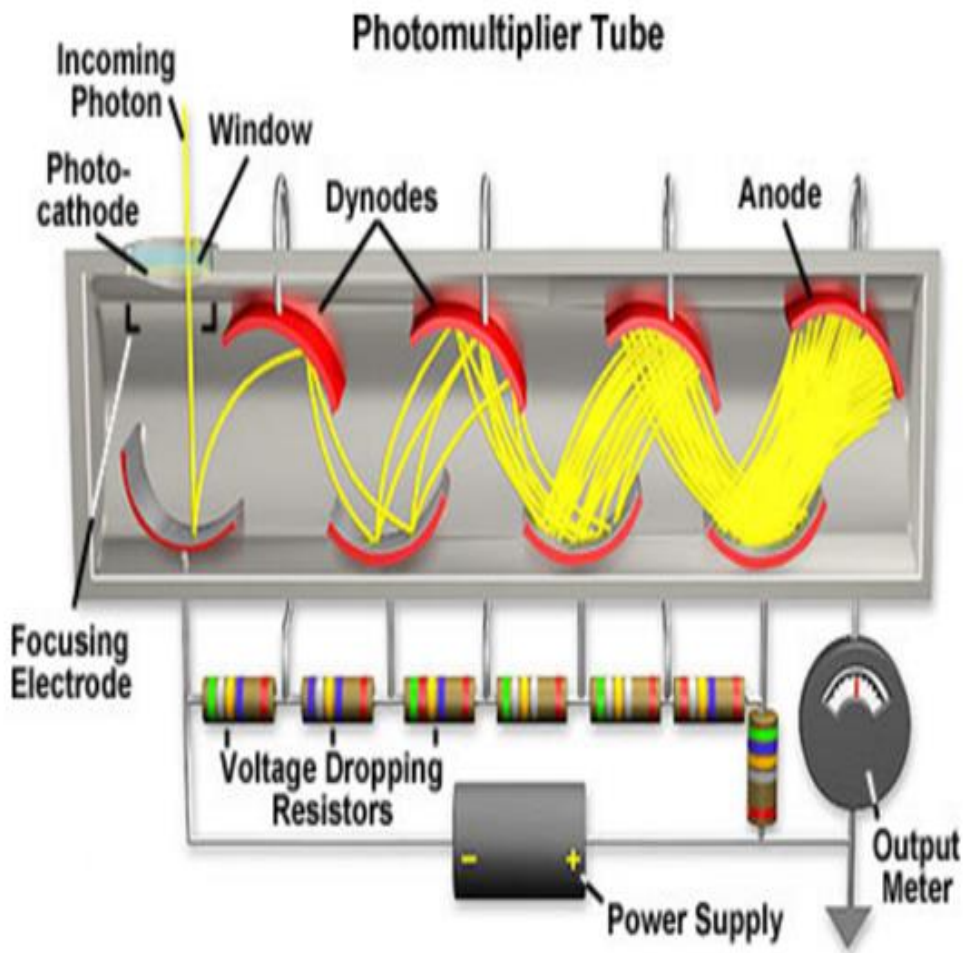


Figure 2.13. the photo-multiplier tube contains dynodes for secondary electron multiplication action (Photonics Hamamatsu)

Not only that, the four photo-diode models no: HUV-1100BQ are installed to measure the H_{α} – emissions from the machine's inboard, outboard, top, and bottom port with the same

poloidal location. It requires a supply voltage of ± 5 V to ± 18 with 5 mA currents, and it has a maximum response at ~ 900 nm with an active area of 5.1 mm^2 (EG&G JUDSON). Output signals from these diagnostics are recorded, digitized, and stored using the central data acquisition (DAQ) system of ADITYA-U tokamak with a temporal resolution of $10\text{ }\mu\text{s}$.

Table 2.4. List of observed emissions with PMT/photodiode

Plasma species (neutral/impurity)	Nomenclature	Wavelength (nm)
Hydrogen	$H_\alpha, H_\beta, H_\gamma$	656.28, 486.1, 434.2
Oxygen	O^+	441.9
Carbon	C^{2+}	464.7
Lithium	Li^0	670.8
Helium	He^0	667.8, 796.5, 728.1
Visible continuum		528, 523

2.3.2.3. VUV survey spectroscopic system

The VUV spectrometer is directly mounted on the machine. It consists of a VUV spectrometer having a focal length of 0.3 m coupled with a multi-channel plate and a visible CCD detector. The spectrometer is UHV compatible and mounted directly on the 100 CF radial port of tokamak at the vertical midplane. The 100 CF gate valve and 63 CF bellow are placed between the tokamak machine and the spectroscopic system. The electrical break is provided to keep the machine and system electrically isolated. The spectroscopic instrument is ~ 2 m away from the center axis of the machine, with a viewing chord diameter of ~ 0.075 m at mid-plane. The slit width is changeable in the $10 - 250\text{ }\mu\text{m}$ range. It consists of three toroidal gratings having groove densities of 2105, 450 and 290 grooves/mm and the corresponding wavelength coverage and its Reciprocal Linear Dispersion (RLD) are, 10 – 31 nm (RLD = 0.122 nm/pixel), 100 – 120 nm (RLD = 0.0813 nm/pixel) and 10 – 180 nm (RLD = 0.020 nm/pixel), respectively. Further details of this system are provided in ref. (S. Patel et al.).

2.3.2.4. NIR survey spectroscopic system

The 0.5 m spectroscopic systems are installed with linear InGaAs photodiode array-based detectors. As the detector efficiency limits the measurements up to 1100 nm for the CCD detector, the InGaAs detector has been used to extend the limit up to 1700 nm. This consists of three gratings 300 grooves/mm blazed at 1700 nm, 600 grooves/mm blazed at 1100 nm, and 1200 grooves/mm blazed at 750 nm. The detector has 1024×1 pixels with each pixel size of $25 \mu\text{m} \times 500 \mu\text{m}$. The spectral resolution measured to be 0.53 nm at 1530 nm for 300 grooves/mm grating, 0.26 nm, and 0.12 nm at 1128 nm for 600 grooves/mm, and 1200 grooves/mm grating, respectively. Initial results from this system are presented, and survey spectrum measurement is carried out (Ramaiya et al.).

2.3.2.5. Visible survey spectroscopic systems

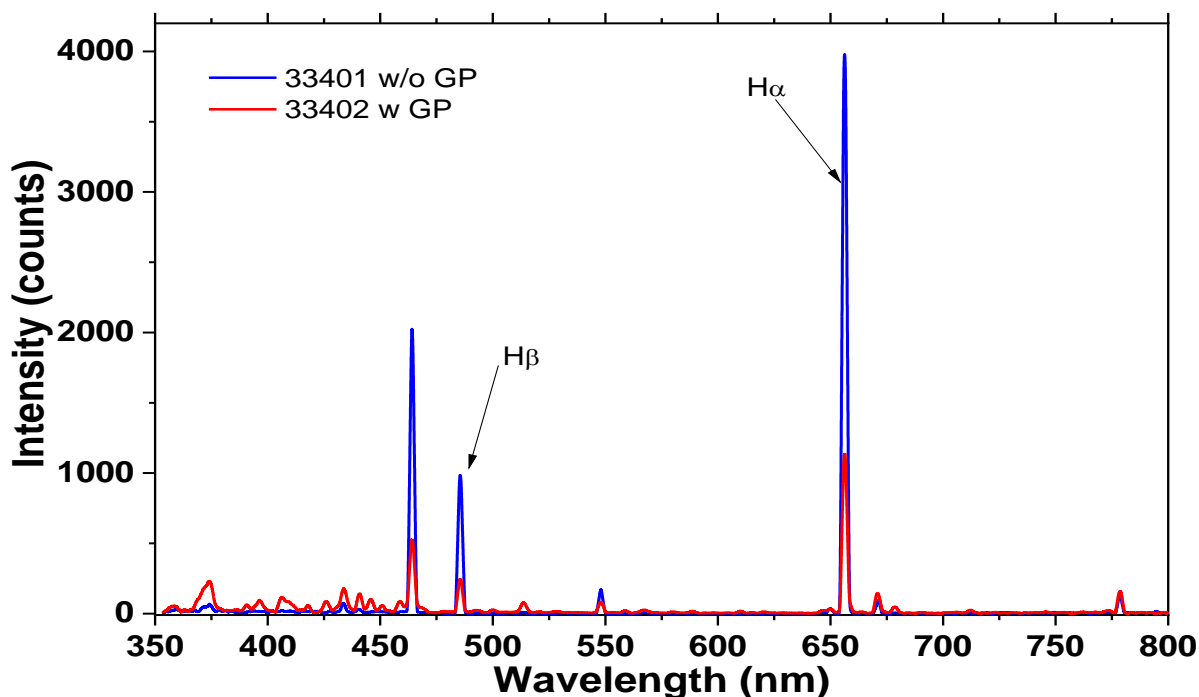


Figure 2.14. Typical survey line emission spectrum acquired using Avantes spectrometer.

The poorer resolution spectrometer has a spectral resolution of 1.5 nm with a $25 \mu\text{m}$ entrance slit width. It covers the wavelength range of 350 – 800 nm and is used as a survey spectrometer to identify the significant line emissions and species in the plasma. The spectrum acquired from this system is shown in Figure 2.14. Another is the 0.5 m visible spectrometer in the Czerny-turner configuration with two entrance slits and two exits (one slit and one port). Three gratings are installed at 600 grooves/mm blazed at 600 nm, 600 grooves/mm blazed

at 300 nm, and 1200 grooves/mm blazed at 600 nm. The spectral resolution of this system is 0.04 nm with 1200 grooves/mm grating and 0.08 nm with 600 grooves/mm grating. The side entrance slit and front exit port are used during the experiments. The exit port is mounted with a CCD-based detector having 1024×256 pixels with each pixel dimension $26 \times 26 \mu\text{m}^2$. The acquired experimental data for shot #36110 is shown in Figure 2.15.

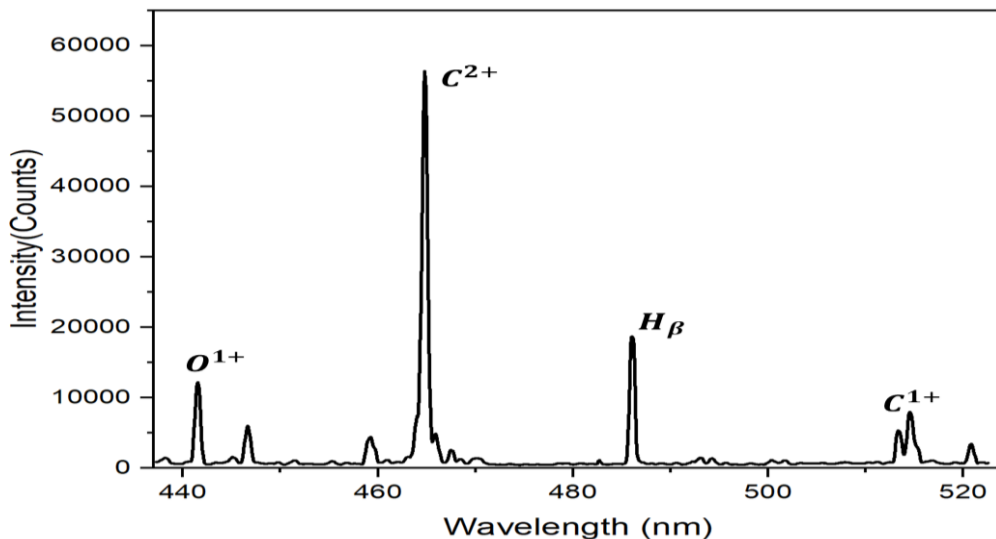


Figure 2.15. Acquired wavelength-calibrated data using a 0.5 m spectroscopic system

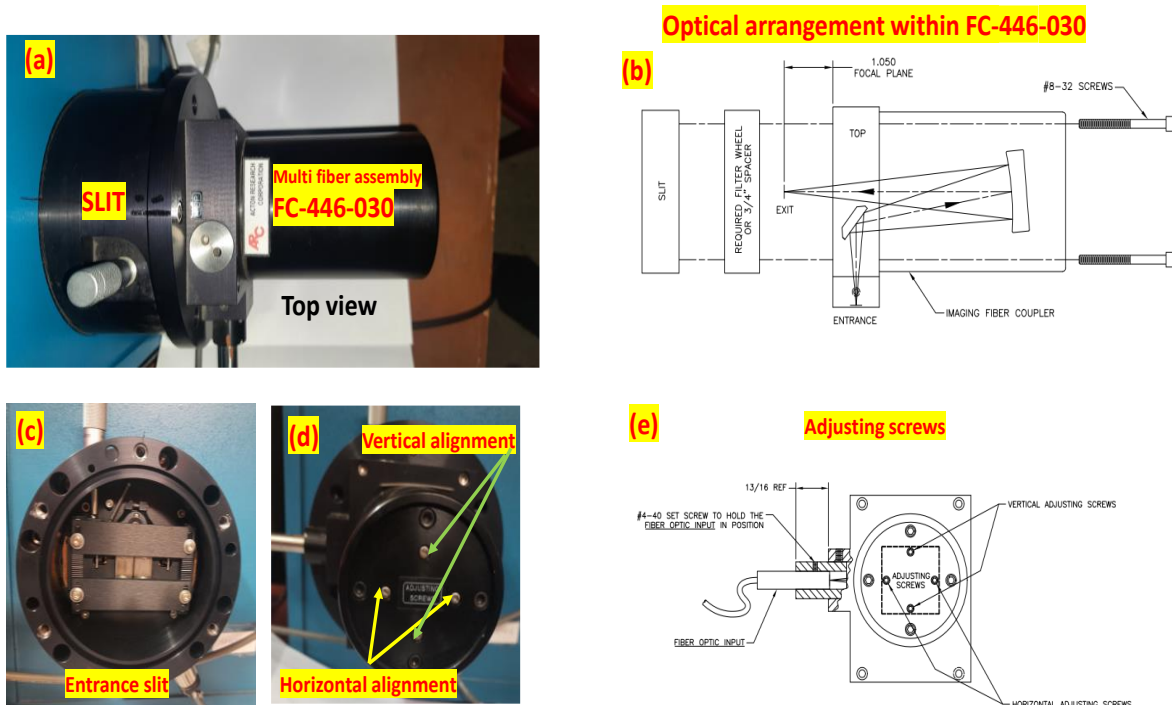


Figure 2.16. Space resolved high-resolution spectrometer entrance: (a) multi-fiber array assembly FC-446-030, (b) the optical schematic of multi-fiber assembly, (c) entrance slit, (d) adjusting screws of the multi-fiber array, (e) schematic of adjusting screw from the datasheet

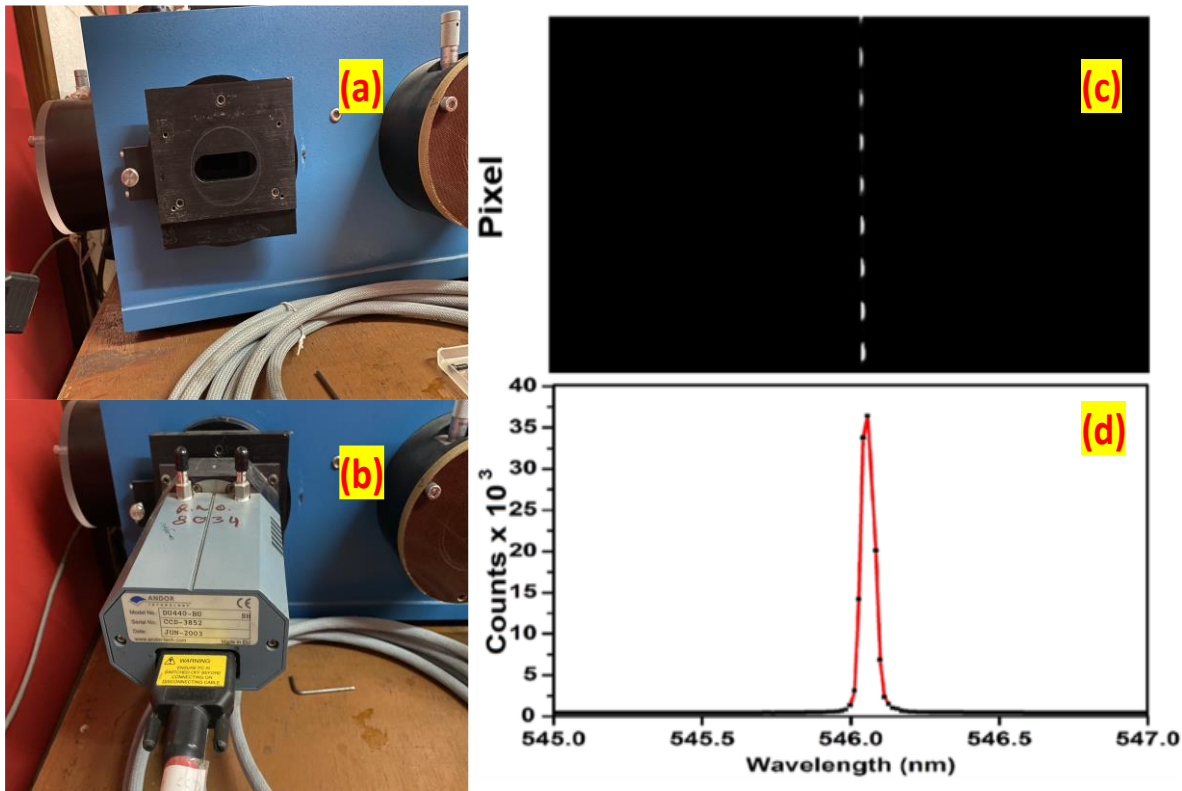


Figure 2.17. Space resolved high-resolution spectrometer exit plane: (a) the exit port in open condition, (b) attached CCD DV440 at the exit port, (c) eight tracks of the spectrometer on CCD image plane, (d) mercury emission line at 546 nmS

2.3.2.6. The space-resolved high-resolution spectroscopic system

System description

This optical system comprises a 1 m focal long Czerny-turner type high-resolution spectrometer with two entrance slits and two exit ports having f/8.7. The side entrance slit has a fiber array installed. This array contains a total of eight 400 μm core diameter fibers with a separation between each fiber is 700 μm . The separate images of the fiber array and the entrance arrangement are shown in Figure 2.16 (a) to Figure 2.16 (e). The light from the entrance slit falls on the collimating mirror and then on a holographic grating with 1800 grooves/mm blazed at 500 nm. The dispersed light is collected at the exit port through a CCD detector via a focusing mirror placed inside the spectrometer. Figure 2.17 (a) and Figure 2.17 (b) show the exit port and mounted CCD. The standard Al + MgF₂ optical coating on mirrors is present for high efficiency. The CCD detector has a total of 2048 \times 512 pixels with 13 \times 13 μm^2 size of each pixel. The reciprocal linear dispersion of this system is 0.5 nm/mm. As the entrance contains fiber array assembly, to see all the LOS together, the vertical binning of the CCD detector has been done. Each fiber array is assigned a 16 – pixel row height (track);

such a total of 9 tracks can be binned together by having a ~ 10 – pixel gap between each track to avoid cross-talk. The binned image on CCD is shown in Figure 2.17 (c), with the acquired mercury line in Figure 2.17 (d). The system is used to monitor neutral H_{α} emission line is Balmer emitted by neutral hydrogen and several impurity ions, mainly C^+ , O^{4+} , C^{2+} and C^{5+} . The exposure time varies depending upon the experiments, which will be discussed in respective experimental details. The spot size diameter inside the tokamak for top and tangential LOS is shown in Figure 2.18 (a) and Figure 2.18 (b), respectively. It is done by back-illuminating the optical fiber used for the space-resolved measurement.

2.3.2.7. Calibration of the system

Spectroscopic calibration is an essential part of the study for quantitative analysis of different plasma properties. The calibration is categorized as wavelength, relative intensity, and absolute intensity calibration. Relative intensity calibration is required when there are multiple measurements made together and requires comparison or profile measurements, and this is done by exposing all the channels with the same source simultaneously. The Absolute intensity calibration has defined the system's efficiency at different wavelengths, which is being done through the known spectral radiance (radiance - the electromagnetic radiation power reflected, transmitted or received by a surface per unit solid angle in a per unit projected area, In this study spectral radiance in terms of the number of photons are known for the calibration source) source. These are discussed in detail here.

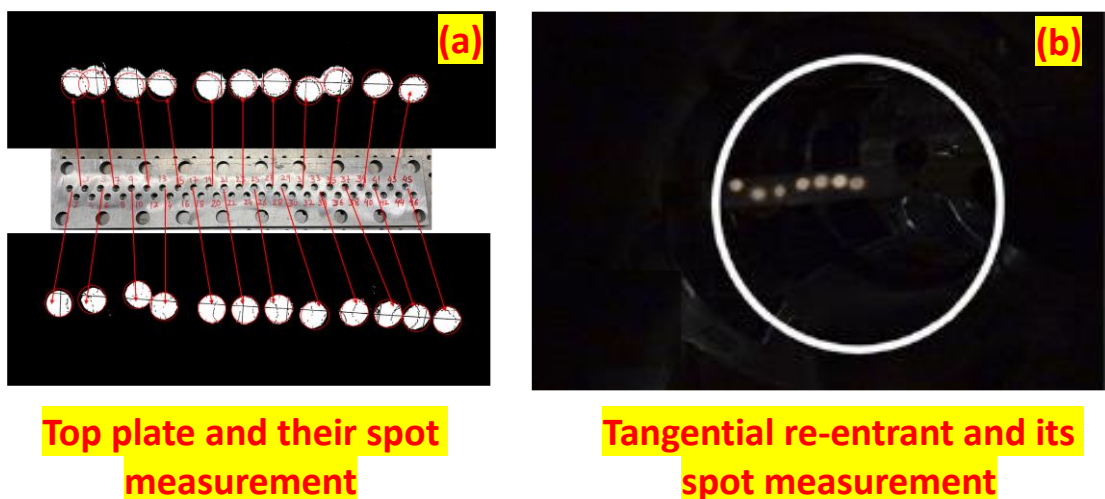


Figure 2.18. Spot size estimation of top and tangential plates with their respective optics attached: (a) spot size of the top plate with collimator 2 from Table 2.3, (b) spot size of tangential port with collimator 3 from Table 2.3.

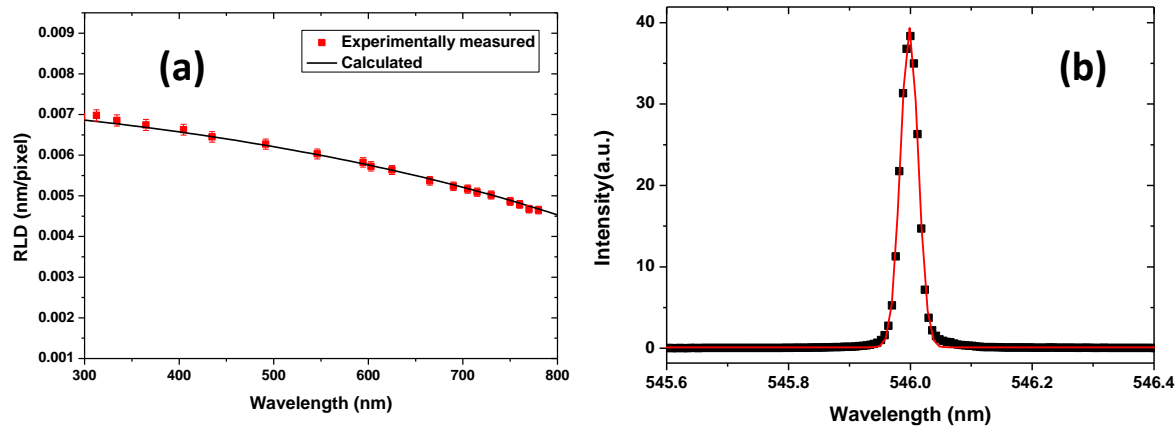


Figure 2.19. Wavelength calibration of space resolved high-resolution spectrometer: (a) reciprocal linear dispersion measurement red data points represent the experimentally measured dispersion, and the solid black line represents the calculated dispersion, (b) 546 nm emission line acquired for FWHM estimation

Wavelength calibration

The wavelength calibration is performed with known standard sources, such as a pen-ray source of mercury, neon, argon, etc. The known wavelengths between 300 to 800 nm have been selected from available known neon and mercury UVP-made pen-ray sources (the lines are also verified from the NIST database)(UVP). The data is acquired at a set wavelength of the spectrometer and from a wavelength region in which two lines are present in the same frame. Here, the pixel position of two known different spectral lines is noted, and the reciprocal linear dispersion is found by obtaining the ratio of differences between the two wavelengths and the difference in the pixel position of those wavelengths. If two lines are not present in the same frame, then set the wavelength of the spectrometer, λ_0 is shifted to $\lambda_0 \pm 3$ nm. The span of the detector is $\sim \lambda_0 \pm 5$ nm with the above-described grating setup. In Figure 2.19 (a), the solid square dots in red represent the experimentally measured dispersion in nm/pixel unit. The solid black line in the same Figure 2.19 (a) represents the theoretically calculated dispersions. The grating equation for dispersion is $\sin\alpha + \sin\beta = m\delta\lambda$ (Jenkins and White). Here α and β are the incident and diffraction angles respectively, m is the order of spectral diffraction and δ is the groove density. For the Czerny-turner configuration, the angle between the entrance slit and the central pixel of the detector is ($\phi = 13.98^\circ$). The reciprocal linear dispersion of the system is derived by the following equation (Banerjee, Kumar, et al.).

$$D(\lambda_0) = \frac{d\lambda_0}{dx} = k \left[(1 - a^2 \lambda_0^2)^{\frac{1}{2}} \cos\left(\frac{\phi}{2}\right) - a \lambda_0 \sin\left(\frac{\phi}{2}\right) \right] \quad 2.5$$

Here $a = \delta/(2 \times 10^6 \times \cos(\phi/2))$ and $k = w/(\delta \times f)$, where w represents the detector pixel size in ($w = 13 \mu\text{m}$), “ f ” is the focal length of the instrument in mm ($f = 1000 \text{ mm}$). Figure 2.19 (a) shows the calculated dispersion curve with a solid black line. The measured value and estimated values match within 2% of the error. For measurement of the instrumental width, the 546 nm mercury emission line is observed, and the Gaussian line profile is fitted to get the full width and half maximum (FWHM) is $\sim 0.034 \text{ nm}$. The fitted profile is displayed in Figure 2.19 (b). The same exercise is done for other tracks of the spectrometer.

Relative intensity calibration

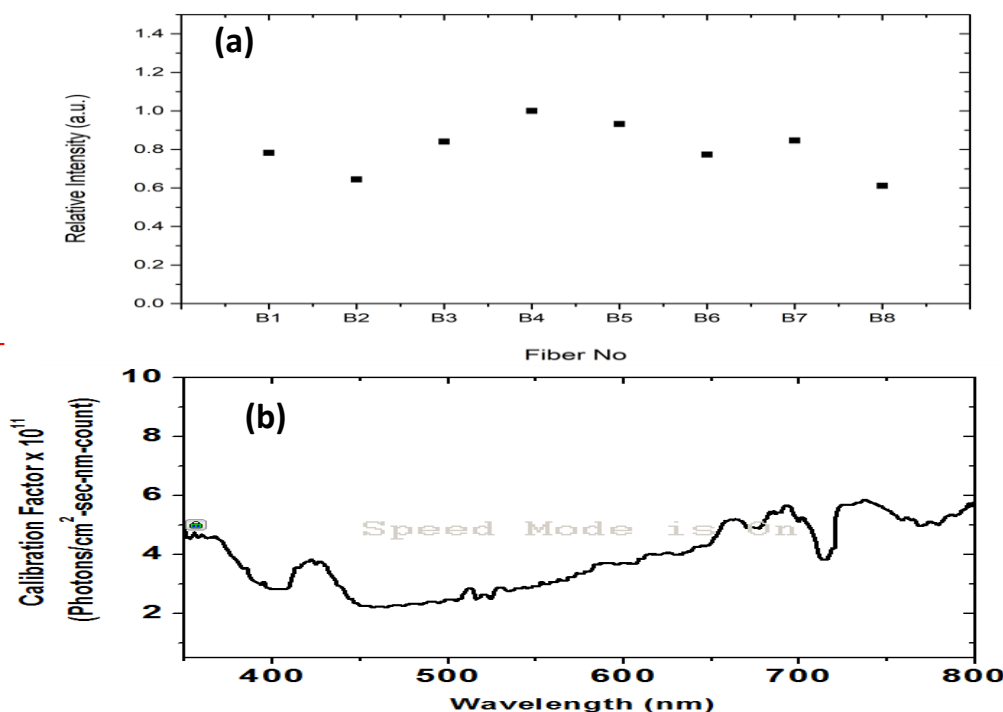


Figure 2.20. Intensity calibrations: (a) relative intensity calibration factors, (b) absolute intensity calibration factors

The eight tracks of the spectrometer have been calibrated. For this purpose, the in-house made, properly diffused light source has been used. This is made using a fluorescent mercury lamp and diffused in a $50 \text{ cm} \times 10 \text{ cm}$ area using a plastic diffuser plate for transmission. The light diffused uniformly is ensured by using the same fiber in different locations. The same exercise was carried out by using a LabSphere Inc. calibration source from 350 to 800 nm. However, it is obtained that relative calibration has no wavelength dependency, i.e., the relative calibration factor between the 8 fibers remains the same at all wavelengths between 300 – 800 nm. The relative intensity calibration hence carried out at 546 nm and the variation of factors are given in Figure 2.20 (a). The intensity variation of a single fiber over the wavelength range

of 300 – 800 nm is also shown in Figure 2.20 (b). The calibration has been carried out for every experiment to verify whether there is any change in relative intensity calibration factors.

Absolute intensity calibration

The standard blackbody source having known spectral radiance made by Labsphere Inc. having model no URS600 has been used. One channel is calibrated absolutely and the absolute calibration for other channels has been produced using the relative factor intensity calibration factor. The absolute calibration is carried out by putting the above-discussed source in front of the optics kept near to tokamak. The spectral radiance of the described source is in photons · m⁻² · sec · Sr · nm and denoted by N_λ . The acquired intensity during calibration is taken in units of counts · sec⁻¹ and noted as C. The calibration factor is defined by $K = N_\lambda/C$.

The calibration factor is a cumulative effect of the spectroscopic instrument and optics; it is quantum efficiency $Q(\lambda)$, dispersion $D(\lambda)$, transmission $T(\lambda)$, and the area, solid angle from where the light is being collected ($A \times \Omega$). It represents in terms of the following equation

$$C = N_\lambda \times A \times \Omega \times D(\lambda) \times T(\lambda) \times Q(\lambda) \times G \quad 2.6$$

Here, G is the detector's number of photons generated by each count. Figure 2.20 (b) describes the calibration factor acquired and its wavelength dependence over 350 to 800 nm of the wavelength range. The sensitivity below 450 nm is anomalous in nature, similar to the earlier observation made in 2008 with different CCDs (Banerjee, Kumar, et al.). The peaks observed in the intensity calibration curve are known as "Rayleigh's anomaly," and the dips observed in the intensity calibration curve are known as "Wood's anomaly" (R. W. Wood; Maurel et al.).

Chapter 3. Investigation of edge plasma through the modelling of spectral line profiles

3.1. Analysis technique for spectral line profile modelling

The atomic and molecular processes in the plasma help to determine the characteristic properties of plasma (Davison and Horie). Spectroscopy diagnostics are best for understanding the emission and absorption processes. This diagnostic tool is the most established and oldest diagnostic. Any plasma emits and absorbs electromagnetic radiation having different photon energies. Also, these radiations can be classified as continuum and line radiations. The thesis is focused on line radiations. This chapter focuses on line shape modelling of the emission and absorption of spectral lines.

The emission and absorption occur due to the transfer of a bound electron from the upper or lower level to the lower or upper level, respectively, as shown in Figure 3.1. In the emission process, the transition of an electron from the upper level to the lower releases the photon energy ΔE , which is the energy difference between the upper and lower levels. In the absorption process, the electron makes the transition from the lower level to the upper level by gaining the energy difference ΔE from some source. Emission and absorption are represented in Figure 3.1. Emission measurement is always passive measurement in nature. It occurs in optically thin plasma. However, the absorption process is the opposite in nature. It is an active process. It requires some broadband radiation as a source to excite the bound electron to the upper level. This occurs in optically thick plasmas. To understand this, let us use the nomenclature m as the

upper level, and n as the lower level. Photon energy with Planck's law is $E = h\nu$ (Here h is Planck's constant and ν is the frequency of corresponding photon). In several ways, the atomic interaction in plasma is classified. Depending upon bound and free electron, the process is classified as bound-bound (b-b) process, bound-free (b-f), and free-free (f-f) processes. In the plasmas, continuum radiations occur due to free-free transitions in plasma. All these processes are tabulated in Table 3.1.

Table 3.1. The basic atomic processes in plasma (B-B is Bound-Bound transitions, F-F is Free-Free transitions, and B-F is Bound-Freeee transitions. C is the collisional process, and R represents radiative process)

Excitation		De-excitation	Example (M is any atom)
b-b	Electron impact excitation (C)	Electron impact de-excitation (C)	$M^* + e \leftrightarrow M + e$
b-b	Photo-absorption (R)	Spontaneous decay(R)	$M + h\nu \leftrightarrow M^*$
f-f	Bremsstrahlung (R)	Inverse bremsstrahlung (C)	$M^+ + h\nu + e \leftrightarrow M^+ + e'$
b-f	Photoionization (R)	Radiative Recombination(R)	$M + h\nu \leftrightarrow M^+ + e$
b-f	Electron impact ionisation (C)	Three-body recombination (C)	$M + e \leftrightarrow M^+ + e' + e''$

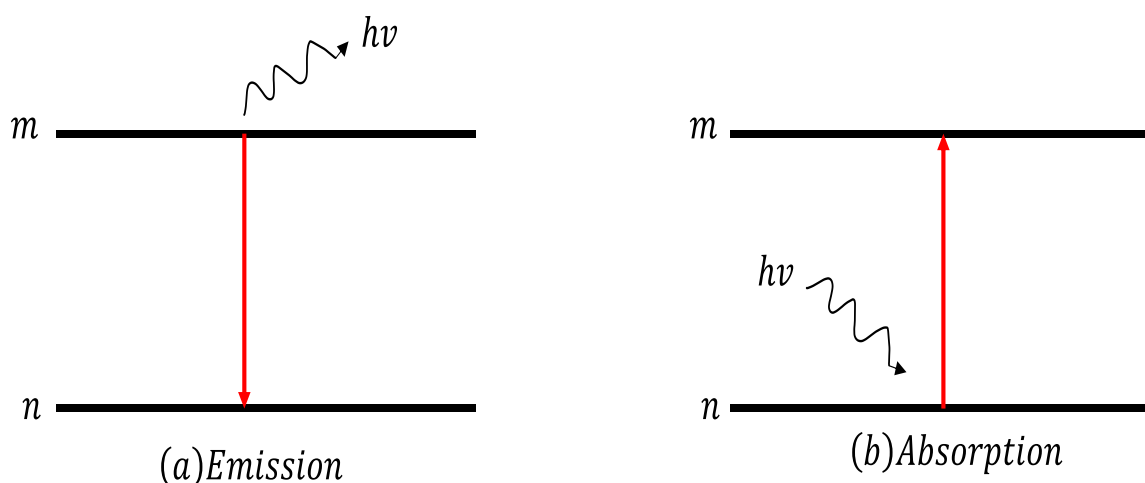


Figure 3.1 In photon emission, an electron in excited state m decays down to a lower energy state n releasing a photon with energy $h\nu$. Absorption is this process in reverse; an electron in lower state n absorbs a photon and enters the excited state m .

3.1.1. Bound-bound transitions

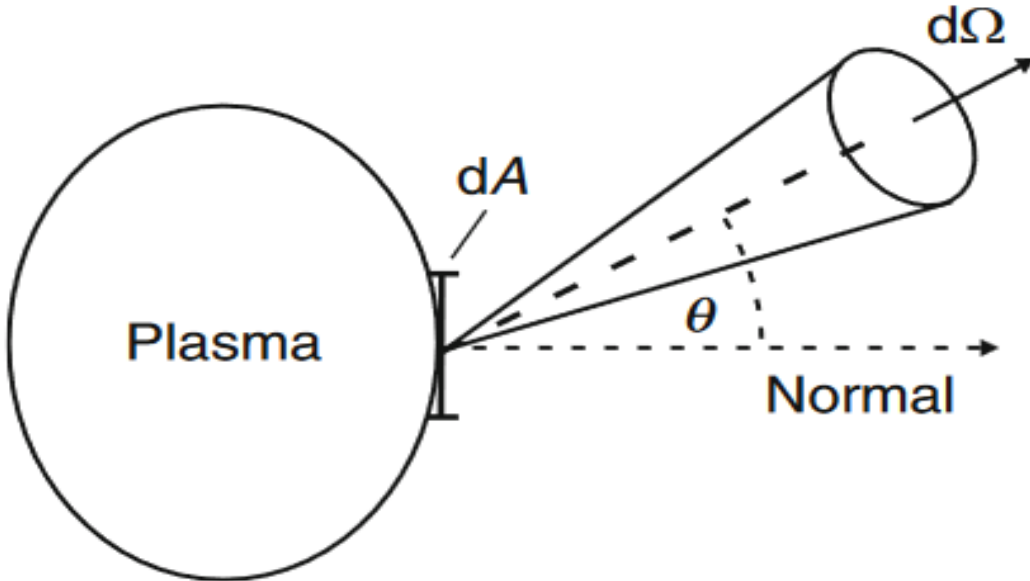


Figure 3.2. Schematic of radiance (L) which is defined by radiant flux per unit solid angle $d\Omega$ (Kunze)

The electron resides in the discrete energy level in the atom/ion. The transitions to another discrete energy level happen during a collision or through the emission/absorption of photon energy. Here, upper and lower energy levels are discrete, and the transition is the bound-bound process. The processes leading to such transition are electron impact excitation and de-excitation, which are induced transitions. Spontaneous decay of electrons occurs without any interaction. Resonant photo-absorption is an inverse process of spontaneous decay. This happens when the photon energy is equal to the difference between lower-level and upper-level energy.

In a bound-bound transition, the frequency ν_{mn} is given by,

$$\nu_{mn} = \frac{E(m) - E(n)}{h} \quad 3.1$$

Where $E(m)$ is the energy of the upper level and $E(n)$ is the energy of the lower level. The decay of density $n_z(m)$ of upper-level electrons of charge species (z) during spontaneous emission is,

$$-\frac{dn_z(m)}{dt}|_{m \rightarrow n} = A(m \rightarrow n)n_z(m) \quad 3.2$$

Here $A(m \rightarrow n)$ is the constant known as the Einstein coefficient or transition probability in units of s^{-1} . With each transition photon of energy $h\nu_{mn}$ is emitted, the emission coefficient is hence given by,

$$\varepsilon(m \rightarrow n) = \frac{h\nu_{mn}}{4\pi} A(m \rightarrow n) n_z(m) \quad 3.3$$

These basic spectroscopic formulas show that the population densities $n_z(m)$ of excited states of atomic species are the quantities obtained from the estimation of the radiance of the line. Equation 3.3 gives the emissivity which is hereafter also called emission coefficient. The experimentally estimated emission coefficient is represented by,

$$\varepsilon(m \rightarrow n) = \frac{d^2\phi(r)}{dV d\Omega} \quad 3.4$$

Here, $d\phi(r)$ is the radiant flux from volume dV at r . As shown in Figure 3.2 $d\Omega$ is the solid angle. The emission coefficient has units of $watt/m^3 Sr^{-1}$. From equations 3.3 and 3.4, if the experimental emissivity (E) is estimated and the transition probabilities are known. The sum of all transition probabilities from A ($m \rightarrow$) one upper level to all the lower levels is given by $\tau_m = \frac{1}{A(m \rightarrow)} = \frac{1}{\sum A(m \rightarrow n)}$. The line is broadened through different broadenings, which will be further discussed in-depth in the next section. The line profile function is represented by $f(v)$. Equation 3.3 is rewritten as,

$$\varepsilon_v(m \rightarrow n) = \frac{h\nu_{mn}}{4\pi} A(m \rightarrow n) n_z(m) f(v) \quad 3.5$$

The unit of derived quantity is $\frac{watt}{m^3 Hz}$. This is also called absolute intensity. If the emission is induced through the electromagnetic wave field, the spectral radiant energy density is $u_v = \frac{L}{c}$, where L is the spectral radiance. Emissivity related to radiance, as it is the ratio of radiance of any surface to the black body surface.

$$-\frac{dn_z(m)}{dt}|_{m \rightarrow n} = B(m \rightarrow n) u_v n_z(m) \quad 3.6$$

The inverse process of this is absorbing the photon energy of electromagnetic radiation is known as absorption and is represented by the following equation,

$$-\frac{dn_z(n)}{dt}|_{n \rightarrow m} = B(n \rightarrow m) u_v n_z(n) \quad 3.7$$

Here $B(m \rightarrow n)$ and $B(n \rightarrow m)$ are known as the Einstein coefficient for induced emission and induced absorption processes, respectively. These coefficients are available and obtained by considering the system in thermodynamic equilibrium (transition rates are balanced in both directions: upper to lower and lower to upper). Also, the population in this follows the Boltzmann distribution and Planck's law of radiation, and the conditions can be described by the following equations:

$$g(m)B(m \rightarrow n) = g(n)B(n \rightarrow m) \quad 3.8$$

$$A(m \rightarrow n) = \frac{8\pi h\nu_{mn}^3}{c^3} B(m \rightarrow n) \quad 3.9$$

In general, the experimentally measured intensity represents the radiance of the plasma L over the cross-section of the column, i.e., line integrated measurement over, say x direction. The local emissivity is estimated through the Abel-inversion technique(Bell; Condrea et al.), as discussed later in section 3.6.3.

3.1.2. Bound-free transitions

The electron of an ion gains sufficient energy to eject bound electrons into the continuum, and the ionization state is promoted by one, or the electron enters the discrete from continuum energy level by reducing the ionization state by one. The electron impact ionization ensues when the free electron interacts with the ion and hits the bound electron into the continuum. Three-body recombination (electron impact recombination) happens when two electrons enter an ion's volume at the same time, one gets captured by the ion, and the second gets free through carrying extra energy. The photo-ionization process is when the bound electron enters the continuum due to the absorbed photon energy, promoting the ionization state of the ion by one. Radiative recombination is when the ion captures one electron, and extra energy gets emitted. Autoionisation is the process that occurs with a doubly excited ion, and the high-energy photon is then resonantly scattered by an atom or ion. The other electron decays to the ground state. The opposite of this process is dielectronic recombination. Here, the free electron gets into an ionic state, and the bound electron transitions to an excited state through excess energy and becomes a doubly excited ion.

3.1.3. Free-free transitions

The free-free transition occurs due to the loss/gain of energy from electrons into the continuum. Two processes fall into this category Bremsstrahlung and Inverse bremsstrahlung. In bremsstrahlung, the electron emits a photon in the vicinity of another ion's Coulomb field.

Opposite to this, an electron is near ions. The coulomb field is captured within the ion, releasing the extra energy.

3.2. Population kinetic modelling in plasma spectroscopy

When the plasma particle is in complete thermodynamic equilibrium (CT), the Planck formula gives the intensity distribution of plasma as a function of frequency and temperature. In that case, all particles exhibit the Maxwellian velocity distribution, population distribution is provided by the Boltzmann equation, and Saha's equation describes ionization. To satisfy all these conditions, the plasma must be optically thick so that no radiation can escape. However, in practice, no plasma follows the CT. Hence several other Population kinetic models are commonly used.

3.2.1. Coronal Equilibrium (CE)

This model applies when plasma has low density ($n_e \leq 10^{18} \text{ m}^{-3}$). Here, the probability of spontaneous decay of an excited atom is much higher than for any collisional depopulation process. So, the assumptions are,

- (a) All upward transitions are collisional
- (b) All downward transitions happen through radiation

3.2.2. Collisional Radiative (CR) model

This is the general model because the collisional frequency is higher for little higher-density cases, which leads to competition between collisional and radiative decay processes. Thus, for available model treatment, one has to include all collisional and radiative processes and solve the population equation stepwise. How one will do it, I shall discuss it later.

3.2.3. Local Thermodynamic Equilibrium (LTE)

In Local Thermodynamic Equilibrium (LTE), if the plasma density exceeds 10^{21} m^{-3} , the collisional rates increase further until radiative processes can be neglected. It means that excited states are depopulated by collisions mainly. In this case, the excited states are in local thermodynamic equilibrium with the ground state.

The emissions generated by the above-discussed processes are continuum (bound-free or free-free) or line radiations (bound-bound). The continuum radiation relies on several factors,

temperature, target material, and integration time. However, the line radiation (emission/absorption) is affected by several broadening mechanisms.

3.3. Line profile due to various types of broadening

3.3.1. Natural broadening

According to the Heisenberg uncertainty principle, an energy level with energy E and uncertainty of lifetime t , then uncertainty line energy is $\Delta E \Delta t \geq \frac{\hbar}{2}$. The broadening, if the $\Delta E = E_1 - E_2$ with lifetimes t_1 and t_2 each then width is $\frac{\hbar}{2\Delta t_2} + \frac{\hbar}{2\Delta t_1}$. This is due to the lifetime of the energy level and is known as “Natural broadening.” The Lorentzian function represents the line profile of this,

$$f_L(\lambda) = \frac{1}{\pi} \frac{\Delta \lambda_1^L}{(\lambda - \lambda_0)^2 + \left(\frac{\Delta \lambda_1^L}{2}\right)^2} \quad 3.10$$

It is inherent in nature and very small, there are more significant broadening mechanisms present, and it is even less than the spectral resolution of a spectroscopic instrument.

The convolution of two Lorentzian function gives the new Lorentzian function, which can be described by the following equation,

$$\left(\Delta \lambda_{\frac{1}{2}}^L\right)^2 = \left(\Delta \lambda_{\frac{1}{2}}^{L1}\right)^2 + \left(\Delta \lambda_{\frac{1}{2}}^{L2}\right)^2 \quad 3.11$$

3.3.2. Doppler broadening

The line emitted by the plasma can be shifted and broadened by the Doppler effect. The angular frequency of this emitted wave is nonrelativistic. Thermal motion of the emitters particle and their movements towards or away from the receiver produces the Doppler Broadening. In general, the velocities of these emitter particles obey the Maxwellian Distribution with temperature T . The Gaussian line profile function describes this distribution $f_G(\lambda)$.

$$f_G(\lambda) = \sqrt{\frac{4 \ln 2}{\pi}} \frac{1}{\Delta \lambda_{\frac{1}{2}}^G} e^{-4 \ln 2 \left(\frac{\lambda - \lambda_0}{\Delta \lambda_{\frac{1}{2}}^G}\right)^2} \quad 3.12$$

Convolution of two gaussian FWHM is represented by

$$\left(\Delta\lambda_{\frac{1}{2}}^G\right)^2 = \left(\Delta\lambda_{\frac{1}{2}}^{G1}\right)^2 + \left(\Delta\lambda_{\frac{1}{2}}^{G2}\right)^2 \quad 3.13$$

Also, the FWHM of this has the following relation with temperature:

$$\Delta\lambda_{\frac{1}{2}}^G = \lambda_0 \sqrt{\frac{8\ln 2 k T}{mc^2}} = 7.16 \times 10^{-6} \lambda_0 \sqrt{\frac{kT}{m}} \quad 3.14$$

Here T is the temperature (neutral T_n / ion T_i) and k is the Boltzmann constant, m is the mass, and c is the speed of light.

3.3.3. Pressure broadening/ Stark broadening

Interaction between the emitter and surrounding particles are categorized as interaction with the same type of atom, different type of atom, and charged particles. The plasma contains charged particles; hence, the emitter and charged particles interact. It is further categorized as electron emitter collision and ion emitter collision. The time scale for ion emitter collision is relatively more significant than the natural lifetime of the state. How can the electron emitter collision occur on a concise time scale if it is shorter than the natural lifetime of the excited state. Hence the electron emitter collisions are more frequent. This requires high plasma density to occur. The Stark FWHM of the line profile can be written in wavelength units as (Kunze):

$$\frac{\Delta\lambda_s}{\lambda_{pq}} \approx 8.4 \times 10^{-22} \frac{\lambda_{pq}}{nm} (n_p^2 - n_q^2) \frac{Z}{Z} \left(\frac{n_z}{m^{-3}}\right)^{2/3} \quad 3.15$$

For Hydrogen Balmer (H_α) spectral line ($p = 3$, $q = 2$ and $\lambda_{pq} = 656.28 \text{ nm}$) with a density $\sim 5 \times 10^{18} \text{ m}^{-3}$, the line broadening due to the Stark broadening is,

$$\Delta\lambda_s(nm) \approx 656 \times 656 \times 8.4 \times 10^{-22} (9 - 4) (5 \times 10^{18})^{2/3}$$

$$\Delta\lambda_s(nm) \approx 2 \times 10^{-15} \times 5 \times 10^{12}$$

$$\Delta\lambda_s(nm) \approx 10^{-2}$$

The FWHM due to Stark broadening at the densities present in the edge region of the ADITYA-U tokamak is very less than the FWHM due to Doppler, hence it has been neglected in the calculations and Gaussian line shapes are used for fitting the spectra. As the densities of impurities are lesser than the hydrogen density, Stark broadening is negligible at the typical impurity (Oxygen, Carbon, etc.) densities in the ADITYA-U tokamak edge.

3.3.4. Instrumental broadening

Even if the line profile of a line is subject to negligible thermal and pressure, it will be subject to an additional broadening due to the instrumental function. Almost any type of spectrograph will broaden a line. The broadening produced by a grating is inversely proportional to the number of grooves in the grating. It is also a function of entrance slit width and detector unit size. The instrumental broadening is proportional to the entrance slit width. In ideal conditions, the entrance slit should be a step function. In practice, it is not. The instrumental profile is a Gaussian function. The instrumental width of a system can be defined through the measurement of FWHM of mercury spectral line at different slits.

3.4. Effect of magnetic field on line profile

In tokamak plasmas, the magnetic fields are reasonably high. Field strength influences the energy level of emission by producing a split energy level. It is known as *Zeeman Effect*, first discovered in 1897. This further results in the line emission due to energy level shifts (Zeeman). A classical theory is incomplete without the Lande vector model (White). However complete Zeeman Effect is explained through quantum mechanical theory (Bransden B.H.H and Joachain C.J). The Zeeman Effect can be described as perturbation through magnetic field strength compared with $l - s$ coupling for weak or strong magnetic field perturbation. However usually the spectrometer is unable to resolve all the lines as an observation. When spin-orbit interaction is dominant, it is known as the weak-field effect, and if the external field is dominant, then it is considered the strong-field effect (Bethe and Salpeter; Bransden et al.). Further, to understand the Zeeman Effect quantum mechanically, the Hamiltonian of Zeeman is written as

$$H_Z = H_0 + H_{SO} + H_{mag} \quad 3.156$$

Here the H_0 is Hamiltonian of the unperturbed system H_{SO} is for spin-orbit interaction and H_{mag} represents the external magnetic field. The Zeeman effect is classified as:

- (a) Normal Zeeman effect: In this case, the effect corresponds to the situation for which the correction to the energy due the presence of the magnetic field is much larger than the relativistic corrections (spin-orbit coupling), the shift in energy level is:

$$\Delta E = \mu_B B m_l \quad 3.17(a)$$

Here, μ_B is Bohr magneton,

(b) Anomalous Zeeman effect: It is also known as the weak field Zeeman effect, in this case, the spin of the atom is non-zero. Hence spin and orbital motion combined and total angular momentum is responsible for the energy level split, shift in energy level is:

$$\Delta E = g_j \mu_B B m_j \quad 3.17(b)$$

Here, g_j is the Lande g -factor which is calculated by, $g_j = 1 + \frac{j(j+1)+s(s+1)-l(l+1)}{2j(j+1)}$

(c) Paschen-back Zeeman effect: It is also known as the strong field Zeeman effect, in this case still spin and orbital motion are no more combined hence there is no total angular momentum however spin is more dominated in this case. shift in energy level is

$$\Delta E = g_j \mu_B B (m_l + 2m_s) \quad 3.17(c)$$

In the above discussion j, l , and s describe total, angular, and spin quantum numbers, respectively. The strong-field Zeeman is defined in terms of the critical magnetic field as,

$$B_C \geq \frac{Z^4}{n^3 l(l+1)} \cdot 12.5 \text{ T} \quad 3.168$$

For Hydrogen-Balmer ($Z = 1$) line where $n = 2$ and $l = 1$, the field strength $B_C \sim 0.78 \text{ T}$. As a result, strong field approximation is considered for hydrogen in the ADITYA-U tokamak operated with 1.0 to 1.4 T. However, for C^+ and O^{4+} ions, the weak field approximation will almost always be valid as the fourth power of Z is dominated and is having smaller quantum number $n (= 2)$ and $l (= 1)$.

The shift in the wavelength is determined by, $\lambda_{\text{shift}} = \frac{hc}{\Delta E}$. This requires the measurement of energy shift corresponding to magnetic field strength. It is proportional to the strength of the magnetic field and the central wavelength λ_0 of unperturbed atomic lines. The polarization of emitted radiation with un-shifted component (π) is parallel to the magnetic field and the shifted components ($\pm\sigma$) are perpendicular to the magnetic field. If \mathbf{B} is parallel to the LOS, then only the σ component is observed, and when \mathbf{B} is perpendicular to the LOS, both σ and π the components are observed. The same has been derived mathematically and added to Appendix A of the thesis.

3.5. Self-absorption and opacity estimation

The radiation transport equation in atomic physics governs the line profile for the transition between two energy levels. It also gives details on how light can be absorbed as it passes through a dense medium. The plasma emitting some amount of radiation at a distance x is represented in terms of spectral radiance as

$$dL_\varepsilon(\lambda, x) = \varepsilon(\lambda, x)dx \quad 3.17$$

Considering some amount of radiation re-absorbed within the plasma at a distance x (depth of the medium), the spectral radiance of absorbed photons (L) is given by(Kunze),

$$dL_\kappa(\lambda, x) = -\kappa(\lambda, x)L(\lambda, x)dx \quad 3.18$$

Here, $\kappa(\lambda, x)$ is the absorption coefficient, and it's description is given in the literature. Spectral radiance will also depend on emission from the plasma along with absorption. Total change in spectral radiance with emission coefficient $\varepsilon(\lambda, x)$ is then,

$$dL(\lambda, x) = \varepsilon(\lambda, x)dx - \kappa(\lambda, x)L(\lambda, x)dx \quad 3.19$$

Introducing the optical depth τ , it is the product of the line absorption coefficient (cm^{-1}) and depth of the medium (cm), which is also known as opacity (dimensionless quantity). Mathematically represented as

$$\tau = -\kappa(\lambda, x)x \quad 3.20$$

For optically thin plasmas, $\tau \ll 1$, and optically thick plasmas, $\tau \gg 1$. The solution of equation 3.21 differs in both conditions. For an optically thin plasma, mainly the emission part comes into the scenario, while for an optically thick plasma, absorption and emission will contribute to total transmission. Using optical depth in equation 3.21,

$$\frac{dL}{dx} = \varepsilon(\lambda, x) - \kappa(\lambda, x)L(\lambda, x) \quad 3.21$$

$$\frac{dL}{d\tau} = L(\lambda, x) - \frac{\varepsilon(\lambda, x)}{\kappa(\lambda, x)} \quad 3.22$$

Defining $\frac{\varepsilon(\lambda, x)}{\kappa(\lambda, x)}$, as source term $S(\lambda, x)$. Now for optically thick plasma, the solution of equation 3.19 is given by,

$$L(\lambda) = \int S(\tau, \lambda)e^{-\tau}d\tau \quad 3.23$$

It can have positive or negative signs depending upon integration limits. To understand equation 3.25, the spectral line profile was observed through spectrograph experimentally. Let the probability that photon of frequency v having wavelength λ propagates an optical depth τ_0 at $x = 0$ (point of emission) through a source without being absorbed $\exp(-\tau)$, where $\tau = \left[\frac{f(\lambda)}{f(0)} \right] \tau_0$.

In general, the spectral line profile of radiation propagating through an optical depth τ over a specific wavelength range defined as T ,

$$T(\tau_0) = \int f(\lambda) e^{-\tau} d\lambda \quad 3.24$$

Here, $f(\lambda)$ denotes different line profile functions, i.e., Gaussian or Lorentzian, as given in equations 3.10 and 3.12. the value of the absorption coefficient is proportional to the neutral density through the following formula (Behringer and Fantz):

$$\kappa(0) = n_n \frac{\lambda}{c} \frac{fe^2}{4\epsilon_0 m_e} \sqrt{\frac{\mu m_p}{2\pi k T_g}} \quad 3.25$$

Here m_p is the proton's mass, μ is the mass of an atom in *a. m. u.* f is the oscillator strength available on NIST and n_n is the density of an atom. Knowing the opacity through experimental results, substituting the same into equation 3.27. The absorption coefficient is determined further. The atom density can be estimated using the absorption coefficient.

3.6. Investigation of Neutral and impurity ion temperatures and their radial profiles

3.6.1. Spectral line profile modelling for temperature estimation

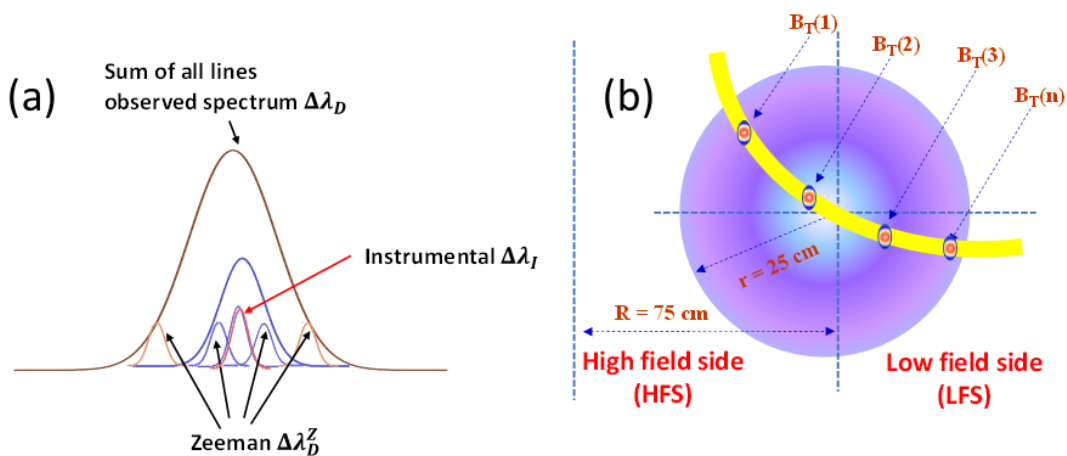


Figure 3.3. (a) broadenings affecting the spectral line profile due to different FWHM including Doppler, Instrumental and Zeeman (b) Magnetic field profile for different radius

In ADITYA-U tokamak, the plasma discharges presented here have magnetic field strength $B > 1$ Tesla. It reveals that the Paschen-Back effect (strong field Zeeman) is present for neutral hydrogen, for other emissions C^+ and O^{4+} , the weak-field Zeeman effect is considered.

The Zeeman shifted components are also Gaussian in shape, having FWHM corresponds to the Doppler broadening of each component. However, as an instrument cannot resolve the Zeeman shifted components, it adds together and can be viewed as a single spectral line profile subsequently producing an error in estimating neutral or ion temperatures using equation 3.14 of Doppler broadening. It means the emission spectra comprise FWHM due to instrumental broadening ($\Delta\lambda_I$), FWHM due to Doppler broadening ($\Delta\lambda_D$) and FWHM produced by Doppler broadening of Zeeman shifted components ($\Delta\lambda_D^Z$), as shown in Figure 3.3 (a). These three broadenings are considered in the simulation to generate the synthetic spectra for modelling the spectral line shape.

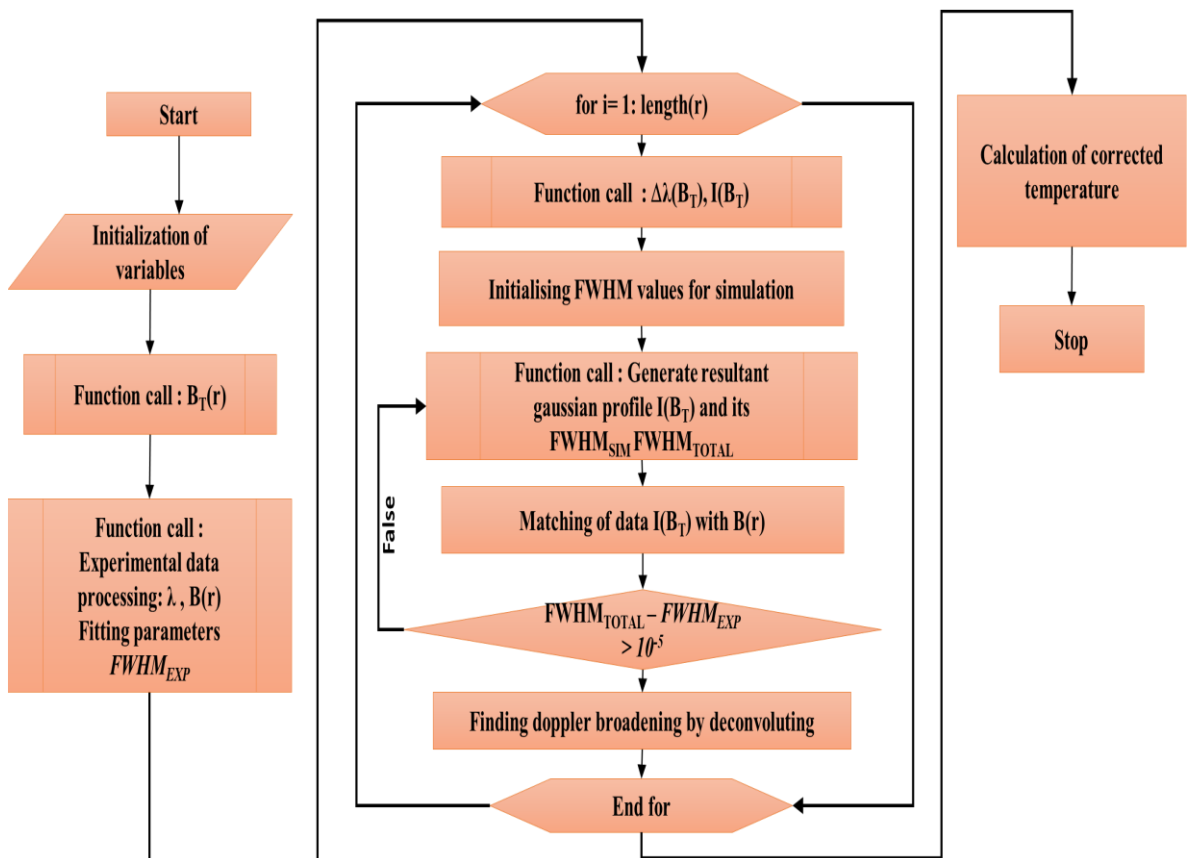


Figure 3.4 Flow chart of simulation cum modelling MATLAB code for Zeeman influenced spectral line profile

The observation of σ and π components of the Zeeman split spectra depends upon the direction of the magnetic field and LOS. The magnetic field strength in ADITYA-U tokamak has a parabolic profile, as shown in Figure 3.3(b). At different plasma radii, field strength varies by $\frac{1}{r}$ as shown in Figure 3.3 (b). The Zeeman shift corresponding to each radial location is different due to different magnetic field strengths. It has been considered in the developed code. The multiple radial locations are treated simultaneously in the code through a loop. Within the loop, the shift in wavelength and its intensity is calculated using a pre-defined excel file

developed through the equation sets of equation 3.17. The line profile is further simulated by convoluting three broadenings, as mentioned above. Further the FWHM of the experimental broadened profile ($\Delta\lambda_D^{Exp}$) and FWHM of simulated broadened profile ($\Delta\lambda_D^{Simu}$) is matched to get the corrected FWHM of Doppler broadening measurement. Here, the total simulated broadening is represented as each Zeeman component is treated by Doppler broadening, which is convoluted with instrumental function. Further, the spectrum is added up to obtain the total simulated broadening. The neutral and ion temperature can be estimated using equation 3.14. The corrected temperature is estimated by inferring the Doppler broadening through the MATLAB code by removing Zeeman and instrumental broadening. A flowchart of the same is given in Figure 3.4.

3.6.2. Experimental arrangements for space-resolved measurements:

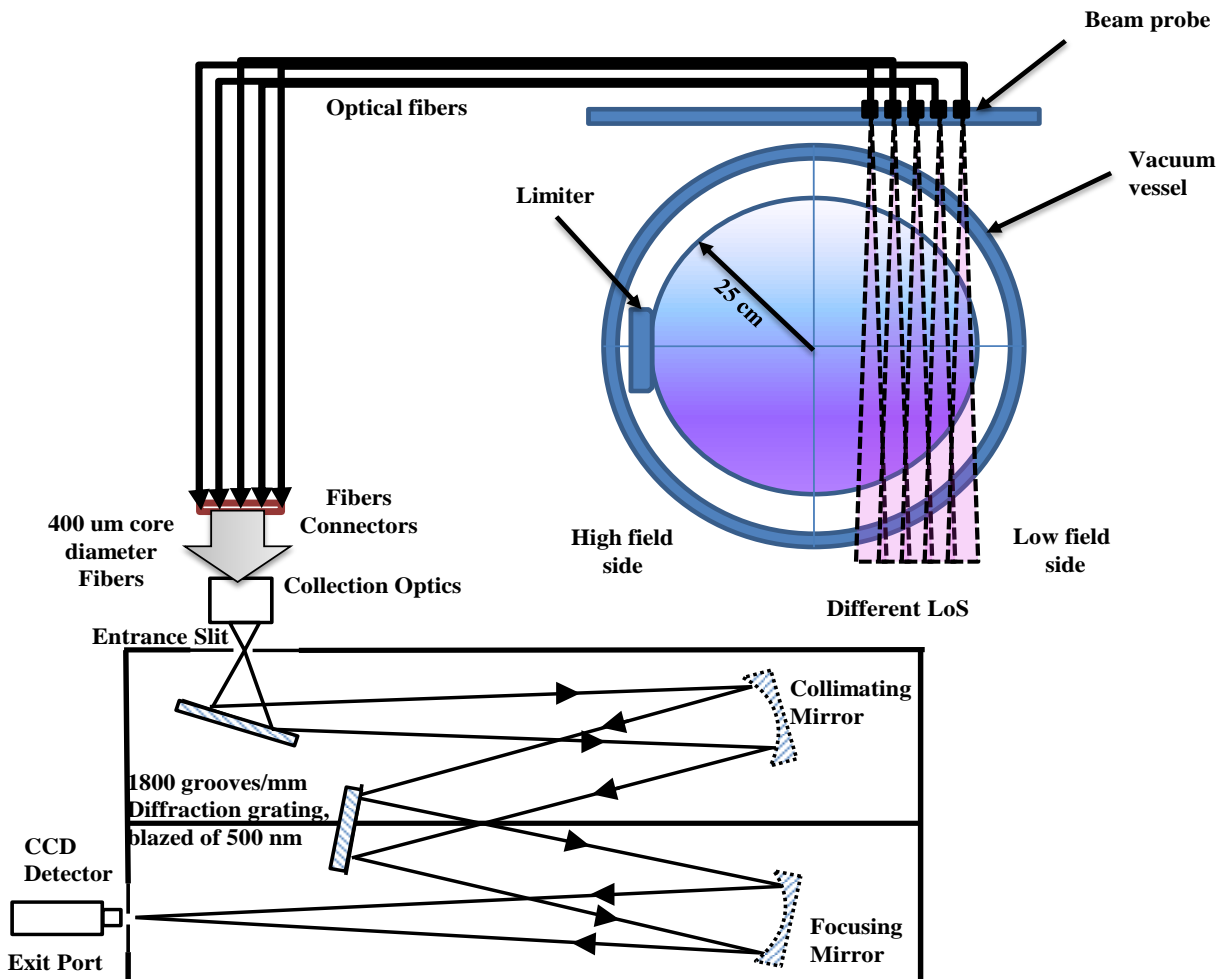


Figure 3.5 Schematic of the viewing geometry used for the multi-track spectrometer. The lines of sight are represented by 1 to 7 fiber passing through the plasma radial locations 0.083, 0.116, 0.149, 0.182, and 0.215 m

The high-resolution spectrometer described in chapter 2 was operated with the CCD detector. The spectral resolution at 650.024 nm is 0.023 nm with a 50 μm slit. It has a pixel size of $26 \times 26 \mu\text{m}^2$ with a total of 1024×256 pixels. The optics setup Collimator 1 from Table 2.3 is used. Binning is done by defining 16 – pixel high rows (tracks) separated with 10 pixels gaps to avoid cross-talk. The spatial resolution with this setup is 2.5 cm. For space resolution of plasma, the LOS is arranged such that it sees the plasma core to the outboard (LFS) plasma captured. The same is displayed in Figure 3.5. The LOS centers in meters are 0.083, 0.116, 0.149, 0.182, and 0.215 m in terms of ρ it is 0.332, 0.464, 0.596, 0.728, and 0.86. Here $\rho = \frac{r}{a}$ is normalized plasma radius and a is plasma minor radius. Fiber arrangements are made here so that each LOS is perpendicular to the same constant toroidal magnetic field in the viewing area. It means a 90° angle present between the toroidal magnetic field and LOS. It is easier to analyze the Effect on temperature present due to the split of the spectral line.

3.6.3. Abel-inverted radial profile measurements

The space-resolved ion temperatures are line integrated as the measurements are done along the chords passing through the whole plasma. Then, an Abel-like matrix inversion technique is adopted to convert the spatial measurement of ion temperature to its radial profile. In this technique, plasma volume is segregated into several zones with constant emissivity E_j , constant temperature T_j and constant velocity (v_j) within the zone. i represents the line of sight (LOS), and j stands for emission zone. Through the Abel inversion technique, the line-integrated emission brightness B_i is represented in terms of emissivity ε_i by, $B_i = \sum L_{ij} \varepsilon_j$ (Bell). With this, the estimated emissivity is given by $\varepsilon_j = \sum L_{ij}^{-1} B_i$. Here L_{ij}^{-1} is the inverted length matrix, generated by the 2D geometry CAD drawing of the measurement cross-section.

The emission profile through the Gaussian is given by (Condrea et al.),

$$\varepsilon_{ij}^\lambda = \frac{\varepsilon_j}{w_i} \sqrt{\frac{4 \ln 2}{\pi}} \exp \left(\frac{-4 \ln 2 \left[\lambda - \lambda_0 - \frac{\lambda_0}{c} |\vec{s}_i \cdot \vec{v}_j| \right]^2}{w_j^2} \right) \quad 3.26$$

Where c is the speed of light, w_j is FWHM, λ_0 is the center wavelength of the spectral line, which is unshifted and unperturbed. s_i is the unit vector of LOS and v_j is rotational velocity vector with, $|\vec{s}_i \cdot \vec{v}_j| = v_j \cos \theta_{ij}$. For inversion of measured integrated temperature, the spectral line width is,

$$\langle(\delta\lambda_i^B)\rangle^2 = \frac{\int B_i^\lambda (\lambda - \lambda_0)^2 d\lambda}{\int B_i^\lambda d\lambda} \quad 3.27$$

The B_i^λ represents the spectral brightness and $\int B_i^\lambda d\lambda$ is line integrated measured brightness collected through the chord i . The integrated temperature T_i for described brightness is given by,

$$T_i = \frac{mc^2}{k\lambda_0} \langle(\delta\lambda_i^B)\rangle^2 \quad 3.28$$

The local-radial profile of ion temperature is calculated by inverting the length matrix and squaring the local velocity,

$$T_j = \frac{\sum L_{ij}^{-1} B_i T_i}{\sum L_{ij}^{-1} B_i} - \frac{m}{k} \frac{\sum L_{ij}^{-1} \sum L_{ij} \cos^2 T_{ij} v_j^2 \varepsilon_j}{\sum L_{ij}^{-1} B_i} \quad 3.29$$

Here, on the right-hand side of the equation, the second term represents velocity contribution in local temperature measurements. However, this term can be neglected due to the low velocity of < 10 km/s (Condrea et al.) in the ADITYA-U tokamak.

3.6.4. Experimental results of ion temperature measurement

Typical ohmic plasma discharge with gas puffs is described in figure Figure 3.6, shot # 33015, plasma current $I_p \sim 130$ kA and duration $t_p \sim 115$ ms. The magnetic field in this shot is 1.3 T. Temporal evolution of loop voltage (V_{loop}), plasma current (I_p), H_α ($656.28 \text{ nm} - 2 \rightarrow 3$), O^+ ($442 \text{ nm} - 2s^2 2p^2 3s \rightarrow 2s^2 2p^2 3p$) and C^{2+} ($464.7 \text{ nm} - 1s^2 2s 3s \rightarrow 1s^2 2s 3p$) line intensities are given in the same diagram. It was obvious that as discharge begins, hydrogen starts to ionize first, then carbon and oxygen impurity ionize subsequently. Along with this, each emission shows typical modulation in the intensity of neutral and impurity emissions, which indicates the change in density due to gas puff. It has a maximum central line averaged density of $2 \times 10^{-19} m^{-3}$.

Spatially resolved H_α spectral emission for *shot no # 33015* is shown in Figure 3.6 captured during 30 to 50 ms of plasma duration (as also marked in Figure 3.6 with red dashed vertical lines). Figure 3.7 shows the space-resolved emission spectra measured through MTS. Each frame covers a 12 nm wavelength range. It also contains the spectral line of H_α at 656.28 nm, O^{4+} at 650.024 nm ($1s^2 2p 2p \rightarrow 1s^2 2p 3d$), and C^+ ($2s^2 3s \rightarrow 2s^2 3p$) (doublet) spectral lines at 657.8 nm and 658.2 nm. To acquire this spectral frame central wavelength is set at 654 nm. The intensity profile shows the peak in the edge region. The details of their

standard ionization energy data are given in Table 3.2. Plasma discharge for shot # 33015 has been analyzed for ion temperature measurement first.

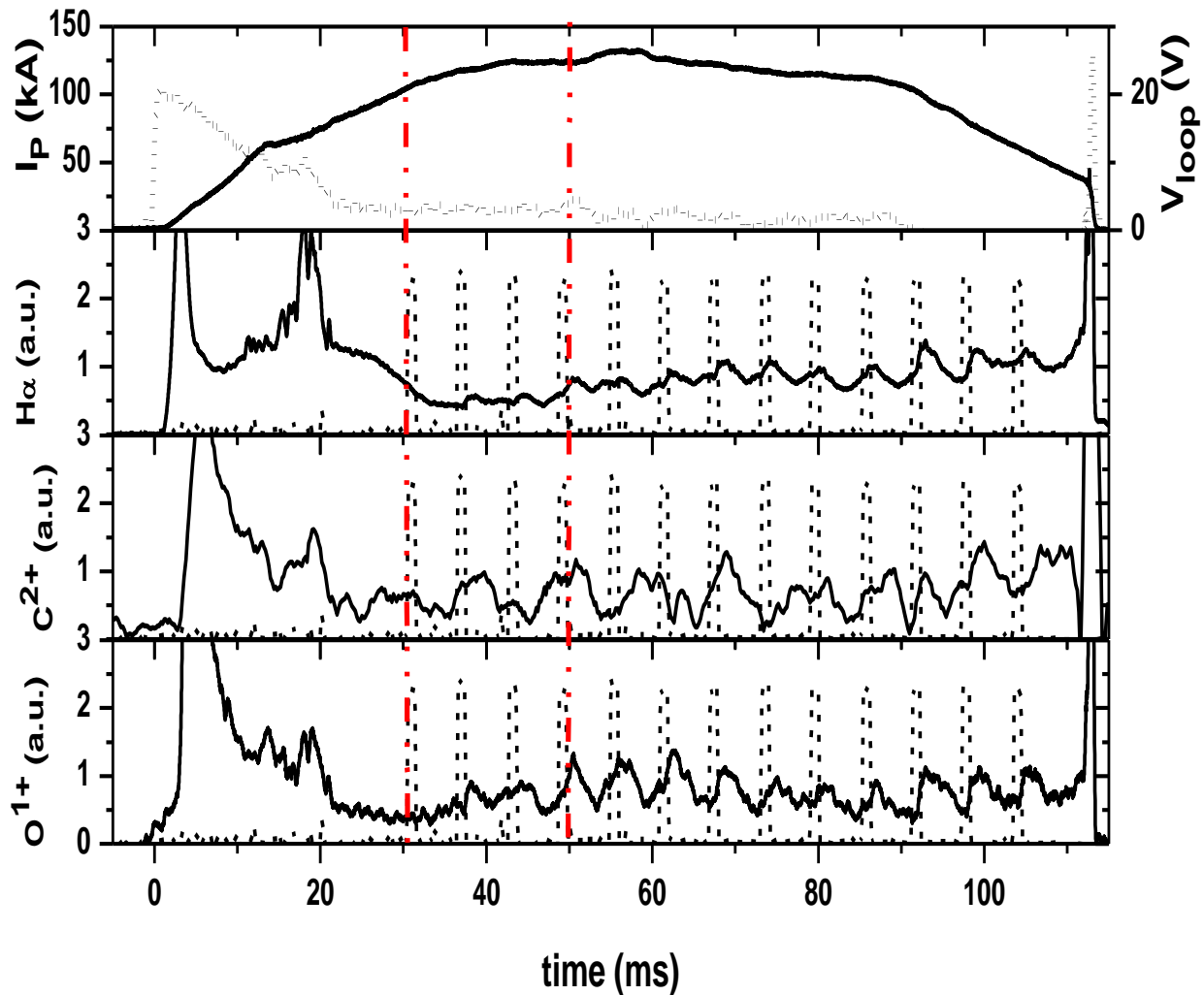


Figure 3.6. Plasma parameters for shot #33015

Table 3.2 Atomic data and ionization energy for all the ionization stages of Hydrogen (H) and all ionization stages of Carbon (C), and Oxygen (O)

Atomic number	Species Name	Ion Charge	Isoelectronic Sequence	Ionization Energy (eV)
1	$H\ I$	0	H	13.59843
6	$C\ II$	1	B	24.38314
8	$O\ V$	4	Be	113.899

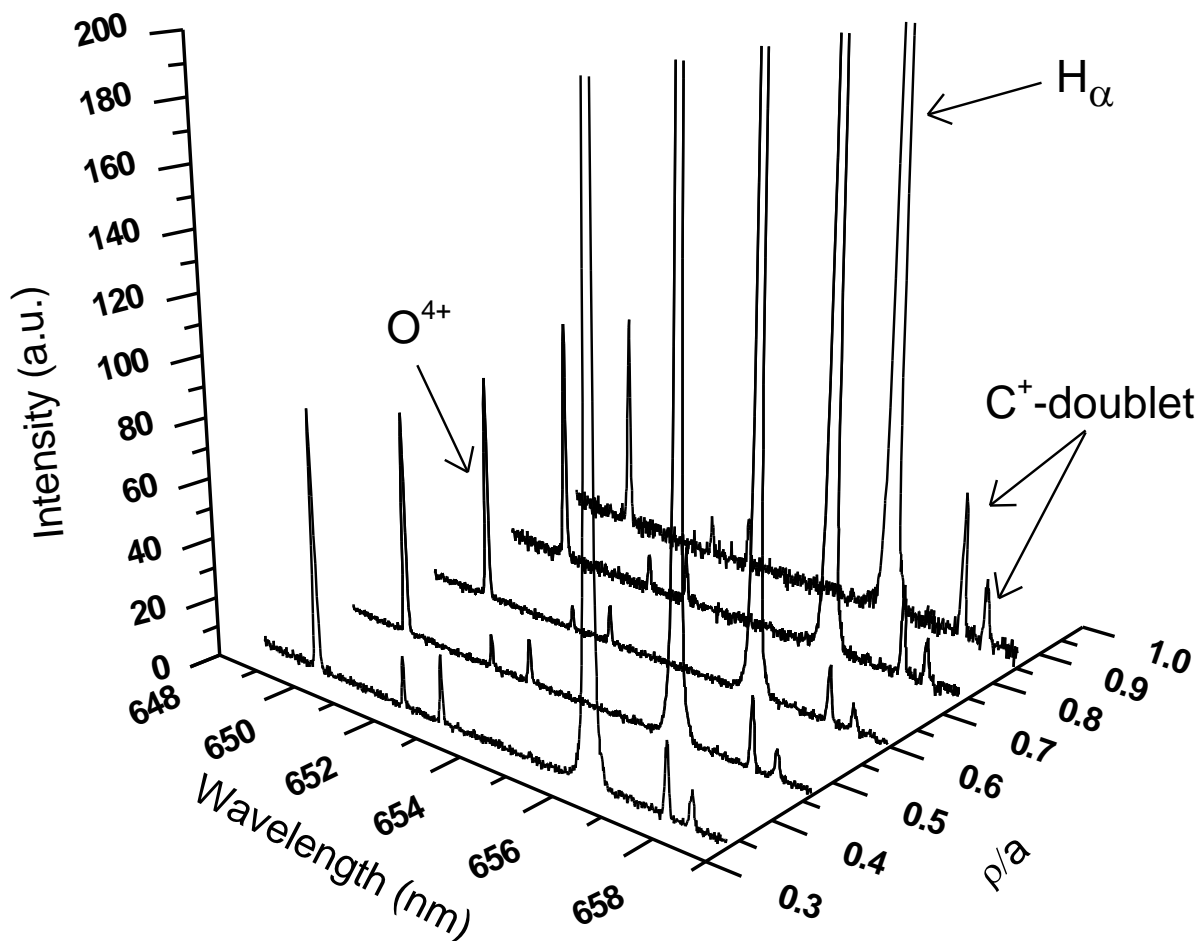


Figure 3.7 Space-resolved measurement of ADITYA-U emission spectra from MTS spectroscopic system

Table 3.3. Zeeman components of C^+ ion

Zeeman components	$C^+ \lambda_{ki} = 657.8 \text{ nm}$
Total	6
π	2
$\sigma \pm$	4

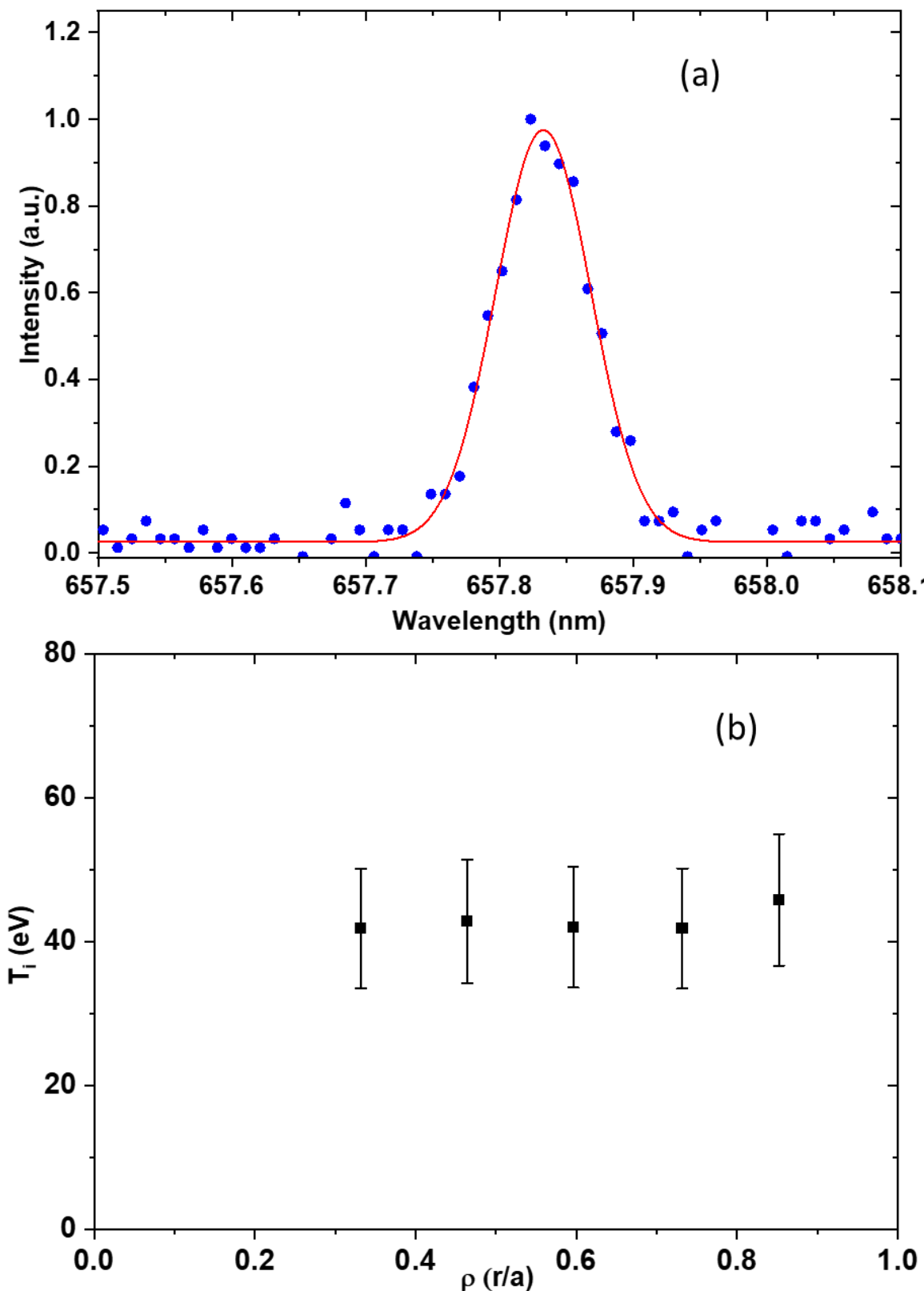


Figure 3.8: Without Zeeman consideration: (a) Gaussian fitted line profile on experimentally observed C^+ spectral line emission FWHM ~ 0.09 nm. Where solid data points represent the experimental data and the line is the Gaussian fitted curve. (b) Spatial profile of C^+ ion temperature estimation without consideration of the Zeeman Effect

3.6.5. Anomaly in C⁺ ion temperature estimation

Using equation 3.14, the C⁺ ion temperature is estimated by considering the spectral line at 657.8 nm. The line emission at 658.2 nm of carbon doublet is not considered for ion temperature estimation because of its lower intensity and which leads to a poor S/N ratio causing an increase in fitting errors. At first, the temperature was estimated through the line shape fitting using observed apparent FWHM $\Delta\lambda$, as presented in Figure 3.8 (a). It can be seen that the quantified spectral line profile does not contain the multiple peaks owing to the Zeeman splitting. The reason for this is that the spectrometer has a resolution of 0.032 nm at 70 μm slit width, and it cannot resolve these small shifts in the lines for a given magnetic field. Then, the Zeeman broadening is not considered initially. The estimated temperature is shown in Figure 3.8 (b). Without Zeeman's consideration, the space-resolved temperature estimation varies between 40 eV to 50 eV and is almost similar at different radial locations. As already mentioned in Table 3.2, the ionization energy IE of C⁺ion is \sim 24 eV (Kramida and Ralchenko), the temperature acquired by the C⁺is higher than this. However, the electron temperature in the ADITYA-U tokamak edge plasma region by Langmuir probe measurement is around 7 – 20 eV at the plasma edge whereas T_i is 45 eV at the same radial location. Therefore, the temperature measured is not justified because the ion in the plasma edge cannot reach such higher energy. Although it can have an energy higher than the T_e of the plasma region where the ion resides (Wesson and Campbell). This provides evidence of the apparent broadening spectral line due to the Zeeman effect in the ADITYA-U tokamak plasma. The magnetic fields affect the energy levels of C⁺ ions and these components are included in the simulation.

The transitions in the presence of the Zeeman Effect are derived and given in Table 3.3. With 2 nos. of π components with observation parallel to the magnetic field and 4 nos. of $\sigma \pm$ components with observation perpendicular to the magnetic field, a total of 6 nos. of Zeeman components are present for this transition. The line profile is modelled using simulated and experimental measurements to obtain the corrected temperature. The corrected temperature has now been estimated by extracting the Doppler width information from the experimental data. The fitting of modelled data (line) on the experimentally measured data (circles) is shown in Figure 3.9 (a), along with the incorporated Zeeman components (dashed lines). The intensity of $\sigma \pm$ components is taken as half of the intensity with π components. It is seen that the corrected spatial temperature measurement is now below 10 eV in all radial locations after including the Zeeman Effect, as shown in Figure 3.9 (b) with square-black data points. This study demonstrates the importance of including the Zeeman Effect in the ion temperature

estimation. The spatially resolved ion temperature measurement is inverted to obtain the radial ion temperature profile. The temperature ranged from 2 to 13 eV and was plotted with circular red points. The T_{C+} shows higher values $\sim 10 - 13$ eV at the radial locations $\rho = 0.5 - 0.6$ (0.12 – 0.15 m) of the plasma radius. Its values are 10 eV at all other radial locations, as shown in Figure 3.9 (b).

3.6.6. O^{4+} ion temperature

For the estimation of the O^{4+} ion temperature, the spectral line emission at 650.02 nm was used. There are 21 Zeeman components for this transition, among them, 7 nos. of π components for observation parallel to the magnetic field and 14 nos. $\sigma\pm$ components for observation perpendicular to the magnetic field as indicated in Table 3.4. These are contributing to the Zeeman splitting of the emission lines. The corrected temperature is estimated according to the method explained in section 3.4. to extract the Doppler broadening information from the experimental data. Figure 3.10 (a) illustrates the modelled line profile (line) fitted to experimentally measured data (circles). The Zeeman lines (dashed lines) are also shown in the same figure. The corrected spatial temperature measurement is below 10 – 30 eV without Abel inversion (black square data points) for this O^{4+} ion having IE of 114 eV, as shown in Figure 3.10 (b). Here also, the space resolved measurement is inverted for the radial profile estimation. The inverted temperature of oxygen ion $T_{O^{4+}}$ is 10 – 40 eV (circle red points), and the highest value of 40 eV lies at $\sim \rho = 0.6$ (0.15 m) of the plasma radius.

Table 3.4. Zeeman components of O^{4+} ion

Zeeman components		$O^{4+} \lambda_{ki} = 650.02 \text{ nm}$
Total		21
π		7
$\sigma\pm$		14

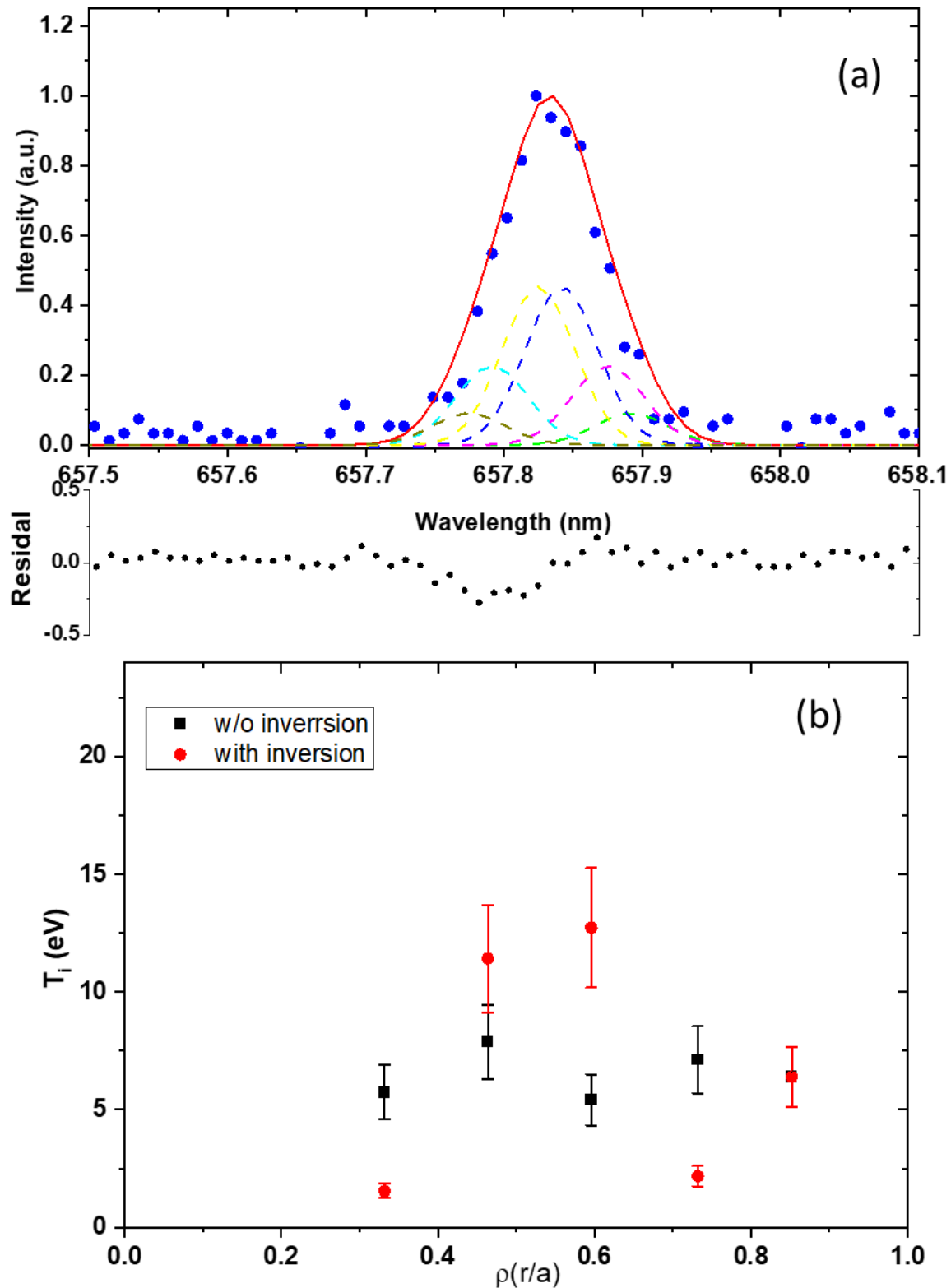


Figure 3.9. With Zeeman's consideration: (a) Gaussian fitted line profile on experimentally observed C^+ spectral line emission where a total of seven Zeeman lines are represented. (b) Spatial profile of C^+ ion temperature estimation (black-square data) with Abel inverted radial ion temperature profile (red-square data) consideration of Zeeman Effect

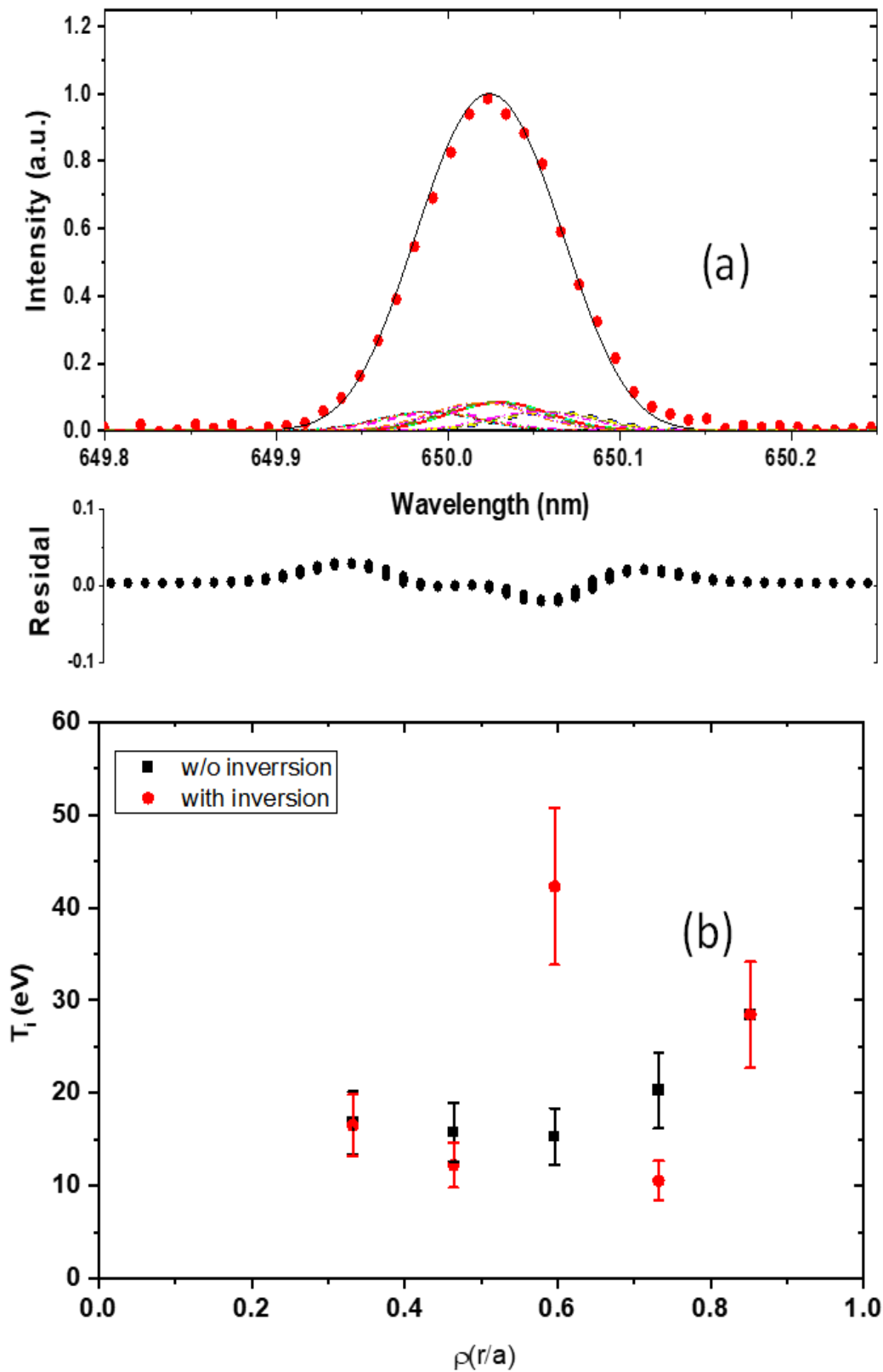


Figure 3.10. With Zeeman's consideration: (a) Gaussian fitted line profile on experimentally observed O^{4+} spectral line emission where a total of seven Zeeman lines are represented. (b) Spatial profile of O^{4+} ion temperature estimation (black-square data) with Abel inverted radial ion temperature profile (red-square data) consideration of Zeeman Effect

3.6.7. Neutral hydrogen temperature estimation

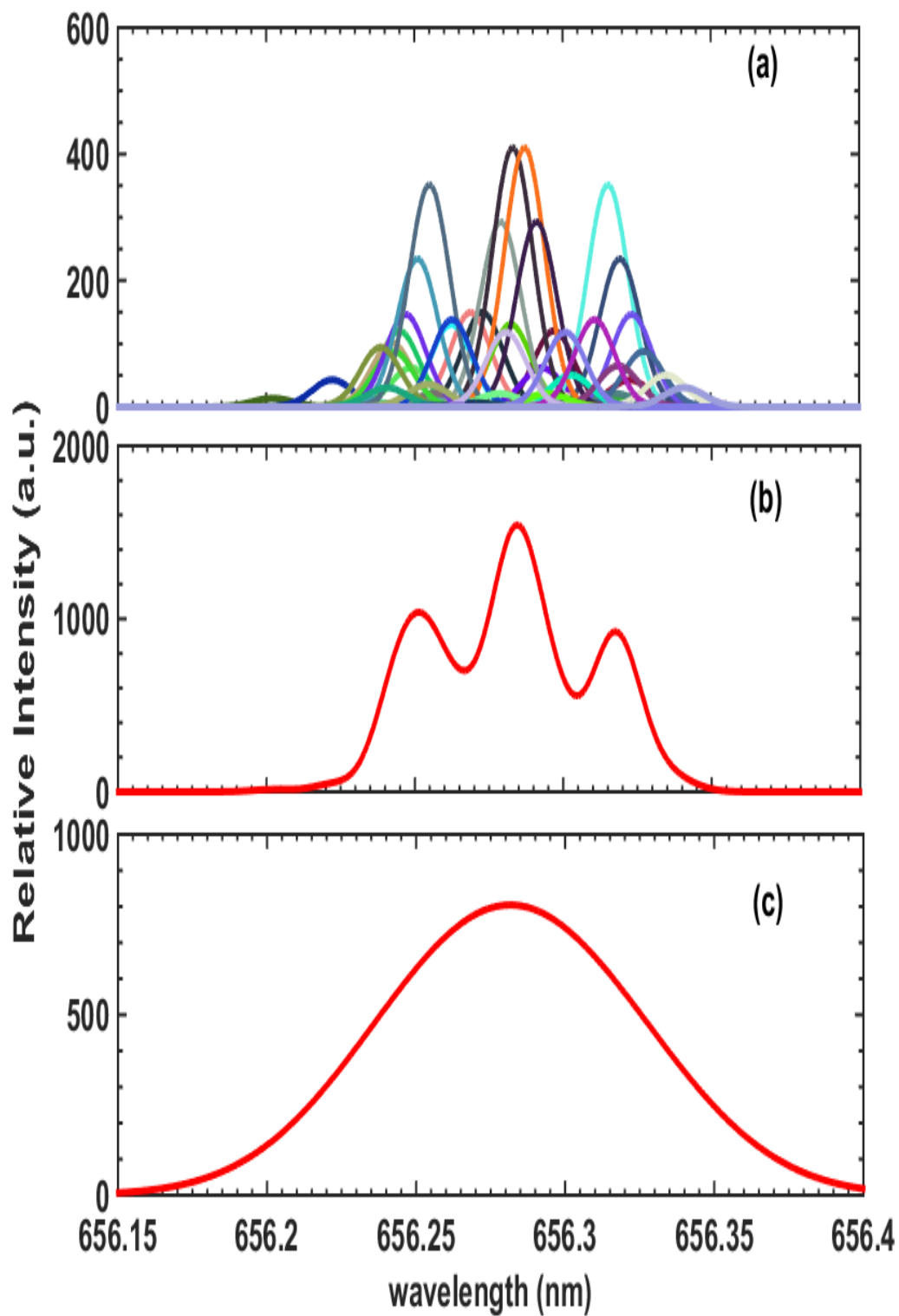


Figure 3.11. Simulated Zeeman spectra under the effect of 1.5 T magnetic field, (a) 48-Zeeman components simulated by convolution of Doppler broadening and instrumental width. (b) Resultant of 48 Zeeman components when $T_e = 0.1$ eV.

The H_{α} emission line fundamentally consists of 7 fine structure components, as tabulated in Table 3.5. These seven components are further split into a total of 54 H_{α} components for Paschen back Zeeman. Of all the 54 transitions, 48 are the allowed transitions. How many components from 7 lines contribute to these transitions are tabulated in Table 3.5. The relative intensities of all components are taken as per their m and J values, as given in Table 3.6. The simulation results from 48 Zeeman broadened components are shown in Figure 3.11 (a) for 0.1 eV temperature and 1.5 T magnetic field strength. The instrumental broadening is already convoluted in this line profile. During experimental observation, these lines are not separated due to insufficient spectral resolution. The Zeeman split lines merge to produce a single line profile, as shown in Figure 3.11 (b), which gives huge resultant broadening and leads to erroneous temperature measurement.

Table 3.5. Fine-structure Transitions of H_{α}

Transition	Number of components
$2^2P_{1/2} - 3^2D_{3/2}$	6
$2^2S_{1/2} - 3^2P_{3/2}$	6
$2^2P_{1/2} - 3^2S_{1/2}$	4
$2^2P_{3/2} - 3^2D_{5/2}$	12
$2^2S_{1/2} - 3^2P_{1/2}$	4
$2^2P_{3/2} - 3^2D_{3/2}$	10
$2^2P_{3/2} - 3^2S_{1/2}$	6

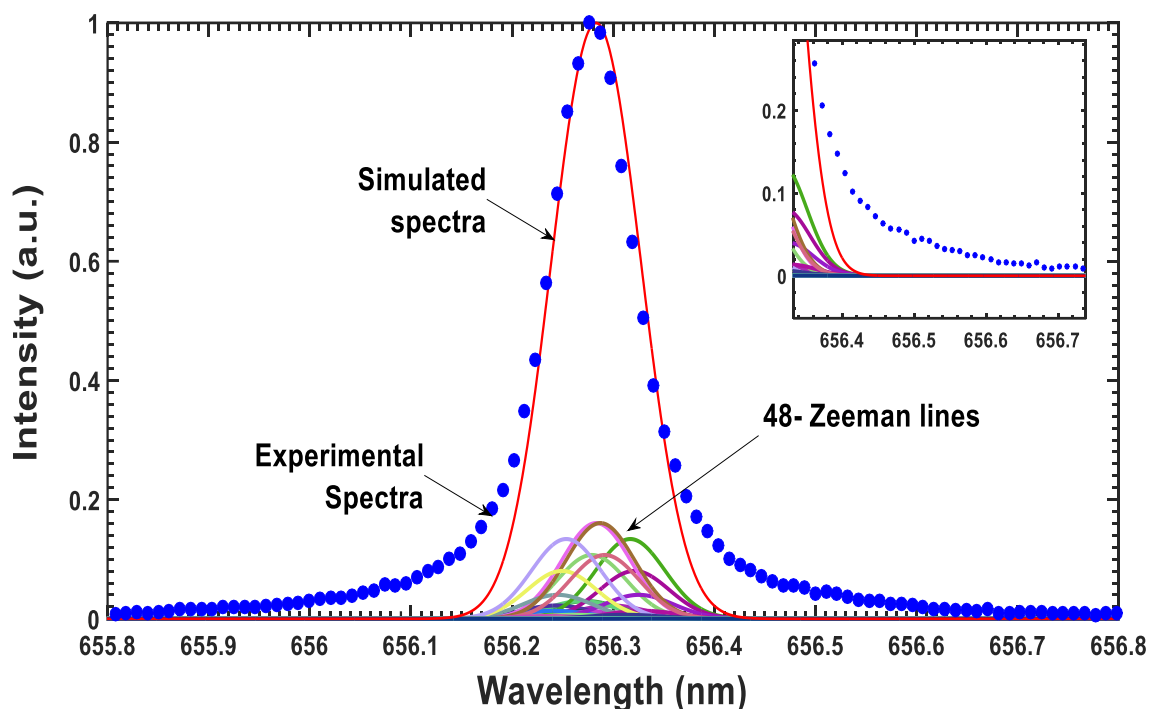


Figure 3.12. Fitting of H_{α} experimental spectrum with simulated spectra by considering all 48 Zeeman lines and single temperature component of the hydrogen atom

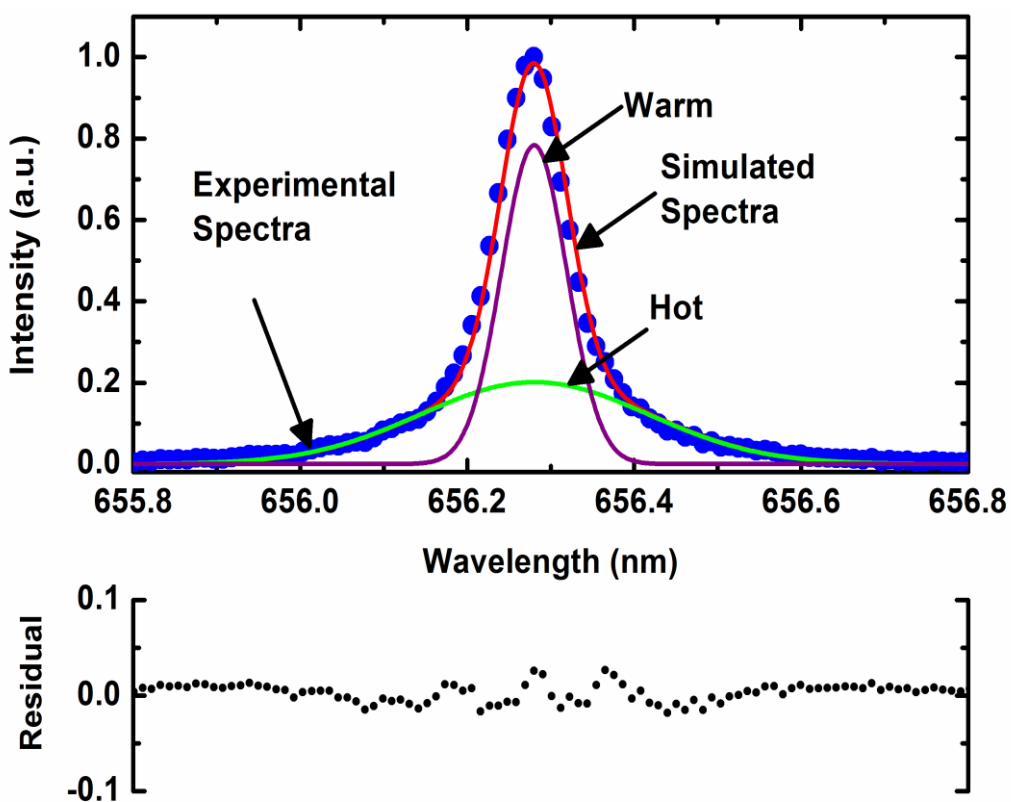


Figure 3.13. Fitting of H_{α} experimental spectrum with calculated spectra by considering all the 48 Zeeman components and two neutral temperature components of the hydrogen atom.

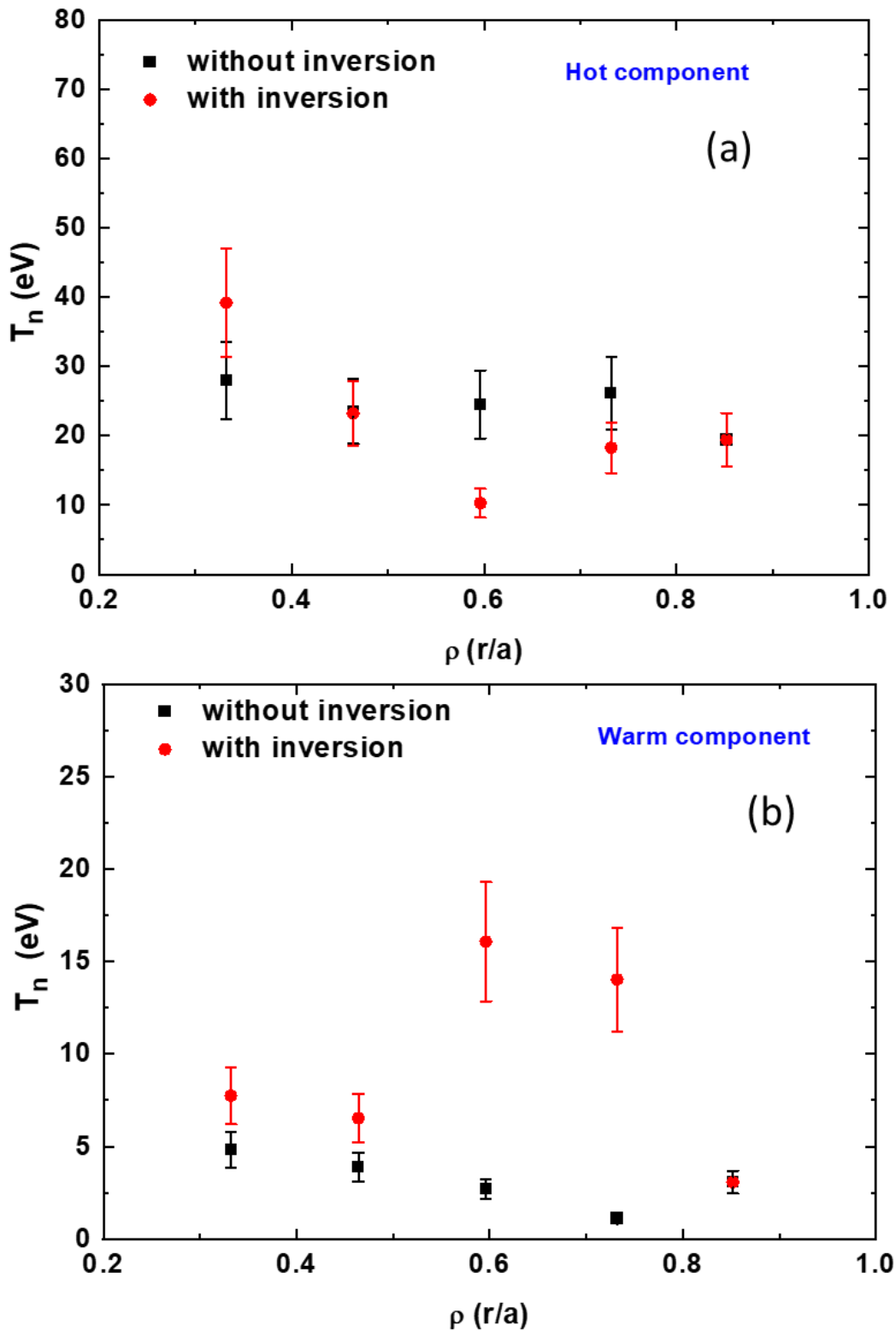


Figure 3.14. With Zeeman consideration: (a) Hot temperature components of H_{α} neutral (b) Warm temperature components (In both (a) & (b): black data points without Abel-inversion temperature, red data points are with Abel-inversion temperature).

Table 3.6. The intensity of different emissions for H_{α}

Transition	Intensity of π Component	Intensity of $\sigma-$ Component $(M \rightarrow M-1)$	Intensity of $\sigma+$ Component $(M \rightarrow M+1)$
$J \rightarrow J$	M^2	$1/4 (J+M) (J+1-M)$	$1/4 (J-M) (J+1+M)$
$J \rightarrow J-1$	$J^2 - M^2$	$1/4 (J+M) (J-1+M)$	$1/4 (J-M) (J-1-M)$
$J \rightarrow J+1$	$(J+1)^2 - M^2$	$1/4 (J+1-M) (J-M+2)$	$1/4 (J+1+M) (J+M+2)$

3.6.8. Two components of neutral temperature (hot & warm)

The spectrum shown in Figure 3.12 is initially fitted with a single Gaussian fit after the inclusion of Zeemann, Instrumental, and Doppler broadenings. This gives a measured temperature of ~ 2.5 eV. However, the simulated data is not very well matched to the experimental data, at the wings of the spectral line profile showing the foremost discrepancy against the experimental H_{α} data. From this, it is found that, the H_{α} is not coming from a similar group of atomic molecular processes. Instead of that, many atomic molecular processes are contributing to the H_{α} emission. And all these processes have different product temperatures. Considering this, the experimental emission spectrum is now fitted with a simulated one by considering two temperature components through two neutral population having Maxwellian velocity distribution function. The temperatures are described as warm (< 10 eV) and hot (> 10 eV) (Yadava, Ghosh, M. B. Chowdhuri, Manchanda, Punchithaya K, et al.). Zeeman Effect influences both temperature components of the hydrogen atom, including this into the MATLAB program gives the result shown in Figure 3.13, which resolves the discrepancy present at the wings of spectrum shape in the previously fitted line profile (Figure 3.12). The residue in the fitting procedure has also been shown in the figure for the qualitative assessment of fittings. Now, the temperatures of warm and hot components are found to be ~ 4.9 eV and 45 eV, respectively. These hot atoms are produced mainly due to charge exchange, which generally comes from the plasma core, as it has a higher temperature than the plasma edge.

3.6.9. Neutral temperature Radial profile

For measurement of the neutral temperature's radial profile, both temperature components are considered in the fitting of H_{α} Line profile modelling the estimated hot temperature component ranges from 15 – 30 eV (without Abel-inversion), as shown in Figure 3.14 (a) having black data square. However, the Abel inverted temperature profile of neutral hydrogen indicates a dip at 0.15 m or $\rho = 0.6$ of plasma radius, and the hot temperature increases towards the plasma core as shown in Figure 3.14 (a) with red data markers. Similarly, for warm atomic hydrogen, temperature varies between 3 eV to 5 eV. Figure 3.14 (b) also shows how the warm hydrogen temperature near the core of the plasma is slightly higher than at the plasma edge, marked with black data markers. This temperature range is mainly an indication of electron impact molecular hydrogen dissociation. This process contributes average kinetic energy of 3 eV for the product atom. Along with this, simultaneously occurring processes are likely to be the molecular hydrogen dissociation (4.3 eV), molecular hydrogen dissociative ionization (0.31 eV to 4.85 eV). However, a slightly higher order of warm temperature is mainly generated by Franck–Condon dissociation has an energy of ~ 7 eV. These ions might reach the ADITYA-U tokamak's central region with reduced energy. It was observed through the modelling of the neutral particle dynamic in Aditya tokamak using DEGAS2 code that the significant contribution in neutral hydrogen is related to molecular hydrogen dissociation processes, and molecular hydrogen ion dissociation and molecular hydrogen ion dissociative recombination also makes substantial contributions to the hydrogen atom density at the plasma edge, (Dey, Chowdhuri, et al.). The Abel-inverted radial profile estimation for warm atomic hydrogen shows more than 10 eV of neutral temperature at the plasma edge, as shown in Figure 3.14 (b), with red data markers. Also, the radial profile shows that the warm temperature is higher at the plasma edge region and reduces towards the core of the plasma. In the edge due to low edge temperature collisions are more frequent and hence neutral gets thermalized with the surrounded electron or ions to attain more temperature

An error estimate was made for the ion temperature. Photon, dark, and readout noises were considered for the standard deviation of the signal observed. Uncertainty in the fitting procedure was also included and it varies depending on the signal-to-noise ratio where the maximum error is in the signal with small amplitude and was found to be less than 5%. The error propagation in the inversion is calculated considering $\sigma_b^2 = [L_{ij}^{-2}] \sigma_a^2$, where b and a are brightness and emissivity vectors, respectively, operated by the matrix $[L_{ij}]$, $b = [L_{ij}]a$, and σ_a and σ_b are the standard deviations of vectors a and b . the length matrix is determined from the geometry and

hence the error in $[L_{ij}]$ is negligible. The error is again $\sim 5\%$ during Zeeman fitting. The maximum 20 % error in all the measurements is considered.

3.6.10. Discussion on neutral and ion temperature profiles

It is seen that the radial profiles of corrected temperatures of both impurity ions have substantially higher values at the plasma region having radius, $r \sim 0.15$ m or $\rho \sim 0.6$. Not only that, T_i values again rise at the extreme plasma edge having $r = 0.22$ m or $\rho \sim 0.86$ as compared to those at $r = 0.18$ m or $\rho \sim 0.72$. These differences in the T_i can be explained in terms of the thermalization time of the ion in plasma. For this purpose, impurity ion-electron thermalization time (Wesson and Campbell; Thomas Morgan) and ionization time due to electron impact (Wesson and Campbell) have been calculated using the relation

$$\tau_{th} = 2.2 \times 10^{17} \frac{\left(\frac{m_I T_e^{\frac{3}{2}}}{m_e^{\frac{1}{2}} n_e Z_{Ee}^2 Z_I^2 \ln \Lambda} \right)}{s} \quad 3.30$$

Here, m_I and m_e are masses of impurity ions and background plasma electrons, Z_I and Z_{Ee} are the charge of impurity ions and background plasma. n_e and T_e are plasma electron density and temperature, respectively. $\ln \Lambda$ is the Column logarithm. The characteristic time for ionization is given by,

$$\tau_{ion} = \frac{1}{n_e \langle \sigma v \rangle_{ion}} \quad 3.31$$

Here, $\langle \sigma v \rangle_{ion}$ is the ionization rate for the respective impurity charge state. The temperature that an ion can attain before being ionized is given by τ_{ion}/τ_{th} . It is independent of density. The determined ionization and thermalization time are tabulated in Table 3.7. With respect to different radial locations the electron temperature changes, especially in the edge electron temperature is less hence the collision frequency increases through this ionizations are faster.

It can be seen from the table that the ionization times of C^+ is remains almost the same at both locations, but thermalization time reduces to 12 ms at $r = 0.22$ m or $\rho \sim 0.86$ from its value of 19 ms at $r = 0.18$ m or $\rho \sim 0.72$. It allows C^+ ion to gain higher energy and resulting in having higher T_i of 7 eV at the plasma edge at $r = 0.22$ m or $\rho \sim 0.86$ as compared to 2 eV at an inner region having $r = 0.18$ m or $\rho \sim 0.72$. In the case of O^{4+} ions, the thermalization time is lower than the ionization time at $r = 0.22$ m or $\rho \sim 0.86$ location, and this leads to a higher O^{4+} ion temperature at this location compared to the inner region, where the ionization

time is lower than the thermalization time. It can be understood better from Figure 3.15. It is seen that the ratio of ionization to thermalization times increases toward the plasma edge for both ions leading to higher T_i of both the ions at $r = 0.22$ m or $\rho \sim 0.86$ as compared to inner regions, where the ratios become almost constant.

Table 3.7 ionization and thermalization time of carbon and oxygen impurity ions

Radial location (m)	Ionization time (ms)		Thermalization time (ms)	
	C^+	O^{4+}	C^+	O^{4+}
0.18 ($\rho = 0.72$)	0.16	6	19	14
0.22 ($\rho = 0.88$)	0.12	24	12	9

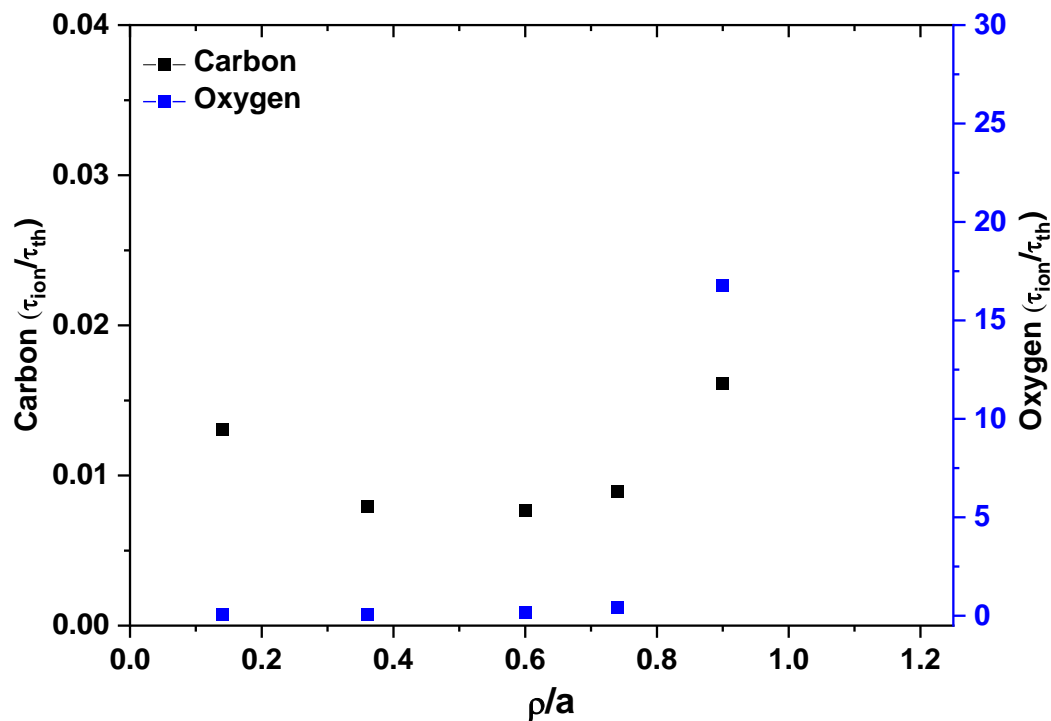


Figure 3.15. The ratio of ionization and thermalization times for C^+ and O^{4+} ions versus plasma radial location of ADITYA-U plasma

However, the higher value of T_i in the plasma region having $r = 0.10 - 0.14$ m ($\rho = 0.4 - 0.6$), cannot be justified by invoking the thermalization and ionization times, as the thermalization time is always higher than the ionization time for both impurity ions. However, it is believed that the presence of a magnetic island associated with magneto-hydrodynamic

(MHD) mode around that radial location influences the T_i of carbon and oxygen impurities ions. The magnetic island due to $m/n = 2/1$ mode resides at around $r = 0.10 - 0.14$ m ($\rho = 0.4 - 0.6$) plasma region of ADITYA-U tokamak (Raj et al.). The peaking of plasma parameters inside the magnetic island has been observed in many devices. The electron density increased in the TEXTOR tokamak (Vries et al.). Similarly, ion temperature peaked in the JT-60 U tokamak (JT-60 Team et al. 60), and the rise of electron temperature was observed in the MST reverse-field pinch device (Stephens et al.). In the JT-60U tokamak, heat transport inside the island explained the peaked ion temperature. Here, it was attributed to the state of the magnetic island with reduced thermal diffusivity in the presence of flow shear (JT-60 Team et al.). This might be the reason for the higher T_i at $r = 0.10 - 0.14$ m ($\rho = 0.4 - 0.6$) region of ADITYA-U plasma.

3.7. Observation of Poloidal Asymmetry estimation in Neutral temperature

3.7.1. Experimental setup

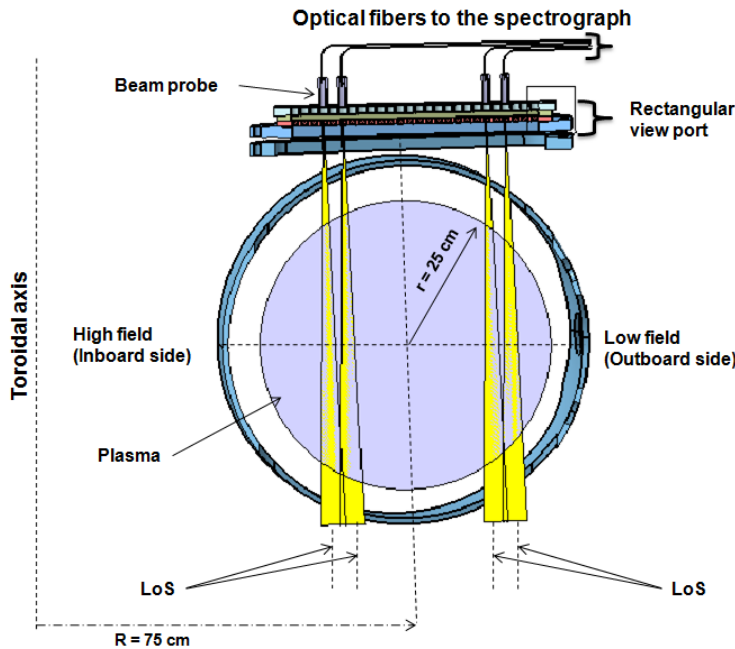


Figure 3.16. Schematic of the viewing geometry used for the multi-track spectrometer. The Line of Sight is at different radial locations $r = -0.16$ m and $r = -0.13$ m on the high field side and $r = 0.11$ m and 0.14 m on the low field sides.

The high-resolution space-resolved visible spectroscopic system is used for this study. However, the arrangement of LOS is now different compared to the LOS setup used during radial profile measurement. Four LOS has been used and arranged for poloidal asymmetry

estimation in such a way that two are at HFS and the other two are at LFS. Figure 3.16 shows the schematic diagram of the LOS representing respective radial locations, HFS: $r = -0.16$ m and $r = -0.13$ m and LFS: $r = 0.11$ m and $r = 0.14$ m. As earlier, fiber arrangements made here are in such a way that each LOS is perpendicular to the same constant toroidal magnetic field present in the viewing area. It is easier to analyze the Effect on temperature present due to the split of the spectral line.

Plasma position has been controlled by a spectroscopic reference signal and real-time feedback control system (R. Kumar, Gautam, et al.). This system simultaneously monitors the H_α emissions using two vertical lines of sight at the same radial location of the plasma's low and high field sides from the bottom port of the machine.

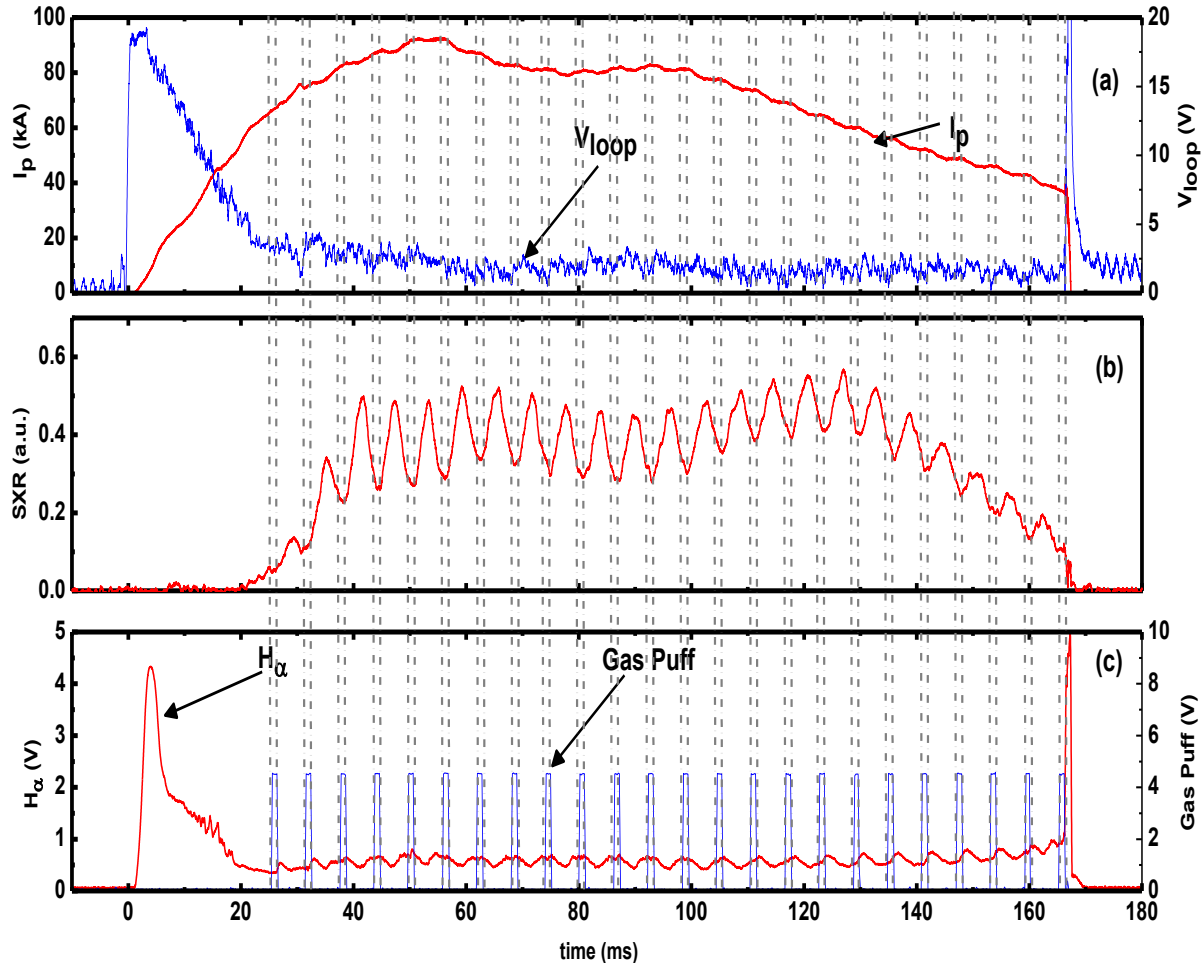


Figure 3.17 Temporal profiles of plasma parameters shot#32357 experiment (a) Plasma current and loop voltage (b) X-ray (c) H_α and Gas puff signals

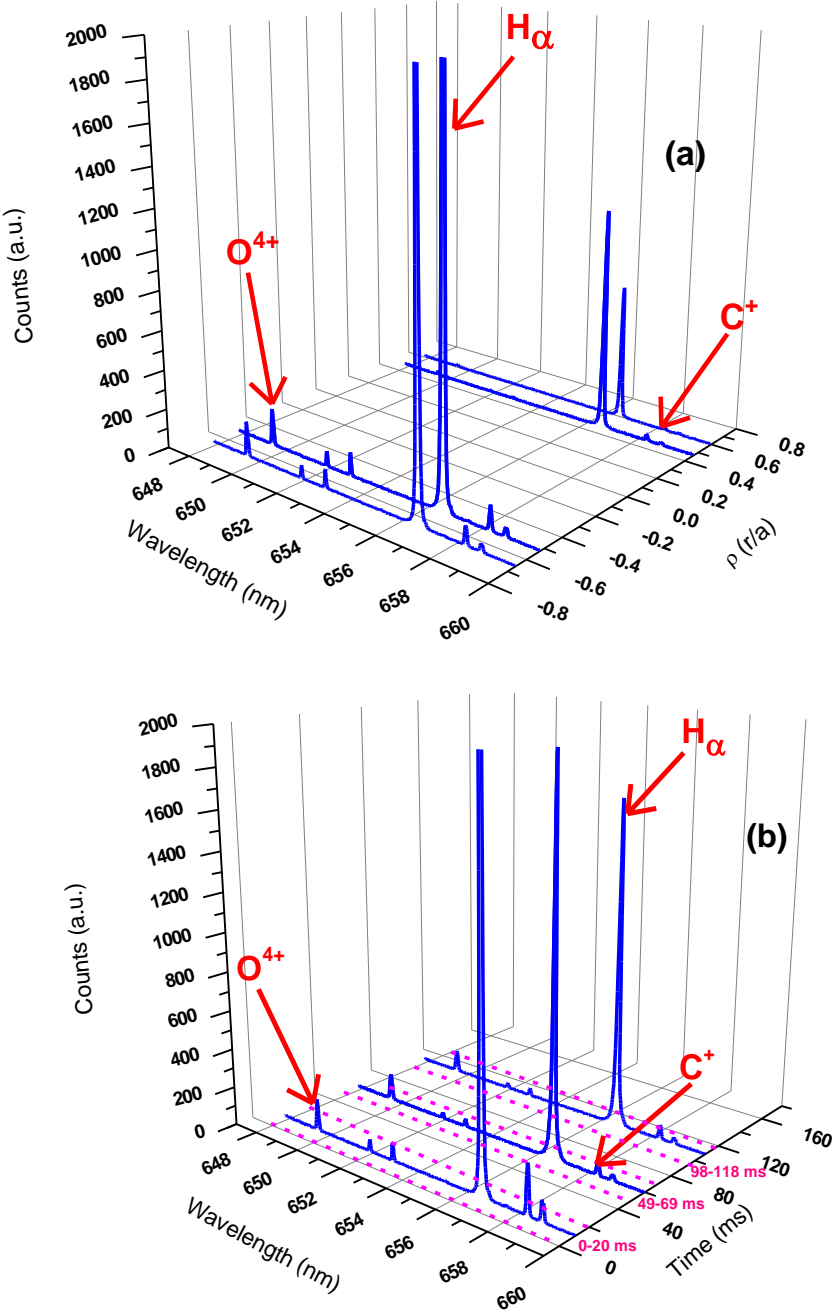


Figure 3.18 (a) Space resolved $H\alpha$, C^+ , and O^{4+} spectra for 4 tracks corresponding to four LOS (b) temporal evolution of $H\alpha$, C^+ , and O^{4+} spectra from a single track ($r=-0.13$ m) corresponding to one LOS of shot#32357

3.7.2. Experimental Result

In this experiment, measurements of shot # 32357 and #32358 have been presented and further processed for neutral temperature estimation, and both have almost identical plasma discharges. The typical plasma discharge parameter for shot #32357 is described in Figure 3.17 (a), (b), and (c). Figure 3.17 (a) represents the temporal evolution of the plasma current (I_P) and loop voltage (V_{loop}). Figure 3.17 (b) indicates the soft X-ray signature emitted from

ADITYA-U plasma. Figure 3.17 (c) is the intensity modulation in H_{α} emission as the shot progresses. The plasma presented in this experiment is having a gas puff. Using a spectroscopic setup, the emission spectra are recorded for three different time stamps by triggering the entire system with V_{loop} . Keeping the exposure time of the CCD detector at 20 ms, three-time frames are (i) 0 – 20 ms, (ii) 49 – 69 ms and (iii) 98 – 118 ms of the discharge. The space-resolved spectral profile in the range of 648–660 nm is given in Figure 3.18 (a). : In this figure, the H_{α} spectral line is accompanied by lines emitted by C^+ and O^{4+} ions (marked in the figure). The temporal evolution of these spectra is given in Figure 3.18 (b). For two identical plasma discharges, #32357 and #32358, the neutral temperature is presented with its spatial and temporal profile.

Figure 3.19 represents the neutral temperature at different radial locations at different times. For the initial period, Figure 3.19 (a) 0 – 20 ms, is the plasma burn-through phase also the current ramp-up during this period. Neutral temperature is $T_n \sim 2.5 – 4 eV$ (Figure 3.19 (a)). There is a negligible difference between HFS (inboard) and LFS (outboard) sides for both plasma discharges. Figure 3.19 (b) represents another time period, 49 – 69 ms. This is the current flat-top phase of plasma with stable plasma parameters. At HFS (inboard) neutral temperature $T_n \sim 4.5 eV$, however at LFS (outboard) neutral temperature $T_n \sim 3 – 1.8 eV$. During this period, gas puffing was used in the plasma discharge presented, as seen in Figure 3.17 (c). Horizontal plasma position measurements for both discharges have been given in Figure 3.19. For the time periods 49 – 69 ms, the plasma position is almost at the geometric center of the machine for both discharges. The poloidal asymmetry in neutral temperatures occurred during this time of plasma discharge. Figure 3.19 (c) represents neutral temperature estimation for 98 – 118 ms. Asymmetry in neutral temperature is again visible with a similar magnitude during this time interval for shot #32357. However, for shot #32358, the neutral temperature rises in both LFS and HFS of the machine, but the fetcher of asymmetry is still retained between LFS and HFS with changed magnitude. This is possibly due to the movement of plasma, shot #32358. The plasma column moves toward the inboard side (HFS) i.e., towards the graphite limiter, as seen in Figure 3.20. As a result, influx increases, and edge plasma temperature decreases as some energy is spent towards the ionization of particles. As the neutrals may acquire the temperature through collisions with ions, the decrease of ion temperature affects the neutral temperature and causes its reduction when the plasma moves inboard.

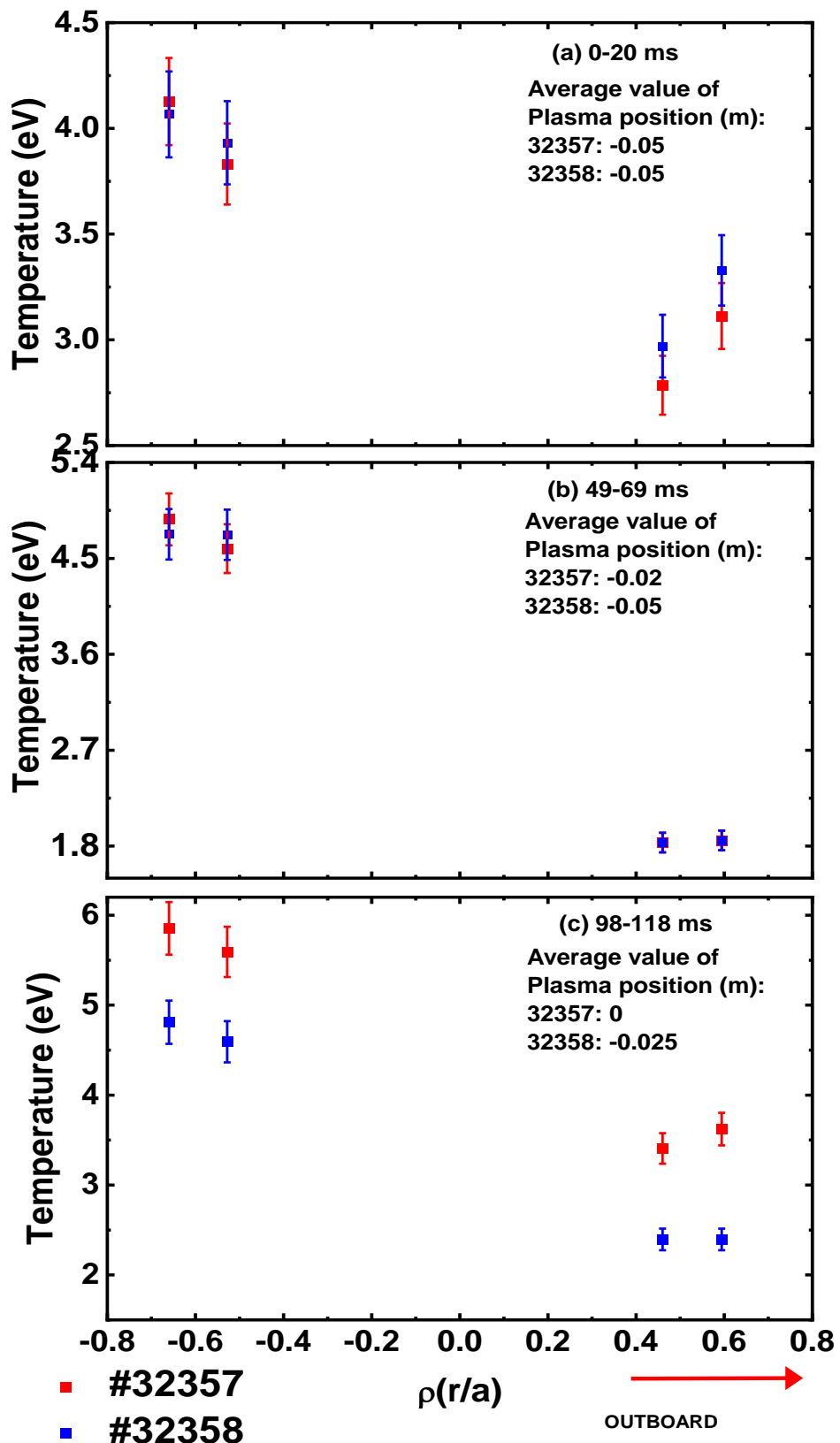


Figure 3.19 Neutral temperature measurement result for shots #32357 and #32358 in low field side (+ve sign, outboard) and high field side (-ve sign, inboard): (a) during 0-20 ms (b) during 49-69 ms (c) during 98-118 ms of discharge

3.7.3. Discussion on poloidal asymmetry

There may be several reasons for the observed asymmetries in neutral temperature (T_n), during the flat-top phase of ADITYA-U plasma. Considering the mechanism of neutral heating, the neutrals can attain the temperature in several ways, ruling out the possible process acting in ADITYA-U tokamak. Thru the Franck-Condon dissociation of molecules, actively entering plasma through gas-puff or passively entering the plasma through the recycling process. The neutrals have energy ~ 4 eV. This process, however, will not produce a change in inboard and outboard regions, hence asymmetry is not possible due to this reason. Also, the neutrals can thermalize with background ions or through charge exchange with ions. If there is a poloidal asymmetry in ions, it can also get reflected in neutral temperatures. The in-out asymmetry in impurity ion temperatures has been observed in several tokamaks, such as in nickel ions in JET (Smeulders) and boron ions in Alcator C-Mod (Chen et al.; Churchill et al.) tokamaks. As it is well known that the confinement is better in the good curvature (high field side) region, the ion temperature and hence the neutral temperature may be higher than in the bad curvature region, where confinement is poor. A previous study by ADITYA tokamak (M. B. Chowdhuri, Ghosh, et al.) has reported higher diffusivity of impurity ions (oxygen) on the low field side compared to the high field side. This further suggests that the impurity ions may have higher temperatures in the high field side, leading to higher neutral temperatures, as observed in our measurements (Yadava, Ghosh, M. B. Chowdhuri, Manchanda, Dey, et al.).

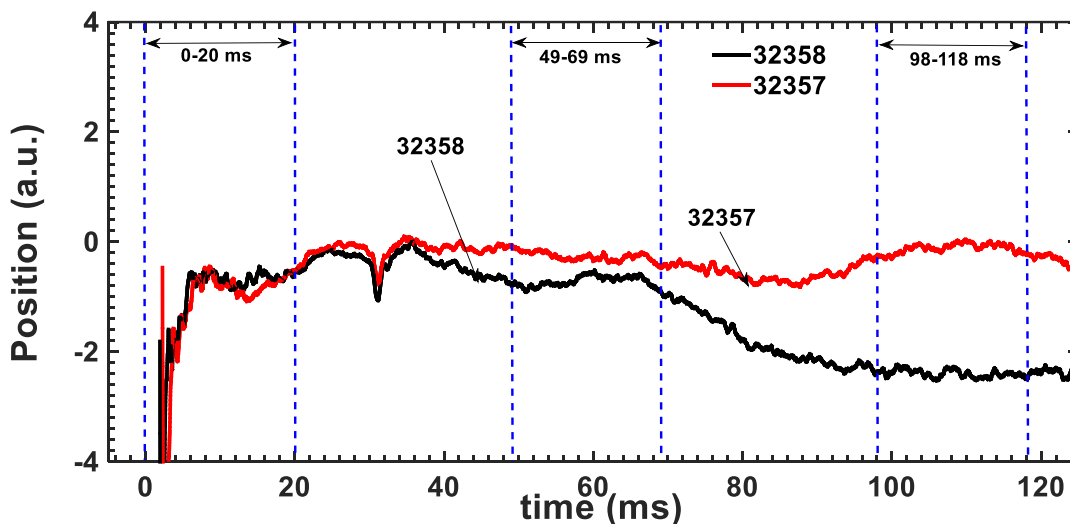


Figure 3.20 Plasma position measurements as a function of time

3.8. Investigation of self-absorption in spectral line profile from tokamak

3.8.1. Li₂TiO₃ pellet injection system

3.8.1.1. Disruption mitigation

For the ITER-like large-scale tokamaks, solving the issue of disruption mitigation is highly important to avoid spontaneous disruption with D-T fuel (Strait et al.). Disruption also affects the tokamak operation limits (Hender et al.). It produces large heat loads on the PFCs, and EM forces can severely damage the main vessel surface (Lehnert et al.). To reduce or control these damages, there have been many works on disruptions mitigation, but it is still undergoing research area. By reducing the heat load on the first wall, the plasma stored energy is radiated, and severe damage from a high heat load is avoided. The Massive Gas Injection (MGI) technique is beneficial and thought to be a basic disruption mitigation technique for ITER DMS(Hollmann, Aleynikov, et al.). Although it has several limitations when applied to ITER, it is related to slow response time and poor gas penetration (Raman et al.). This can be overcome by Shattered Pellet Injection (SPI), which has a faster response time, sharper density increases, and deeper penetration. In this technique, solid frozen high – Z gas is injected deep into the plasma (L.R. Baylor et al.). DIII-D tokamak has experimentally demonstrated the advantages of SPI over the MGI in all regards (Strait et al.), achieving pellet velocities of $\sim 200 \text{ m/s}$, before fragmentation. The Tracer-Encapsulated Solid Pellets (TESPEL) of $\sim 900 \mu\text{m}$ are injected in the Large Helical Device (LHD) with a velocity of $300 - 500 \text{ m/s}$ velocity (Sudo, Tamura, Suzuki, et al.). However, during MGI, massive gas has been injected which produces a radiative burst, and suddenly, emitter density becomes high, giving rise to the probability of plasma becoming optically thick for wavelength of interest (Kunze; Rezaei and Mieno). This medium provides a likely environment to produce self-absorption of the incident radiation that weakens the spectral line peak.

The limitations of associating with SPI bring in the concept of injecting low – Z solid particles into the plasma core for disruption mitigation. The radiative dissipation of the plasma stored energy during a significant disruption in ITER by fast injection of massive pellets of low – Z impurities, such as Li and Be, has been numerically modelled by Lukash et al. (Lukash et al.). Several advantages exist for a solid material injected directly into the plasma core without significantly perturbing the plasma current channel for disruption mitigation.

Depositing the radiative material directly in the runaway current channel formation region, the Thermal Quench (TQ) and the formation of runaway electrons could be suppressed (Sudo and Tamura). It has been suggested by Raman et al. (Raman et al.) that a radiative payload can be delivered to the plasma core on a < 10 ms time scale by accelerating a sabot containing the payload electromagnetically. The Inductive Particle Injector (IPI) conceptualizes accelerating a metallic capsule to desired velocities by an electromagnetic impeller to overcome drawbacks of MGI and SPI for the removal of high heat loads (L. R. Baylor et al.; Joydeep Ghosh, Sambaran PAHARI, et al.). During the disruption phase, the solid pellet is injected into the plasma. For this purpose, in ADITYA-U tokamak, a novel concept of inductively driven particle Injector (IPI) delivering a cluster of particles weighing in grams with high velocities up to 200 m/s has been developed and operated successfully during the ADITYA-U tokamak's circular plasmas operations. Although the concept of an electromagnetic particle injector was put forward by several authors, it has been experimentally demonstrated for the first time in ADITYA-U.

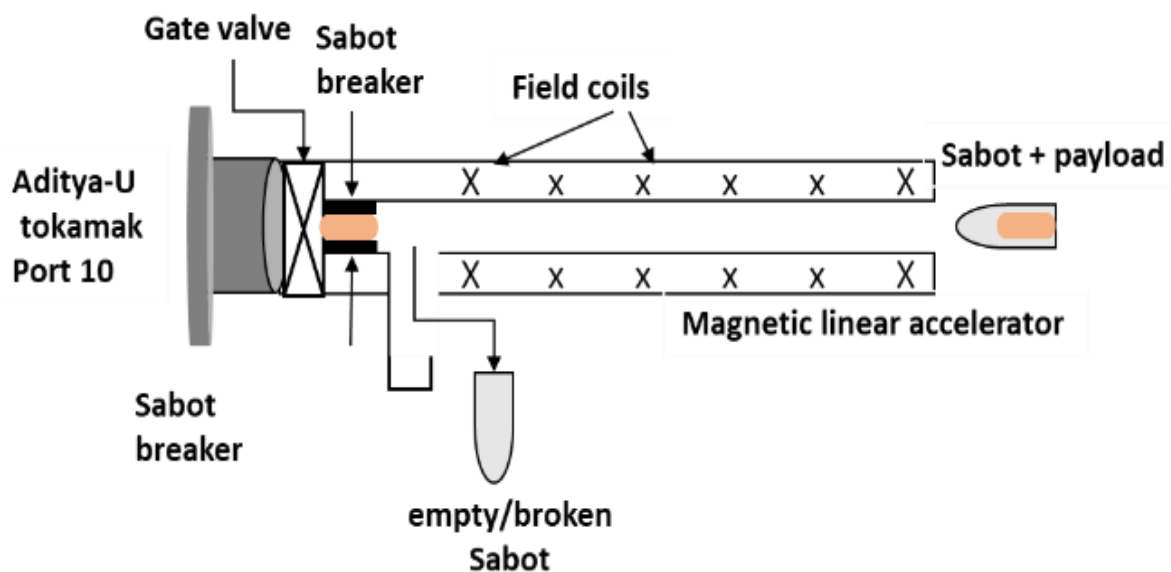


Figure 3.21 Schematic of experimental electromagnetically driven pellet injection based on the concept of magnetic linear accelerator

Figure 3.21 illustrates the working principle of a single module of an IPI. A cartridge within an electromagnet is accelerated by the resultant Lorentz forces generated by a pulsed magnetic field and the induced currents on the cartridge. A capacitor bank powers the electromagnet. The cartridge accelerates through the flyway tube, gaining energy incrementally. The position and velocity of the cartridge are ascertained by a “time-of-flight” velocity measurement system using a paired collimated light beam source (laser).

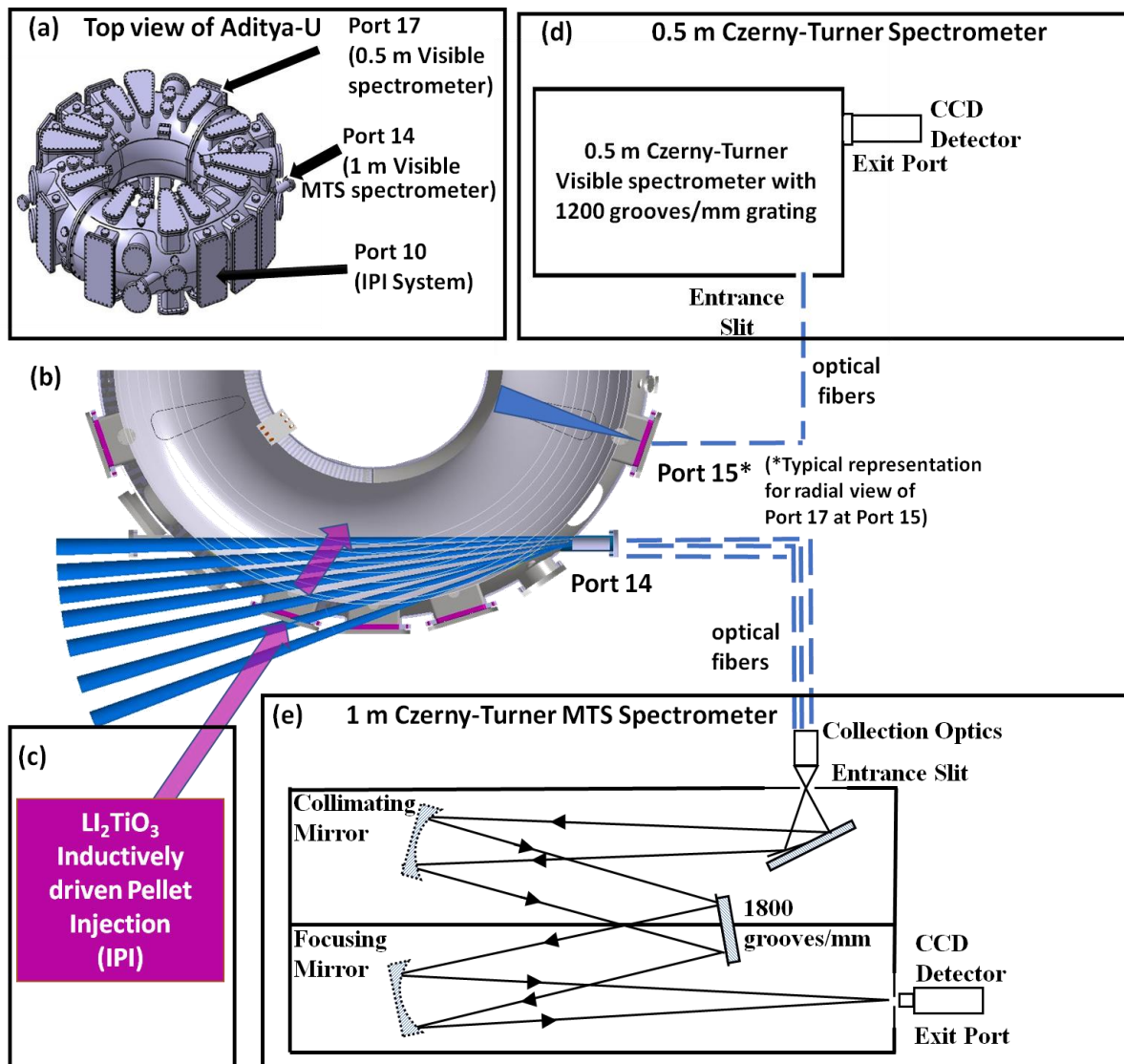


Figure 3.22. Schematic of the experimental setup (a)Top view of the machine showing ports 10, 14, and 17 for IPI and spectroscopy setup. (b) all the diagnostics (0.5 m visible spectrometer and 1 m multi-track spectrometer) are consolidated on the machine, and their respective LOS are presented. (c)IPI - Li_2TiO_3 setup. (d) 0.5 m spectrometer for time evolution measurement of Li spectral line shape profile and (e) represents the 1 m high-resolution spectrometer measurement of spectral line shape and its radial profile.

As shown in Figure 3.21, the basic design idea involves a set of magnetic coils when coupled with equal spacing to produce oscillating electric field potential in a linear direction. It accelerates the charged subatomic particle or ions at high speed. By coil radius ~ 1 cm, length ~ 1 m and pellet radius $\sim 3 - 4$ mm. The 2 modules of IPI are configured to accelerate cartridges to velocities in the range of 100 m/s to 200 m/s. During such high accelerations of the pellet called a “payload,” it is needed to be protected inside some capsule, which is called a “sabot.” A shape is designed at the end of the coil, which provides breaking/ de-accelerating action to the sabot, and only the pellet will be fired. The whole system is connected to the machine through a gate valve to keep the system isolated. After each plasma operation, the

empty/broken sabot is removed, and a new one is loaded. 25 mm sabot is (14 gm) pre-filled with a cluster of Li_2TiO_3 or Li_2CO_3 particles (particle size 50 – 100 μm diameter) weighing 50 – 200 mg are loaded inside the payload. The vacuum vessel housing the core system is pumped down using a turbo molecular pump (750 liter/sec) and monitored using a cold-cathode gauge. The Gate valve, isolating the IPI chamber with the main tokamak vessel, is opened only after the IPI system has been evacuated to a base pressure equivalent to that of the Tokamak vessel (10^{-8} mbar). A transistor-to-transistor (TTL) logic pulse from the Tokamak Control System generated 52 ms into the discharge current flat-top phase is used to trigger the IPI system.

The machine's IPI system is installed on port 10 (as shown in Figure 3.22 (b)), located at ~ 170 degrees. It has been triggered using a delay generator from the triggering system of ADITYA-U tokamak. Details of this system are given in the paper by J. Ghosh et al. (Joydeep Ghosh, Sambaran PAHARI, et al.). The tokamak was operated in a limiter configuration and with a toroidal magnetic field of 1.28 T during the IPI experiments presented in this paper. The results presented here are for a 50 mg payload pellet of Li_2TiO_3 .

3.8.2. Spectroscopic observation system

Visible spectroscopic diagnostics are used on tokamak to monitor the pellet material's spectral line emission/absorption. A high-resolution spectroscopic system (section 2.3.2.6) along with a 0.5 m survey spectrometer (section 2.3.2.5) is used for modelling line shape and to see the temporal evolution of spectral lines, respectively. The PMT, along with Li (670.8 nm) 3 nm bandwidth filter-based detector systems, are also used during this experiment for the temporal evolution of the Li emission line.

The 0.5 m visible spectrometers to see the temporal evolution of the plasma through the radial viewport located at the horizontal mid-plane of port 17 of the machine capture the radiation from the center of the plasma, as shown in Figure 3.22 (b). This port is away from the pellet injector location, thus giving the idea about the pellet's effect along the machine's toroidal direction. The light is collected with collimator 1 (Table 2.3) in combination with 1 mm core diameter optical fiber. The entrance slit of the spectrometer is kept at 100 μm , the exposure time of CCD is 5 ms, and the spectrum is captured every 8 ms.

The high-resolution space-resolved spectroscopic system is used for space-resolved measurement of the Li spectral line profile. A tangential viewport is used for this purpose, located at port 14, as shown in Figure 3.22 (e). The collection optics was placed inside a

customized re-entrant viewport to cover the whole plasma radius from the core to the outboard edge, as shown in Figure 3.22 (b). The arrangement is made at port 14. It allows full radial coverage from the core to the outboard edge (Shah et al.). A total of seven LOS are set up for space-resolved lithium emission measurement, as shown in Figure 3.22 (b). Collimator 3 (Table 2.3) is used as the collection optics along with 400 μm core diameter optical fibers. The spectrometer is operated with a 70 μm side entrance slit. The CCD is operated in multi-track mode, readout time of the CCD becomes 47 ms. It is clear from Figure 3.22 (b) that the LOS is intercepting the IPI pellet injection path, thus directly capturing the radiation during the pellet's burst (Yadava).

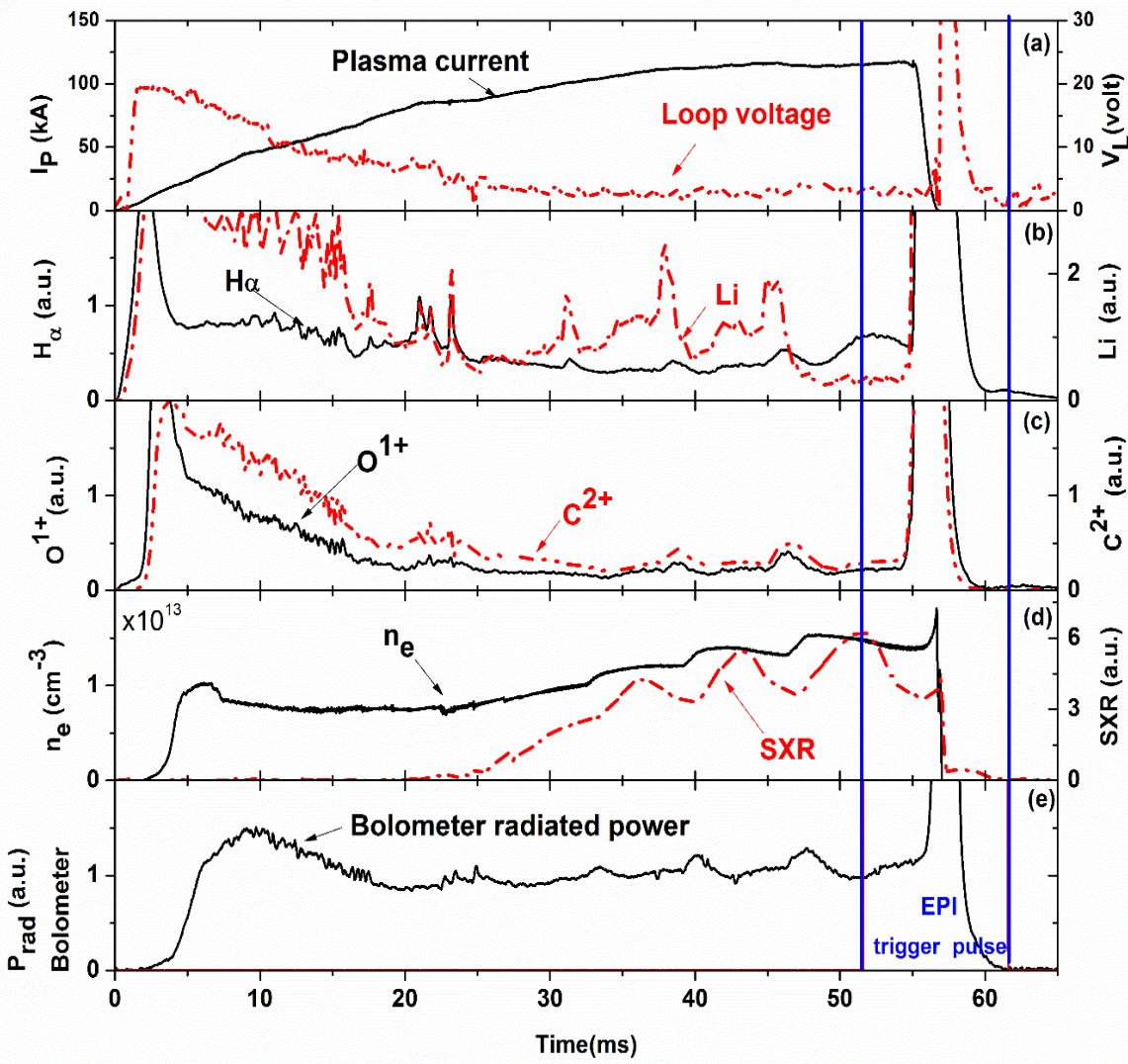


Figure 3.23. Shot #33317, a typical IPI discharge (a) plasma current (solid black line) and loop voltage (red dash-dot line) (b) Fuel H_α (656.28 nm, solid black line) and lithium (670.8 nm, red dash-dot line) line emission (c) oxygen (441.2 nm, solid black line) and carbon (464.7 nm, red dash-dot line) emissions(d) electron density (solid black line)and soft X-ray signal (red dash-dot line) (e) radiative power, solid blue line represents IPI trigger pulse at 52-62 ms.

3.8.3. Typical plasma discharge parameters

The shot with Li_2TiO_3 the pellet was performed with $B_T \sim 1.3$ T. Plasma shot #33317 contains Li_2TiO_3 pellet experimental data. The plasma parameters for this discharge are shown in Figure 3.23, where (a) shows $I_P \sim 118$ kA at plasma flat-top with pellet injection triggered at 52 ms, represented by a solid blue line on the plot. It is affecting all the plasma parameters suddenly within 3 ms. The plasma discharge was terminated by a disruption as can be seen in the same figure (Figure 3.23). In the first few milliseconds of plasma discharge, the breakdown and burn-through phases and atomic and molecular excitation processes dominate. It gives the first spike in fuel neutral $\text{H}\alpha$ (656.28 nm), impurity neutrals and ions Li (670.8 nm), O^+ (441.2 nm), and C^{2+} (464.7 nm), as shown in Figure 3.23 (b) and (c). In the flat-top period, the plasma becomes stable, as seen in Figure 3.23 (a), and emissions from fuel and impurity are maintained via almost constant plasma limiter interaction. At ~ 52 ms time of plasma, the IPI pulse has been fired, and within 3 ms of time, plasma gets disrupted with huge radiation loss, as can be seen in Figure 3.23 (b), Figure 3.23 (c), and Figure 3.23 (e), all the emitted radiation signals are showing saturation. Plasma electron density also falls sharply, as shown in Figure 3.23 (d). The spectroscopy data analyzed from shot #33375, which is almost reproducible to shot #33317 presented in Figure 3.23. Shot #33375 has a plasma current of ~ 115 kA with ~ 59 ms of plasma duration.

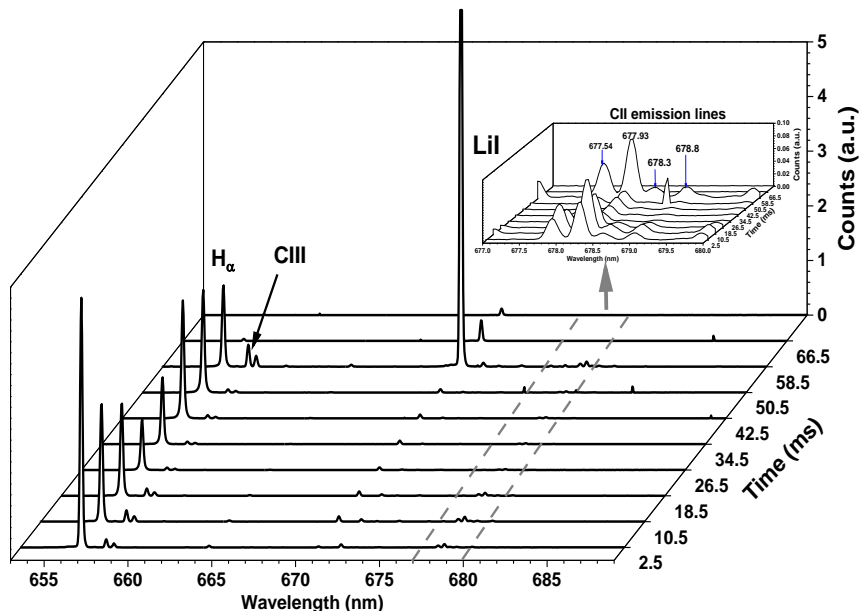


Figure 3.24. The emission spectrum was acquired using a 0.5 m spectrograph to see the temporal evolution of plasma during the IPI experiment

3.8.4. Results and discussion on self-absorption of *Li* spectral line

Figure 3.24 shows the temporal evolution of spectral lines around 670 nm captured from the core of the plasma using a 0.5 m visible spectrometer. From the beginning of discharge, when even the pellet was not fired, one can observe that H_{α} at 656.28 nm and C^{2+} at 658.2 nm is appearing along with some small trace of spectral lines of atomic Li present at 670.8 nm ($2s\ ^2S - 2p\ ^2P$). This small trace is mainly occurring now due to the recycling process as Li was trapped into PFCs during earlier experiments. The pellet was fired between 52 – 62 ms. In Figure 3.24, it is visible that at ~58.5 ms, the sudden increase in the Li emission line was stirring and saturated. This frame signifies the total 8 ms times, including 5 ms exposure and 3 ms readout time. The plasma duration exposed to the spectrometer is 56 – 61 ms. The lithium flux was beyond expected, with a very high flux of Li contributing to the increase in plasma density. However, with such high density, plasma is likely to produce both absorption and emissions. The self-absorption phenomenon occurs in the plasmas. It is identified from the line profile by analyzing the dip present in the spectrum.

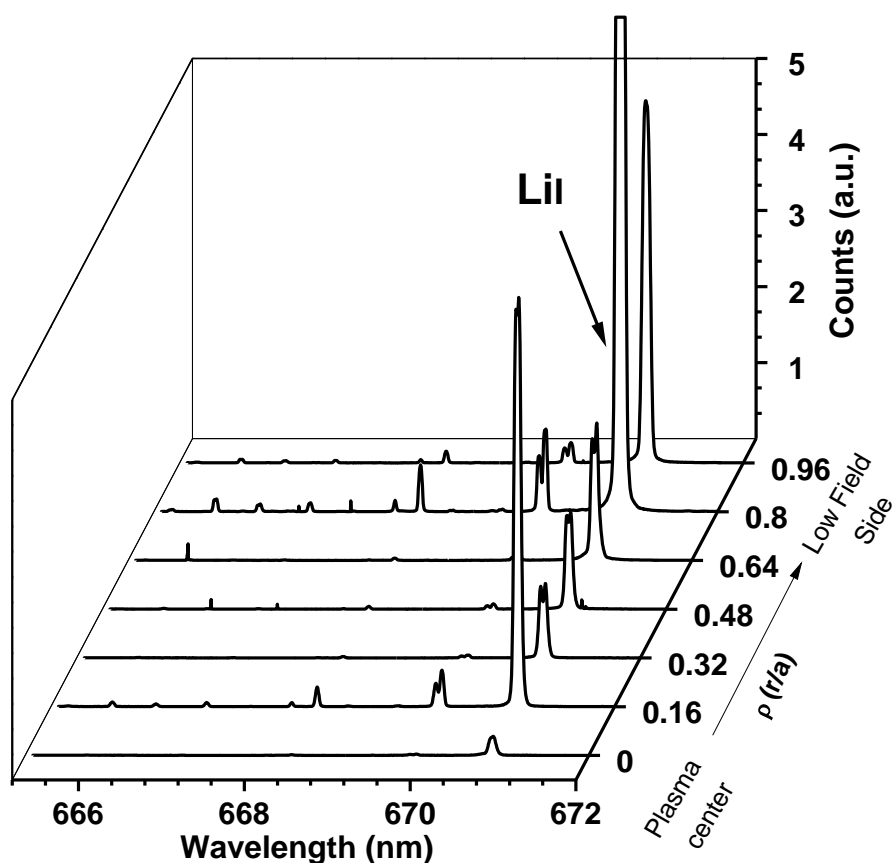


Figure 3.25. The emission spectrum was acquired using a 1 m spectrograph to see the spatial evolution of plasma during the IPI experiment

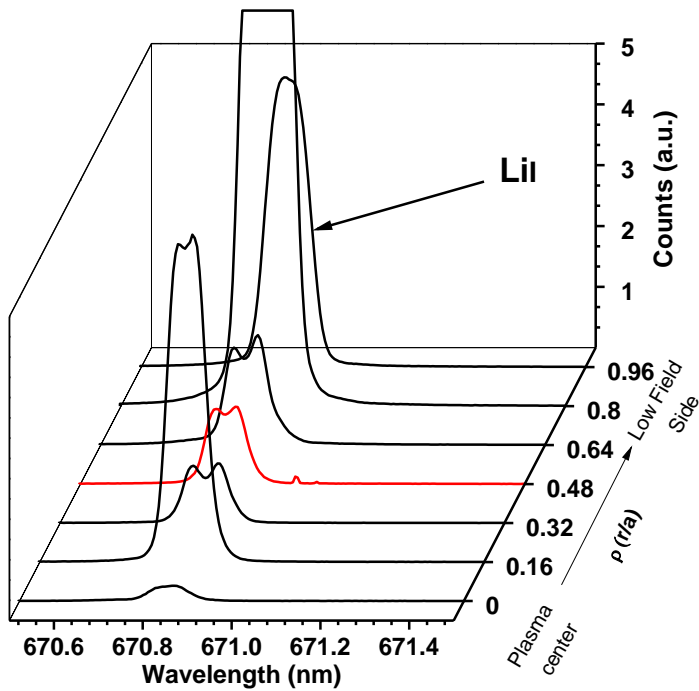


Figure 3.26. Zoom part of space resolved spectra acquired with the multi-track visible spectrometer

The space-resolved data is acquired by the high-resolution spectrometer, with an exposure time of 8 ms and a delay of 48 ms. The plasma duration exposed to the spectroscopic system is 48 – 56 ms. The captured space resolves spectrum is given in Figure 3.25. It is interesting to see how Li emission is changing with the radial locations. The enlarged portion of the Li emission line is therefore provided in Figure 3.26. Here $\rho = 0$ represents the plasma location towards the core, and $\rho = 0.96$ is the location towards the plasma edge. Pellet was fired from the tokamak edge from the outboard side. Li emission was getting saturated at radial location $\rho \sim 0.8$. There is no dip in the spectral line profile observed up to this radial location (between $\rho \sim 0.8 - 0.96$). Hence no self-absorption has been observed at plasma edge locations directly viewing the pellet path. However, there has been a significant dip in the measured line profile beyond the edge towards the core of the plasma. It tells that the absorption dip in the spectral line profile is more prominent in the plasma core than at the edge. Also, the edge plasma is optically thin, and the plasma becomes optically thick towards the core of the plasma. Similar observations have been made through the bolometer radiated power, which is maximum at the core, and then not much radiation is present from an edge. This agrees with spectroscopic measurement (Joydeep Ghosh, Sambaran PAHARI, et al.).

3.8.5. Opacity estimation

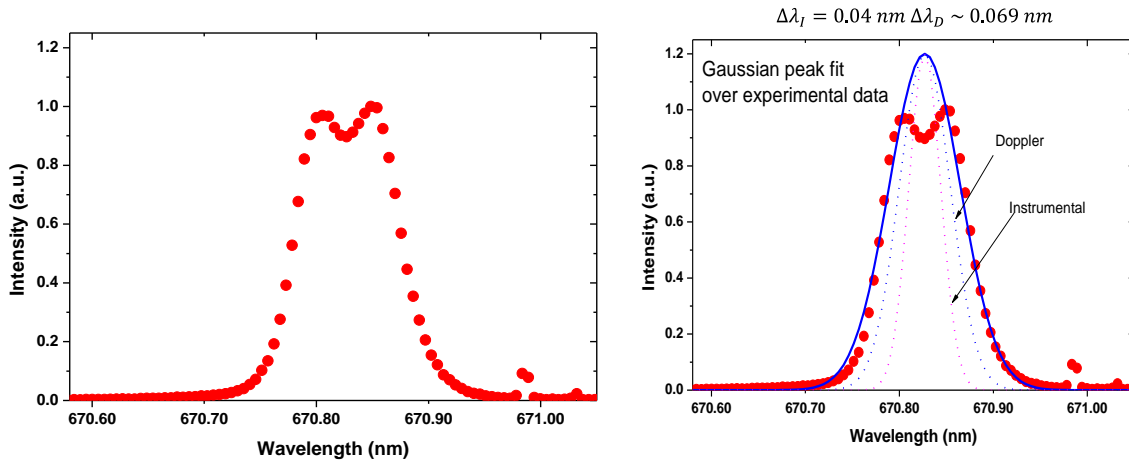


Figure 3.27. (a) experimental line profile (b) gaussian fitted spectra without absorption

The data from the chord passing through the radial location of 0.12 m was further examined in depth. The experimental data points of the raw spectroscopic observation are present in Figure 3.27 (a). Additionally, these experimental data were fitted by convoluting instrumental Gaussian line profile with Doppler broadened Gaussian line profile. The measured spectra using equation 3.12 fitted well with experimental spectra having the FWHM due to Doppler broadening $\Delta\lambda_D \sim 0.06 \text{ nm}$ and FWHM due to instrumental broadening $\Delta\lambda_I = 0.04 \text{ nm}$ (total FWHM $\Delta\lambda \sim 0.08 \text{ nm}$). With this, the absorption dip was not fitted, as seen in Figure 3.27 (b). Red data points represent the experimental data, two dashed lines are Doppler and Instrumental broadening, and the solid blue line is the resultant simulated spectra.

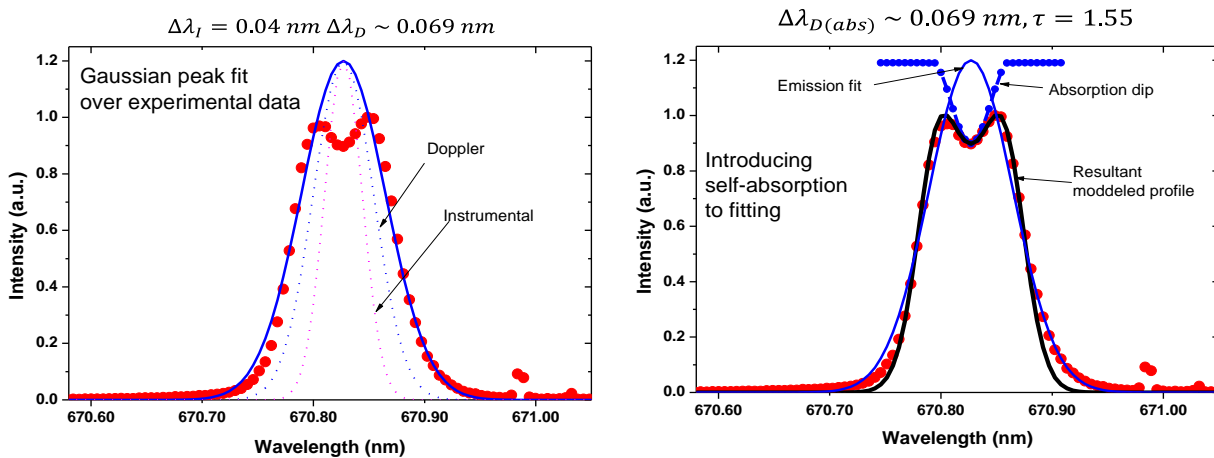


Figure 3.28. (a) gaussian fitted emission spectra, (b) matched self-absorption line profile

The spectrum was fitted to answer the absorption dip present in the spectral line profile using equation 3.26. The best fit is generated with the reduced total FWHM $\Delta\lambda \sim 0.05 \text{ nm}$, similar to FWHM due to instrumental broadening $\Delta\lambda_I = 0.04 \text{ nm}$ and FWHM due to Doppler broadening

$\Delta\lambda_D \sim 0.04$ nm. Figure 3.28 (b) represents the solid black line as plotted using equation 3.26, Figure 3.28 (a) is the same as Figure 3.27 (b). Also, in Figure 3.28 (b), the reversed absorption dip with a solid blue line is given. The absorption dip is represented by the opacity parameter τ in equation 3.26. Here for fitting, $\tau = 1.55$. As in equation 3.22, τ is nothing but the product of the line absorption coefficient and depth of the medium in which radiation is passing as given in the equation. The depth of the medium is approximately known using the cord length, and it is ~ 6 mm. It also gives a measurement of the absorption coefficient $\kappa \approx 0.25 \text{ cm}^{-1}$. The absorption coefficient varies linearly with neutral lithium density, oscillator strength $f = 0.248$ (Kramida and Ralchenko), and the wavelength of the line, while it is inversely proportional to the square root of lithium atom temperature. The absorption coefficient formula is given as equation 3.27. Using this formula, the lithium density was calculated by considering a lithium temperature of ~ 0.025 eV. As injected pellet is of average room temperature, the derived lithium density $n_{Li} \sim 2 \times 10^{22} \text{ m}^{-3}$. Edge radiative cooling is essential to establish future tokamak devices, as the radiation losses in plasma prevent the damage of PFCs and other vessel parts. A highly radiative plasma gets distributed uniformly over the first wall of the machine; thus, it will reduce the local damages produced by the heat. The impurity concentration decreases as the erosions caused by high heat flux will be reduced. Then, using these temperature and density values, the radiative power losses (P_{loss}) have been derived using the equation;

$$P_{loss} = n_e n_{Li} L_{Li} \quad 3.32$$

In this case, it is the product of electron density ($n_e \sim 1.12 \times 10^{19} \text{ m}^{-3}$), lithium density ($n_{Li} \sim 2 \times 10^{22} \text{ m}^{-3}$), and radiative cooling rate coefficient (L_{Li}) the value of $L_{Li} \sim 0.66 \times 10^{-34} \text{ watt m}^3$ has been taken from reference no. (D E Post et al.). The estimated value of power loss is ~ 148 kW over the plasma volume, while the Ohmic input power (P_{In}) just before the pellet injection is ~ 260 kW. It shows that more than 60% of power radiated due to the pellet, and then it can be said that the sudden plasma disruption has happened due to radiative cooling of the plasma. This result is measured through line integrated single cord, and then this value tends to be an overestimation. Still, it gives the idea of the radiation loss caused by the pellet. However, getting a radial profile from line-integrated space-resolved data is crucial, and the inversion technique is helpful for the radial profile.

3.9. Summary

In this Chapter, the high-resolution visible spectroscopic instrument is used for emission line measurements from eight LOS with a large rectangular view port present on the top port of ADITYA-U tokamak. The line profile modelling is done for neutral and ion temperature estimation along with opacity measurement. The following conclusions are made from the measurements presented in this chapter.

- **Demonstration of Zeeman Effect correcting the ion and neutral temperature estimation anomaly:** Plasma was initially seen for the outboard cross-section of the machine. The carbon emission line C^+ (657.8 nm) was acquired in spectrometer through this line ion temperature was estimated using Doppler broadening of spectral line profile. The measured ion temperature was $T_{C^+} \sim 30 - 60$ eV at various radial locations of plasma. This measurement was surprising as it exceeds the ionization potential of C^+ ions (~ 24 eV). This has been further answered by introducing Zeeman component into the simulated spectrum for modelling the line shape. Using this the corrected ion temperature was found to be ~ 10 eV. This is a clear demonstration of how crucial the Zeeman Effect is in the estimation of ion/neutral temperatures from the spectral line-broadening measurements. With the same technique the 48-Zeeman component of H_α spectral emission line is done. However, it is first observed that with single gaussian temperature components, the wings of the spectrum remain unmatched. Further, the problem is solved in a separate section.
- **Radial profile measurement of C^+ and O^{4+} impurity ion temperatures:** The Abel-like matrix inversion technique was used for radial profile measurements of C^+ and O^{4+} ions, the estimated ion temperatures are, $\sim 2 - 15$ eV and $\sim 10 - 30$ eV respectively. At extreme edge ($\rho = 0.86$), the ion temperatures are found to be higher. This can be explained by the lower thermalization time than the ionization time. However, at $r = 0.12 - 0.15$ m ($\rho = 0.5 - 0.6$) the ion temperature is peaking and it is explained through the presence of magnetic island $m = 2$ MHD mode, where transport inside the island increases the ion temperature.
- **Identification of hot and warm Neutral temperature components:** While fitting the simulated H_α the spectral line obtained through modelling, with the measured spectra using a single Gaussian spectrum, it has been observed that the wings of the spectral lines are not fitted properly even after the Zeeman Effect is taken into account. Hence the two temperature components (hot- charge-exchange process and warm- molecular

dissociation, dissociative ionization, and Franck–Condon dissociation processes) were considered for Zeeman based simulation. It was found that the temperature components range as, $T_{H\alpha|HOT} \sim 15 - 30$ eV and $T_{H\alpha|WARM} \sim 3 - 5$ eV for various plasma radial locations. Tin Abel-inverted temperature measurement, at $\rho = 0.6$ the temperature rise is observed like the case of ion temperature.

- **Discovery of poloidal asymmetry in neutral temperature:** In ADITYA-U tokamak, the poloidal asymmetry in neutral temperatures is observed for the first time in tokamak history. For this experimental purpose, the LOS are arranged to see LFS and HFS of plasma simultaneously. LFS and HFS of ADITYA-U tokamak plasma have warm component neutral temperatures of 2 eV and 4 – 5 eV, respectively. The neutral gain temperature from impurity ions in many tokamaks is poloidal. The asymmetries in ion temperature were also measured in several tokamaks which is mainly due to high curvature drift at HFS.
- **Investigation of plasma opacity during disruption mitigation experiments:** To protect the vacuum vessel from bulk PWI disruption mitigation comes to the rescue. For the said study in ADITYA-U tokamak, the experiments were carried out at ADITYA-U tokamak by launching the Li_2TiO_3 pellet using an inductively driven pellet injection technique. During this experiment, with high-resolution spectroscopic setup, the neutral Li emissions were measured at 670.8 nm. In the line profile significant dip is found, with a thorough investigation, it was discovered that the self-absorption phenomenon taking place for Li emission (plasma is optically thick for incoming radiations). By investigating the dip of spectral line shape through modelling, it was found that opacity of $\tau = 1.55$ is occurring which gives the lithium density, n_{Li} of $\sim 2 \times 10^{22} m^{-3}$, and the estimated power loss is ~ 148 kW. This is more than 60% of input power which is radiated due to the pellet causing the sudden disruption of plasma and enable us to understand the physics behind developing the technique for disruption mitigation.

Chapter 4. Investigation of impurity influxes and recycling in ADITYA-U tokamak

4.1. Introduction

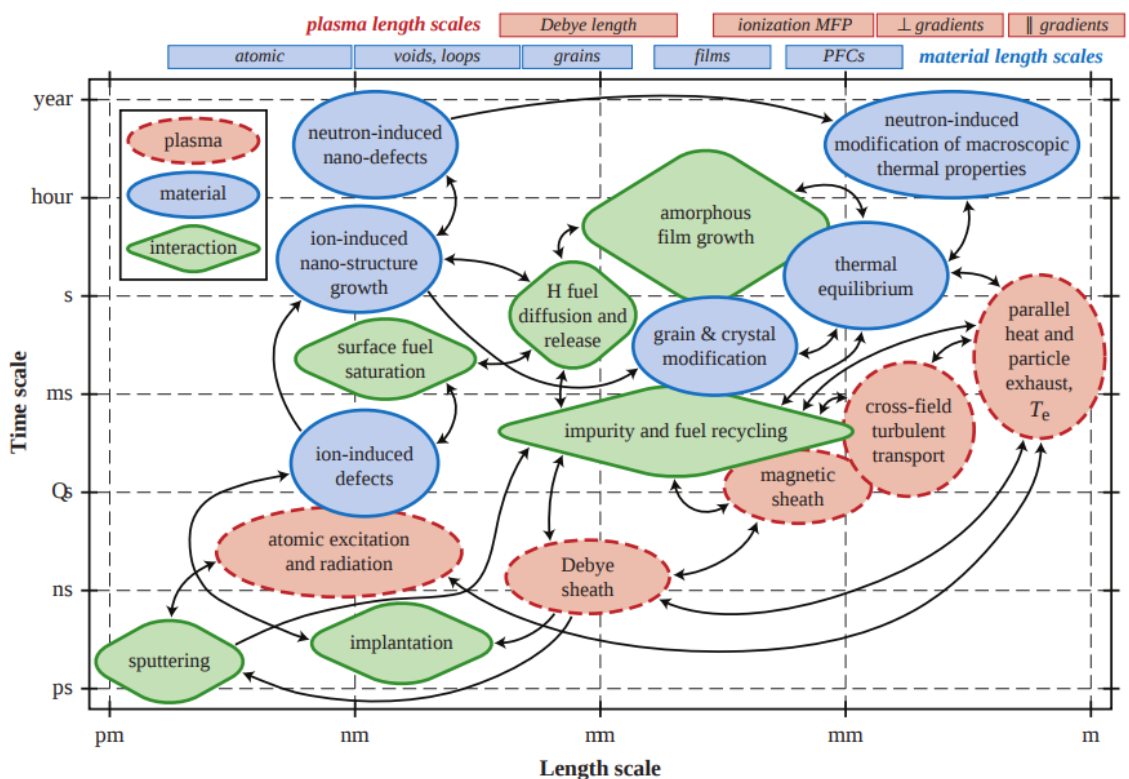


Figure 4.1. time and scale lengths of different PWI processes figure taken from (Hartwig)

It is observed that plasma surface interaction plays a crucial role in the phenomenon occurring in the edge region of plasma during plasma confinement. An understanding of the primary processes that take place within this region is helpful for future plasma operations and their predictions. Here, two areas of investigation have been dealt with, (i) hydrogen wall recycling and (ii) impurity influxes in this work. Also, this part of the thesis overviews the critical physical and chemical processes which play an important role in the neutral particle dynamics and particle and impurity influxes in the plasma. This investigation has been done under different wall conditionings and for the different first wall surfaces of ADITYA-U tokamak plasma. Plasma-surface interaction occurs within a few millimeters regions of the adjacent plasma layer from the PFCs. This layer is also known as a sheath. The mechanism is intense within the first few layers of the nanometre range. The processes that take place during PWI take place on different time scales and different length scales as shown in figure 4.1 (Hartwig). In the following sections, the details of several physical and chemical processes for PWI have been discussed.

4.2. Erosion and sputtering processes

Physical or chemical processes that can remove the material surface and their particle during PWI interactions in a tokamak or fusion devices are known as erosion processes. It can be classified into two events. The first one is transient, during which the dense plasma interacts with the material surface in an undesirable fashion and causes macroscopic material loss. The second one is the steady state surface loss, which occurs due to physical and chemical erosion processes at the atomic scale. This second type of event is quite common in the tokamaks and occurs in every fusion device. Transient events cover a wide range of plasma phenomena occurring at a short time-scale length. For example, edge localized modes (ELMs) occur due to the unexpected collapse of pressure gradient produced by the micro instability-driven turbulence. It further leads to huge power loss across the separatrix. From $\sim 2\text{--}6\%$ of the total plasma stored energy, up to 80% of that is being deposited on the divertor PFCs between $0.1 - 1 \times 10^{-3}\text{ sec}$ (Leonard et al.). Plasma disruptions are also another important transient event. This is the process by which the plasma confinement losses suddenly. This leads to the dissipation of plasma stored energy onto a material surface, including vessel-walls and limiter or divertor surfaces. Due to these events, erosion occurs as the melting of the PFCs and the ablation of materials from PFCs. It is a direct macroscopic erosion process. During the erosion process of metal surfaces, other local forces EM, gravitational, and vibrations, also come into the picture and decide the dynamics of the melted portion of metal (Hassanein). The low-Z

graphite material sublimates instead of melting. Also, the rate and magnitude of erosion depend on deposited energy, interaction area, and interaction time (Federici et al.).

Physical sputtering is a steady-state source of erosion of the PFC surface due to the bombardment of highly energetic plasma ions on the surface and transfers its energy to the surface atom. The energy of the incoming particle should be higher than the binding energy of the surface atom. Hence sputtering yield is inversely proportional to the surface binding energy. To reduce the sputtering during PWI, a layer of cold plasma is created between incoming particles and the material surface. This process is the reason for the impurity released and is independent of the chemical property of the material surface. The chemical sputtering occurs when plasma neutral or impurity ion interacts with a limiter or wall surface and forms volatile molecules. However, this is possible with certain combinations between incoming particles and surface atoms, such as CO and CO₂ molecules. Hydrogen can produce a hydrogen-oxygen combination and metal oxides can also be formed. Hydrogen interacts with carbon, which can produce hydrocarbons. The chemical sputtering process depends upon the surface's temperature, the energy of the incoming particle, and the fluxes of the incoming particle.

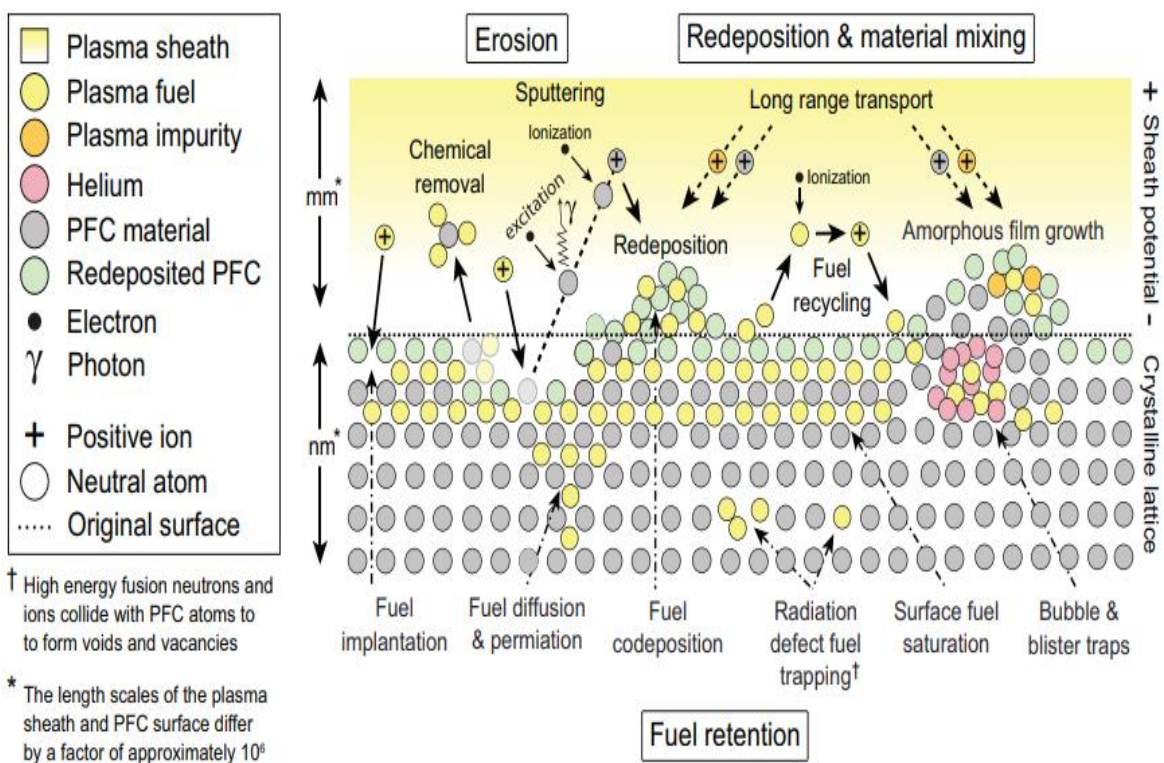


Figure 4.2. Physical and chemical processes occurring during plasma surface interaction, a figure taken from (Hartwig)

Particle transport helps to understand the movement of material species that is eroded from the PFC within the fusion device. Fuel neutrals and impurity ions leave the PFC surface due to the sputtering or desorption process. The charged ions from neutrals are produced through the various atomic and molecular processes as described in Chapter 3. These are mainly electron impact ionization, charge exchange, and dissociation through electrons. The product ions are further subjected to plasma transport, moving towards the core plasma, or returning to the PFC surfaces. This will further be re-deposited on wall surface material. It can be also transported away on other the first wall materials through re-deposition by the particle transport along the magnetic field lines, known as a remote deposition. However, these depositions are functions of temperature gradient forces, plasma flows, and the origin of neutral atoms (limiter, first wall, or divertor)(Stangeby). In the divertor tokamaks, the deposition and erosion are depicted by the migration from the first wall and limiter to the divertor surface. It has already been experimentally studied in the DIII-D, JET, and ASDEX-Upgrade tokamaks with different geometries, PFCs, and sizes (Pitts et al.; Whyte, Coad, et al.).

Further, the different composition of materials then changes the material migration in modern tokamaks. Currently, beryllium, tungsten, boron, molybdenum, and lithium are used at different tokamaks in different regions in the form of coatings or complete materials, this acts as an additional source of the material surface. Eventually, the coating or mixing of different materials can lead to modifications in the sputtering, erosion, fuel retention, recycling, and a lifetime of PFCs. Material mixing also leads to modifying the thermo-mechanical properties of the PFCs due to alterations in their chemical composition and surface morphology (Psoda et al.; Federici).

4.3. Brief description of recycling

Particle confinement time is defined as the time during which a particle remains confined before escaping the confinement region and reaching the wall surfaces. The total time of plasma discharge is much larger, ~ 100 times than the particle confinement time. This means the fuel gets exchanged many times with the material surface during a single plasma discharge. This fuel recycling is essential for global particle balance processes and fuel inventories. When the plasma interacts with the first wall, the bare wall gets loaded with heat and particles. However, due to earlier plasma discharges, some ions were already trapped within the wall being released by the wall, known as the influx to the plasma. Outflux or outflow from the plasma occurs due to the charge exchange neutrals and diffused ions from the plasma are released to the wall. This

process is called recycling, also the ratio of in-flux to outflux is known as the recycling coefficient ($R = \text{influx}/\text{outflux}$). It is estimated with the help of the following formula.

$$\frac{dN_e}{dt} = \eta \Gamma_f + \frac{(R - 1)N_e}{\tau_p} \quad 4.1$$

Here, N_e is the total plasma electron density, η is the fuelling efficiency, Γ_f is the fuelling rate determined through the piezoelectric valve τ_p is the particle confinement time defined as the time taken by the particle to escape the plasma. Fuel recycling and retention can occur due to embedded hydrogen in the material surface reoccurring in plasma through thermally activated diffusion and recombination. Diffusion and trapping of fuel near the surface, diffusion is minimal and trapping is mainly the co-deposition of fuel on eroded material surface forms the mixed material layers (V). Recent measurements on tokamaks have demonstrated that trapped hydrogen isotopes are desorbed from the first wall during a discharge and dominate plasma refuelling (Bauer).

4.4. Experimental arrangement

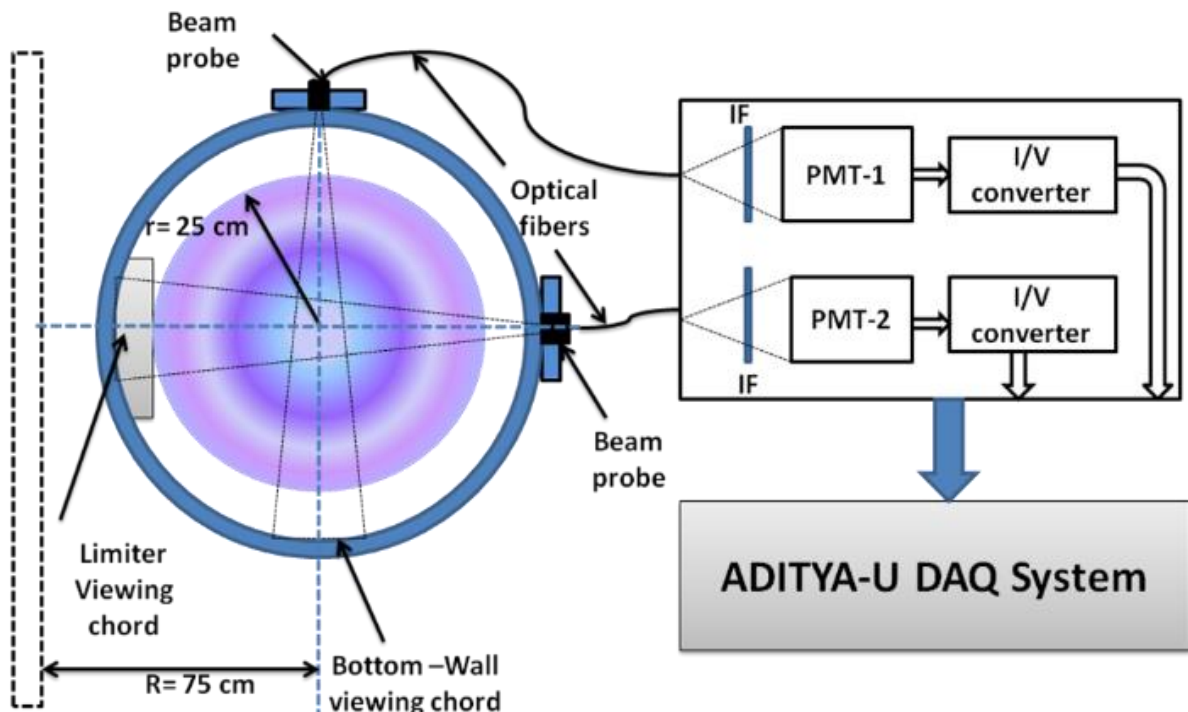


Figure 4.3. The PMT-based experimental setup consists of two sets of PMT, each having three separate PMTs with interference filters for wavelength 656.3 nm, 464.7 nm, and 441.6 nm (total of six PMT). One set collect emissions along the lines of sight terminating on the bottom wall, and another set terminates on the inboard toroidal belt limiter.

In the present experiments, the spectroscopy plasma diagnostic PMT-based setup (section 2.3.3.1) is used to estimate the particle influxes from the stainless-steel (SS) first wall and the graphite limiter surfaces, as shown in Figure 4.3 (YADAVA et al.). The optical arrangement uses optical fiber of 1 mm core diameter with 13 m long optical fiber and collimator one combination (section 2.3.3.5). The LOS is arranged on the top part of the machine, it is terminating on the SS first-wall surface on the bottom (bottom-wall viewing chord) and another LOS is arranged on the radial port of the machine, it is terminating on the graphite limiter surface at the inboard side (limiter viewing chord). Interference filters (IF) for wavelength selection are used at the entrance of the PMT. The output of the PMT is current, which is further converted to voltage through the I/V converter circuit, having a gain of 10^5 . The data is acquired in the ADITYA-U tokamak's data acquisition system as described in Chapter 2. A total of six PMTs are used in the experiment, three for the SS-first wall (H_α at 656.3 nm, O^+ at 441.6 nm and C^{2+} at 464.7 nm) and three for graphite limiters (H_α at 656.3 nm, O^+ at 441.6 nm and C^{2+} at 464.7 nm).

Also, a microwave interferometer is used for chord averaged density estimation. Langmuir probes measure the particle outflux, electron temperature, and density at the plasma edge. The major chord averaged electron density is calculated using a 7-channel microwave interferometer diagnostic. A total 15 numbers of Langmuir probes have been installed into the machine on different radial, poloidal, and toroidal locations. These are made of molybdenum material and have a mushroom shape with a tip diameter of $\sim 4 \times 10^{-3}$ m. The probe is placed at a 0.24 m outboard location for the measurement of particle outfluxes.

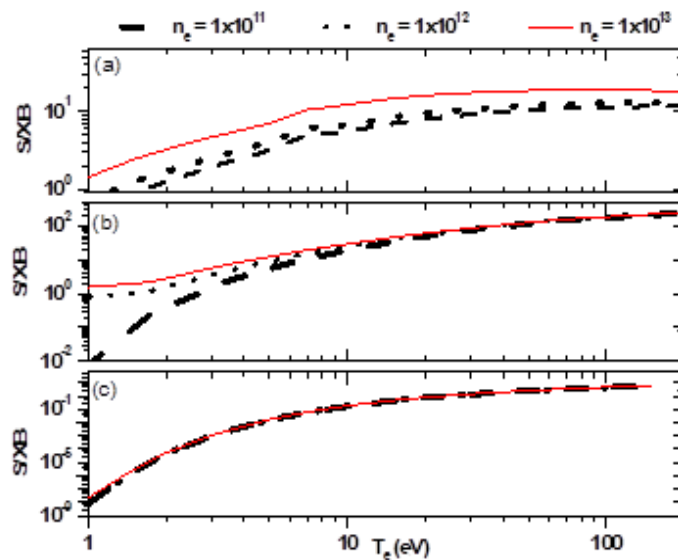


Figure 4.4. The S/XB values for (a) neutral hydrogen neutral, (b) O^+ , and (c) C^{2+} ions when corresponding line emission measured at 656.3, 441.6, and 464.7 nm

4.5. Measurement technique

For the estimation of particle influx, the detected spectral line emissions from an atomic or ionic emitter primarily reside in the plasma edge and emissions are mainly in the visible range. The higher ionization stage of species stays inside the inner region of plasma due to its higher energy. However, these emissions fall in the lower wavelength range due to higher emitter energies. The particle influx in the steady state phase of the plasma operation can be estimated by considering the ionization equilibrium with the measured brightness where the number of ionization events and emitted photons is related (R.C. Isler et al.; K. H. Behringer). The following equation gives the flow rate:(Strangeby and McCracken; Behringer et al.):

$$\Gamma_{particle} = 4\pi \left(\frac{S}{XB} \right) I_{abs} \quad 4.2$$

The S and X represent the effective ionization and excitation rate coefficients. B is the branching ratio of the observed spectral line from an atom or ion. I_{abs} is absolute calibrated brightness or intensity in units of $\text{photon} \cdot \text{m}^{-2} \cdot \text{s}^{-1}$. The values of S/XB ratio for neutral hydrogen, O^+ , and C^{2+} ions for different densities and temperatures are given in Figure 4.4 (a), (b), and (c), respectively. Here S/XB is utilized in the study from the open-ADAS database (Summers). With negligible recombination, the atomic rate coefficient is also required to be approximately constant in the temperature range. Hydrogen neutral and O^+ and C^{2+} have ionization potential having IE of 13.6 eV, 35.1 eV, and 47.8 eV, respectively. The low ionization energy atoms and ions remain in the radial thin shell in the plasma edge. If the S/XB becomes almost independent of electron temperature it can be used for the influx estimation. The S/XB values in this study are considered at $1 \times 10^{18} \text{ m}^{-3}$ electron density and 10 eV electron temperature for H_α and O^+ (edge plasma parameters of ADITYA-U tokamak). However, for C^{2+} an ion, the S/XB is used at the temperature of 20 eV, but at with same electron density. The estimation of influx is described by equation 4.4. The total integrated influx per sec is estimated by multiplying the influxes with the effective surface area, 2 m^2 for limiter and 5.4 m^2 for a functional wall area exposed to plasma other than the limiter.

The particle confinement time of the plasma can be obtained through the ratio of total particle content inside the plasma and outflux of the ions and is defined by (Strangeby and McCracken; Rowan et al.).

$$\tau_p = \left(\frac{N}{\phi} \right) \quad 4.3$$

Here N stands for the total fuel particle content of the plasma, and ϕ is the total outflux of the fuel ions. In the steady state phase of the discharge, the outflux can be considered the same as the neutral influx. The particle confinement has been estimated in the present work from the available single-chord measurement of n_e and by considering particle influxes obtained from LOS terminating on the graphite limiter and SS bottom wall surfaces. The above Equation of particle confinement time was rewritten in terms of working relationship by assuming the parabolic profile of n_e and experimentally measured chord averaged and edge n_e . Also, the influx measurements for fuel-hydrogen and carbon and oxygen impurity ions have been done for GDC and GDC with Li coating wall conditioning.

From the estimated particle influx, the recycling coefficient, which is the ratio of particle influx by outflux, has also been measured. The outflux has been estimated from the probe measurement. As the radial transport in the plasma edge is dominated by fluctuation-driven transport, the radial drift of the particle can be obtained from the low-frequency fluctuation in a poloidal electric field. When the radial drift velocity is correlated with electron density fluctuation, the radial particle flux(Wootton et al.; Levinson et al.) can be written as:

$$\Gamma_{out} = \langle n_e v_r \rangle \quad 4.4$$

where n_e and v_r are the DC components of electron density and the radial drift velocity. In ADITYA-U tokamak, the density measurement through the Langmuir probe is available, but the radial velocity measurement is currently not available. With similar plasma parameters in ADITYA tokamak, Jha et al. (Jha et al.) carried out experiments to measure the radial velocity, and its maximum value was found to be 2 km/s. This value of v_r is taken here for the estimation of particle outflux.

4.6 Plasma discharge and typical plasma parameters

The spectral line emissions by neutrals and impurities were measured in several discharges. One of these plasma discharges, having shot #33821, is given in Figure 4.5. It has a plasma current of $I_p \sim 87$ kA and a plasma duration of ~ 102 ms. Figure 4.5 (b), (c), and (d), show the temporal evolution of H_α and line emission at 441.6 nm from O^+ and at 464.7 nm from C^{2+} ions, respectively. Black dot lines represent the signal collected from LOS terminating on the SS

wall material surface, and a solid red line represents the signal collected from the LOS terminating on the graphite limiter surface. H_{α} intensities and impurities signals signify the behaviour of neutral hydrogen and impurities species during various phases of the discharge, such as the initiation phase having the ionization of bulk hydrogen and impurities, the current rise phase having significant interaction of plasma with wall and limiter steady state phase dominated by almost regular recycling of hydrogen and impurities influxes, disruption and termination of the phase of plasma with the sharp spike in signals. To carry out the statistical analysis of the particle influxes, many discharges operated with $B_T \sim 1.1$ T at the device center have been analyzed where plasma duration was more than 100 ms and $I_P \sim 78 - 84$ kA. Plasma electron density varied between $2 - 3.5 \times 10^{19} \text{ m}^{-3}$. The experiments are carried out with GDC wall-conditioning, as mentioned in section 2.2.6, and with Li coating in addition to GDC. Results described in sections (4.7 & 4.8) are with GDC wall conditioning, and section 4.9 contains the results with Li coating wall-conditioning.

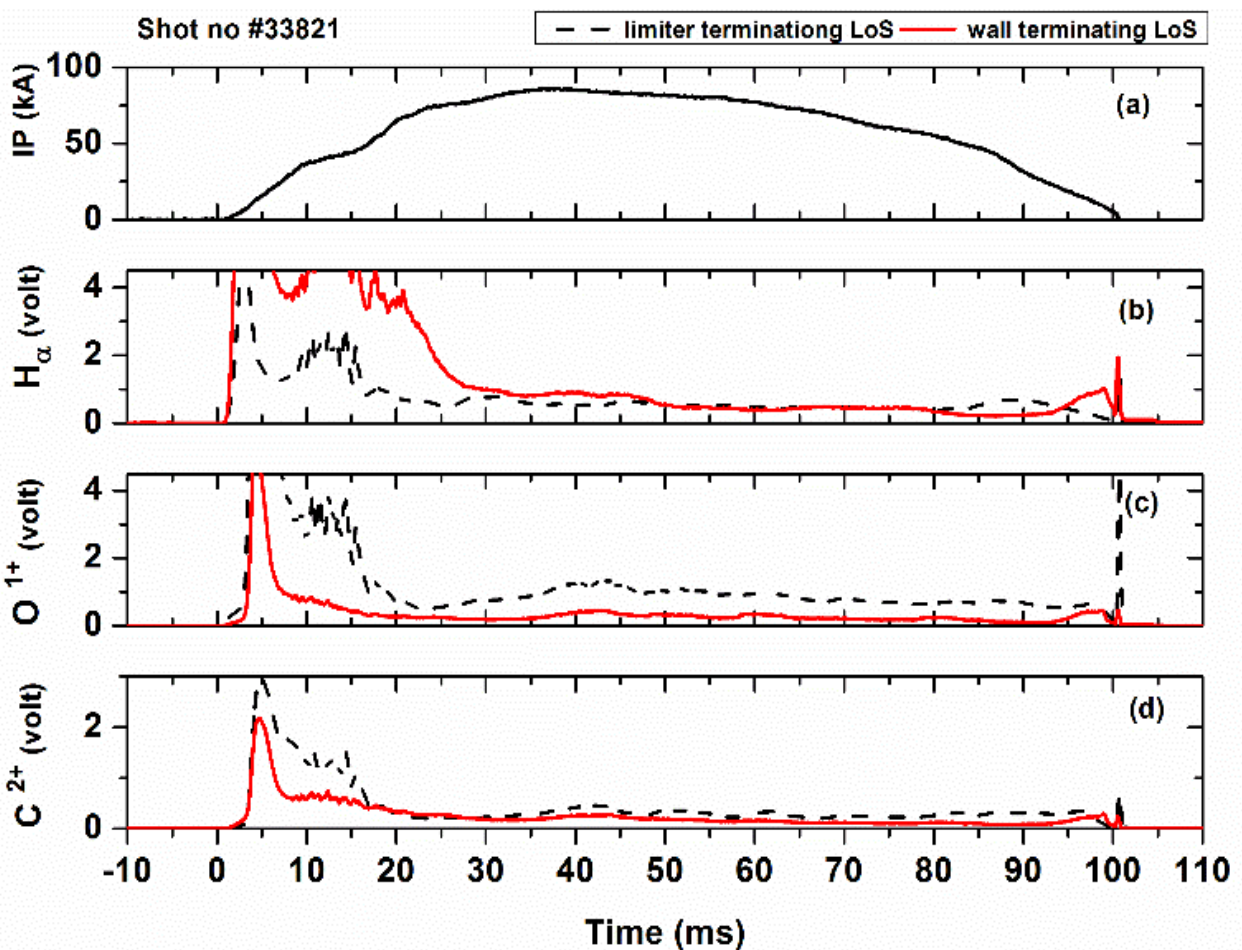


Figure 4.5. Temporal evolution of (a) plasma current I_P , (b) H_{α} at 656.28 nm, (c) spectral line at 441.6 nm (mentioned as OII) from O^+ , and (d) line at 464.7 nm (mentioned as CIII) from C^{2+} ions. The dashed black and solid red lines represent the signals recorded from two different LOS terminating on the limiter and bottom wall, respectively. 4.7. Estimation of particle confinement and recycling coefficient

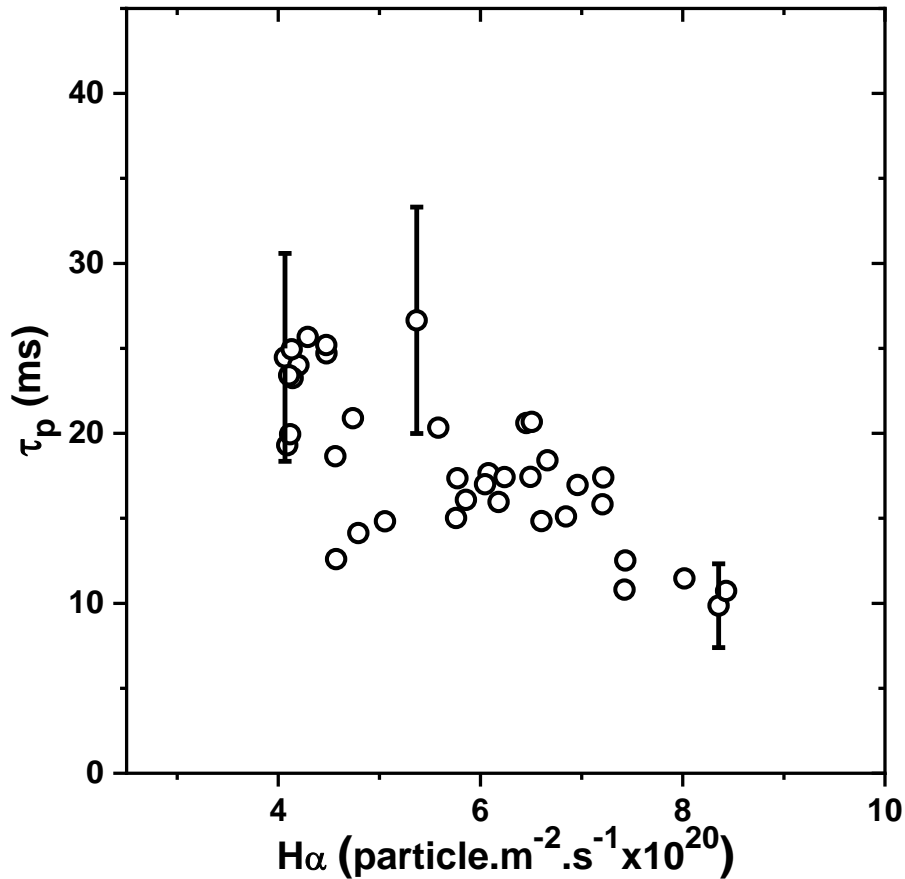


Figure 4.6. Change in particle confinement time, τ_p with hydrogen influx (Γ_H)

Using equation 4.5, the particle confinement time has been estimated by taking the ratio of total particle content in the plasma with the number of particles coming to the SS wall surface. For this measurement, the particle influxes from both LOS terminating on the limiter and bottom wall have been included to get the total particle influxes, and analysis has been done during the current flat top phase and considering the particle outflux is the same as the influx. The particle confinement time lies in the range of 5 – 25 ms, as shown in Figure 4.6. It can be seen from the figure that particle confinement times are higher with lower hydrogen influxes. This indicates that plasma confinement becomes higher with lower recycling, as observed in many tokamaks (Stangeby and McCracken; Whyte, Lipschultz, et al.; Jha et al.).

The hydrogen neutral particle influxes have also been used for the approximate estimation of the recycling coefficient, and the outflux has been measured using the Langmuir probe as per the technique discussed in section 3. As the measurement from the array of Langmuir probe array placed at various radial locations of the plasma edge was not available during this experiment, a constant value of radial velocity has been taken for the estimation of particle outflux. Figure 4.7 shows the estimated recycling coefficient for the shots having numbers from

#31000 to #31600. The values of the recycling coefficient vary between 0.6 – 1.4. Although the data is quite scattered in nature, still a definite trend is visible that it is gradually increasing with the shot numbers.

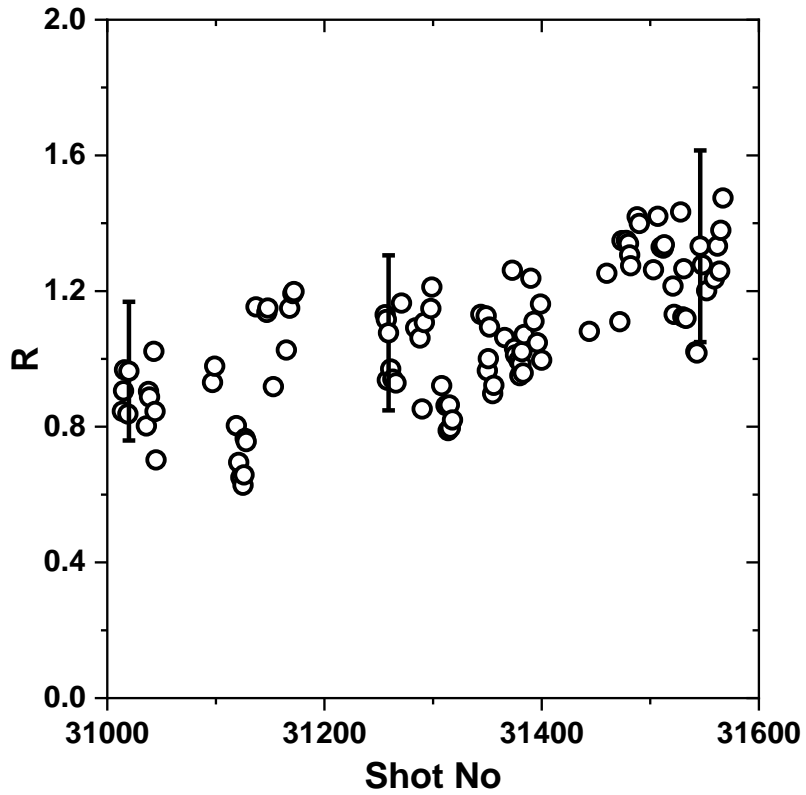


Figure 4.7. The recycling coefficient, R , with respect to plasma shots number.

The scattering and considerable variation might be related to the use of constant values of radial velocity in the estimation of particle outfluxes. It is seen at the beginning of the campaign when the machine was clean. The recycling coefficient has values less than one indicating plasma-facing components (PFC) acting as sinks. With the progress of the plasma operation in time, PFC gets contaminated due to the absorption of plasma particles, and the recycling coefficient value increases and reaches its maximum value of ~ 1.4 , and one can say that now PFC is acting as a source. A similar observation has been made in many tokamaks (Michelis and Mattioli; Wagner) and even in single discharge during the long pulse operation of TRIAM-1M (Sakamoto et al.) and HT-7 (Juan et al.) tokamaks, where wall acting as both source and sink has been observed.

4.8. Behaviour of neutral and particle influxes in discharge produced after GDC

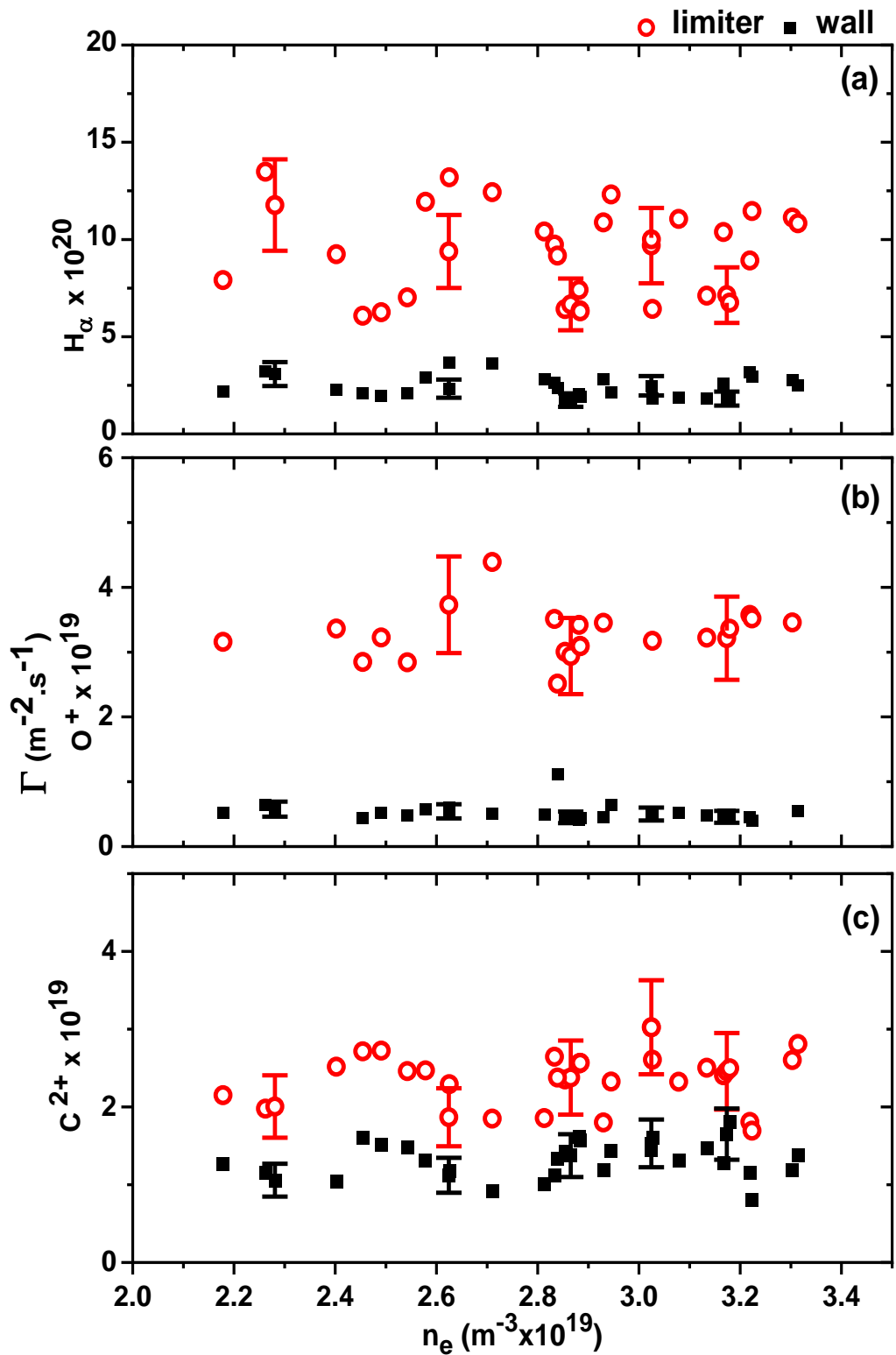


Figure 4.8. Particle influxes of (a) neutral hydrogen, (b) oxygen impurity ion, and (c) carbon impurity ion. The red circle and black square represent the influxes measured along the LOS terminating on the limiter and bottom wall, respectively.

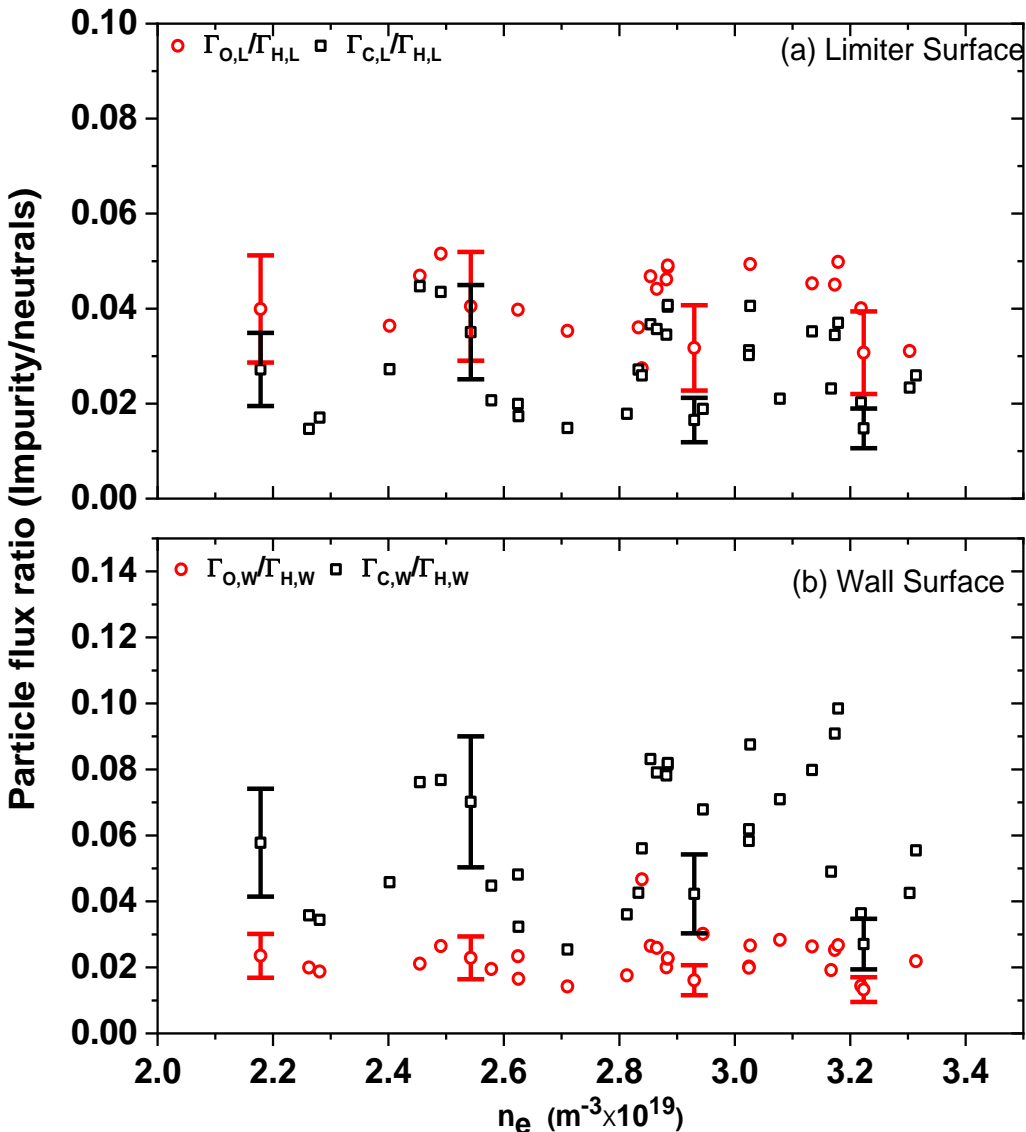


Figure 4.9. The ratio of impurities influxes with neutral hydrogen influxes for the LOS terminating on (a) limiter (b) bottom wall

Particle influxes of neutral hydrogen, oxygen impurity ion, and carbon impurity ion have been estimated using the measurement along the LOS terminating on the limiter and bottom wall, respectively. As shown in Figure 4.8 (a), the influx of the neutral particles measured for LOS terminating on graphite limiter is $\sim 8 - 12 \times 10^{20}$ particle $\cdot m^{-2} \cdot sec^{-1}$. The influx measured along the LOS terminating on the bottom wall surface is $2 - 4 \times 10^{20}$ particle $\cdot m^{-2} \cdot sec^{-1}$. It is clear from this measurement that graphite limiter contributes 6 – 8 times higher hydrogen influx than the SS wall surface. However, the integrated influx estimation over a total surface area is given in table 4.1, the integrated influx contributions from the graphite limiter and SS surface are $16 - 24 \times 10^{20}$ particle/sec and $10 - 22 \times 10^{20}$ particle/sec respectively (YADAVA et al.). This comparable integrated influx indicates that the wall also plays a

significant role in introducing the neutral particles in ADITYA-U tokamak. Similar observations were made on other tokamaks. It indicates that the first wall plays a vital role in particle balance and recycling processes by introducing an almost equal amount of particles compared to the limiter surface(Stangeby and McCracken; Juan et al.; R.C. Isler et al.; Stott et al.). For example, the Beryllium rail limiter at ISX-B tokamak is present, and total integrated flux estimation from the first wall is found to be three times the limiter surface (R.C. Isler et al.).

Figure 4.8 (b) illustrates the particle influx estimation for O^+ impurity ion. The estimation of flux terminating on the graphite limiter surface is $\sim 2.5 \times 10^{19} \text{ particle} \cdot \text{m}^{-2} \cdot \text{sec}^{-1}$ and the flux from the surface terminating on the wall surface is $\sim 0.6 \times 10^{19} \text{ particle} \cdot \text{cm}^{-2} \cdot \text{sec}^{-1}$. From this, it is clear that graphite limiter flux is ~ 4 times higher than the SS wall surface. At the same time, the integrated particle flux measurement from the graphite limiter and SS wall contributes $\sim 5.5 \times 10^{19}$ particles/sec and $\sim 2.7 \times 10^{19}$ particles/sec, respectively. Hence it is said that the graphite limiter is a major source of oxygen impurity for ADITYA-U tokamak plasma. For carbon impurity, the estimated limiter influx is $\sim 1.9 \times 10^{19} \text{ particle} \cdot \text{m}^{-2} \cdot \text{sec}^{-1}$ and particle influx from the LOS terminating on the SS bottom wall is $\sim 1.6 \times 10^{19} \text{ particle} \cdot \text{m}^{-2} \cdot \text{sec}^{-1}$ as shown in Figure 4.8 (c). It means the particle influx from the LOS in ADITYA-U tokamak is similar. However, the integrated influx estimation of carbon ions from the limiter and wall surfaces is given in Table 4.1, it is seen that the graphite limiter contributes $\sim 3.8 \times 10^{19}$ particles/sec and the SS wall contributes slightly higher particles, $\sim 8.1 \times 10^{19}$ particles/sec . This flux measurement on ADITYA-U tokamak is also summarised in Table 4.1. The ratio of impurities influxes from different surfaces concerning hydrogen influxes of those surfaces is determined and presented in Figure 4.9. The ratio of oxygen influx to the hydrogen from the limiter is $\Gamma_{O,L}/\Gamma_{H,L} \sim 4\%$ (as shown in Figure 4.9 (a) with red circles) while the same ratio from the wall surface $\Gamma_{O,W}/\Gamma_{H,W} \sim 2\%$ (as shown in Figure 4.9 (b) with red circles). In the same way, the ratio of carbon influx to the hydrogen from the limiter, $\Gamma_{C,L}/\Gamma_{H,L} \sim 2\%$ as shown in Figure 4.9 (a) with black squares, while the same ratio from the wall surface $\Gamma_{C,W}/\Gamma_{H,W} \sim 4 - 6\%$ as shown in Figure 4.9 (b) with black squares. This ratio of influxes can be considered as the indicative value of impurity concentration at the plasma edge. Then it can be stated that the concentration of carbon and oxygen impurities in ADITYA-U tokamak is almost similar to those found in ADITYA tokamak through both spectroscopic estimations (M. B. Chowdhuri, Ghosh, et al.; M. B. Chowdhuri, Manchanda, Ghosh, Bhatt, et al.) and modelling ADITYA tokamak plasma by TSC code (Bandyopadhyay et al.).

Table 4.1 Summary of measured influxes from different LOS and integrated influx per sec

Species	Influx when LOS terminates on a limiter (particle/m ² ·sec)	Influx when LOS terminates on the bottom wall (particle/m ² ·sec)	Integrated influx per sec when LOS terminating on a limiter	Integrated influx per sec when LOS terminating on the bottom wall
H	9.17×10^{20}	2.38×10^{20}	1.83×10^{21}	1.28×10^{21}
O ⁺	2.51×10^{19}	0.6×10^{19}	5.50×10^{19}	2.70×10^{19}
C ²⁺	1.9×10^{19}	1.67×10^{19}	3.80×10^{19}	9.00×10^{19}

4.9. Behaviour of neutral hydrogen and impurity influxes in discharge produced after GDC with Lithiumization

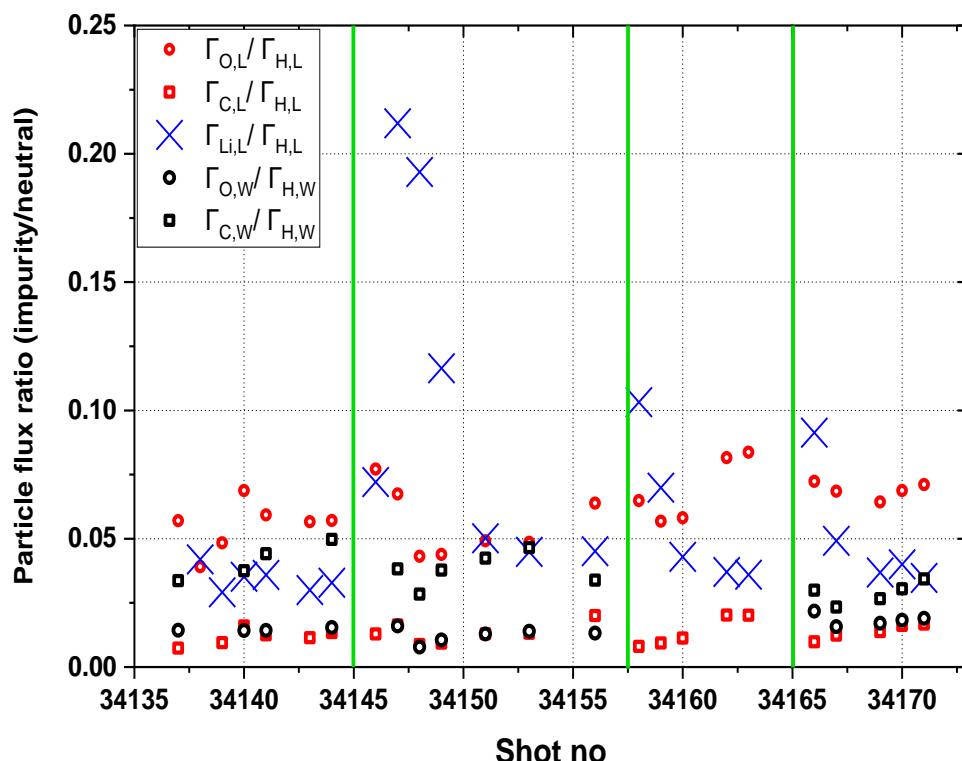


Figure 4.10. Variation in flux of hydrogen neutral and carbon, oxygen impurity ion emissions

The behaviour of the influx of hydrogen and O^+ and C^{2+} is studied for the plasma with modified wall conditioning. The GDC + Li coating is done many times in the evenings via different techniques to coat the PFC and wall with Li and the voltage of GDC was also varied. However, the Li-rod technique was found to be more efficient (K. A. Jadeja et al.). Figure 4.10. represents the variation in PMT-based measured Li, H_α , O^+ and C^{2+} emissions, blue cross marks in the figure represent the Li emission at 670.8 nm. The maximum lithiumization was done before shot #34148. Here the quantity of Li is ~ 80 mg with Li evaporation along with 2 hrs of GDC (see section 2.2.6 for details of Lithium coating). In Figure 4.11, it was observed that there is a reduction in H_α , O^+ and C^{2+} emissions with the increase in neutral Lithium emission. However, the reduction of emissions in terms of percentages is different. Hydrogen reduces by 60% and 30% from Limiter and wall surfaces respectively due to Li coating. Similarly, there has been a reduction in oxygen emission by 80% and 50% from limiter and wall surfaces. But there is the same percentage of reduction in the carbon ion emission from both limiter and wall surfaces; both are reduced by 50% due to Li coating. Hence it is seen that Li coating acts more effectively on oxygen released from the limiter surface. Also, all emissions along LOS viewing the limiter are reduced more significantly than those along LOS viewing the wall surface. The same has been tabulated in Table 4.2.

The influxes for the same have been estimated through equation 4.4. As shown in Figure 4.12 (a), the hydrogen influx of the neutral particles measured for LOS terminating on graphite limiter is $\sim 1.29 \times 10^{21}$ particle $\cdot m^{-2} \cdot sec^{-1}$. The average influx measured along the LOS terminating on the bottom wall surface is 5.50×10^{20} particle $\cdot m^{-2} \cdot sec^{-1}$. It is clear from this measurement that graphite limiter contributes ~ 20 times higher hydrogen influx than the SS wall surface. The integrated influx estimation over the total surface area is given in Table 4.2., here it is seen that the integrated influx contributions from the graphite limiter and SS surface are 2.57×10^{21} particle/sec and 3.19×10^{21} particles/sec, respectively. It is also that hydrogen fuel influxes increase in this condition as compared to the previous measurements, which were done only with GDC wall conditioning.

Table 4.2. Reduction in the emissions from Graphite limiter and SS wall surfaces

Reduction in emission	$H\alpha$ 656.28nm	O^+ 441.2 nm	C^{2+} 464.7 nm
Limiter	60 %	83 %	50 %
Wall	30 %	50 %	50 %

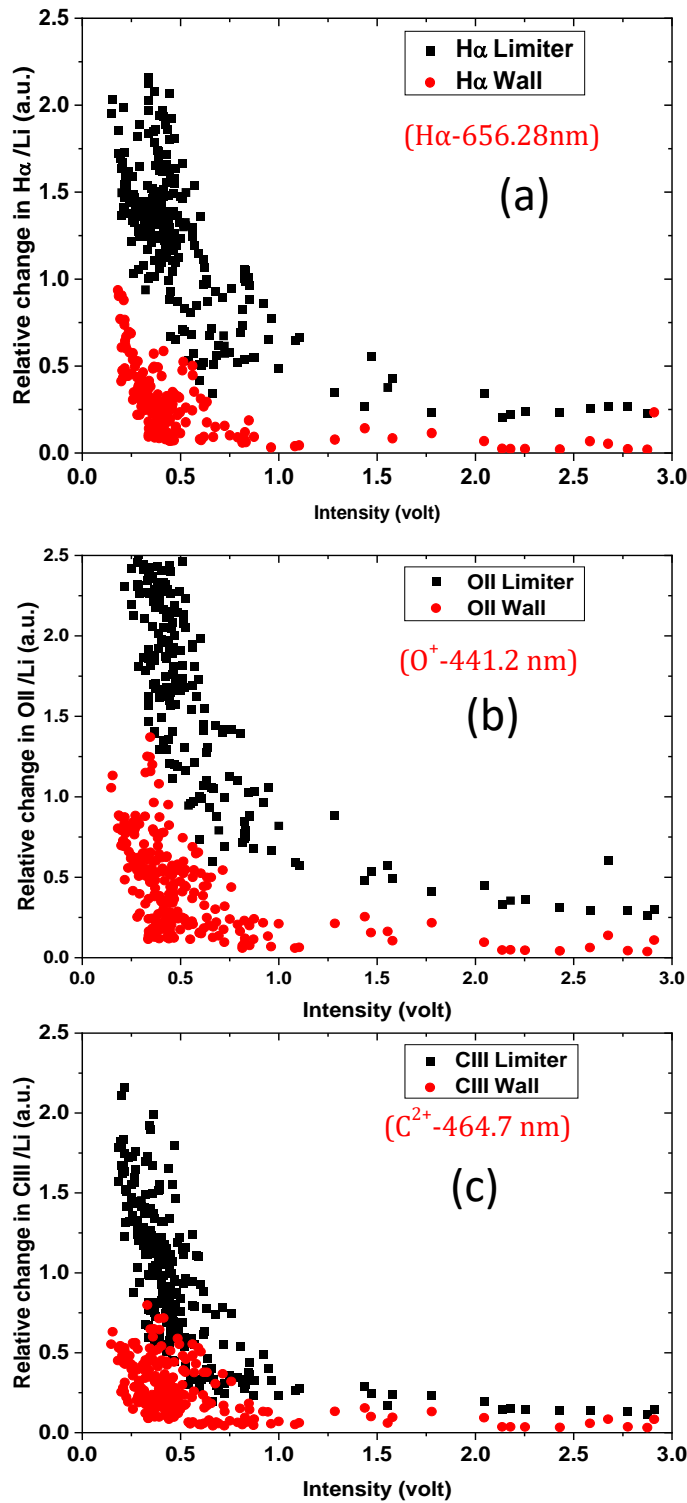


Figure 4.11. Relative change in neutral and impurity emissions with lithium emission

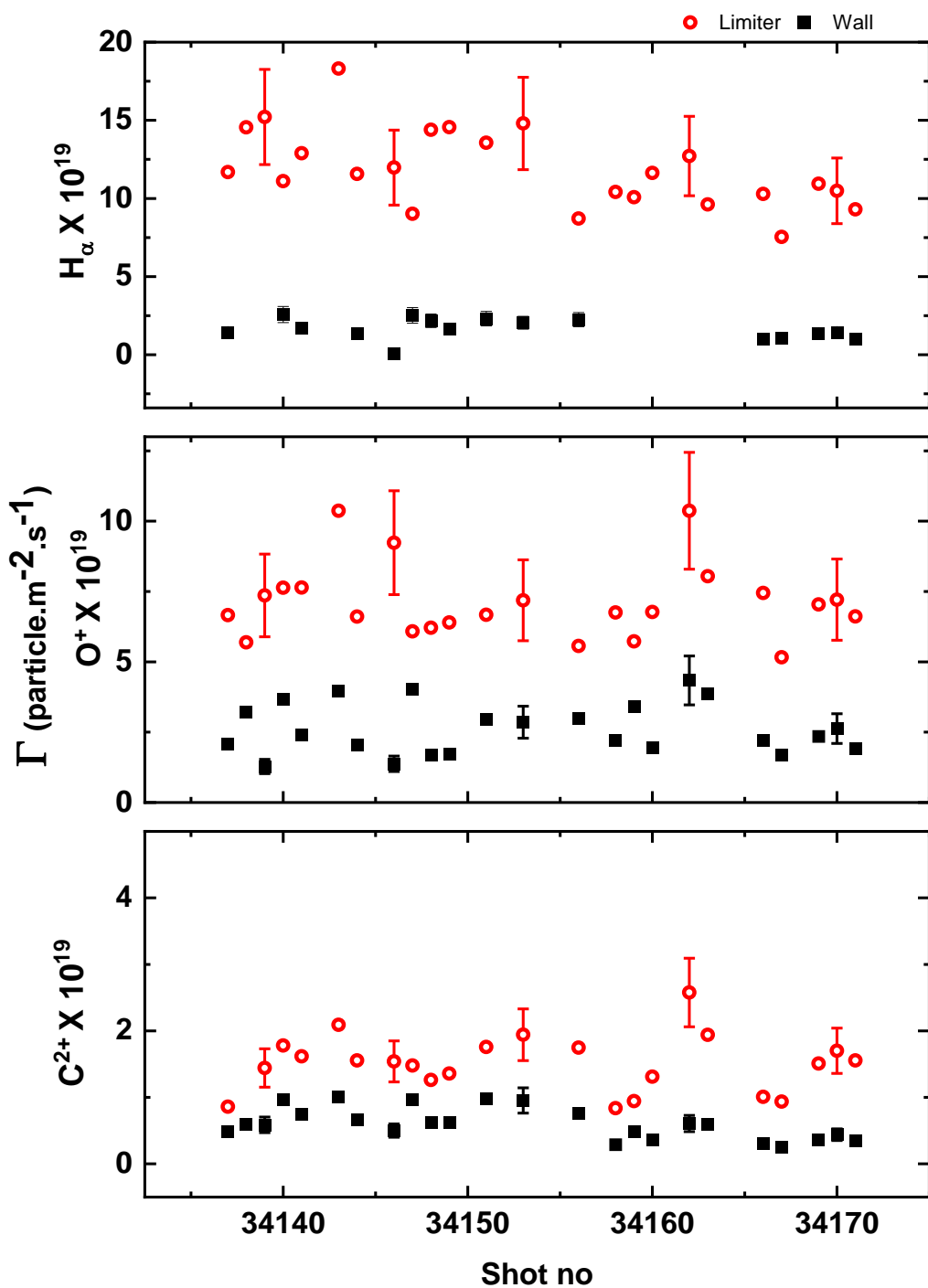


Figure 4.12. Particle influxes of (a) neutral hydrogen, (b) oxygen impurity ion, and (c) carbon impurity ion. The red circle and black square represent the influxes measured along the LOS terminating on the limiter and bottom wall, respectively.

Table 4.3. Summary of measured influxes from different LOS and integrated influx per sec

Species	Influx when LOS terminates on a limiter (particle/m ² ·sec)	Influx when LOS terminates on the bottom wall (particle/m ² ·sec)	Integrated influx per sec when LOS terminating on a limiter	Integrated influx per sec when LOS terminating on the bottom wall
H	1.29×10^{21}	5.50×10^{20}	2.57×10^{21}	3.19×10^{21}
O ⁺	6.79×10^{19}	3.00×10^{19}	1.36×10^{20}	1.74×10^{20}
C ²⁺	1.64×10^{19}	0.86×10^{19}	3.28×10^{19}	3.94×10^{19}

For O⁺ impurity ion particle influx as shown in Figure 4.12 (b), the average value of the influx terminating on the graphite limiter surface is $\sim 6.79 \times 10^{19}$ particle · m⁻² · sec⁻¹ and the influx from the surface terminating on the wall surface is $\sim 3.00 \times 10^{19}$ particle · m⁻² · sec⁻¹. From this, it is clear that graphite limiter flux is ~2 times higher than the SS wall surface. These factor differences between a limiter and wall impurities were double in the previous study with GDC only. The integrated particle flux measurement from the graphite limiter and SS wall contributes $\sim 13.58 \times 10^{19}$ particles/sec and $\sim 17.4 \times 10^{19}$ particles/sec, respectively. Hence, graphite limiter is no more a bigger oxygen impurity source for ADITYA-U tokamak plasma with Lithium coating. For carbon impurity, the estimated limiter influx is $\sim 1.64 \times 10^{19}$ particle · m⁻² · sec⁻¹, and particle influx from the LOS terminating on the SS bottom wall is $\sim 0.86 \times 10^{19}$ particle · m⁻² · sec⁻¹, as depicted in Figure 4.12 (c). It means the carbon impurity influxes from limiter LOS is more compared to the wall. Integrated influx estimation of carbon ions from the limiter and wall surfaces is given in Table 4.3. The graphite limiter contributes $\sim 3.2 \times 10^{19}$ particles/sec and the SS wall contributes slightly higher particles, $\sim 3.9 \times 10^{19}$ particles/sec. The carbon integrated fluxes are almost similar from both surfaces in lithium coating wall conditioning. These results have been summarised in Table 4.3.

The ratio of impurities influxes from different surfaces concerning those surfaces' hydrogen influxes is determined and presented in Figure 4.13. The ratio of oxygen influx to the hydrogen from the limiter is $\Gamma_{O,L}/\Gamma_{H,L} \sim 5\%$ (as shown in Figure 4.13 (a) with red circles) while the same ratio from the wall surface $\Gamma_{O,W}/\Gamma_{H,W} \sim 2\%$ (as shown in Figure 4.13 (b) with red circles). In

the same way, the ratio of carbon influx to the hydrogen from the limiter, $\Gamma_{C,L}/\Gamma_{H,L} \sim 1 - 2 \%$ as shown in Figure 4.13 (a) with black squares, while the same ratio from the wall surface $\Gamma_{C,W}/\Gamma_{H,W} \sim 4 - 6 \%$ as shown in Figure 4.13 (b) with black squares. This influx ratio can be considered the indicative value of impurity concentration at the plasma edge.

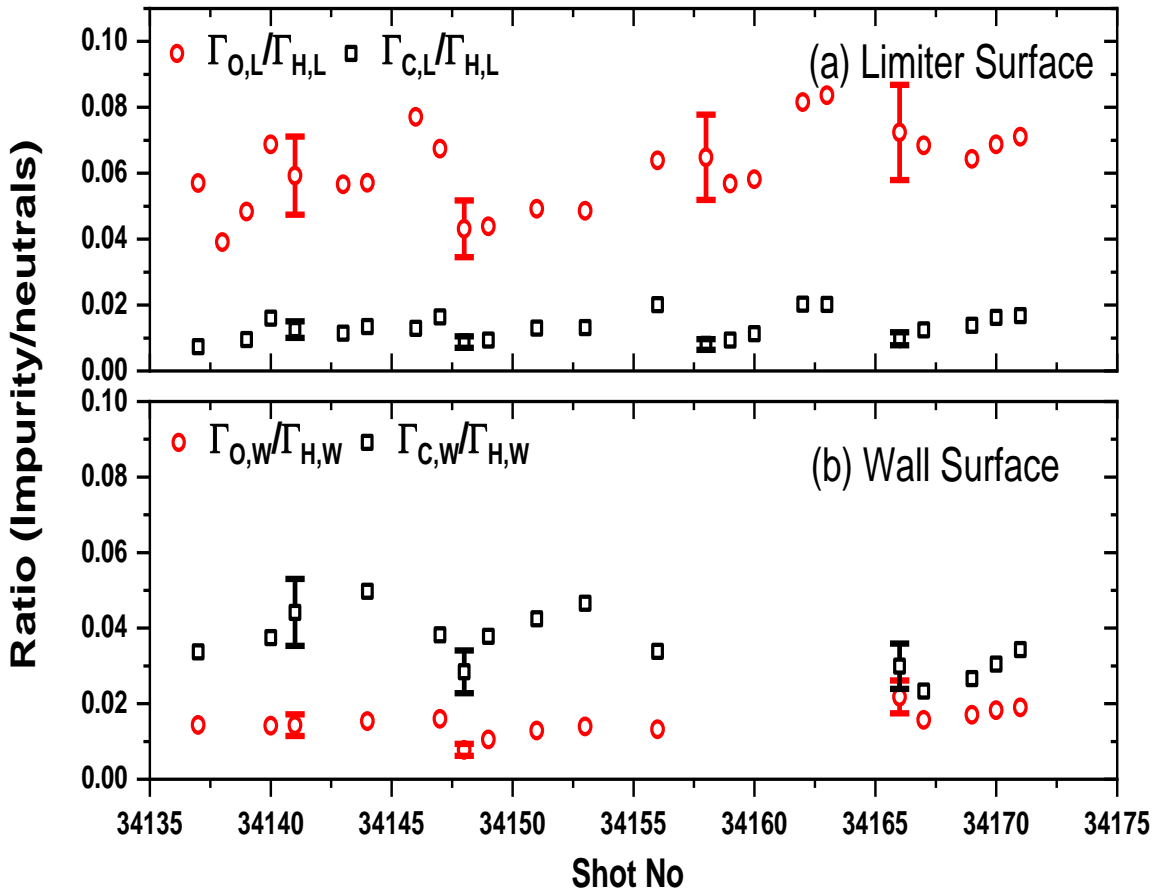


Figure 4.13. The ratio of impurities influxes with neutral hydrogen influxes for the LOS terminating on (a) limiter (b) bottom wall

4.10. Summary

A detailed investigation of influx measurement has been carried out on ADITYA-U tokamak when operated with the limiter. Two sets of spectroscopic diagnostics, each having three channels, based on optical fiber, interference filter, and PMTs, have been used to measure the visible spectral lines of neutral hydrogen, carbon, and oxygen ions along the two LOS terminating on the graphite limiter and SS bottom wall.

The particle confinement time is also measured using central line averaged electron density and by considering both hydrogen influxes obtained from the LOS terminating on both the limiter and bottom wall. The values come in the range of 5 to 25 ms. The increase of particle

confinement time with decreasing hydrogen influxes suggests better plasma confinement when particle recycling is reduced. The initial measurement of the recycling coefficient suggests that the machine acts as a sink at the beginning of the experimental campaign while it starts to act as a source later days of the campaign.

The particle influxes and integrated influxes have been estimated from the measurement of H_α emission at 656.3 nm, and it is seen that the contribution of hydrogen integrated influx from the limiter and wall are almost similar in GDC wall conditioning it is $\sim 10 - 24 \times 10^{20}$ particle/sec (YADAVA et al.). The oxygen influx has been estimated by monitoring the spectral line at 441.6 nm from O⁺ ions. It is found that the limiter surface contributes moderately higher oxygen impurity influxes than that from the wall. The particle influx of carbon, estimated through monitoring the spectral line at 464.7 nm of C²⁺ ions are almost similar in both LOS terminating on the wall and limiter. It can be stated that the obtained results provide essential information for a comprehensive understanding of particle controls to achieve further improved operation of the ADITYA-U tokamak. In the future, this study will be further extended during the operation of the ADITYA-U tokamak plasma in divertor configuration. During lithium coating along with GDC the estimated influx reduces for each species. However, percentage of reduction is different for each species. Oxygen emission is reduced by 50% from the wall and 83% from the limiter surface with increased Li emissions. Then hydrogen emission reduces by 30% from the wall and 60% from the limiter surface. The carbon emission shows an equal reduction from both surfaces by 50%.

Chapter 5. Neutral and impurity transport studies on ADITYA-U Tokamak

5.1. Theory of particle transport in Tokamak plasmas

Plasma particles move along the magnetic field lines and they have also a gyration motion with a Larmor radius $\rho_L = mv_\perp/qB$ with the direction perpendicular to the magnetic field. If no collisions are present in plasmas, the displacement of the particle will be in the direction of a magnetic field. There is no displacement in a perpendicular direction to the magnetic field in plasma, hence no perpendicular transport in the straight field lines. With collisions present in plasma particles, it leads to diverting the trajectory of particles in perpendicular to the magnetic field direction. The particle gets displaced in the perpendicular direction in order proportional to ρ_L . The time between two collisions can be defined by $1/\nu$, where ν is the collision frequency (this can be explained by the random walk problem). The diffusion coefficient is defined by the following Equation

$$D = \rho_L^2 \nu \quad 5.1$$

When plasma is fully ionized, the ion-ion and electron-ion collisions are dominant. The transport due to the collisions between particles is known as “classical transport”. In tokamak plasma, losses involved with the classical transport are not of concern due to its small contribution. However, due to the drift in tokamak plasma because of inhomogeneity in the magnetic field, the displacement of particles increases significantly than ρ_L . Hence the diffusion coefficient becomes considerably higher. The neoclassical transport theory is proposed to

understand the contribution of magnetic field shape and nature in particle diffusion. However, the experimental observations of diffusion won't match with either classical or neoclassical transport theory. Then anomalous transport has been introduced further. In the next section, a brief overview of different transport mechanisms has been given.

5.2. Classical, neoclassical and anomalous diffusion

To understand the evolution of plasma particle density on the transport time scale, the fluid theory is used. One dimensional radial transport equation for bulk plasma particle is given by the following particle balance equation:

$$\frac{\partial n_e}{\partial t} = -\nabla \vec{\Gamma} + Q \quad 5.2$$

Here n_e is the plasma electron density, $\vec{\Gamma}$ is the particle flux density and Q represents the source and sink terms which include ionization, recombination, and charge exchange processes. The $\vec{\Gamma}$ can be derived by diffusivity and convective velocities, which are given by:

$$\nabla \vec{\Gamma}(r, t) = -D(r) \vec{\nabla} n(r, t) + n(r, t) \vec{V}(r) \quad 5.3$$

v represents the convective velocity also called pinch velocity. D is the diffusion coefficient. D has a positive value, however, V can have positive and negative values, saying outward and inward convective flux, respectively. During steady-state plasma operations the rate of change in density $\frac{\partial n_e}{\partial t} = 0$, also source and sink are equal with $Q = 0$. Hence,

$$\frac{\vec{\nabla} n}{n} = \frac{\vec{V}}{D} \quad 5.4$$

With negative convective pinch velocity, the density profile is peaked at the center with a density gradient negative. With positive pinch velocity the density profile peak in the edge (hollow profile). Then, it is important to study the diffusivity and convective velocity profiles for every device.

In the non-uniform toroidal magnetic field in the poloidal plane, or the field with a large aspect ratio. There is a variation in the toroidal field is $B \cong B_0 \left(1 - \frac{r}{R} \cos\theta\right)$. The B_{\max} is at the inboard side and B_{\min} at the outboard side. The relation between particle energy is E and magnetic moment $\mu = \frac{mv_\perp^2}{2B}$, with B magnetic field and kinetic energy (E_k) of a particle in the

perpendicular direction $E_k = \frac{1}{2}mv_\perp^2$. When particles have $E > \mu B_{\max}$ it will pass and be known as a passing particle, however particles with $E < \mu B_{\max}$ are get reflected by the high magnetic field and trapped inside it. The motion of trapped particles is known as the “banana” shaped trajectory. The particle in this orbit becomes trapped and un-trapped to consecutive banana orbits. The displacement of the particle changes from ρ_L to the width of the banana orbit, i.e., the step is larger. As a result, the diffusion coefficient increases, and this diffusion is known as “neoclassical diffusion”. The neoclassical diffusivity derivations involve detailed calculation and it is not the scope of this work. However, it can be understood in terms of the collisionality parameter which is defined as $v^* = \frac{v}{\omega_{be}} = \frac{v_{ei}qR}{\epsilon^{3/2} v_{th}}$, where ω_{be} is the bounce frequency of electrons in banana orbit, v_{ei} is electron-ion collision frequency, R is the major radius, v_{th} is the thermal velocity, ϵ is the aspect ratio $(\frac{r}{R})$ and q is the safety factor. The variation in diffusivity can be described in Figure 5.1(Shaing et al.). When $v^* < 1$, the particle is said to be within the “banana regime”. In this regime, the D and v^* has linear dependence. The particle collisions are sufficient to overcome trapping, the particles in the low magnetic field region are described by $v^* > \epsilon^{-3/2}$, it is said to be in the “Pfirsch-Schlüter regime”. The increased v^* further has linear increase relation with D . The intermediate regime is the “plateau regime”, in this case, the particle changes its trapped orbits before producing coulomb scattering. The diffusion coefficient is independent of collisionality within this regime. Overall, in all the regimes of neoclassical diffusion, the diffusivity is higher than the classical diffusion. The classical, Pfirsch-Schlüter and banana-plateau flux and their diffusivity are tabulated in table 5.1, as per details given in (Wenzel et al.; Dux and Peeters).

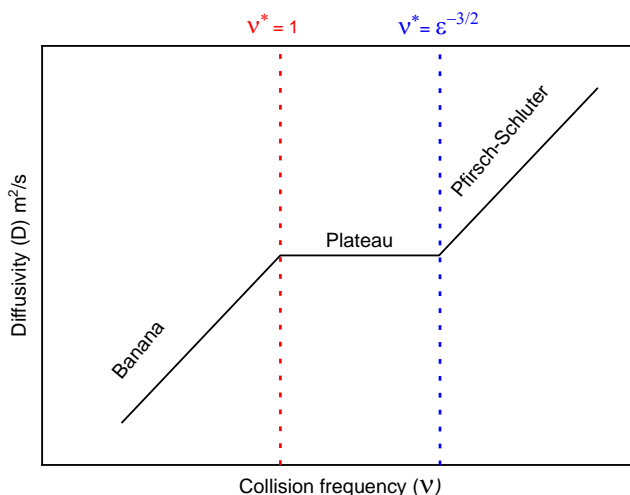


Figure 5.1. Variation in diffusion coefficient with collision frequency and different plasma regions

The experimentally observed diffusivity is usually large due to several physical phenomena, including instabilities, magnetic field, and electric field fluctuations. This is called “anomalous transport”. The anomalous transports through the physical displacement of plasma on a scale larger than the Larmor radius are called macroscopic instabilities, and described by the magneto-hydrodynamics theory. These are mainly the ideal and resistive ballooning modes, kink instabilities, tearing modes, and sawtooth and edge localized instabilities. The small fluctuations created by electric or magnetic fields give rise to changes in the particle’s velocity and radial position. Here, the length of change in displacement is smaller than the Larmor radius, it is called microscopic instabilities. This occurs due to destabilized drift waves mainly due to ion temperature gradient (ITG) and trapped electron mode (TEM).

Table 5.1. Different classical and neo-classical regimes and their particle flux, diffusivity, and convective terms

Classical		Pfirsch-Schlüter	Banana-plateau
Γ_Z	$(\Gamma_Z^{cl}, D_Z^{cl}, \frac{v_Z^{cl}}{D_D^{cl}})$	$(\Gamma_Z^{PS}, D_Z^{PS}, \frac{v_Z^{PS}}{D_D^{PS}})$	$(\Gamma_Z^{BP}, D_Z^{BP}, \frac{v_Z^{BP}}{D_D^{BP}})$
D_Z	$-D_Z^{cl} \left[\nabla n_Z - \frac{v_Z^{cl}}{D_Z^{cl}} n_Z \right]$	$-D_Z^{PS} \left[\nabla n_Z - \frac{v_Z^{PS}}{D_Z^{PS}} n_Z \right]$	$-D_Z^{BP} \left[\nabla n_Z - \frac{v_Z^{BP}}{D_Z^{BP}} n_Z \right]$
$\frac{v_Z}{D_Z}$	$\frac{8\sqrt{\pi}}{3} \frac{e^2 \ln \lambda_{DZ}}{(4\pi \epsilon_0)^2 B^2} \sqrt{\frac{m_D}{2kT_i} \frac{n_D}{Z_D}}$	$2q^2 K D_Z^{cl}$	$\frac{3}{2} \frac{kT_i A_Z^{BP}}{Z^2 e^2 B^2 R^2 n_Z}$
	$\frac{Z}{Z_D} \left[\frac{\nabla n_D}{n_D} - \left(\frac{1}{2} + \frac{Z_D}{Z} \right) \frac{\nabla T_i}{T_i} \right]$	$\frac{Z}{Z_D} \left[\frac{\nabla n_D}{n_D} + \frac{H}{K} \frac{\nabla T}{T} \right]$	$\frac{Z}{Z_D} \frac{\nabla n_D}{n_D} + \alpha_{T_D}^{BP} \frac{\nabla T_i}{T_i}$
Where, in Pfirsch-Schlüter, $H = -\frac{1}{2} + \frac{0.29+0.68\alpha}{0.59+\alpha+1.34\left(\frac{3}{\epsilon^2 v_D^*}\right)^{-2}}$, $K = 1 - \frac{0.52\alpha}{0.59+\alpha+1.34\left(\frac{3}{\epsilon^2 v_D^*}\right)^{-2}}$ and $\alpha_Z = \frac{n_Z Z^2}{n_D Z_D^2}$ and in Banana-plateau $\alpha_{T_D}^{BP} = \frac{3}{2} \left(1 - \frac{Z}{Z_D} \right) + \left(\frac{Z}{Z_D} \frac{K_{12}^2}{K_{11}^D} - \frac{K_{12}^2}{K_{11}^D} \right)$ The coefficients A_Z^{BP} and K_{ij}^a can be calculated from Appendix A of reference (Wenzel et al.). These are a function of Z, m_z, n_z .			

5.3. Mass dependency study of impurity transport

The electron temperature of large machines is in the range of $\sim 10 - 20$ keV, and ITER H-mode plasma operations are predicted to have temperatures of ~ 20 keV (Afonin and Petrov). At high temperatures, the possible impurities charge would be W^{62+} . Along with this, several non-fuel atoms are injected into tokamaks for certain operational or diagnostic purposes. Hence, there is a wide range of impurities present in a tokamak with different Z numbers. From the diffusivity equations, D_Z^{cl} , D_Z^{PS} and D_Z^{BP} given in Table 5.1. The diffusivity is independent of atomic mass number Z, in the classical or Pfirsch Schlüter regimes. This holds as long as they're the main ion collisionality is less. In banana-plateau regimes, the diffusion coefficient is an increasing function of Z, as the collisionality of impurity ions increases. Further, towards the higher collisionality of particles, diffusivity approaches to anomalous value for lower Z, because of its high relative contribution in the Pfirsch-Schlüter term.

In several tokamak devices, the Z dependencies have been studied for intrinsic impurity ions, this includes Helium ($Z = 2$), Nickel ($Z = 28$), molybdenum ($Z = 42$) and tungsten ($Z = 74$)(Sertoli et al.). Although this field is vibrant and still large efforts are needed towards the experimental studies to become sure about the theoretical predictions for future fusion devices.

5.4. Methodology for studying the mass dependency of transport in ADITYA-U tokamak

ADITYA-U tokamak consists of several low-Z: Helium ($\text{He}, Z = 2$), Carbon ($\text{C}, Z = 6$), Nitrogen ($\text{N}, Z = 7$), Oxygen ($\text{O}, Z = 8$), Medium Z: Neon ($\text{Ne}, Z = 10$), Argon ($\text{Ar}, Z = 18$) and high Z: Iron ($\text{Fe}, Z = 26$). These are used to study impurity transport. The spectral lines in visible and VUV ranges from those impurities that have been captured using visible and VUV spectroscopy systems from several similar ADITYA-U plasmas. The spatial profile of visible spectral lines and single chord measurement of VUV spectral lines from a few ionization stages of the impurities are modelled using the impurity transport code to get the diffusivity and convective velocity. The impurity transport code solves the empirical equation of radial transport numerically.

The radial impurity transport equation (RITE) for any Z impurity ion using equations 5.2 and 5.3 is:

$$\frac{\partial n_z(r,t)}{\partial t} = \frac{D(r) \frac{\partial^2 n_z(r,t)}{\partial r^2} + \frac{\partial D(r)}{\partial r} \frac{\partial n_z(r,t)}{\partial r} + \frac{D(r)}{r} \frac{\partial n_z(r,t)}{\partial r} -}{v(r) \frac{\partial n_z(r,t)}{\partial r} - n_z(r,t) \frac{\partial v(r)}{\partial r} - \frac{v(r)}{r} n_z(r,t) + Q_z(r,t)} \quad 5.5$$

The $Q_z(r,t)$ represents source and sink term in which the ionization, recombination, and charge exchange process can be incorporated through its rate coefficients with the following Equation:

$$Q_z(r,t) = \frac{n_e(r)n_{z-1}(r,t)S_{z-1}(r) - n_e(r)n_z(r,t)S_z(r) + n_e(r)n_{z+1}(r,t)\alpha_{z+1}(r)}{-n_e(r)n_z(r,t)\alpha_z(r) + n_e(r)n_{z+1}\alpha_{z+1}^{CX}(r) - n_e(r)n_z\alpha_z^{CX}(r)} \quad 5.6$$

Z is the mass number of species, S is the ionization rate coefficient, α is the recombination rate coefficient, and α^{CX} is the charge-exchange recombination rate coefficient. In the above equation, r represents the plasma radius (m) and t stands for time (s).

There are many computational codes to solve this empirical equation (Houlberg et al.; Peeters). In the STRAHL code, (Lackner et al.; Dux R.; K. Behringer) the RITE is solved by considering diffusion and convective term with the implicit Crack-Nicholson method. Ionization and recombination terms in this solution are alternatively implicit and explicit with time iteration.

In this method the solution is not stable in nature and coordinate transformation from radial to the generalized magnetic flux surface coordinates (Dux R.), must take care that Δr remains below $\pm 10\%$. The initial condition for solving equations 5.5 and 5.6 are given as,

$$n_z|_{t=0} = 0 \text{ for all } r \in [0, r_0] \quad 5.7$$

Boundary conditions for solving the Equation, (i) $\frac{dn_z}{dr}|_{r=r_0} = -\frac{n_z}{l_d}$, for all $0 \leq t \leq t_s$ and (ii) $\frac{dn_z}{dr}|_{r=0} = 0$, for all $0 \leq t \leq t_s$. Here l_d is the decay length (m) and t_s is the time when the steady state of plasma is achieved. Recently an impurity transport code has been developed, it is called SITA for Semi-implicit Impurity Transport code for ADITYA-U tokamak, it solves the RITE equation by discretizing it with forward-difference in time and central-difference (FTCS) scheme in space (radius). The diffusivity, velocity, ionization, and recombination terms are rearranged after discretization and assigned an implicit or an explicit time treatment (Bhattacharya, Ghosh, M. B. Chowdhuri, and De; Bhattacharya, Munshi, et al.; Bhattacharya, Ghosh, M. B. Chowdhuri, and Munshi; Bhattacharya, Ghosh, Malay B. Chowdhuri, et al.). The

detailed computational description and its stability using von Neumann are present in reference (Bhattacharya, Munshi, et al.).

However, in this study, the STRAHL code has been used to understand the mass dependency of impurity transport. The inputs to this code are, electron temperature and density profiles, impurity source rate, tokamak geometry, atomic data (ionization and recombination), diffusion, and convective velocity profiles. In this thesis, the STRAHL code is used to estimate the impurity ion densities of different impurities having different ionized states. The contribution from charge exchange recombination is neglected as there is no neutral beam heating in ADITYA-U tokamak. The classical and neo-classical modules of the code are turned off while calculating the impurity charge densities. Further in the IDL environment, the emissivity profiles are calculated with the following equation,

$$\varepsilon_z(r) = n_z(r) \cdot n_e(r) \cdot PEC_z(r) \quad 5.8$$

Here, n_z and n_e are the impurity charge density and electron density, PEC_z is the photon emissivity coefficient. The atomic data including ionization, recombination, and PECs are taken from the open ADAS database (Summers).

Electron temperature and density profiles

The modelling of various impurities emissions has been done using the plasma discharges having similar core and edge parameters of electron density and temperature. But, the radial profiles of plasma n_e , T_e and impurity-neutral density (n_I) are generated from the following equations,

$$n_e(r) = n_{e,a} + (n_{e,0} - n_{e,a}) \left[1 - \left(\frac{r}{r_0} \right)^2 \right]^a \quad 5.9$$

$$T_e(r) = T_{e,a} + (T_{e,0} - T_{e,a}) \left[1 - \left(\frac{r}{r_0} \right)^2 \right]^b \quad 5.10$$

$$n_I = n_{I,peak} \left[- \left(\frac{\frac{r_0 - r}{2\pi r_0}}{\gamma} \right)^{2.65} \right] \quad 5.11$$

The core and edge plasma density and temperature are taken from the measurement from ADITYA-U tokamak and mentioned in Table 5.2. Generated electron density and temperature profiles are shown in Figure 5.2.

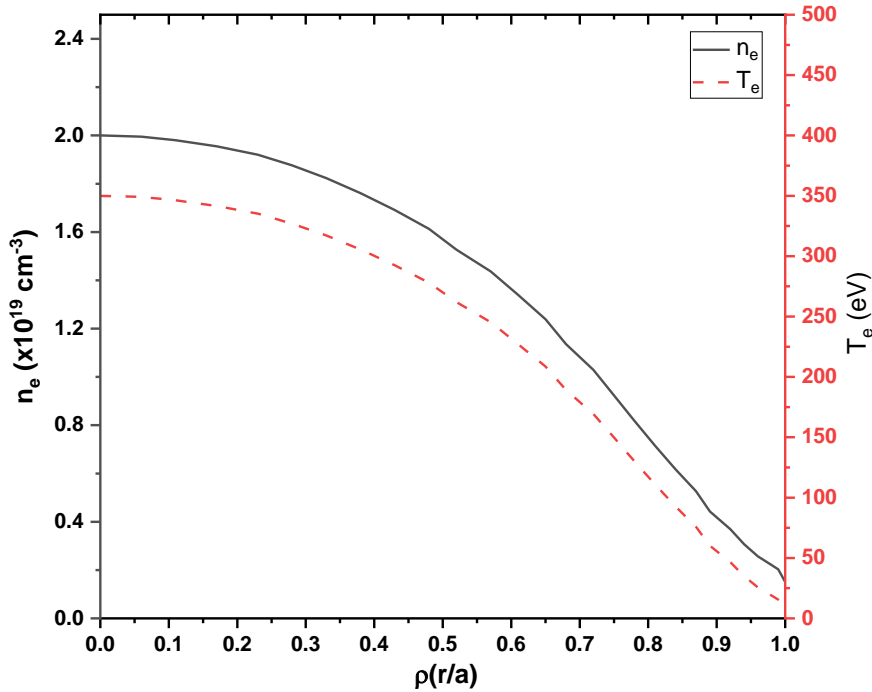


Figure 5.2. Electron density and electron temperature profile used for impurity transport study

Table 5.2. ADITYA-U plasma parameters set in the program for modelling n_e , T_e and n_I profiles using equation 5.9, 5.10 and 5.11

Plasma parameters	value	unit
$T_{e,0}$	350	eV
$T_{e,a}$	12.5	eV
$n_{e,0}$	2.05×10^{19}	m^{-3}
$n_{e,a}$	2.3×10^{18}	m^{-3}
a, b	1.75	

Diffusivity and velocity profiles

In the code, the following diffusion and drift velocity radial profile equation is used to model the impurity transport:

If, $r \leq r_m$

$$D(r) = D_a + (D_m - D_a) \exp\left[-\frac{(r-r_m)^2}{p_1^2}\right] \quad 5.12$$

$$v(r) = v_a + (v_m - v_a) \exp\left[-\frac{(r-r_m)^2}{q_1^2}\right] \quad 5.13$$

If, $r > r_m$

$$D(r) = D_0 + (D_m - D_0) \exp\left[-\frac{(r-r_m)^2}{p_2^2}\right] \quad 5.14$$

$$v(r) = v_0 + (v_m - v_0) \exp\left[-\frac{(r-r_m)^2}{q_2^2}\right] \quad 5.15$$

In the above equations, r is the plasma minor radius, r_m is the $p \times r_{LCFS}$, where p is a dimensionless constant value. p_1, p_2, q_1 and q_2 are the variable numbers having a dimension of length. D_m, D_a, D_0 are the variables used to adjust the diffusivity profile and v_m, v_a, v_0 are the variables to adjust the convective profile. By varying different variable parameters in these profiles, the shape and magnitude of D and v profiles can be calculated to model the experimental data.

5.5. Investigation of Mass dependency study on impurity transport in tokamak:

The visible and VUV spectral line emissions from Carbon (C, Z = 6), Oxygen (O, Z = 8), Neon (Ne, Z = 10), Argon (Ar, Z = 18) and Iron (Fe, Z = 26) are used to study the impurity transport in ADITYA-U tokamak (Yadava, Ghosh, M. Chowdhuri, et al.). The obtained results are described here.

5.5.1. Transport of carbon Z=6(Intrinsic impurity)

The time evolution of loop voltage and plasma current for typical ADITYA-U discharge is given in Figure 5.3. The spectrum during 40 – 56 ms, has been recorded using space resolved

visible spectroscopic system, which is described in the previous section. The set wavelength in the spectrometer was kept at 464.7 nm, C^{2+} emission. The space resolved measurement for the same is given in Figure 5.4. It is seen from the figure that, along with 464.7 nm, C^{2+} emission, there are spectral lines of O^+ , O^{2+} and other lines of C^{2+} ($464.9 - \text{O}^+$ and O^{2+} , $465.0 - \text{C}^{2+}$ and O^+ , $465.12 - \text{C}^{2+}$, $465.14 - \text{C}^{2+}$, $465.16 - \text{C}^{2+}$). To calculate the brightness and emissivity from the spectral line, the Gaussian fitting is performed and the area under the curve is used for the measurement (see Figure 5.5). The radial profile of the emissivity profile is obtained through the Abel-Inversion technique (Condrea et al.; Bell) from the space-resolved measurement. The experimentally measured radial profile of emissivity is given in Figure 5.6 for C^{2+} emission at 464.7 nm.

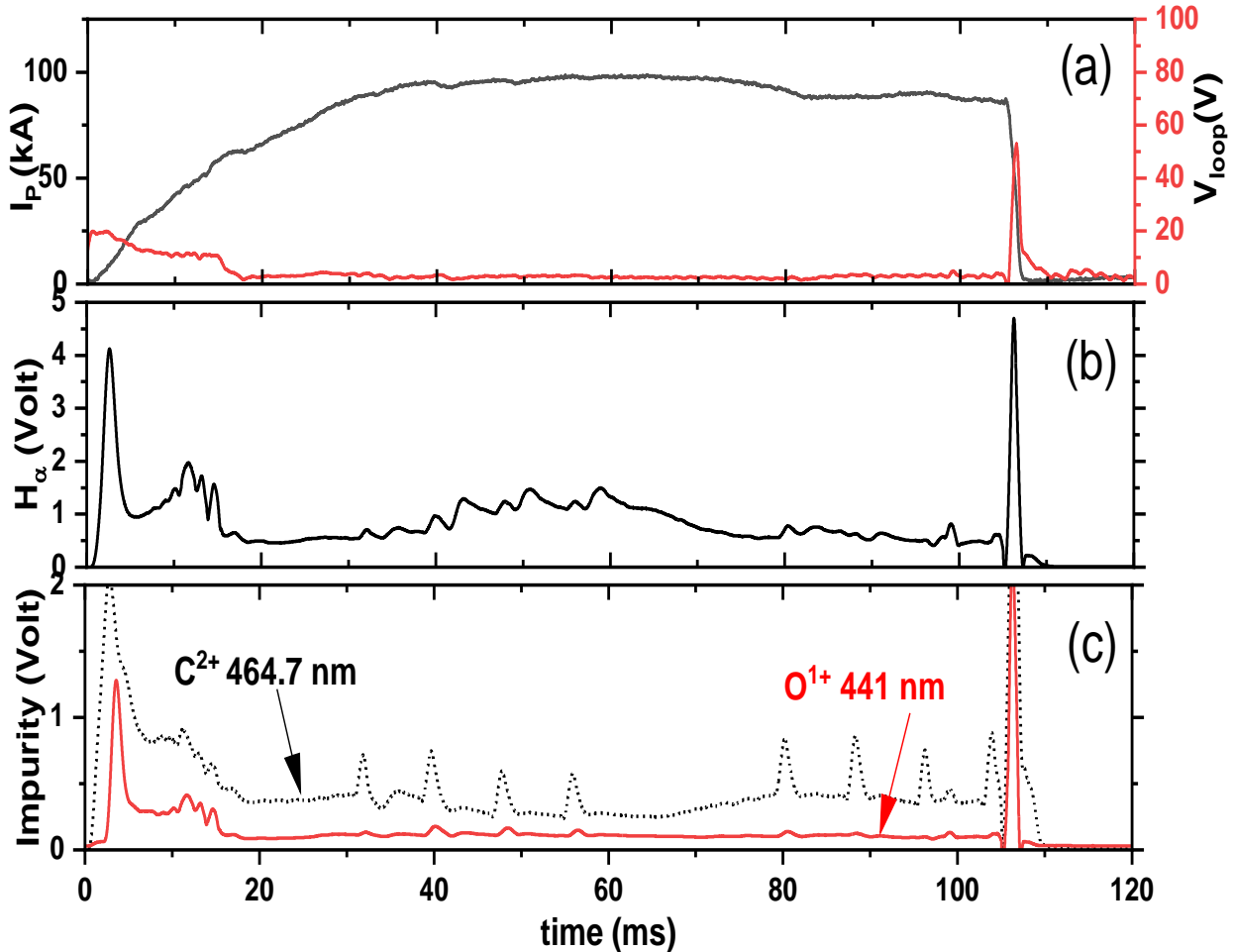


Figure 5.3. Temporal evolution of Typical Plasma discharge shot #33880 (a) black solid line represents plasma current I_p , maximum~100 kA, red solid line represents loop voltage; (b) H_α emission measured with PMT having wavelength 656.28 nm and (c) intrinsic impurity emissions at 464.7 nm C^{2+} (black small dashed line) and O^+ at 441 nm monitored (red solid line) with PMT diagnostic

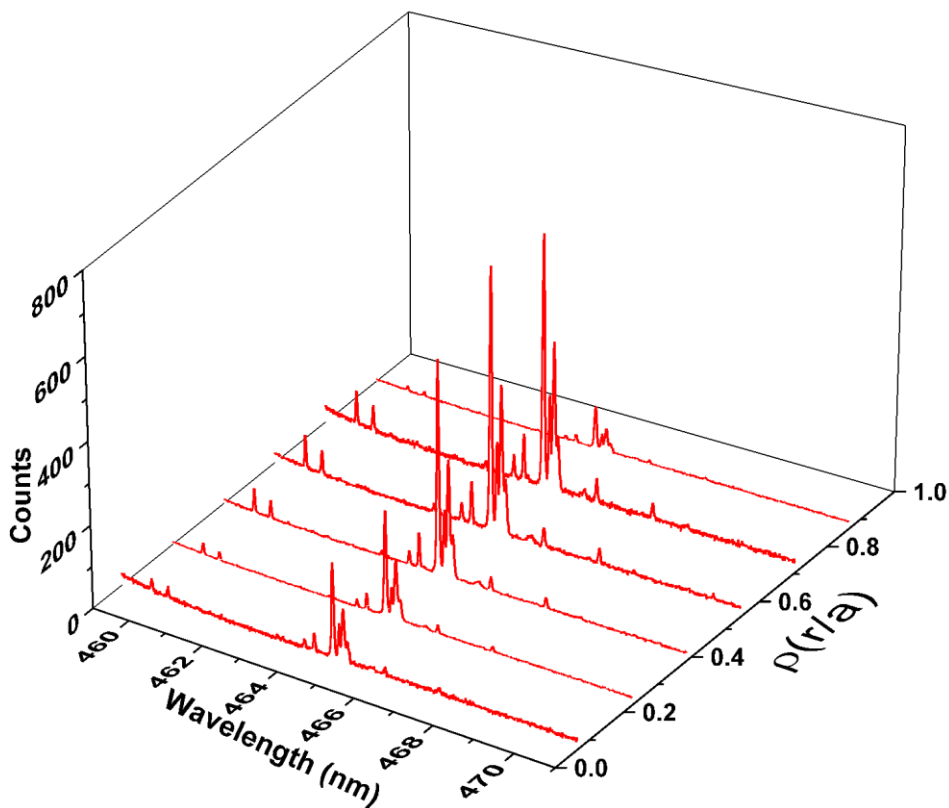


Figure 5.4. Space resolved measurement of Carbon emission present at 464.7 nm, having ionization state C^{2+}

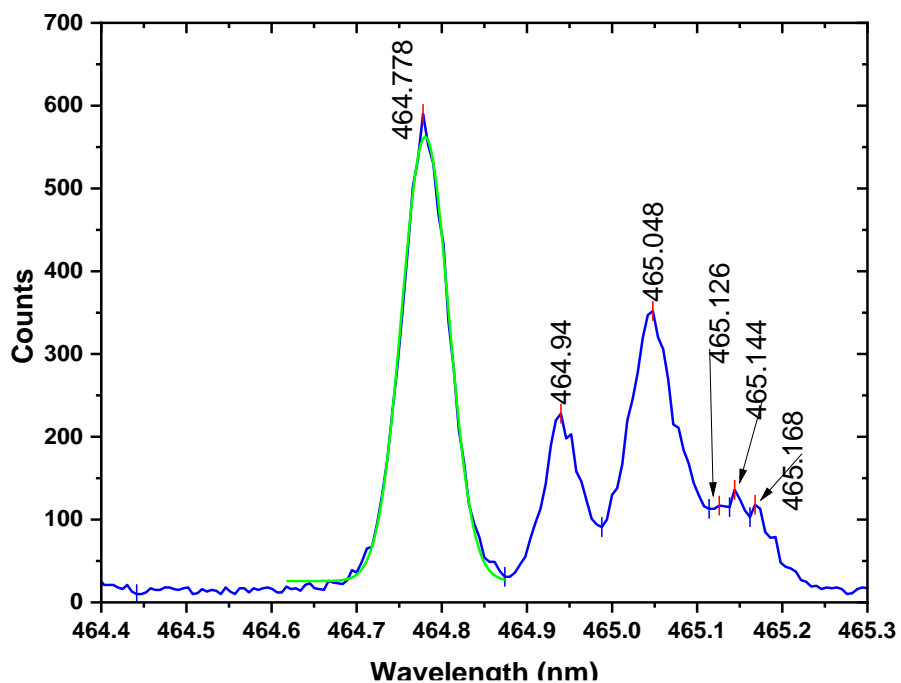


Figure 5.5. Identification of other nearby emission lines along with carbon emission

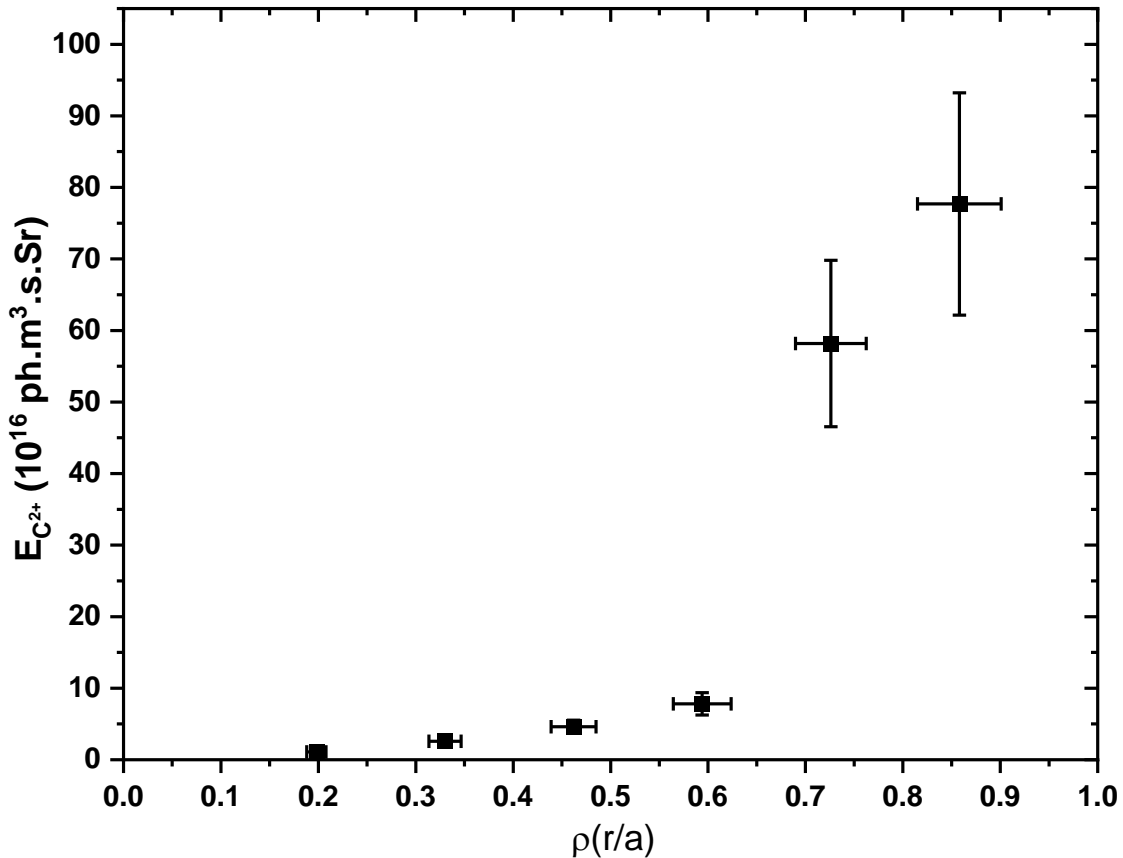


Figure 5.6. Experimentally measured emissivity profile of C^{2+} emission line at 464.77 nm

Carbon is the low-Z impurity ion, it mostly remains in the edge region of ADITYA-U tokamak plasma. Hence the drift velocity term is taken as zero while carrying out the simulation.

The experimental emissivity profile has been modelled using STRAHL. To obtain the best match the magnitude and shape of D has been varied by changing the various terms in Equation 5.12 and 5.14. The best-matched profiles are shown in Figure 5.7. It is observed that the experimental profile is peaking at $\rho = 0.88$ and the simulated profile is peaking at $\rho = 0.81$. This comes within the given 5% error bars to the ρ axis value. Through the modelling of the radial profile of emissivity, the peak diffusivity is found to be $60 \text{ m}^2/\text{sec}$ at the plasma edge region, as shown in Figure 5.8. The shaded region in diffusivity profile has been generated with 20% uncertainty. The impurity density profiles of different carbon ions at best-matched conditions are given in Figure 5.9 and the C^{2+} ion density peak at normalized radius, $\rho = 0.8$, at plasma edge region.

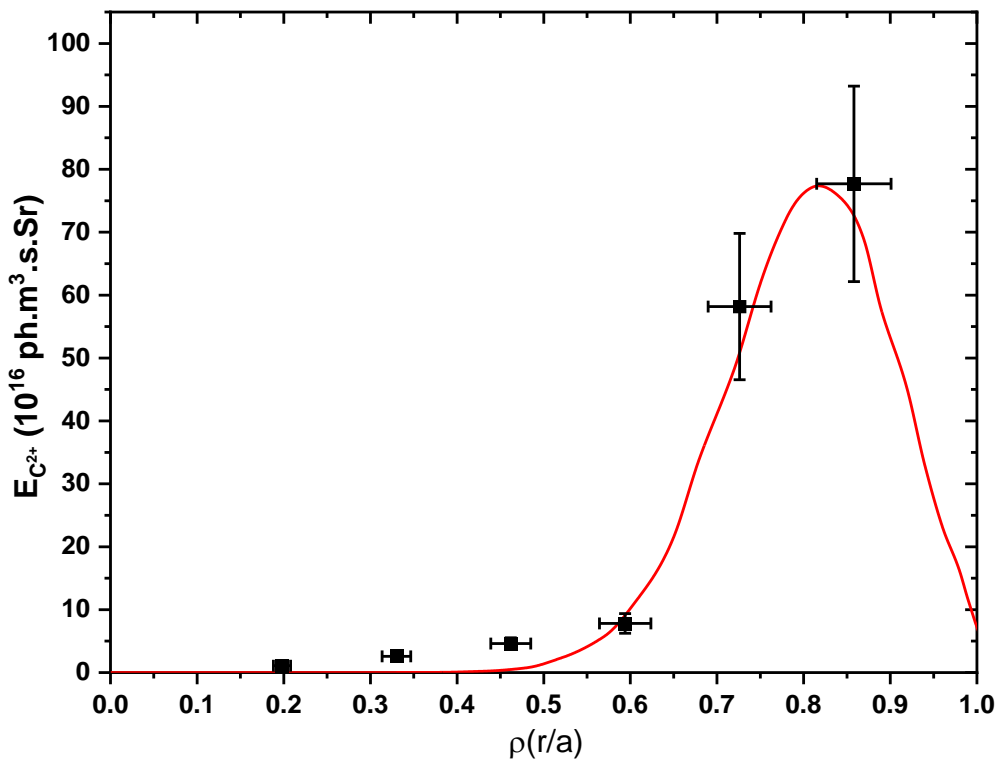


Figure 5.7. Matched emissivity profile of C^{2+} impurity ion

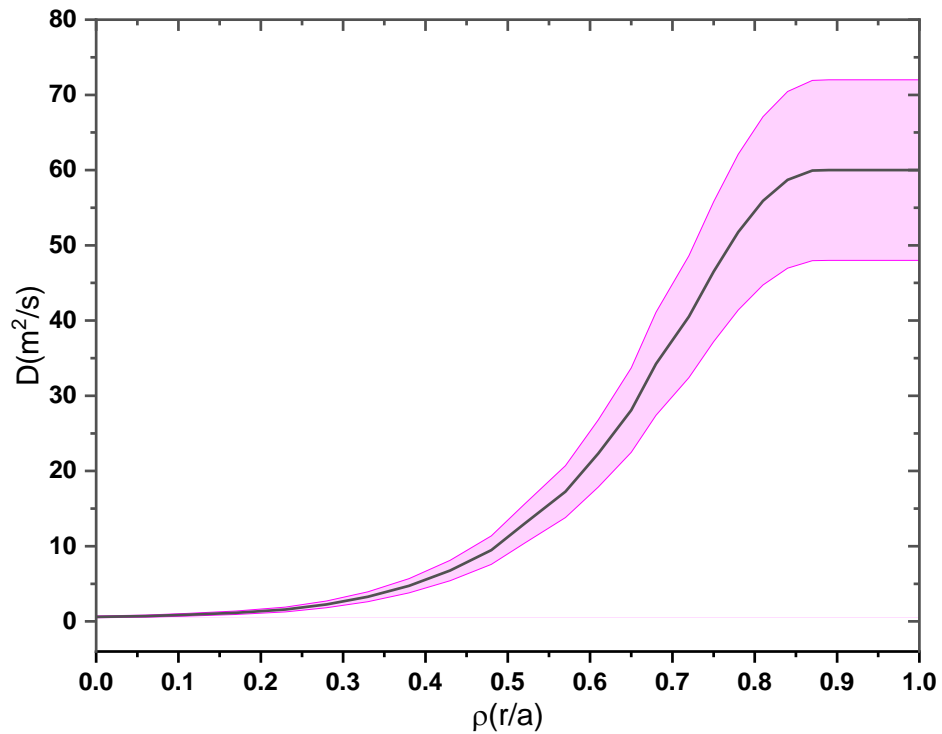


Figure 5.8. Diffusivity profile for C^{2+} emission

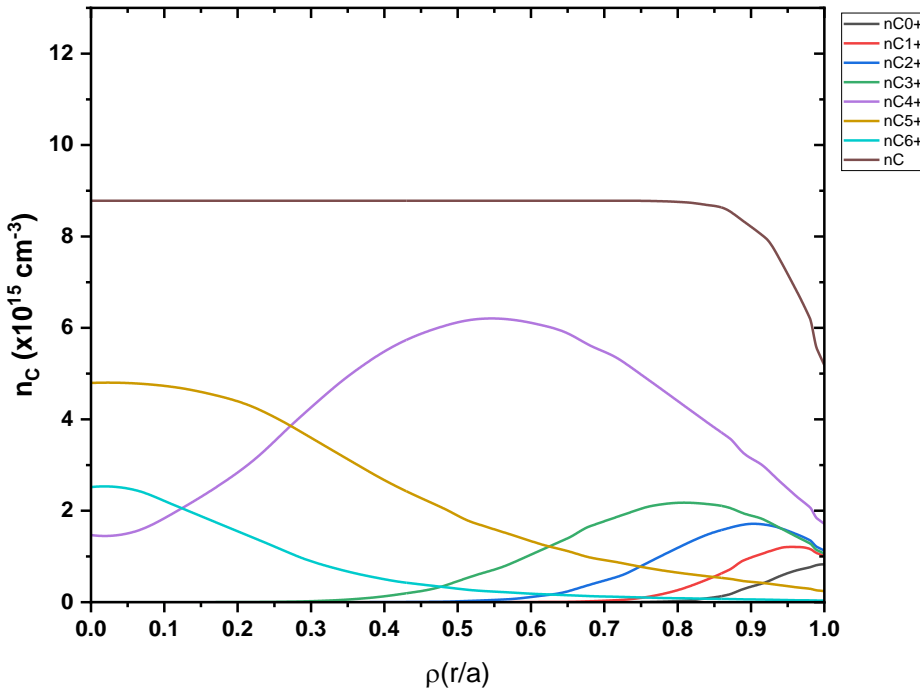


Figure 5.9. Impurity density profile of several carbon ions

5.5.2. Transport of oxygen Z=8 (Intrinsic impurity)

The emission spectra of O^{4+} ion is recorded at 650.024 nm by setting the set wavelength of the spectrometer at 654 nm, exposure time of 10 ms (at 40 – 56 ms of plasma), and a slit width of 70 μ m. Space-resolved spectra from different LOS are plotted in Figure 5.10. In the same wavelength region, along with O^{4+} emissions, H_α at 656.28 nm and carbon doublet C^+ at 657.08 nm and 658.28 nm is observed. The observed spectral lines are also marked in this figure. Here also, the radial profile of emissivity is obtained using Abel-inversion of the spatial profile. The modelling of the radial profile of O^{4+} emissivity studies had been done for ADITYA tokamak by M. B. Chowdhuri et al.(M. B. Chowdhuri, Ghosh, et al.) using the STRAHL code. This study was further done using an indigenously developed impurity transport code (Bhattacharya, Ghosh, M. B. Chowdhuri, and Munshi) for benchmarking this newly developed code. However, the result presented in this thesis is from ADITYA-U tokamak limiter plasma discharges.

As in the case of carbon ion, the convective term is here also kept zero as the diffusivity plays an important role at the plasma edge region. Experimentally observed emissivity profiles are best matched with simulated emissivity profiles by varying magnitude shapes of the diffusion coefficient D in the STRAHL code. In the best-matched condition, the maximum value of

diffusivity is $37 \text{ m}^2/\text{s}$ as shown in Figure 5.11. The best-matched experimental and simulated profiles are shown in Figure 5.12.

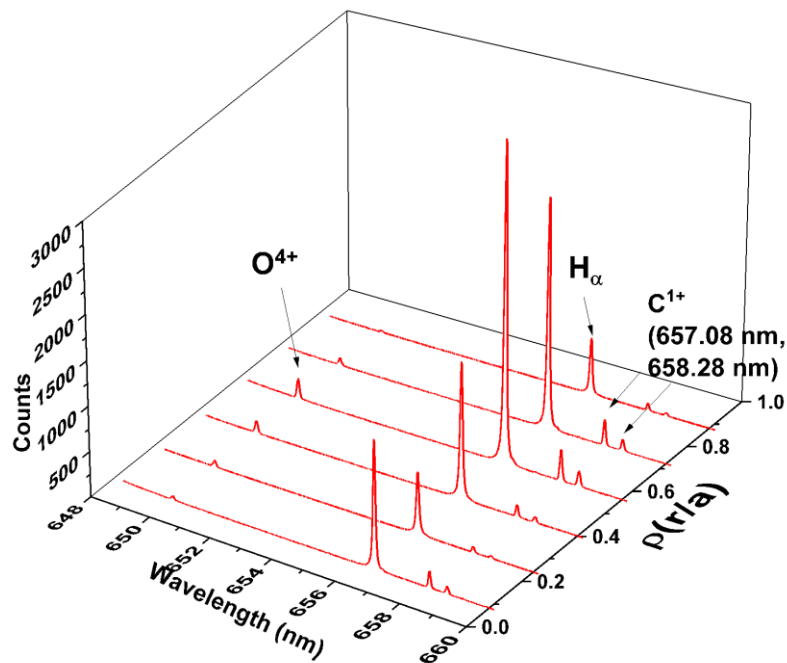


Figure 5.10. Space resolved measurement of Carbon emission present at 650 nm, having ionization state O^{4+}

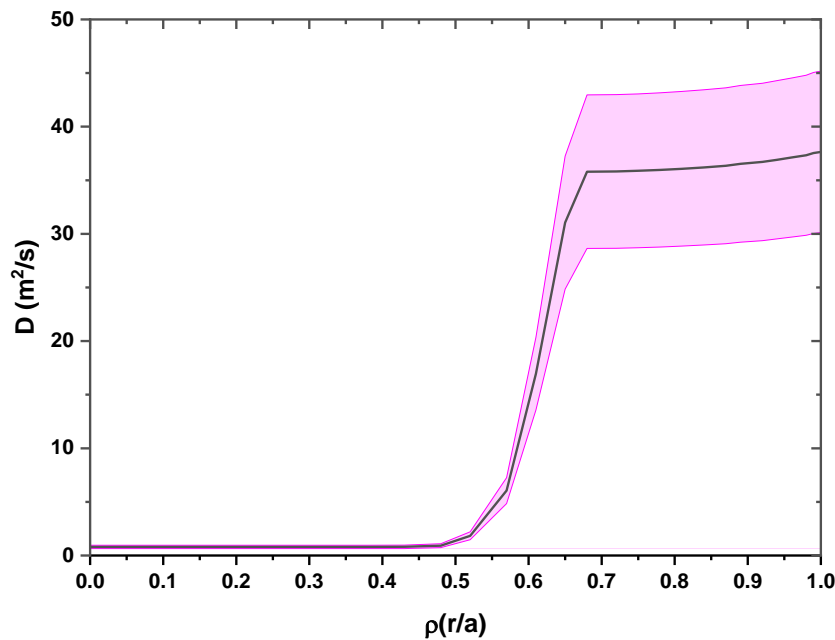


Figure 5.11. Diffusivity profile for modelling of O^{4+} emission

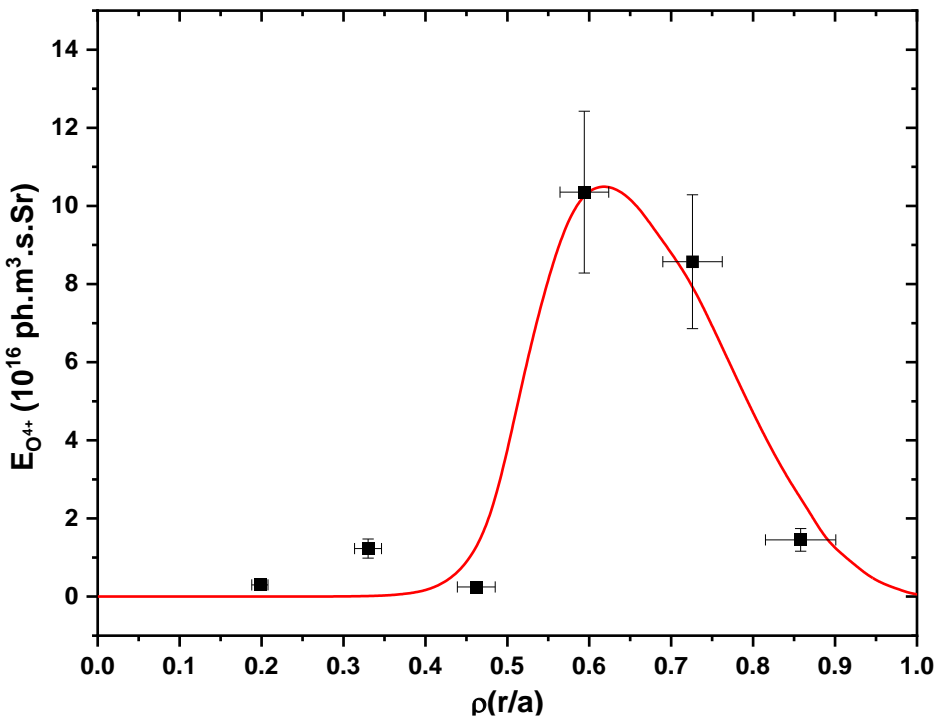


Figure 5.12. Simulated and experimental emissivity profile of O^{4+} impurity ion

5.5.3. Transport of neon Z=10 (non-intrinsic impurity)

Neon is the non-intrinsic medium-Z impurity ion. It is seeded in ADITYA-U to produce plasma having radiative improved confinement mode (Malay Bikas Chowdhuri et al.; Bisai, Chowdhuri, et al.). During these experiments to understand the neon impurity transport, the high-resolution spectroscopic system was set up with a set wavelength of ~ 377 nm, having a slit width of ~ 200 μm and an exposure time of 15 ms (during 55 – 70 ms of plasma). The data acquisition has been set up in such a way that the spectrometer acquires the neon spectral line after gas-puff. The space-resolved measurement of the same is given in Figure 5.13. All the lines are identified and shown in Figure 5.14. It is seen that along with Ne^+ emission line at 371.8 nm the carbon emission lines are also present. An Abel inversion technique was used to get a radial profile from the space resolved measurement. However, for this medium-Z impurity, the drift velocity is not kept at zero as the particles can reach up to the plasma core, as shown in Figure 5.13. The experimental and simulated emissivity profiles are modelled and the best-matched profiles are shown in Figure 5.16. The maximum values of convective velocity, $V \sim -4$ m/s and Diffusion coefficient, $D \sim 30$ m^2/s .

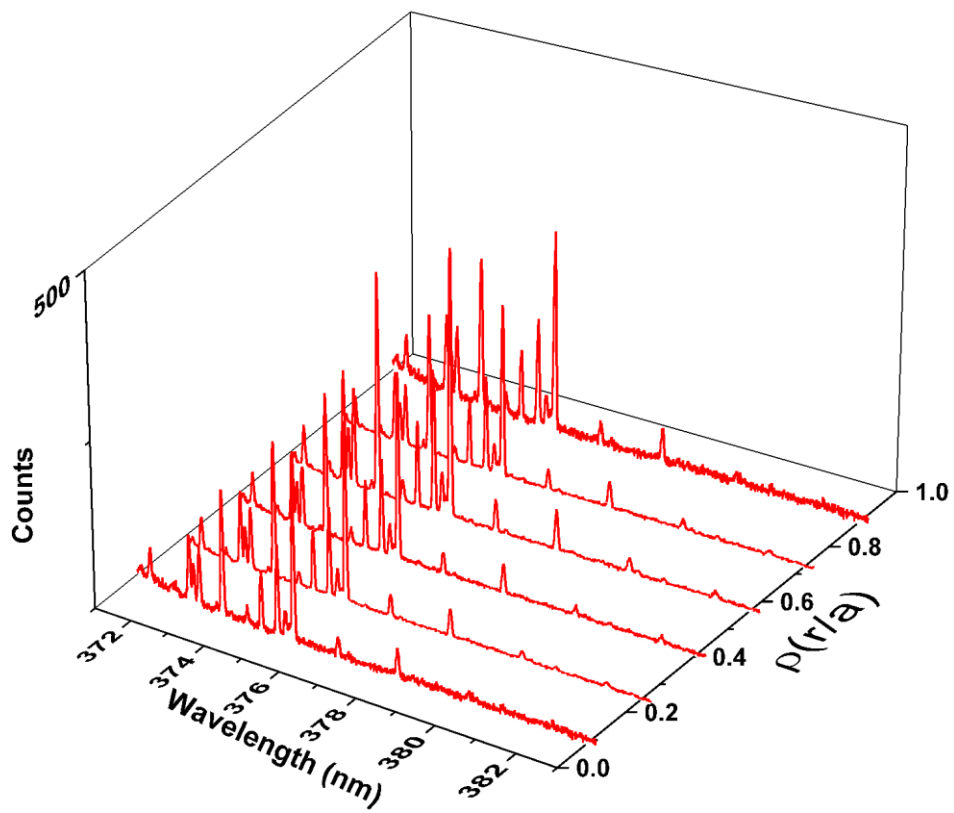


Figure 5.13. Space resolved measurement of Neon emission present at 371.8 nm, having ionization state Ne

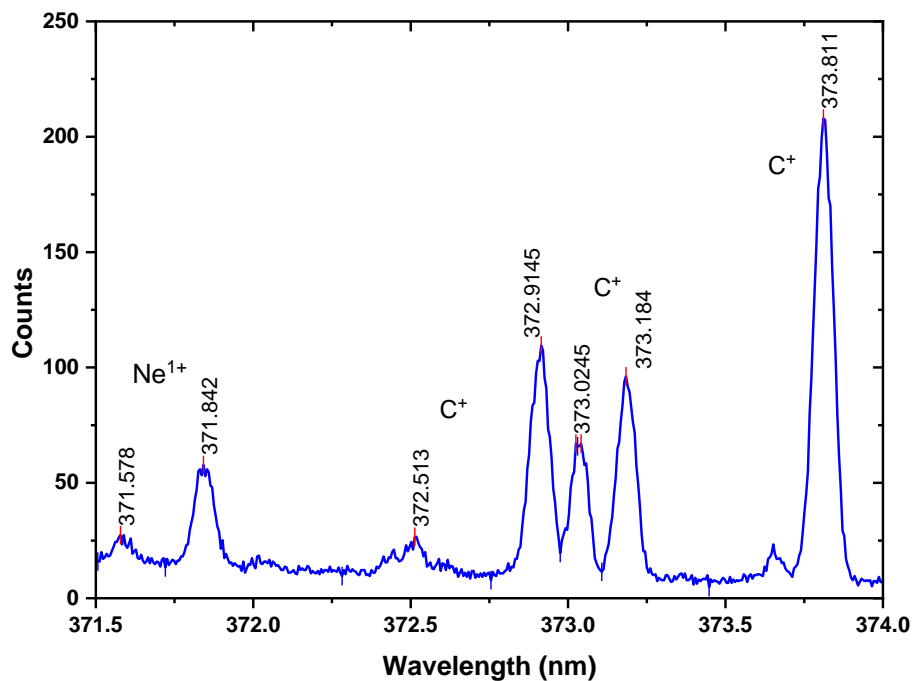


Figure 5.14. Wavelength resolved spectrum contains Neon 371.8 nm along with other carbon emission lines

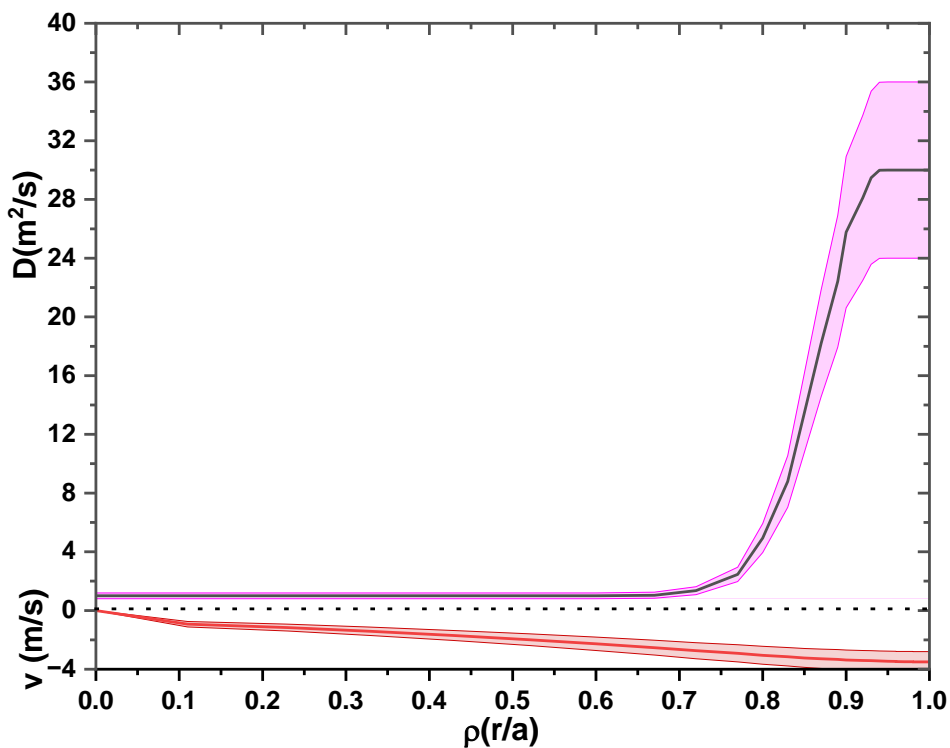


Figure 5.15. Diffusivity profile for Ne^+ emission

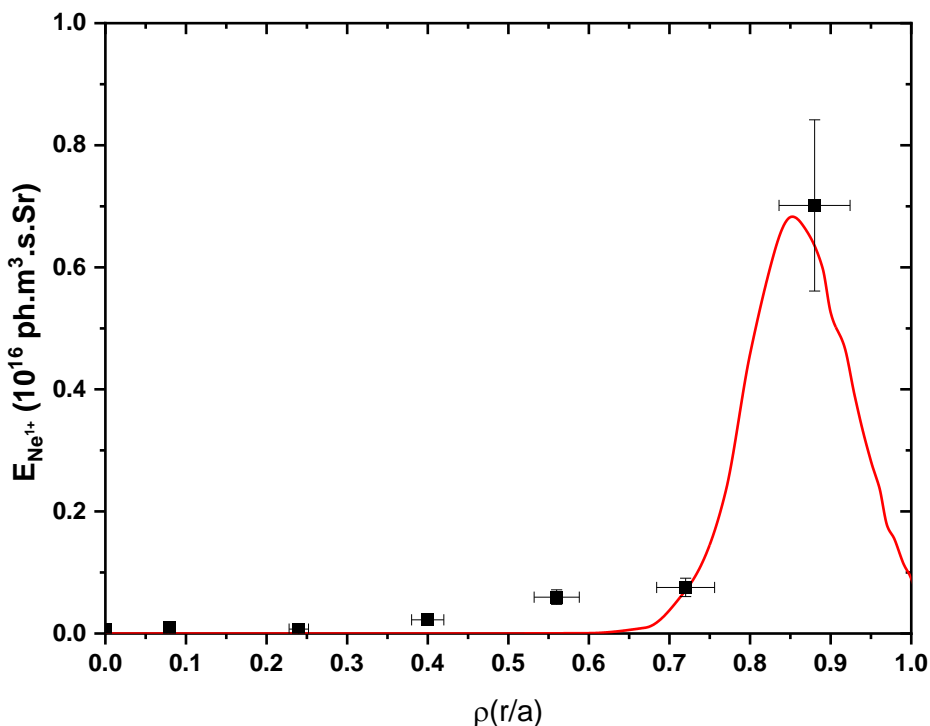


Figure 5.16. Matched emissivity profile of Ne^+ impurity ion

5.5.4. Transport of argon Z=18 (non-Intrinsic impurity)

Argon is also a non-intrinsic impurity in ADITYA-U tokamak plasma. It is also introduced to plasma for the improvement of plasma performance and to carry out argon spectroscopy in ADITYA-U tokamak. The space-resolved spectra have been measured by keeping slit width \sim 100 μm , central wavelength 476 nm, and the spectrum is acquired during the plasma duration of 66 – 86 ms. The space-resolved measured spectrum is given in Figure 5.17. The experimental and simulated emissivity profiles for the Ar^+ line at 480.01 nm is best matched with Ar diffusivity and convective velocity (Figure 5.18), and the simulated and experimental profiles are shown in Figure 5.19, The required diffusivity profile and drift velocity profiles to get the best-matched condition are given in Figure 5.18, with maximum $D\sim 18 \text{ m}^2/\text{s}$ and $v\sim 10 \text{ m/s}$.

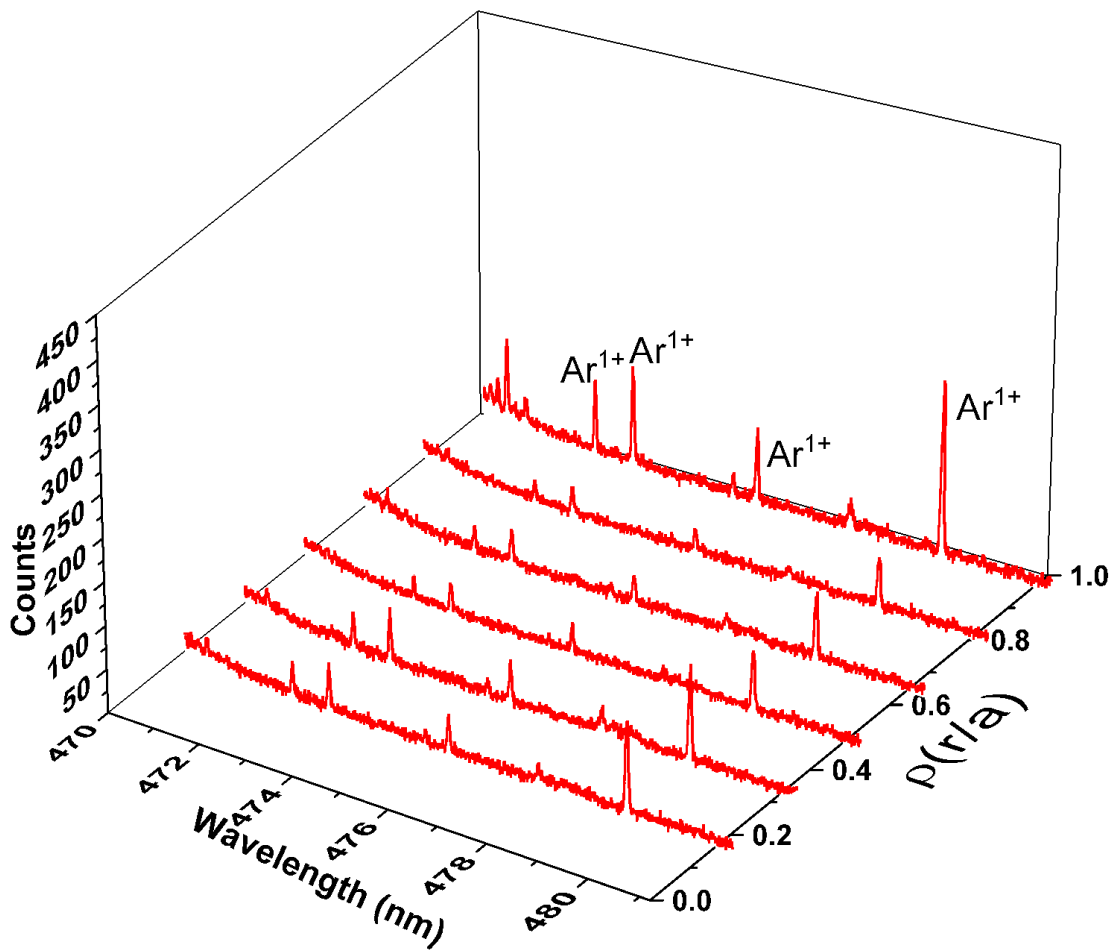


Figure 5.17 Space-resolved measurement of argon emission

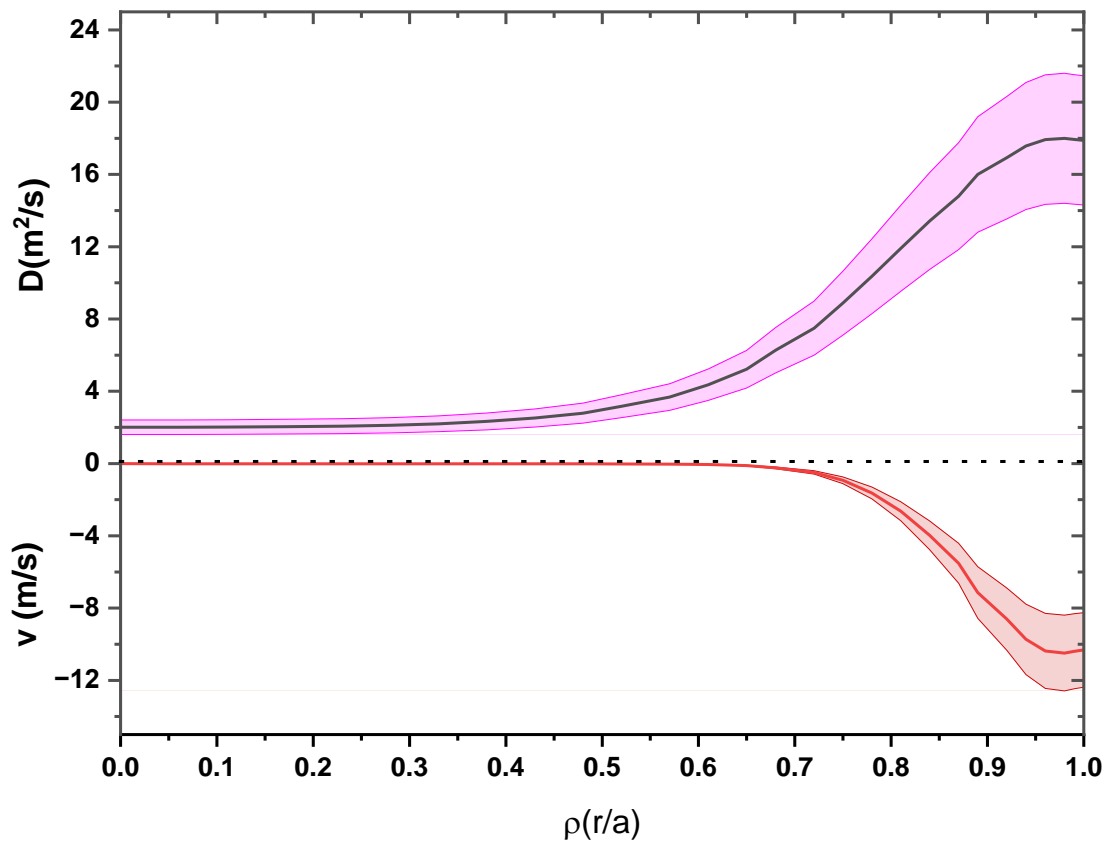


Figure 5.18. Diffusivity and drift velocity profiles for Ar emission

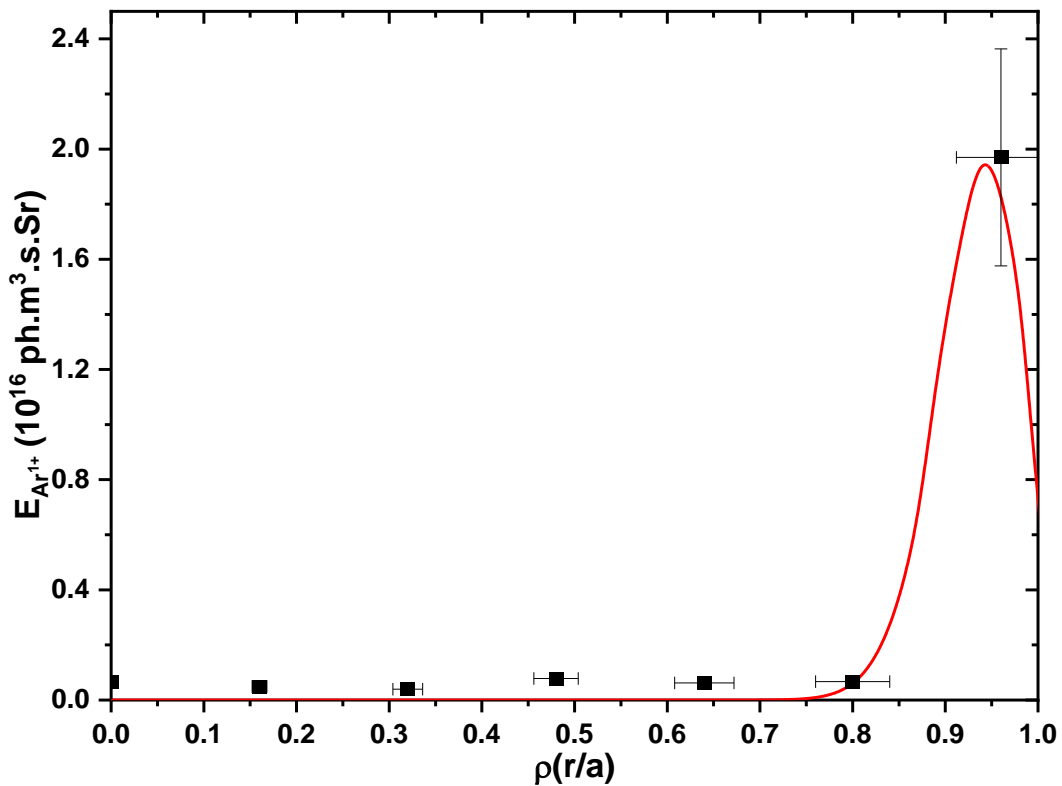


Figure 5.19. Matched emissivity profile of Ar^+ impurity ion

5.5.5. Transport of iron Z=26 (Intrinsic impurity)

The ADITYA-U tokamak vessel-walls are made up of stainless steel and it is having iron as one of the composites. Hence, iron becomes the intrinsic impurity in ADITYA-U tokamak plasma. Iron emissions are not normally observed in the visible range of the spectrum. Hence, the iron emissions of Fe^{14+} and Fe^{15+} are identified in the VUV range of the spectrum. The VUV spectroscopic system is not capable of having space-resolved measurements. Hence, the line ratio from the two ionization stages of iron is used to determine the transport properties of iron. Similar techniques were adopted previously to study iron impurity transport in ADITYA tokamak (S. Patel et al.).

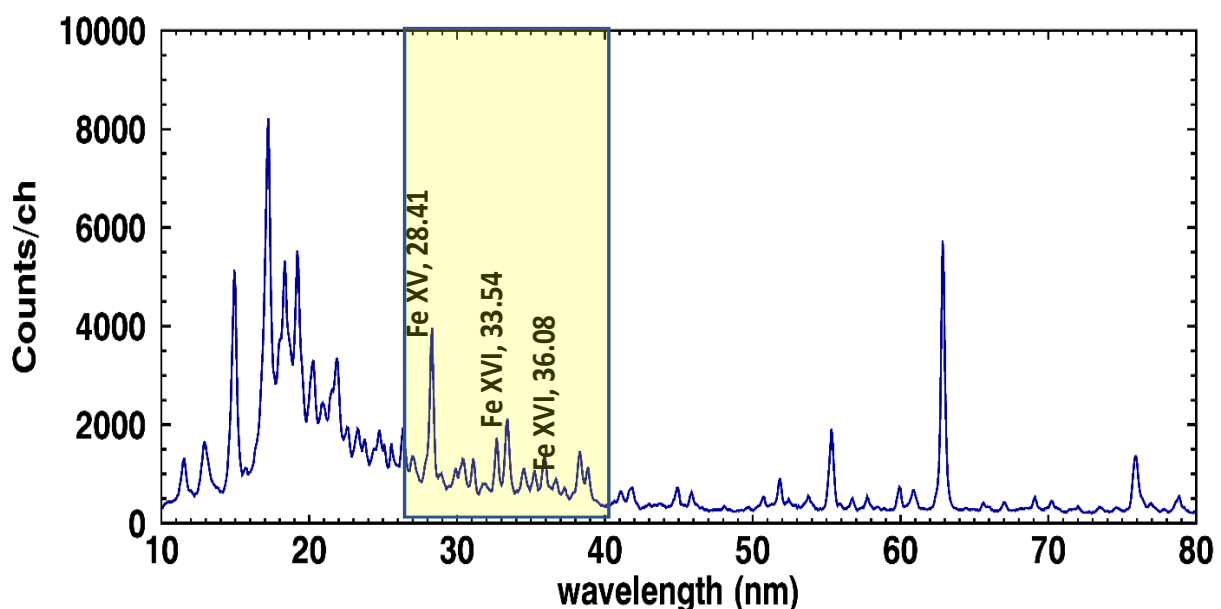


Figure 5.20. VUV survey spectrum and identification of iron emission lines

In ADITYA-U tokamak plasma, the VUV spectrum was acquired at every 10 ms using a VUV survey spectrometer (S. Patel et al.) The experimental spectrum is given in Figure 5.20 and it contains VUV lines from Fe^{14+} at 28.41 nm and two lines of Fe^{15+} at 33.54 nm and 36.08 nm. The VUV survey spectroscopy system is absolute calibrated using a combination of branching ratio and Collisional radiative modelling techniques for quantitative analysis (S. Patel et al.). The experimentally measured ratio of $\frac{\text{Fe}^{14+}(28.41)}{\text{Fe}^{15+}(33.54)} \approx 1.1$ and $\frac{\text{Fe}^{15+}(33.54)}{\text{Fe}^{15+}(36.08)} \approx 1.5$. The experimental line ratio and individual line intensities were modelled through simulation using STRAHL code. The obtained diffusivity profile and the drift velocity profile are given in Figure 5.21. It can be seen that now the maximum diffusivity is $14 \text{ m}^2/\text{s}$ and convective velocity is $V = 7 \text{ m/s}$. The simulated emissivity profiles have also been plotted in Figure 5.22. The emissivity

of Fe^{15+} has an almost flat profile at the plasma central region, while Fe^{14+} has a hollow profile and peaking at the normalized radius of $\rho = 5.5$.

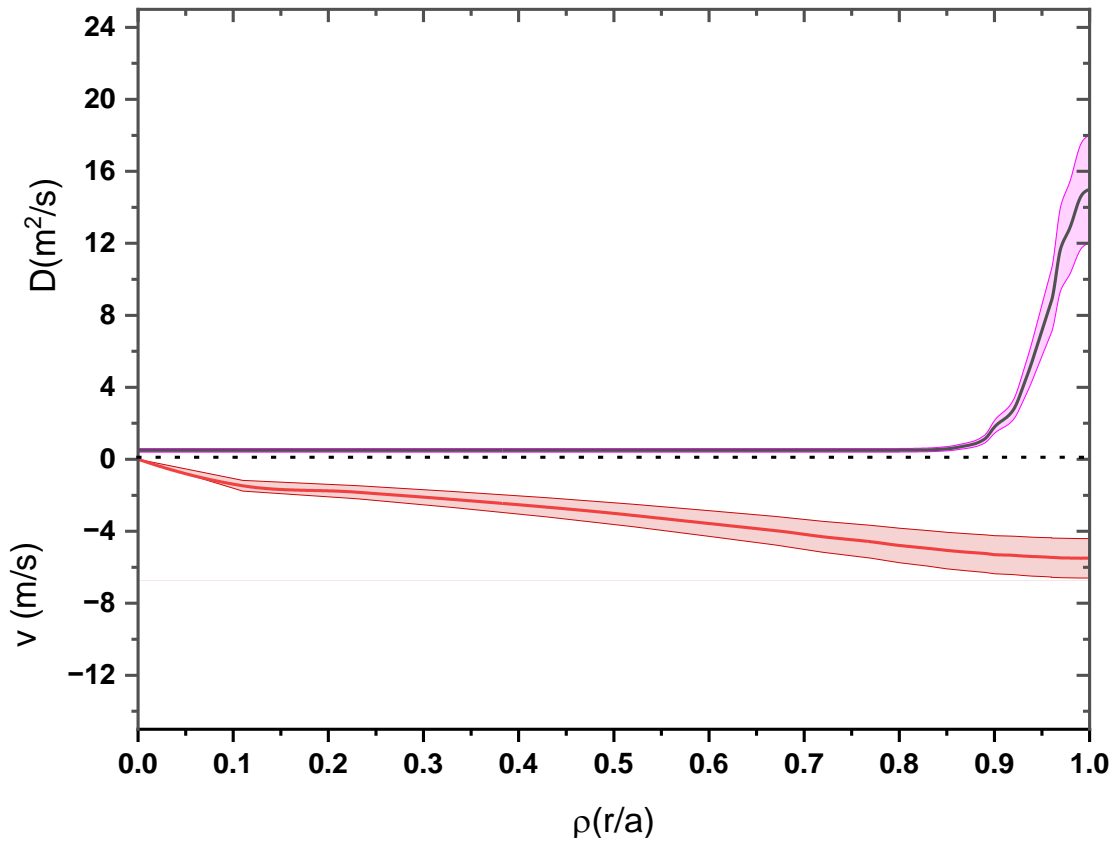


Figure 5.21. Diffusivity and drift velocity profiles for Fe emission

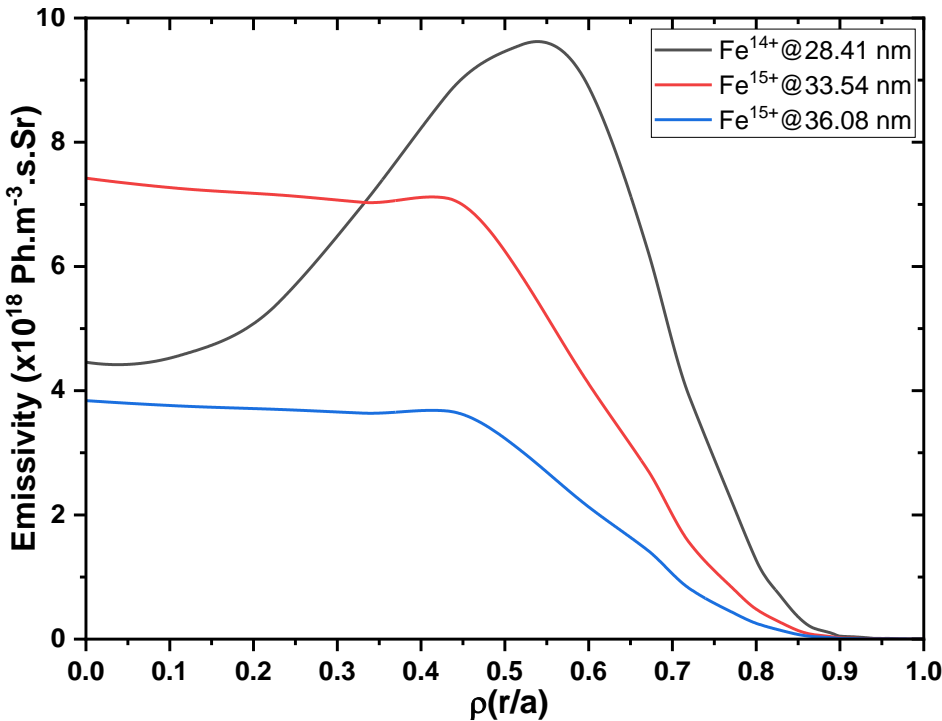


Figure 5.22. the emissivity of iron emission lines simulated by STRAHL code

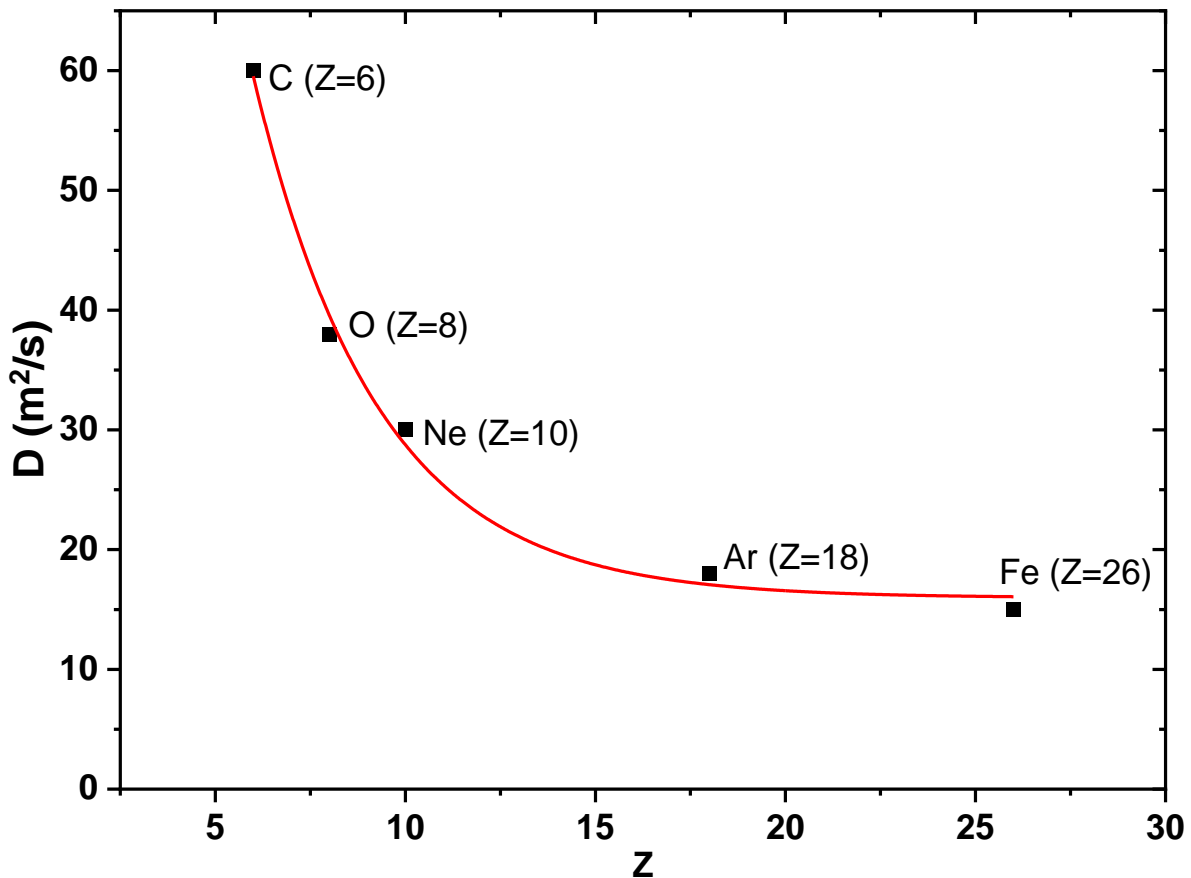


Figure 5.23. The mass dependency (in terms of Z) on impurity transport diffusivity parameter

5.5.6. Discussion on the mass dependency on impurity transport:

Figure 5.23 show the plot of obtained maximum diffusivity for different impurities. It seen from the figure diffusivity fall quickly from ~ 60 to $37 \text{ m}^2/\text{s}$ when Z increase from 6 to 10. Later the variation of D with atomic number slowed down and becomes almost flat with further increase of the Z and correspondingly with mass. As described earlier, the impurity diffusion coefficients in classical and Pfirsch-Schlüter regimes of neo-classical transport are independent of impurity charge state Z when the main ion collisionality is low (Fussmann et al.). The impurity diffusion coefficient in the Banana-Plateau regime of neo-classical theory is anticipated to be a weak function of the impurity collisionality and a decreasing function of the impurity charge state Z . Further, the turbulent diffusion coefficient corresponding to the random walk of every particle about the fluctuating potential, with the $E \times B$ drift velocity is also found to be independent of the particle charge state Z . However, experimental studies of the Z dependency of the impurity diffusion coefficients are found to be varying from machine to machine. In ASDEX Upgrade tokamak, during H-mode plasma discharges the Z dependence on impurity transport has been studied through Ne, Ar, Kr and Xe impurities (Dux et al.). It

strongly claims about the convection becomes dominated by increasing Z, leading to peaked impurity density profiles at the plasma core. In LHD it is seen that diffusivity almost independence of impurity specifies as investigated using C, Al, and Ti impurities, But convective velocity decreases with increasing atomic number (Morita et al.). However, in ADITYA-U tokamak, convection does not show a clear trend with increasing Z number or mass of the impurity. But diffusivity strongly depends on the atomic number Z and then correspondingly with atomic mass. The reason behind this dependency is not clear at this stage.

5.6. Molecular contribution in particle influx estimation:

Particle influxes are estimated with equation 4.4 as described in the previous chapter. In the earlier estimation, S/XB coefficient values were taken from the ADAS database, which was calculated through the collisional radiative model (Summers) in which only atomic processes were considered. However, as the neutrals occur at the plasma divertor region with low electron temperature the population of the hydrogen excited state may happen due to molecular processes. The molecular contribution in particle influx estimation is nowadays a subject of interest (Kremeyer et al.). Experimental investigation of molecular flux has been carried out through measurement of atomic, molecular, and total particle fluxes of deuterium on graphite limiter surface of TEXTOR tokamak through observation of D_α and D_2 fulcher band (Brezinsek et al.). In DIII-D tokamak, with passive visible spectroscopy diagnostic technique within the far edge/SoL experimentally D_2 molecular flux was estimated with D_2 fulcher bands (Hollmann, Brezinsek, et al.). However, it is a challenging task to get the direct measurement of H_α/D_α molecular Fulcher bands due to their low population densities. Hence, modelling of hydrogen spectral line with available neutral transport codes is helpful to understand the impact of molecular processes on particle influx.

5.6.1. Theoretical background

In equation 4.4 of Chapter 4, hydrogen influx is measured considering only atomic contribution to excitation and ionization. However, if the atomic and molecular contributions along with the charge exchange process are considered having processes mentioned in Table 5.3, the total brightness is given by the following formula,

$$I|_{total} = I_{H_\alpha}|_H + I_{H_\alpha}|_{H_2} + I_{H_\alpha}|_{H_2^+} + I_{H_\alpha}|_{H_{CX}} \quad 5.16$$

The influence of charge exchange is omitted from the total H_α emissions in equation 5.13. These particles are produced inside the plasma, not from the wall and plasma-facing components. The contribution in H_α emissions due to the charge exchange process is not included in the realistic estimation of particle influxes. The following equation represents influx:

$$\Gamma|_{total} = 4\pi \left(\frac{S}{XB} I_{H_\alpha}|_H + \frac{S}{XB} I_{H_\alpha}|_{H_2} + \frac{S}{XB} I_{H_\alpha}|_{H_2^+} \right) \quad 5.17$$

The charge-exchange contribution is switched off during simulation in the neutral transport code to get the H_α emissivity due to molecular processes. The ionization and excitation rate coefficients, represented by dissociative ionization S_{H_2} , $S_{H_2^+}$ and dissociative excitation X_{H_2} , $X_{H_2^+}$ for H_2 and H_2^+ ions are shown in Figure 5.24. The branching ratio is given by,

$$B = \frac{A_{32}}{A_{32} + A_{31}} \quad 5.18$$

Where A_{32} and A_{31} are Einstein's coefficients. The reaction processes considered in the estimation are tabulated in Table 5.3. The reaction rate coefficient for processes 1 to 5 in Table 5.4 depends on the electron temperature (Janev, Post, et al.). The rate coefficients are hence plotted in Figure 5.24. Dissociative ionization for H_2 and H_2^+ ion (Table 5.3 - Equations 1 and 2) and dissociative excitation process (Table 5.3 - Equations 3 and 4) in Figure 5.24 changes sharply up to ~ 20 eV temperature. However, for reaction process 5 (Table 5.3), the rate coefficient reduces with an increase in temperature. This is the electron impact dissociative recombination process of H_2^+ . The plasma electron temperature and H_2^+ ion has coulomb attraction acting between them, hence the reaction cross-section is large at small energies (Wigner). This cross-section has an inverse variation with collision energy. The threshold energy for the 5th reaction process is less than 1 eV (Janev Ratko et al.). Another reaction has threshold energies more than the reaction 5th's threshold energy (Janev, Reiter, et al.; Kubo et al.). The rate coefficient used for $\frac{S}{XB}$ estimations are plotted in Figure 5.24. It is important to note that molecular activated recombination and charge-exchange processes with protons have no significant contribution for above ~ 5 eV temperatures and those are not considered.

The simulated intensity (I_{H_α}) is estimated from calculated emissivity (ϵ_{H_α}). Here, the emissivity from the direct contributions of the atomic, molecule, and molecular ion are calculated using the DEGAS2 code (Dey, Chowdhuri, et al.; Dey, Ghosh, et al.). For ADITYA-

U discharge parameters, the experimental intensity is in terms of Photons m⁻² sec⁻¹ Sr⁻¹. The calculated intensity via code is derived using the following equation,

$$I_{H\alpha} = \frac{1}{4\pi} \int \varepsilon_{H\alpha} dx \quad 5.19$$

The molecular contribution is estimated with an equation,

$$\varepsilon_{H\alpha}|_{H_2} = n_{H_2} R_{H_2}(n_e, T_e) \quad 5.20$$

Where, n_{H_2} is the molecular hydrogen density obtained using the DEGAS2 code. The function R_{H_2} is the product of the branching ratio, electron density, and the reaction rate coefficient ($\langle \sigma v \rangle$), for process (3) in Table 5.3. R_{H_2} is given by,

$$R_{H_2} = n_e \frac{A_{32}}{A_{32} + A_{31}} \langle \sigma v \rangle_{3(} \text{Table 5.3)} \quad 5.21$$

Here, A_{32} is Einstein's coefficients of $3 \rightarrow 2$ transition and A_{31} is the t Einstein's coefficients of $3 \rightarrow 1$ transition. In the same way, the H_2^+ participate in H_α and emissivity for this is given by the modified form of equation 5.20 and rewritten as,

$$\varepsilon_{H\alpha}|_{H_2^+} = n_{H_2^+} R_{H_2^+}(n_e, T_e) \quad 5.22$$

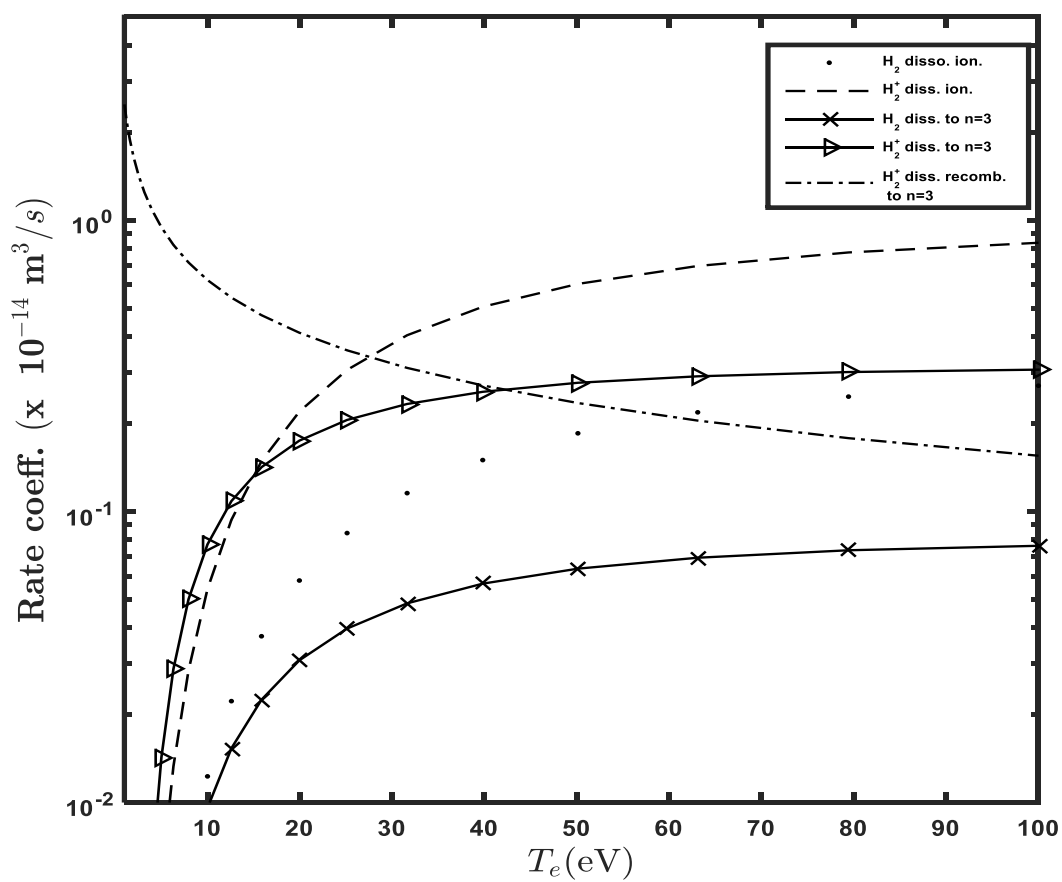
Where $R_{H_2^+}$ is given by,

$$R_{H_2^+}^+ = n_e \frac{A_{32}}{A_{32} + A_{31}} \langle \sigma v \rangle_{4 \& 5} \text{ (Table 5.3)} \quad 5.23$$

In equations 5.21 and 5.23, the $\langle \sigma v \rangle$ is the reaction rate coefficient of the molecular hydrogen excitation (process 4 Table 5.3) and molecular hydrogen ion dissociative recombination to $n = 3$ (process 5 Table 5.3). In the DEGAS2 code, the H_2^+ ions are taken as dissociative instantaneously as H_2^+ density is equal to the ratio ionization rate to the destruction rate.

Table 5.3. Molecular processes considered for influx estimations

No.	Process	
1	$H_2 + e \rightarrow H(1s) + H^+ + 2e$	Dissociative ionization for H_2
2	$H_2^+ + e \rightarrow H^+ + H^+ + 2e$	Dissociative ionization for H_2^+ ion
3	$H_2 + e \rightarrow H(1s) + H(n = 3) + e$	Dissociative excitation for H_2 to $n = 3$
4	$H_2^+ + e \rightarrow H^+ + H(n = 3) + e$	Dissociative excitation for H_2^+ ion to $n = 3$
5	$H_2^+ + e \rightarrow H(1s) + H(n = 3)$	Electron impact dissociative recombination process of H_2^+

Figure 5.24. The reaction rate coefficients as a function of electron temperature are used for calculations of S/XB of H_2 and H_2^+ ions.

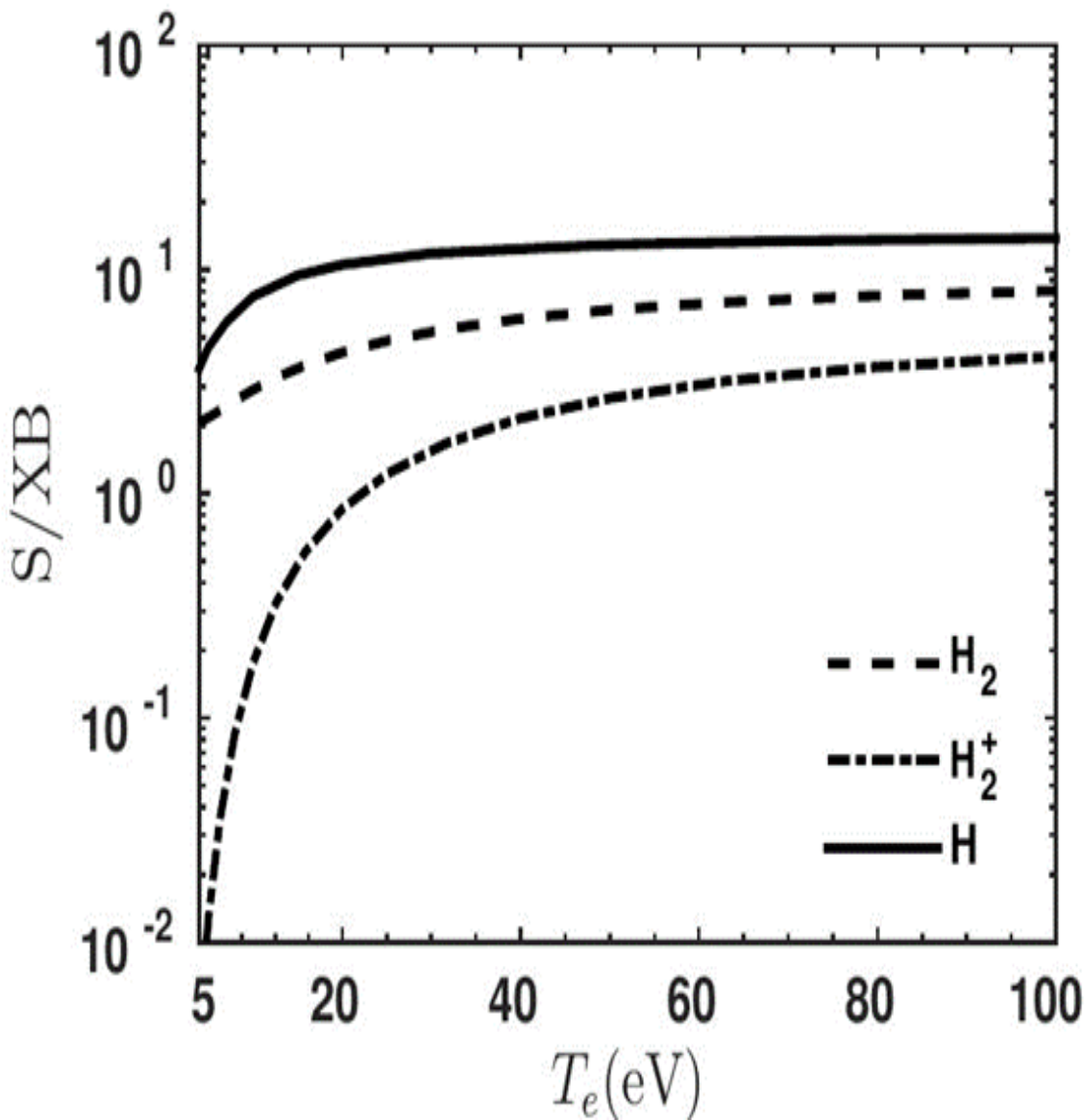


Figure 5.25. The S/XB of atomic H (solid line) and H_2 (dashed line) and H_2^+ (double dashed line) ion.

5.6.2. Experimental setup

During measurements at ADITYA-U tokamak, the LOS-1 and LOS-2 are used for terminating the chord on the toroidal graphite belt limiter surface as shown in Figure 5.26. Here, LOS-1 sees the plasma from the top port at an angle such that only the plasma edge gets into the LOS, and hence maximum molecular contribution can be present in this plasma region. LOS-2 is arranged on the radial port and terminates on the graphite limiter through the vertical mid-plane of the machine. The measurement has been done using PMT-based diagnostic as discussed in section 2.3.2. The interference filter used here is 656.28 nm of center wavelength. PMT current signals are converted to voltage using an I-V converter and acquired in DAQ. The full system is calibrated for absolute intensity.

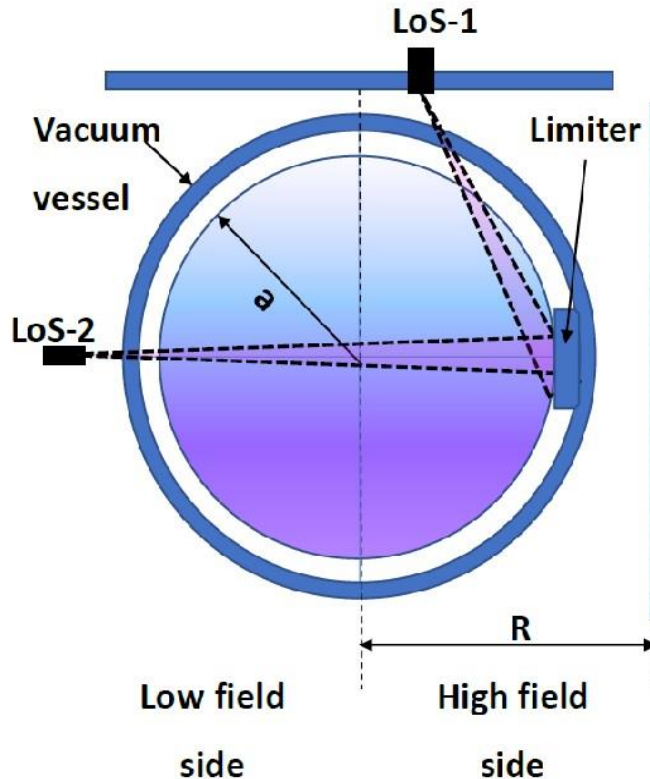


Figure 5.26. Schematic diagram of the viewing geometry in ADITYA-U tokamak. One Line of Sight (LOS-1) passes through the edge region only. The other Line of Sight (LOS-2) passes through the center of the machine.

5.6.3. Results about molecular contributions to particle influx

As seen in Figure 5.25, $\frac{S}{XB}$ for atomic H ions (solid line), and molecular H₂(dashed line) and H₂⁺ (dash-dot line). The S/XB ratio of H₂ molecule is expressed by $\left(\frac{S}{XB}\right)_{H_2}$ and the $\frac{S}{XB}$ of molecular ions is expressed as $\left(\frac{S}{XB}\right)_{H_2}^+$. The $\frac{S}{XB}$ varies with plasma electron temperature T_e. The atomic $\frac{S}{XB}$ are obtained from ADAS database. The molecule and molecular ion contributions for processes are mentioned in Table 5.1. It is important to observe that, the $\left(\frac{S}{XB}\right)_{H_2}$ are two times lower compared to the $\left(\frac{S}{XB}\right)_H$ for electron temperature \sim 5 to 20 eV. Additionally, $\left(\frac{S}{XB}\right)_{H_2}^+$ is \sim 17 times lower compare to $\left(\frac{S}{XB}\right)_H$ up to T_e \sim 12 eV. Also, the $\left(\frac{S}{XB}\right)_{H_2}^+$ is much lower than $\left(\frac{S}{XB}\right)_H$ for all the temperatures presented in Figure 5.25. In Wendelstein 7-X (W7-X) Stellarator, the molecular contribution of H_α was included and S/XB ratio is calculated by three different methods and used the estimation of H_α photon flux for the divertor target and baffle

the S/XB comes out to be 34 ± 2.3 (horizontal and vertical divertor targets and baffle). However, heat shields and steel panels have lower n_e and T_e , it produces a value of temperature is 14 ± 3.1 eV. In this study, only hydrogen atom is considered for S/XB estimation the contributions from molecular hydrogen ions are required to be incorporated for the estimation of particle influx

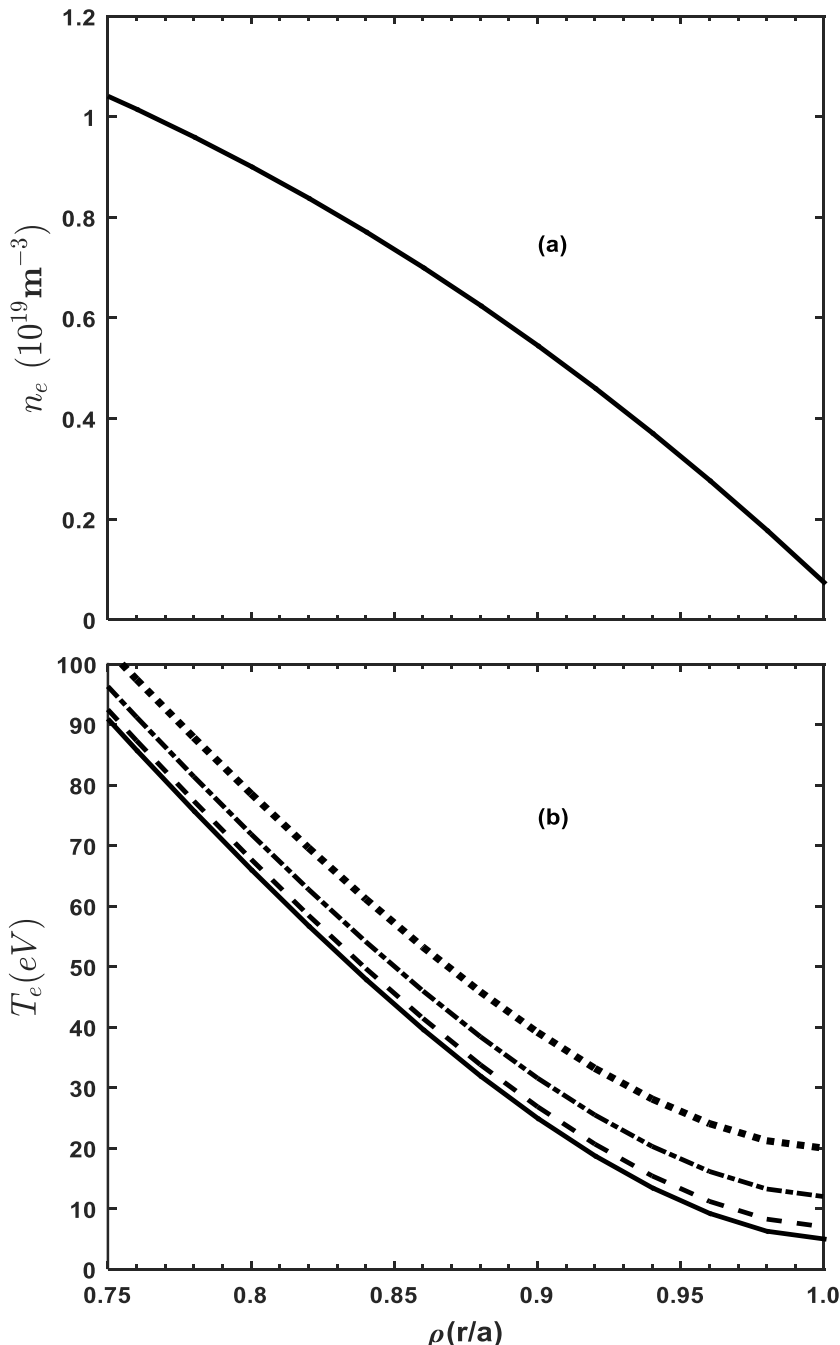


Figure 5.27. Radial profiles of electron (a) density and (b) temperature are used for the simulation. In the Zoom view of Figure (b) the solid, dashed, and dash-dot curves represent the edge electron temperature ($T_{e,a}$) of 5, 7, and 10 eV, respectively. The x-axis represents the ρ , which is the normalized radial location given by “ r / a ”.

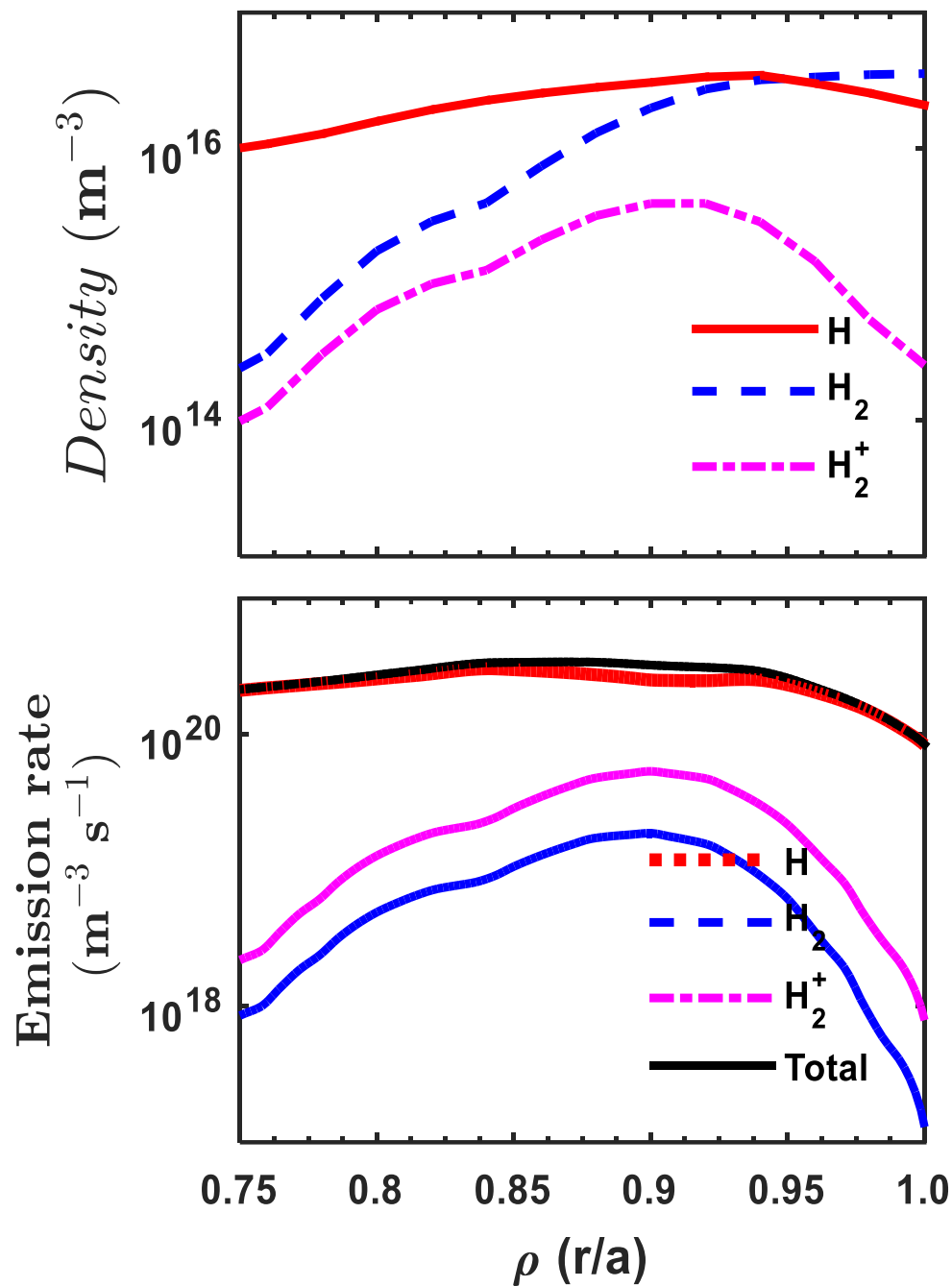


Figure 5.28. (a) Simulated density profiles of H , H_2 , and H_2^+ for the line-average density ($\langle n_e \rangle$) $1.37 \times 10^{19} m^{-3}$ and edge electron temperature is fixed to 7 eV (The dashed curve of Figure (4b)). The solid curve represents total neutral hydrogen density, the dashed curve represents the density of H_2 , and the dash-dot curve represents the density of H_2^+ ions. (b) The simulated emission rate of H , H_2 , and H_2^+ . The solid curve represents the total emission rate, the dotted curve represents the emission rate of H , the dashed curve represents the emission rate of H_2 and the dash-dot curve represents the emission rate of H_2^+ . The x-axis represents the ρ , which is the normalized radial location given by “ r / a ”.

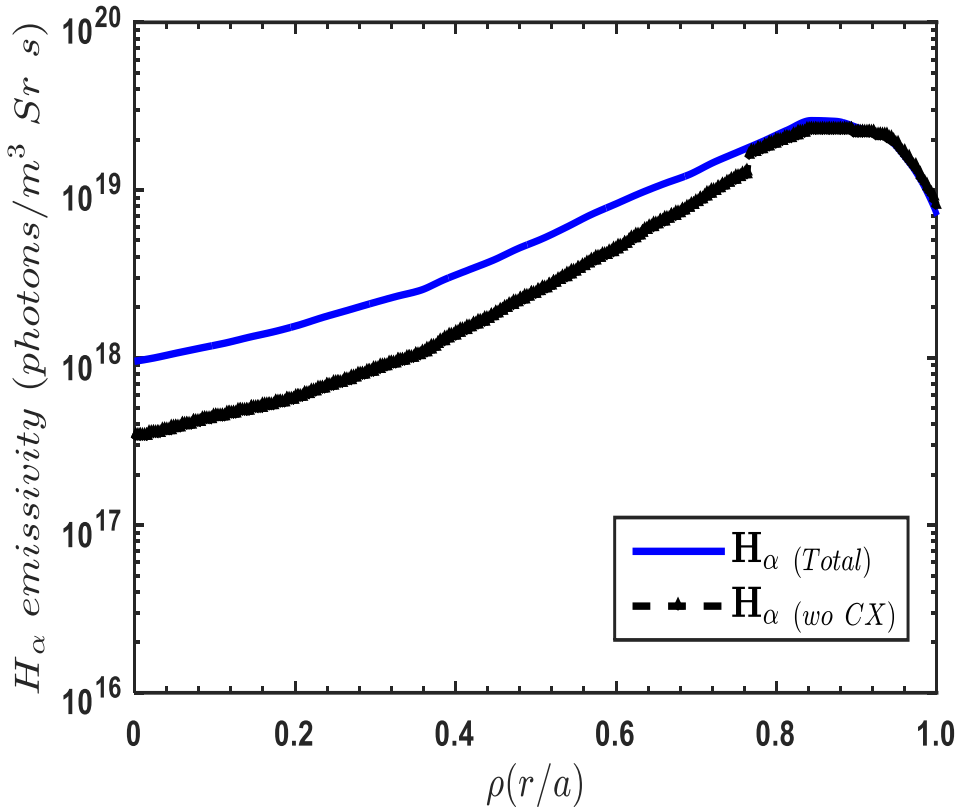


Figure 5.29. The simulated emissivity profile for the line-averaged electron density is $1.3 \times 10^{13} \text{ cm}^{-3}$ and $T_{e,a}$ is of 10 eV. The solid curve represents total H_α emissivity and the dashed curve represents H_α emissivity excluding the charge-exchange process.

Table 5.4 H_α intensity and particle influxes from atomic H , molecular H_2 , and molecular H_2^+ ion based on Equations (4) and (1), respectively, for various edge electron temperatures ($T_{e,a}$). This estimation is done by considering a viewing chord passing through the whole plasma and along the horizontal midplane (LOS-2 as per Figure 5.26).

$T_{e,a}$	I_{H_α} from H	I_{H_α} from H_2	$\frac{I_{H_\alpha}}$ from H_2	I_{H_α} from H_2^+	$\frac{I_{H_\alpha}}$ from H_2^+
	$(m^{-2}s^{-1}Sr^{-1}) \times 10^{18}$	$(m^{-2}s^{-1}Sr^{-1}) \times 10^{18}$	$\frac{I_{H_\alpha}}$ from H	$(m^{-2}s^{-1}Sr^{-1}) \times 10^{18}$	$\frac{I_{H_\alpha}}$ from H
5	3.65	0.17	0.05	0.49	0.13
7	4.15	0.08	0.02	0.24	0.06
10	4.06	0.06	0.01	0.18	0.04
	Γ_H $(m^{-2}s^{-1}) \times 10^{20}$	Γ_{H_2} $(m^{-2}s^{-1}) \times 10^{20}$	Γ_{H_2}/Γ_H	$\Gamma_{H_2}^+$ $(m^{-2}s^{-1}) \times 10^{20}$	$\Gamma_{H_2}^+/\Gamma_H$
5	3.48	0.06	0.02	0.01	0.003
7	3.94	0.03	0.008	0.005	0.001
10	3.86	0.02	0.005	0.004	0.001

Table 5.5 The H_α intensity and particle influxes from atomic H, molecular H₂, and molecular H₂⁺ ion based on Equations (4) and (1), respectively, for various edge electron temperatures (T_{e,a}) only at the edge region. This estimation done for the experimental condition when viewing the chord is passing through the edge plasma (LOS-1 as per Figure 5.26).

T _{e,a}	I _{H_α} from H (m ⁻² s ⁻¹ sr ⁻¹) × 10 ¹⁷	I _{H_α} from H ₂ (m ⁻² s ⁻¹ sr ⁻¹) × 10 ¹⁷	I _{H_α} from H ₂ I _{H_α} from H	I _{H_α} from H ₂ ⁺ (m ⁻² s ⁻¹ sr ⁻¹) × 10 ¹⁷	I _{H_α} from H ₂ ⁺ I _{H_α} from H
5	5.28	0.77	0.15	2.13	0.40
7	5.00	0.38	0.05	1.08	0.21
10	4.77	0.29	0.06	0.83	0.17
	Γ_H (m ⁻² s ⁻¹) × 10 ¹⁹	Γ_{H_2} (m ⁻² s ⁻¹) × 10 ¹⁹	Γ_{H_2}/Γ_H	$\Gamma_{H_2}^+$ (m ⁻² s ⁻¹) × 10 ¹⁹	$\Gamma_{H_2}^+/\Gamma_H$
5	7.30	0.45	0.06	0.33	0.05
7	7.23	0.24	0.03	0.20	0.03
10	7.19	0.22	0.03	0.22	0.03

The S/XB is temperature dependent and different for the hydrogen atom (H), molecule (H₂) and molecular ion (H₂⁺). The S/XB for H is present in the ADAS database. As discussed in the previous section, the S/XB for H₂ and H₂⁺ is calculated for processes mentioned in Table 5.3. As shown in Figure 5.27, in the temperature range of T_e ~ 5 – 20 eV, the S/XB of H₂ is ~2 times less than H, up to T_e ~ 12 eV, the S/XB of H₂⁺ is ~17 times less than H. It is clear from Figure 5.27 for all the temperature ranges,

$$\frac{S}{XB}|_H > \frac{S}{XB}|_{H_2} \text{ and } \frac{S}{XB}|_H \gg \frac{S}{XB}|_{H_2^+}$$

In ADITYA-U tokamak with its n_e and T_e profiles, the contribution of molecular H₂ with atomic H are estimated by knowing molecular fluxes through the modelling of the experimental radial profile of H_α using DEGAS2 neutral transport code. The input set in the code are particle source rate through the recycling process and n_e and T_e profiles of ADITYA-U plasma. The output of this code is a neutral particle radial profile. The line averaged plasma density n_e is ~1.3 × 10¹⁷m⁻³ and temperature T_{e,0} = 370 eV with b = 1.75 used in equation 5.9 to get the n_e and T_e profiles(Dey, Chowdhuri, et al.). The electron temperature at the edge and core is obtained from the Langmuir probe and soft X-ray respectively. The emissivity of H_α dominantly change at lower temperatures and its dependency on edge in both H_{α(A+M)} is 3.88 ×

$10^{20} \text{ m}^{-2} \text{s}^{-1}$. Atomic S/XB values are taken from the ADAS. The estimated particle influx using the DEGAS2 code is in the order of $10^{20} \text{ m}^{-2} \text{s}^{-1}$, it matches well with the influx estimated in the previous chapter. However, in the previous chapter influx was measured through the atomic contribution only. During the calculation of atomic contribution, the charge exchange is not considered. As shown in Figure 5.29, the total H_{α} emissivity from atomic and charge-exchange contributions are presented with solid lines. However, the dashed line represents the H_{α} emissivity from only the atomic process by turning-off the charge-exchange in the DEGAS2 code. It is clear from Figure 5.29, that the charge-exchange process is contributing towards the plasma core region, not at the edge. In ADITYA-U, with some experimental conditions such as gas-puff the edge temperature becomes ≤ 10 eV, sometimes even becomes much less than 5 eV (Krasheninnikov and Kukushkin; Macwan et al.; Dimitrova et al.). For the tokamak with a detached divertor the temperature decreases $< 2 - 5$ eV, this gives rise to the molecular processes that occur. Although the difference is very less as discussed in the description of Table 5.4. It is a fact that the H_{α} present toward the inner region of plasma due to relatively low plasma density ($1.0 - 2.5 \times 10^{17} \text{ m}^{-3}$) at ADITYA-U tokamak (Dey, Chowdhuri, et al.). However, the molecular contributions are there within the last ~ 4 cm of plasma from LCFS, as reflected in Figure 5.29 (a). The LOS-2 (Figure 5.29), nullifies the molecular contributions during influx estimation. The molecular contribution is apparent when seen from LOS passing through the edge region only, i.e., LOS-1 (Figure 5.29). The estimated values for the edge contribution only are tabulated in Table 5.5. The intensity of H_{α} is $\sim 30 - 55$ % is from molecular H_2 and H_2^+ at lower $T_{e,a}$ values. The influx is $\sim 6 - 11$ % from atomic H (column 2 of Table 5.5). With experimental conditions with $T_{e,a} = 7$ eV, total influx due to atomic and molecular both processes $H_{\alpha(A+M)} = 7.6 \times 10^{19} \text{ m}^{-2} \text{s}^{-1}$. The same is seen in Table 5.5, where the molecular processes occur significantly with edge/SOL temperatures below 5 eV, this is possible in detached divertor plasma conditions. Using EMC3-EIRENE modelling in Wendelstein 7-X (Kremeyer et al.), the S/XB is calculated using various four methods to estimate the H_{α} photon flux. During the investigation, it was found that S/XB for horizontal and vertical divertor targets and the baffle is 34 ± 2.3 and for the heat shield and steel panel having lower n_e and T_e is 14 ± 3.1 . Also from different methods, the S/XB values are matching well. With this it becomes important to if only atomic hydrogen is considered in all the studies (as in Chapter 4), the molecule and molecular ion contributions need proper estimation for influx measurement. In principle, the molecular contributions can be measured by measuring the hydrogen Fulcher band. In limiter tokamak plasma it is difficult to have the spectrum having molecular bands due to its plasma density and temperatures in the edge and

SOL. Then the approach described here, can be another way to get the molecular contribution is through modelling with neutral transport code.

5.6.4. Summary

Particle influx at the tokamak plasma's edge is studied, with a focus on the molecular contribution. This is done by separately calculating the S/XB ratios of atomic H, molecular H₂, and H₂⁺ ions in H_α emission. The neutral particle transport code DEGAS2 is used to first simulate the radial profile of H emissivity, and then the measurements along two viewing chords that pass through the entire and only edge region of the ADITYA plasma are compared with the simulated data to estimate particle influxes from the molecule. In this case, we see one chord from the machine's radial port and another from its top port. Particle fluxes are also estimated for ADITYA-U tokamak plasma at different edge electron temperatures. It has been determined that the molecular contribution to the particle influx is not particularly large for an edge T_e~ 10 eV. When the S/XB is computed taking into account only atomic processes, the value of total influxes is $4.09 \times 10^{20} \text{ m}^{-2}\text{s}^{-1}$, while when both atomic and molecular processes are considered, the value is $3.88 \times 10^{20} \text{ m}^{-2}\text{s}^{-1}$. When measuring through a viewing chord that does not traverse the entire plasma, the effect of the molecular contribution becomes more apparent. When edge-chord measurements are included, the molecular contribution drops to around 6 – 9 % of the total flux. When the edge/SOL temperature drops below 5 eV, as it does in the detached divertor plasmas, the contribution from molecular processes grows significantly.

Chapter 6. Determination of gas-temperature for developing a technique to characterize divertor plasma

The existence of experimental tokamaks around the world allows a huge amount of experimental research on the MCF, including creating operation scenarios, testing developed components, and expanding our understanding of the underlying plasma physics phenomena. However, the intricate design of tokamaks can make it difficult to get an accurate understanding of certain ports or areas of interest. Furthermore, completing investigations on specific plasma behaviour or accessing certain conditions is challenging due to the competitive nature of getting the time slot in the experimental campaigns of large fusion experiments. There is a need to supplement the tokamak research with the studies of fundamental plasma experiments in small devices designed to reproduce specific features of tokamak plasma physics. Performing fundamental experiments in laboratory plasmas by recreating specific conditions of the tokamak plasmas can help to address some of the unexplained issues of tokamak physics. In comparison to tokamaks, these machines are easier to diagnose since they are built with a linear shape that simplifies the problem. Diagnosing plasma parameters and the behaviour of atoms and molecules in smaller and more manageable chambers is possible by conducting laboratory studies of the plasmas. This way, databases, and predictive models can be strengthened by

focusing on the information currently missing. One such device is an RF capacitively coupled plasma discharge source, which can be used in this research and allows for the exploration of the key processes in low-temperature plasmas that would otherwise be inaccessible in large tokamaks.

This chapter presents the RF capacitively coupled plasma device to simulate the experimental conditions relevant to ADITYA-U tokamak's detached divertor plasma conditions. In this study, characterization techniques for divertor plasma have been developed which can be useful for ADITYA-U detached divertor plasma operations. The machine was also used for the tungsten coating of limiter tiles of ADITYA-U tokamak.

6.1. Low-temperature plasma discharges

Laboratory plasma takes the form of a gas discharge when the application of sufficient electrical energy ionizes the neutral gas. In its simplest form, plasma can be created by applying a potential difference between two electrodes. The potential difference accelerates electrons which ionize the atoms present in the background gas. The neutral gas could become a conducting medium and undergo ionization and the formation of a plasma if the electric field is sufficiently strong. The core plasma, where fusion occurs, is extremely hot and has a moderate to high density. In magnetically confined fusion reactors, the electron temperature and density in the outermost regions are typically lower than the plasma central region. In the lab, Low-pressure plasma discharges with lower T_e is produced by the use of vacuum pumps. The operating pressure is kept lower than that of the surrounding atmosphere. These types of plasmas are created for the production of liquid crystal displays, the etching of semiconductors, and the deposition of thin films via sputtering. All these applications benefit from working at such low pressures due to longer mean-free paths. This broadens the distribution of energy, which in turn facilitates a wide range of significant interactions in the plasma. There are many ways to generate low-pressure plasmas, such as microwave plasmas, hollow cathode arc plasmas, magnetrons, DC glow discharges, and radio frequency (RF) plasmas. This chapter will concentrate on capacitively coupled radio frequency plasmas.

Capacitively coupled plasmas (CCP) and inductively coupled plasmas (ICP) are types of plasma discharges that use radio frequency power to ignite a plasma. CCP sources are distinguished by having only one of their two electrodes connected to the RF power supply while the other electrode is grounded. In an electrical circuit, this arrangement functions like a

capacitor. Diagnostic measurements are presented in this thesis that was taken using a CCP discharge source to develop a technique to estimate gas temperature and how other molecular bands affect the estimation of parameters in low-temperature plasmas. The results of these measurements are included in this thesis.

6.2. Relevance of low-temperature plasma device to tokamak

As discussed in (Koepke), there is a wealth of research that demonstrates the value of conducting experiments in a controlled laboratory setting to verify or refute theoretical plasma models, find unexpected results that might not be accessible in larger machines, and gain physical insight into phenomena. It is possible to investigate plasma-material interactions, plasma detachment, and the impact of gas pumping on the evolution of detachment using linear plasma devices like NAGDIS-II, PISCES-B, GAMMA-10, and MAGNUM PSI (Ohno; Y. Hirooka et al.; Nakashima et al.; Hayashi et al.). Magnum-PSI (Buzi et al.) and PISCES-A (Schmitz, Lehmer, et al.; Schmitz, Merriman, et al.), are experiments using linear devices that focus on the interaction between plasma and material surfaces and basic plasma devices by understanding the effects of deuterium irradiation on tungsten samples. The extent to which transient events in the plasma, including edge localized modes (ELMs), cause damage is a crucial factor. An essential objective is to investigate the impacts of these events (for instance, in Magnum-PSI(Morgan et al.), which can momentarily raise the power fluxes to as much as 10 GW/m^2 (the projection for ITER).

Using linear plasma devices greatly simplifies the process of creating diagnostic tools. It is more practical to create and test instruments on smaller machines since large machine, like tokamak is expensive and has limited experimental time. Examples include the use of quick imaging measurements to extract information on coherent waves in the plasma in CSDX (Light et al.) and the development of a vorticity probe for the Large Plasma Device (LAPD) (Horton et al.). There have been numerous applications of CSDX to the study of turbulence in plasma flows, including the tracing of transitions between turbulent and shear flow regimes (see e.g. (Tynan, Diamond, et al.; Chakraborty Thakur et al.)). The implications for tokamak confinement from these studies are substantial. There is some evidence to suggest that shear fluxes in the plasma's boundary area have a role in the emergence of the high-confinement, or H mode, which results in more favorable conditions for fusion (Tynan, Schmitz, et al.). Plasma instabilities like turbulence and drift waves have been investigated in the machines like

Mirabelle (Gravier et al.) and Mistral (Jaeger et al.). In addition, simulations of a detached divertor have been examined using Mistral to study plasma recombination (Brault et al.). Similarly, The studies of plasma recombination for detachment experiments (Macwan et al.) using gas puffing have been done in linear devices (Rusbridge et al.; Willett). Fusion reaction-produced ion behaviour and cesium-free alternatives to the negative ion sources for auxiliary power injection into tokamaks can be investigated in discharge plasmas (Schenkel et al.; Barnes). Some of the conditions found in tokamaks' edge plasmas can be recreated using Inductively Coupled Plasmas (ICPs) and other low-temperature discharge plasma. To simulate the low-temperature plasma conditions of the tokamak divertor, devices with a few eV temperatures and lower densities than linear plasma can be used. With the ability to precisely control the discharge conditions and, in turn, the plasma parameters, the study of these parameters becomes possible in ICP devices.

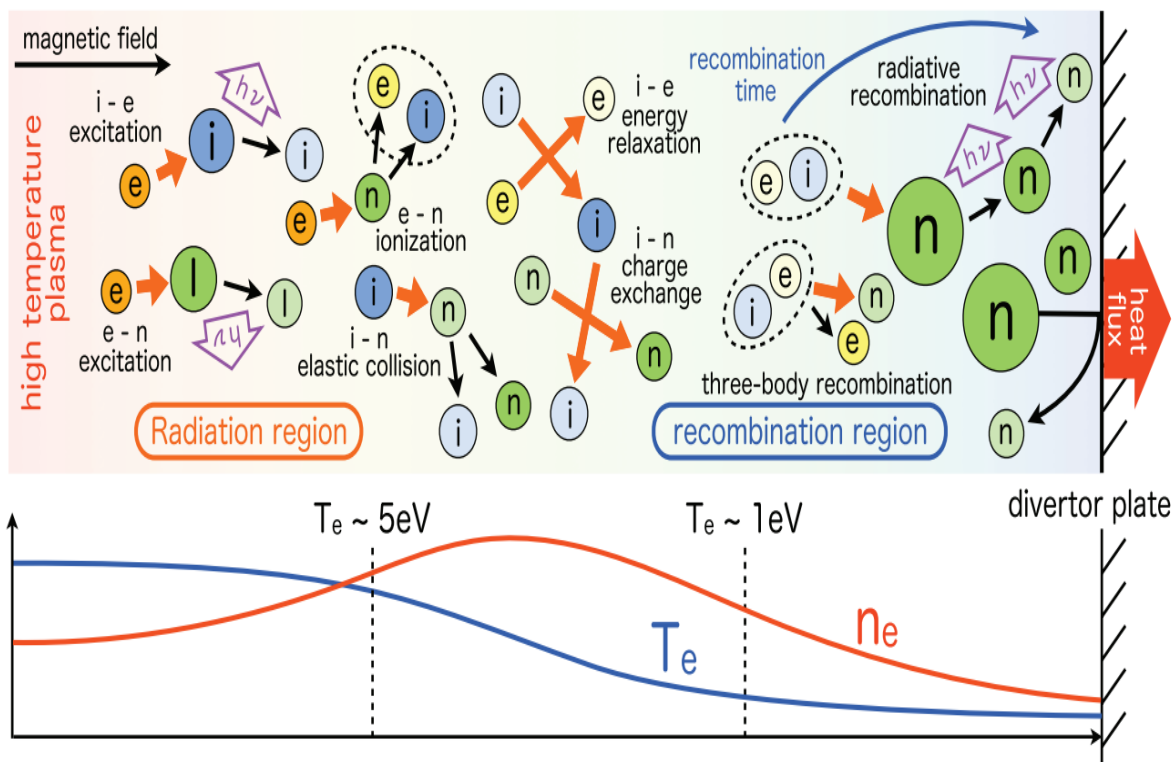


Figure 6.1 Schematic depiction of the divertor plasma in a fusion device and the axial profiles of n_e and T_e as they form during transport into the divertor plate at high neutral pressure. Electron (e), Ion (i), Neutral (n), and Impurity are all denoted by their respective labels on the periodic table. Large bubbles represent atoms with a high level of excitation, as indicated by their colour (Hayashi et al.).

The following are examples of typical plasma parameters found in linear devices: The electron density n_e is about 10^{19} m^{-3} , and the temperature T_e is about 10 eV. T_e is a few eV

less than the temperature of an ion, T_i . The plasma parameter in the divertor area having detached plasma is depicted schematically in Figure 6.1. Due to electron impact excitation and ionization, electrons in the upstream region with high electron temperature are cooled down to around $T_e \sim 5$ eV nearby to target plate. When the plasma density is high and the electron energy is around 1 eV, electron-ion recombination (EIR) occurs, decreasing both the particle flux and the heat flux to a divertor plate.

Capacitively Coupled Plasma (CCP)

Capacitively coupled RF reactors typically take on a cylindrical or rectangular shape, with parallel circular or rectangular electrodes. The electrodes in these systems can have a variety of forms and geometries, including those of a showerhead or hollow cathode. Adjusting the distance between the electrodes is made possible by vacuum linear motion feed-throughs built into the reactors. To contain the discharge within the gap between the electrodes, either the electrodes must be in direct contact with the discharge or the electrodes must be surrounded by a grounded shield. To produce radio frequency energy, a typical CCP RF system employs an RF generator, two parallel electrodes, and a matching network. The latter is positioned between the generator and reactor to optimize power transfer by matching the complex reactor impedance to the generator's characteristic impedance. A CCP RF discharge can generate a base pressure value anywhere from 1 mTorr to 10 Torr. The electron densities in these discharges range from 10^{12} m^{-3} to 10^{16} m^{-3} and can approach 10^{17} m^{-3} (Popov) at higher frequencies. Near the powered electrode, the ion energy can range from tens to hundreds of eV. The 13.56 MHz is the most common although multiple RF frequencies have been used. This is simply the maximum frequency at which a given amount of energy can be radiated without interfering frequency used for communications (Chapman, Brian and J. L. Vossen).

During experiments presented in this chapter, the 13.56 MHz RF plasma reactor is used. This device has two purposes, one is the plasma-enhanced chemical vapor deposition (PECVD) which is used for depositing the tungsten (W) on graphite limiter tiles of ADITYA-U. Another purpose is to have a low-temperature environment, to study the diverter-like plasma and use it to develop diagnostics techniques for divertor characterization.

6.3. Experimental setup

The primary goal of the experiment is to create a reactor for producing a plasma that is comparable to the divertor plasma temperature. For this, a stainless-steel vacuum vessel of cylindrical shape (360 mm in diameter) and 300 mm in height has been developed (SS 304). Five 35 CF viewports are mounted on the top, and eight 63 CF viewports are arranged radially for viewing and accessing various components of the pumping system, gauges, probes, etc. To generate the glow discharge plasma, an RF source with a frequency of 13.6 MHz and a power of 600 W is used in a chamber with two circular metallic disc electrodes with a diameter of 100 mm and a spacing of 25 mm. A voltage is applied to the top electrode, while the bottom is grounded. A rotary pump with a capacity of $12 \text{ m}^3/\text{hr}$ is used to bring the system to the roughing vacuum, subsequently, a turbo-molecular pump with a capacity of 60 liters/sec is used to bring the system to the desired base pressure. Pirani and Cold cathode gauges are used to measure and track the vacuum. Tungsten hexafluoride (WF_6) is typically used as a precursor gas and introduced into a background hydrogen plasma in tungsten coating experiments. In this research, the system is pumped down to $2 \times 10^{-5} \text{ mbar}$ before the hydrogen gas is fed into it, and hydrogen discharge is produced with hydrogen fill pressure $5 - 8 \times 10^{-3} \text{ mbar}$ using 80 W of RF power.

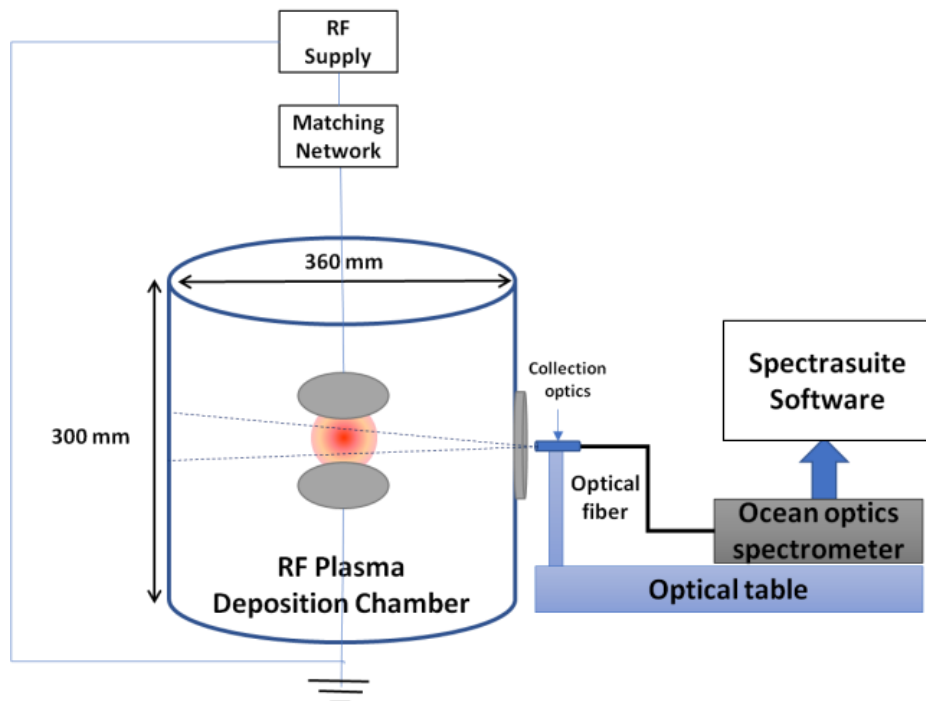


Figure 6.2. Experimental setup on linear plasma device

As shown in Figure 6.2, an optical emission spectroscopy measurement is performed. The optical window is made of fused silica, and adequate light is transmitted to the spectrometer with light-collecting optics, all of which are mounted on the 63 CF radial view port. The optics for collecting light consist of a collimating lens and an optical fiber with a 1 mm core diameter. After that, the light is coupled to the spectrometer's entry slit. The experiment uses a high-performance miniature spectrometer that is both portable and compact (Make: Ocean Optics; USB4000). It has a 3648 – pixel, built-in detector (Make: Toshiba; TCD1304AP). The visible spectrum can be covered by a grating with 300 grooves/mm and operates between 350 and 900 nm. The grating is blazed at 650 nm. The SpectraSuit software and a computer with a USB port provide both power and control for the spectrometer. The exposure time is variable and the slit width is a constant 20 μm . The exposure time was kept constant at 1 sec for all of the experiments that provided the data presented here. Pen ray lamp sources (UVP-made) with a variety of mercury lines were used to calibrate wavelengths. As shown in Figure 6.2, the line of sight follows a chord that passes through the plasma's midplane as it enters the deposition chamber. Here, we present data collected after the plasma inside the chamber has been stabilized.

6.4. Measurement technique

At low temperatures the ion temperature (T_i) and gas temperatures (T_g) of plasma become equal (Lopez). To know the gas temperatures in the detachment region, where temperatures are low, the Boltzmann plot method can be used to characterize the detached plasma region. Using the Boltzmann plot method, the temperature of the plasma gas is represented by the molecule's vibrational temperature (T_{VE}). The visible molecular bands produced by N_2 molecules are numerous and easily detectable. The addition of a negligible quantity of nitrogen gas to a hydrogen-generated plasma makes gas temperature characterization easy going assignment. While keeping a close eye on the plasma's spectral emission, nitrogen (air) is slowly leaked into the stable hydrogen plasma. The air leak of nitrogen is controlled so that spectrally intense N_2 molecular lines are seen.

Electronic, vibrational, and rotational temperatures in plasmas are typically calculated using the most well-known Boltzmann plot method (Kunze). With the help of this idea, we were able to extrapolate vibrational temperatures from observed spectra of N_2 vibrational bands and thus provide a better understanding of the nature of N_2 molecule and it is mentioned as the

experiment-based temperature estimation here. You can learn all about diatomic molecular spectra and the terminology used to describe them in references (Huber and Herzberg; Mulliken). The following equation describes the strength of the spontaneous emission radiated by excited molecules as they jump from an upper-level vibrational state to a lower-level vibrational state (Herzberg; Nassar et al.).

$$I_{v'v''} = \frac{h\nu_{v'v''}}{4\pi} g_v A_{v'v''} n_0 e^{-\frac{E_{v'}}{k_B T_{VE}}} \quad 6.1$$

Here, we have the vibrational quantum numbers of the excited and ground states, denoted by v' and v'' . The transition intensity, $I (v' v'')$, the Einstein coefficient, $A (v' v'')$, the statistical weight of the vibrational level of the molecule, g_v , the vibrational temperature, T_{VE} , and the Boltzmann constant, k_B , are all represented in this equation. The vibrational energy is denoted by E'_v and varies with v . The kinetic energy associated with vibration at a given v' is modelled as an anharmonic oscillator.

$$E_{v'} = \omega_e \left(v' + \frac{1}{2} \right) - \omega_e \chi_e \left(v' + \frac{1}{2} \right)^2 \quad 6.2$$

Where the constant of vibration is denoted by ω_e and the constant of anharmonicity by $\omega_e \chi_e$. The current computational model ignores the impact of higher-order anharmonicity (Roux and Michaud). For N₂ upper energy level the values are, $\omega_e = 17.33 \text{ m}^{-1}$ and $\omega_e \chi_e = 0.14 \text{ m}^{-1}$ (Roux and Michaud). The equation can be further reduced to:

$$\ln \left(\frac{I_{v'v''} \lambda_{v'v''}}{g_v A_{v'v''}} \right) = - \frac{E_{v'}}{k_B T_{VE}} + C \quad 6.3$$

vibrational temperature (T_{ve}) is calculated from the slope (m) of the line ($y = mx + c$) where

$y = \ln \left(\frac{I_{v'v''} \lambda_{v'v''}}{g_v A_{v'v''}} \right)$ and $x = E(v')$ with $g_v = 1$.

Temperature can also be estimated through a different method, which is called simulated estimation here, which relies on modelling the spectral line profiles of the vibrational bands under the same intensity distribution shown in equation 6.1. This is based on the assumption that the profile function $P(\lambda, \text{FWHM})$ of the spectral line is a Gaussian function.

$$P(\lambda, \lambda_{FWHM}) = \sqrt{\frac{4 \ln 2}{\pi}} \frac{1}{\Delta \lambda_D} \exp \left[-4 \ln 2 \left(\frac{\lambda - \lambda_0}{\Delta \lambda_D} \right)^2 \right] \quad 6.4$$

Here, $\Delta\lambda_D$ is the FWHM of the Gaussian profile produced by Doppler broadening. The FWHM of the line shape determines the final modelled intensity of a single molecular transition, but the intensity itself is a temperature-dependent parameter, as shown in equation 6.1. Consequently, the experimental spectra agree with the simulated or modelled spectra at a certain temperature value, which can be achieved by adjusting the FWHM and temperature. Then, the simulated spectra measurements are compared to the direct experimental measurements.

The simulated estimation technique is likely to be more accurate than the experimental measurement technique as described here. The spectra measured from the RF plasma are in a steady state and have very good signal strength, and the signal-to-noise ratio is $\sim 2\%$ considering the white noise. The fitting error in the linear fit to the data points in the Boltzmann plot is $\sim 2\%$. The main error arises from the transition probabilities, which are reported to be $\sim 10\%$ (Ribes and Caremoli). Hence, an error of 10% is considered in our estimations. Similar error estimations are reported in the Boltzmann plot methods claiming an uncertainty of $\sim 10\text{--}13\%$ in the temperature estimations (Muhammad Fahad, Sajjad Ali, Khizar Hussain Shah, Asim Shahzad, and Muhammad Abrar; Deeba et al.)

In the experimental measurement method, the fitting error is introduced twice; once during multi-peak Gaussian fitting and another during the linear fitting of the Boltzmann plot. But only Gaussian fitting error remains in the estimation process. Then, proper iteration in the simulation-based measurement yields more accurate temperature readings.

6.5. Plasma neutral-gas temperature measurement using two different approaches

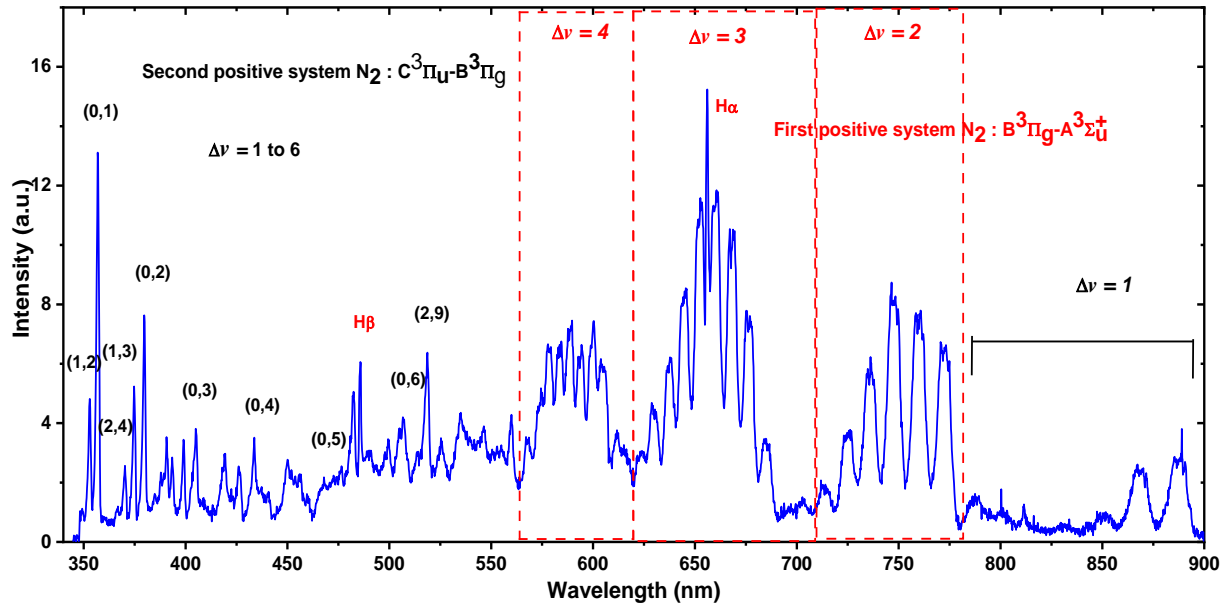


Figure 6.3 Identified molecular bands of nitrogen along with H_α and H_β lines

Figure 6.3 depicts the observed spectrum, this emission spectrum is marked with N_2 1PS and the bands are present mainly in the wavelength range of 550 to 800 nm. Three band having transitions $\Delta\nu = 2, 3$, and 4 , are marked, it corresponding to the transition $B^3\Pi_g - A^3\Sigma_u^+$ from N_2 first positive system (1PS). The second positive nitrogen system (C – B) can also be seen in Figure 6.3. In addition, the 656.28 nm and 486.81 nm atomic lines of hydrogen, marked as H_α and H_β , are strikingly visible.

6.5.1. Experimental estimation of temperature

(a) Description of $\Delta\nu = 4$

The wavelength range of $\Delta\nu = 4$ band is 560–620 nm as shown in Figure 6.4 (a). A total of nine vibrational transitions are identified in this range, these transitions are tabulated in Table 6.1. In the experimental data, the background has been removed. Using Origin 8.5 Software, the multi-Gaussian fit is made to the spectrum. The peak values of the resulting intensities are used to generate a Boltzmann plot along with the vibrational level energy deduced using equation 6.2. The Boltzmann plot is given in Figure 6.4 (b). Using slope $m_{\Delta\nu=4} =$

-3.09×10^{-4} of Boltzmann plot, the vibrational temperature is calculated to be $T_{\text{vib}}|_{\Delta\nu=4} = 4680 \text{ K} (\sim 0.40 \text{ eV})$ from the slope .

(b) *Description of $\Delta\nu = 3$*

For vibrational transition $\Delta\nu = 3$ of $\text{N}_2 - 1\text{PS}$, the identified spectrum is in the wavelength range of 620 to 820 nm. $\Delta\nu = 3$ band is shown in Figure 6.5 (a) also the identified transitions of this band are given in

Table 6.2. The eight transitions are identified and analyzed for temperature measurement in this study. The multi-Gaussian fit is performed on this spectrum. Using resultant intensity and upper-level vibrational temperature from equation 6.2, the Boltzmann plot is generated and shown in Figure 6.5 (b). Using equation 6.3, it is found that the vibrational temperature is $T_{\text{vib}}|_{\Delta\nu=3} = 7931 \text{ K} (\sim 0.68 \text{ eV})$, where the slope, $m_{\Delta\nu=3} = -1.82 \times 10^{-4}$.

(c) *Description of $\Delta\nu = 2$*

The $\Delta\nu = 2$ band of $\text{N}_2 - 1\text{PS}$ is presented in Figure 6.6 (a), it occurs between 700 and 800 nm of wavelength range.

Table 6.3 lists the wavelength and respective transition probabilities of all the identified vibrational transitions. Again, with the same technique, the multi-Gaussian fitting is done over the entire wavelength range of $\Delta\nu = 2$ band. The deduced intensities along with upper-level vibrational energy is used to get the Boltzmann plot as shown in Figure 6.6 (b). Vibrational temperature is found to be is $T_{\text{vib}}|_{\Delta\nu=2} = 7851 \text{ K} (\sim 0.67 \text{ eV})$, where the slope, $m_{\Delta\nu=2} = -1.84 \times 10^{-4}$.

It is clear from this that the temperature predicted by the $\Delta\nu = 4$ band is different from the temperature predicted by the $\Delta\nu = 2$ and 3 bands, which give temperatures of $7800 \text{ K} (\sim 0.67 \text{ eV})$ to $8000 \text{ K} (\sim 0.69 \text{ eV})$. The B-triplet state should have the same vibrational temperature as the ground state because the emission occurs at the same upper energy level.

Table 6.1. Wavelength data for $\Delta v = 4$

$\Delta v = 4$	Wavelength		Transition Probability
$v' - v''$	(nm)	Observed	$\times 10^4 \text{ (sec}^{-1}\text{)}$ (Gilmore et al.)
	(Gilmore et al.)	Observed	
13-9	569.6	567.8	11.0
12-8	574.4	574.1	10.0
11-7	579.2	578.5	9.5
10-6	584.2	583.5	8.1
9-5	589.4	588.8	6.4
8-4	594.7	594.0	4.6
7-3	600.1	600.1	2.9
6-2	605.7	605.1	1.5
5-1	611.4	612.8	0.6

Table 6.2. Wavelength data for $\Delta v = 3$

$\Delta v = 3$	Wavelength		Transition Probability
$v' - v''$	(nm)	Observed	$\times 10^4 \text{ (sec}^{-1}\text{)}$ (Gilmore et al.)
	(Gilmore et al.)	Observed	
10-7	630.9	628.2	7.6
9-6	638.0	637.9	9.1
8-5	645.4	644.7	9.9
7-4	653.0	652.7	9.6
6-3	660.8	660.1	8.2
5-2	668.9	668.3	5.9
4-1	677.2	676.4	3.5
3-0	685.8	685.0	1.1

Table 6.3. Wavelength data for $\Delta\nu = 2$

$\Delta\nu = 2$ $v'-v''$	Wavelength (nm)	Transition probability $\times 10^4$ (sec $^{-1}$) (Gilmore et al.)
	(Gilmore et al.)	Observed
7-5	714.7	713.5
6-4	725.5	725.0
5-3	736.8	735.9
4-2	748.4	747.7
3-1	760.6	759.9
2-0	773.2	772.4

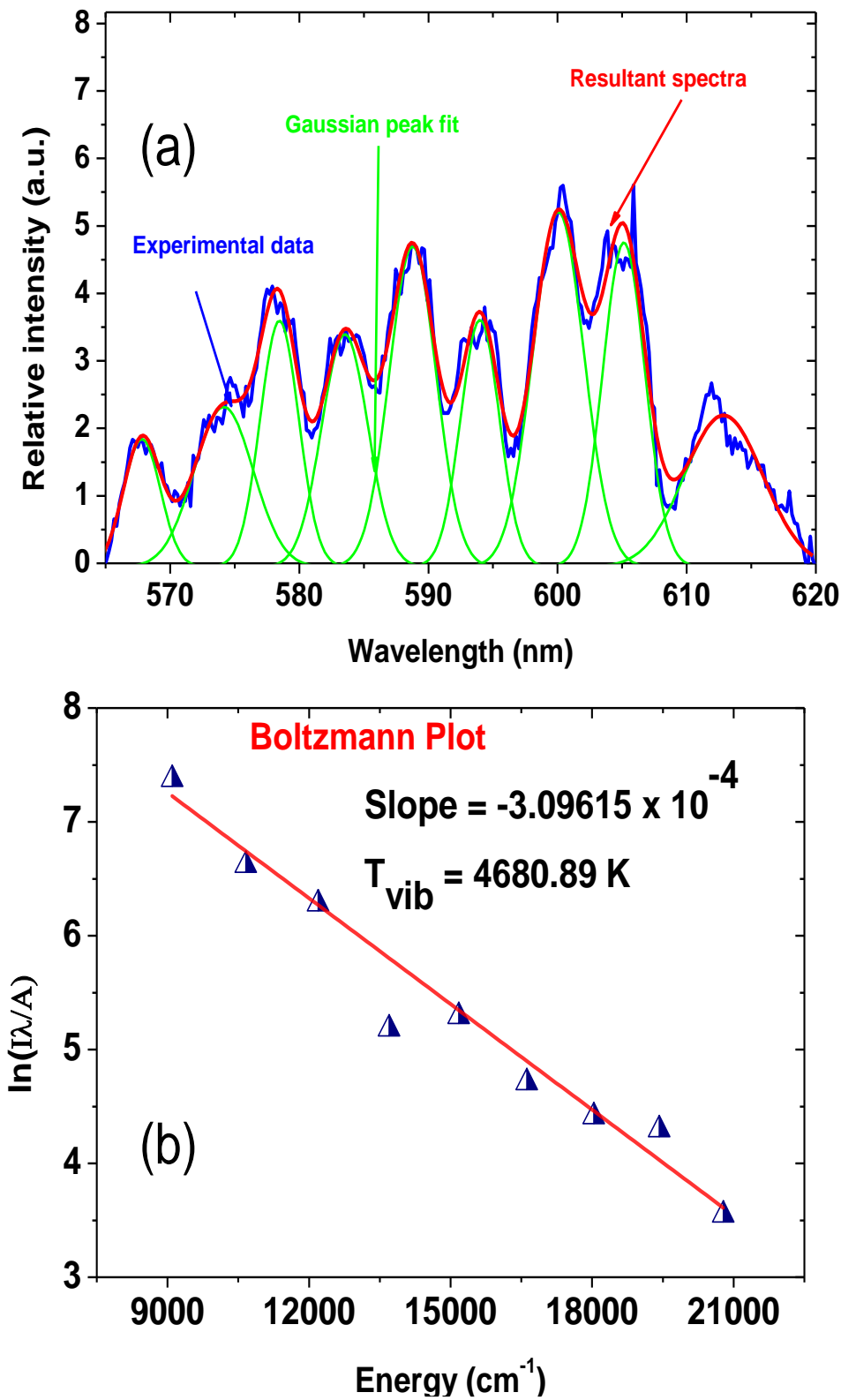


Figure 6.4 Experimentally measured temperature with Boltzmann plots for $\Delta v = 4$ band (a) Experimentally measured data and Gaussian fittings of each transition, (b) Boltzmann plot

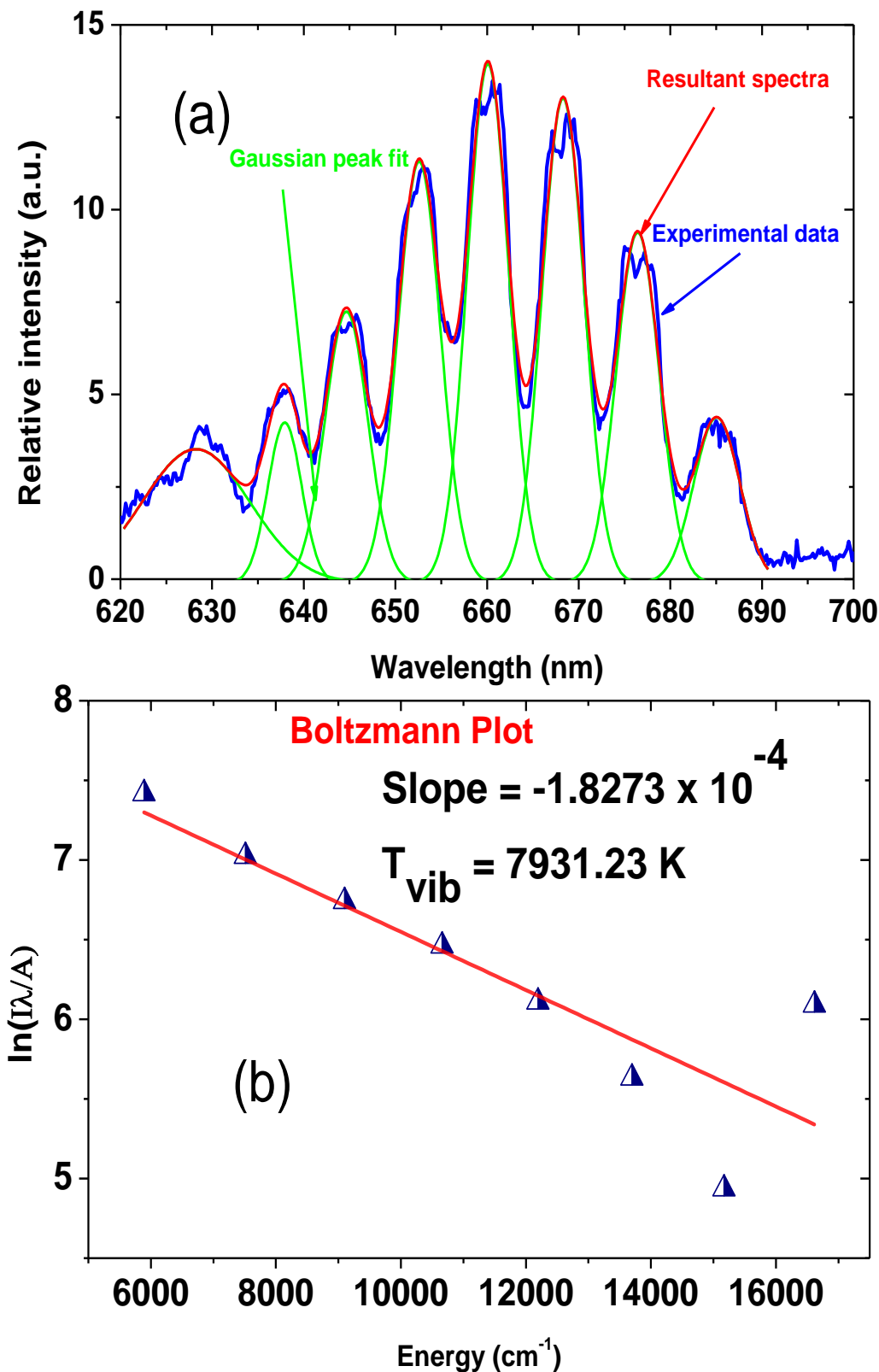


Figure 6.5. Experimentally measured temperature with Boltzmann plots for $\Delta v = 3$ band (a) Experimentally measured data and Gaussian fittings of each transition, (b) Boltzmann plot

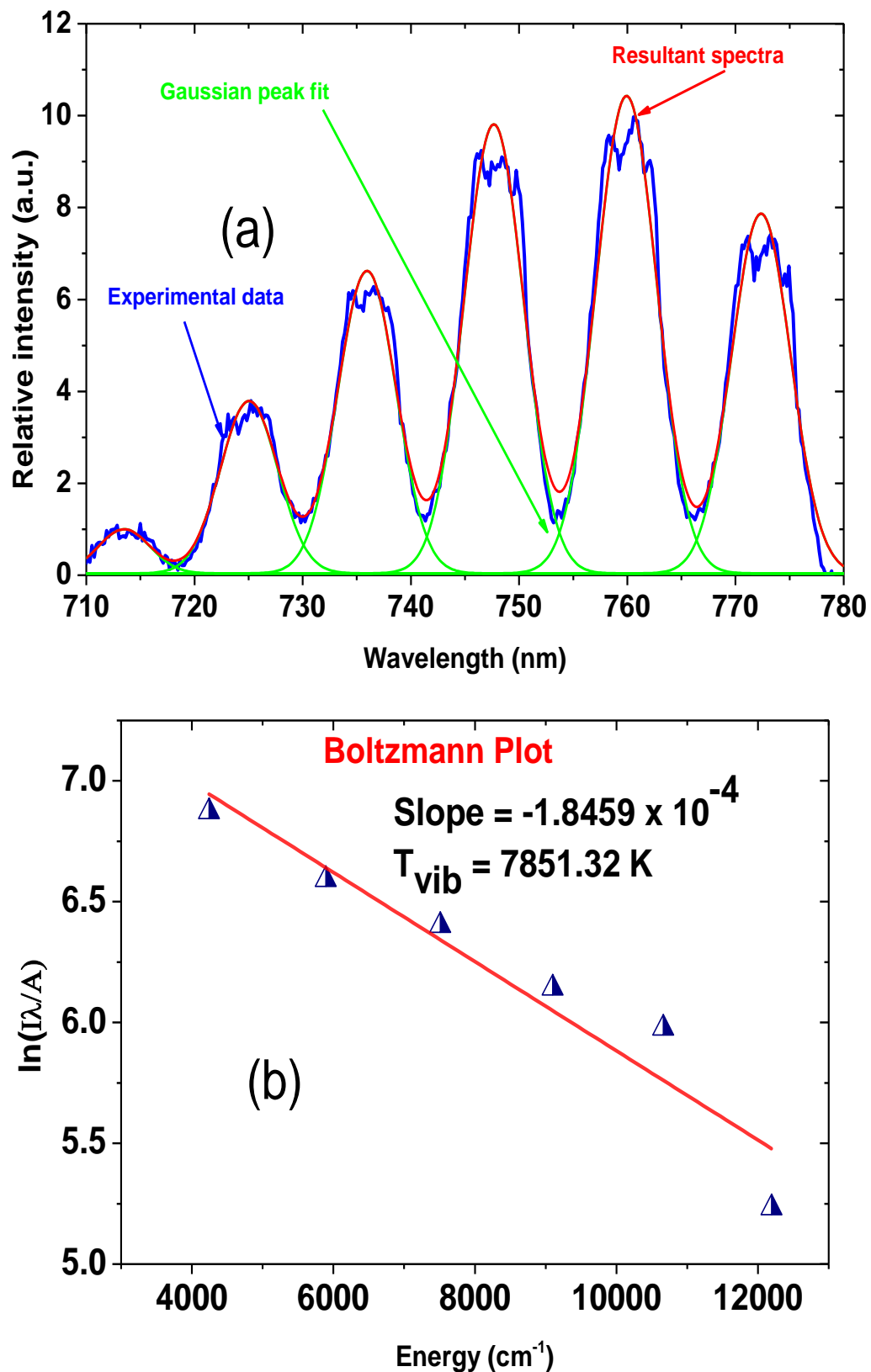


Figure 6.6. Experimentally measured temperature with Boltzmann plots for $\Delta v = 2$ band (a) Experimentally measured data and Gaussian fittings of each transition, (b) Boltzmann plot

6.5.2. Simulated estimation of temperature

The molecular band spectra of nitrogen 1PS have been simulated using a MATLAB-based code, as earlier described in section 6.5. The transition probability and wavelength information for each band is the primary inputs required by the code. It uses equation 6.4 to produce intensity Gaussian profile values for each transition. In this case, the intensity of the lines is affected by a vibrational temperature or neutral gas temperature. Following this, the intensity is plotted using a profile function with a Gaussian line as shown in Figure 6.7.

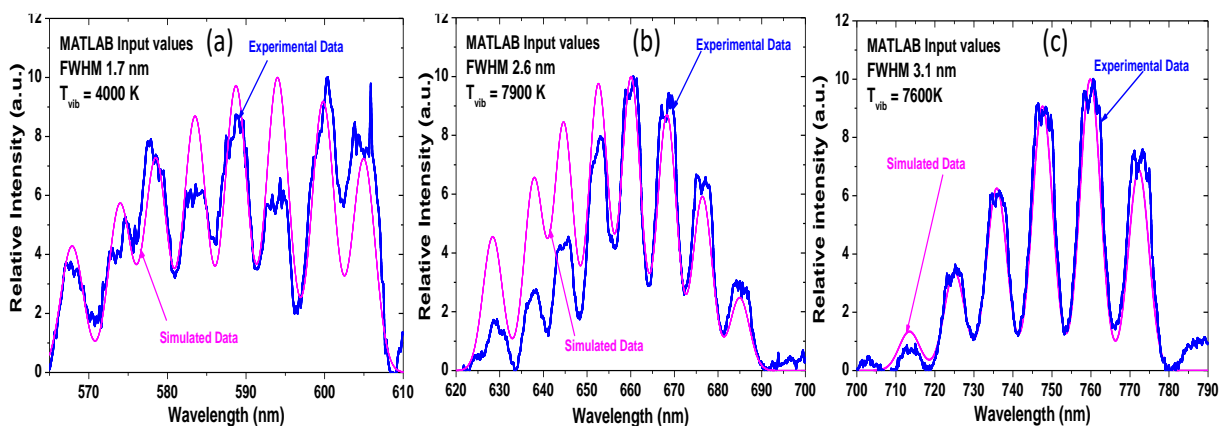


Figure 6.7. Simulated spectra for band (a) $\Delta\nu = 4$, (b) $\Delta\nu = 3$ and (c) $\Delta\nu = 2$

In the case of the $\Delta\nu = 4$ band, the FWHM is fixed at 1.7 nm, meaning that the width of each vibrational transition is always the same. It has been observed in previous studies that the line-profile of the N₂ the molecular band is less sensitive to rotational temperature, i.e. the rotational FWHM value (Kim et al.), so the FWHM is taken as a fixed parameter for each vibrational transition within a single band. It is also clear from the simulation measurements that the FWHM values of individual bands as measured experimentally do not vary by a large amount, as indicated in Figure 6.7.

As shown in Figure 6.7 (a), the simulation is done for $\Delta\nu = 4$ band. The vibrational temperature is estimated to be 4000 K ($\sim 0.34 \text{ eV}$) (FWHM = 1.7 nm) after the simulated spectra were iterated for different temperatures to model with the experimental data. The spectra on the longer wavelength end of the band are not matching.

Similarly, in Figure 6.7 (b), the $\Delta\nu = 3$ band is modelled for temperature estimation. The temperature is iterated and the best-matched condition with experimental data is found to be

7900 K (~ 0.68 eV) with a fixed FWHM of 2.6 nm for each transition (Figure 6.7 (b)). Here, at the shorter end of the band, the experimental and simulated spectra do not match up.

For $\Delta\nu = 2$ band the molecular band is simulated and modelled with the experimental data as shown in Figure 6.7 (c). The FWHM held constant at 3.1 nm across all transitions during simulation, and the temperature is similarly iterated. The best-matched temperature for this band is 7600 K (~ 0.65 eV). This band shows excellent agreement between experimental and simulated results. In addition, this temperature is very close to the value obtained using the Boltzmann plot method, which was 7851 K (~ 0.67 nm) for the same band ($\Delta\nu = 2$).

In conclusion till now, with experimental measurements, the $\Delta\nu = 4$ band gives a different temperature than the $\Delta\nu = 2$ and 3 bands, which give temperatures of 7800 K (~ 0.67 eV) to 8000 K (~ 0.69 eV). Also, the simulated results are at best agreement with experimental results for $\Delta\nu = 2$ band. However, $\Delta\nu = 3$ and 4 are not matching at shorter and longer wavelength sides of the spectrum (Figure 6.7). The following section addresses this ambiguity present in the results.

6.6. Removal of ambiguity present in gas temperature estimation

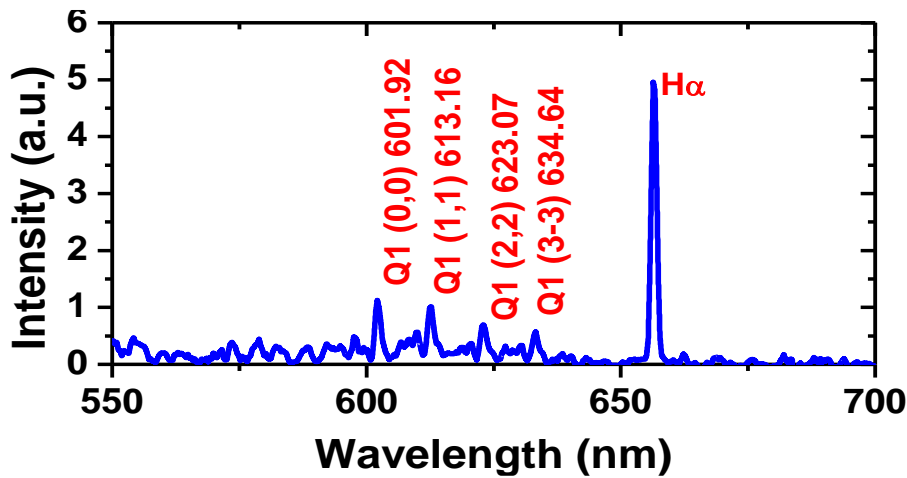


Figure 6.8. Identified molecular bands of hydrogen

Some other spectral lines may be contaminating $\Delta\nu = 2$ and $\Delta\nu = 3$. It is necessary to generate pure hydrogen plasma under the same experimental conditions as the one used to generate the band that was subsequently corrupted by other spectral lines. The experimental

spectra were recorded, and the Fulcher band with the transition $d^3 \Pi_u \rightarrow a^3 \Sigma_g^+$ between 560 – 700 nm was found (Farley et al.).

The Q-branch lines of Fulcher – α are identified and labeled in Figure 6.8. The identified vibrational levels are, 601.92 nm (0,0), 613.16 nm (1,1), 623.07 nm (2,2), and 634.64 nm (3,3). Thus, it is evident that the measurements of the nitrogen molecular band in the range of 600–650 nm are primarily impacted by these bands. However, it has a greater impact on the near 600 nm, due to the maximum intensity of (0,0) transition. Because of this discrepancy, the temperature of the band that spans 560 – 620 nm ($\Delta\nu = 4$) ($T_{vib} = 4600$ K as shown in Figure 6.4 and Figure 6.7) is contested. The Fulcher band can be removed from the primary measured nitrogen band spectra to reduce its impact. This is now reflected in the experimentally estimated temperature $T_{vib|\Delta\nu=4} = 8141$ K (~ 0.70 eV), as shown in Figure 6.9. It is close to the measurement in which the band $\Delta\nu = 2$ and 3. Hence the ambiguity present in experimental measurement is corrected for the $\Delta\nu = 4$ band.

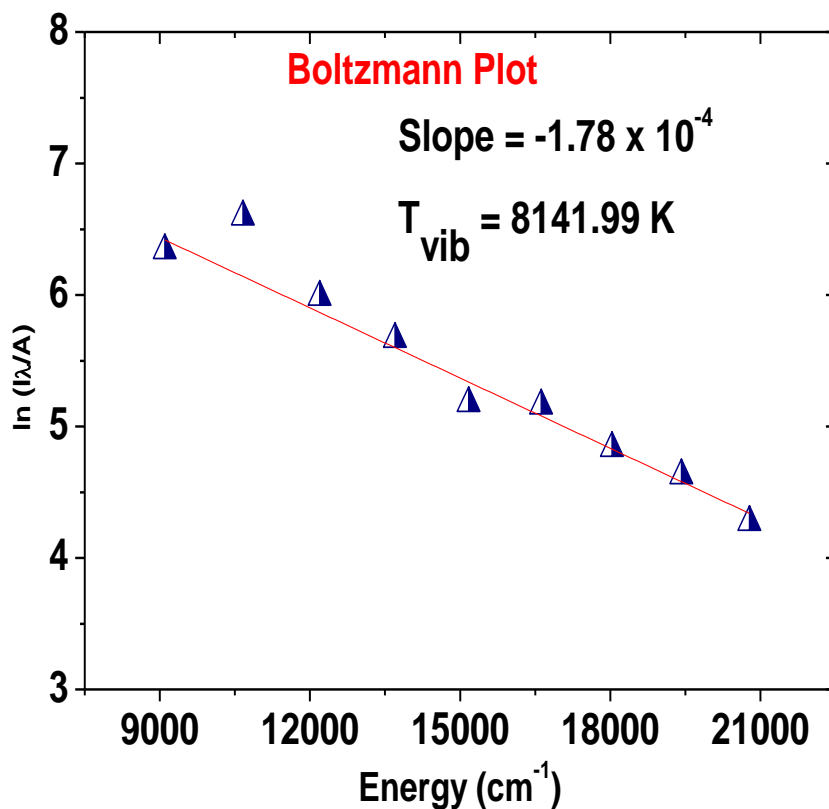
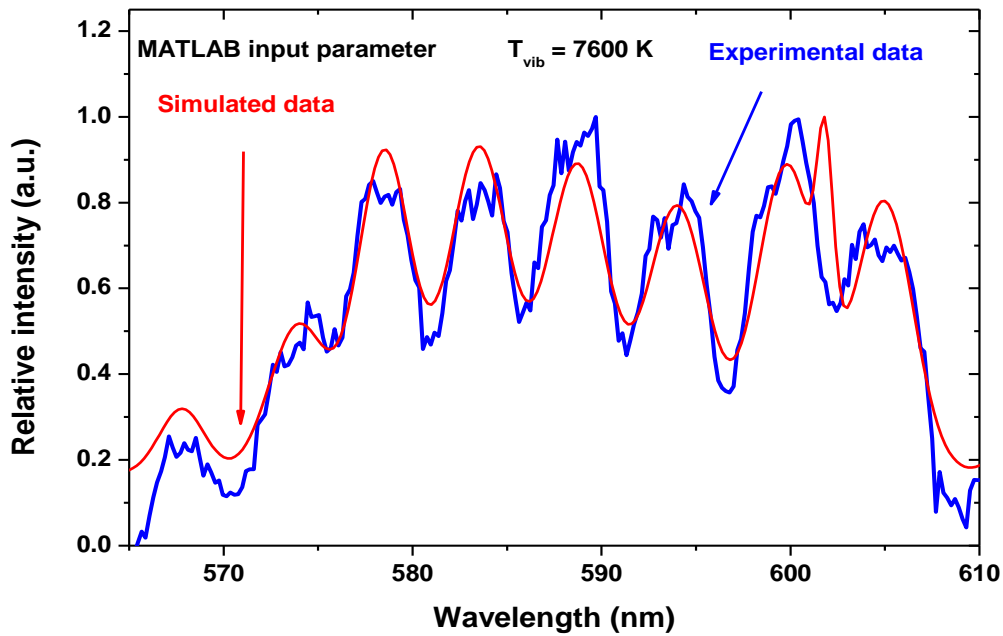
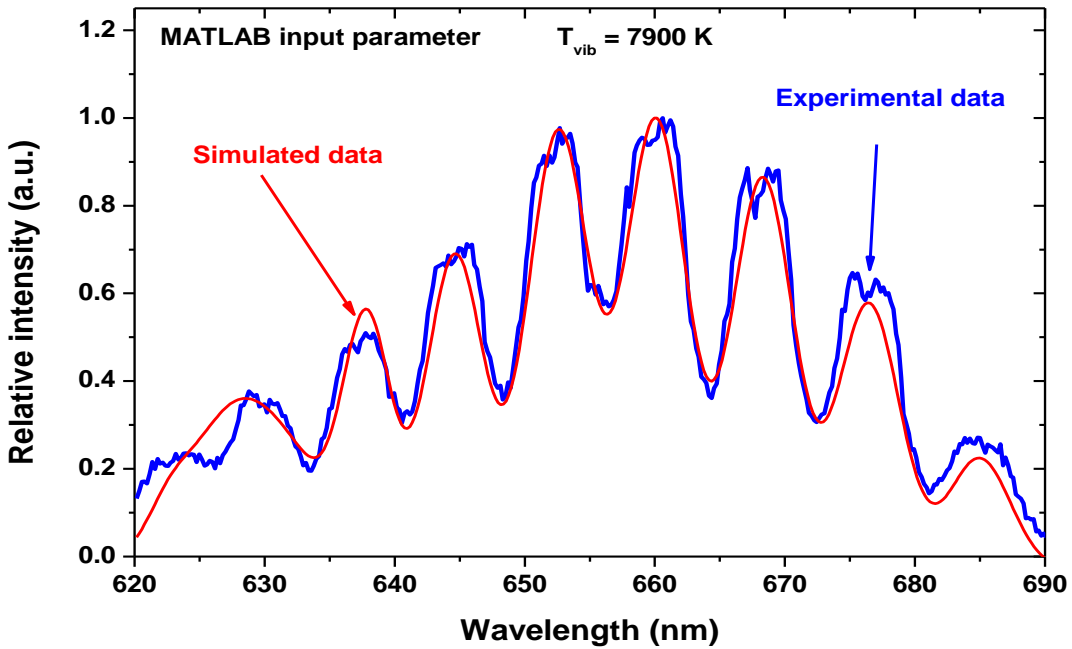


Figure 6.9. Estimated temperature using Boltzmann plot method for $\Delta\nu = 4$ band after suppressing effect of Fulcher band in measurement

Figure 6.10. Simulated spectra for band $\Delta v = 4$ Figure 6.11. Simulated spectra for band $\Delta v = 3$

The ambiguity present in the mismatch of the experimental and simulated band has also been addressed by adding the Fulcher band to the N_2 band. Simulation of the same band is hence given in Figure 6.10 having $T_{\text{vib}} = 7600 \text{ K}$ ($\sim 0.65 \text{ eV}$). Similarly in the simulation of $\Delta v = 3$ band the mismatch at lower wavelength side of the band is answered by Fulcher spectral

correction. After correction measured gas temperature with this band fitting is shown in Figure 6.11, $T_{\text{vib}} = 7900 \text{ K} (\sim 0.68 \text{ eV})$ (Yadava, Chouhan, et al.).

Temperature estimated using $\Delta v = 2$ band remains unaffected by any other band. This correction makes the estimated temperatures from the three bands very close to one another, within the margin of error from the experiments. However, note that if the hydrogen's rovibrational temperature varies with and without the presence of nitrogen, the contribution from the molecular hydrogen bands may be altered.

Chapter 7. Conclusion and Future Scope

The edge plasma region of any tokamak is clasped in between the high-temperature core plasma and the material boundary of its container. Hence, it influences both the core and material boundary in terms of maintaining their respective properties and protecting both from deteriorating or getting damaged. Therefore, it is very important to understand the edge plasma performance and its control. Due to its proximity to the material boundary on one side, neutral and impurity ions dominate this region, whereas the core-plasma on its other side demands minimum penetration of these neutrals and impurities into the core plasma via particle transport. To contribute to the understanding of the characteristics of the edge plasma and its consequence on the core plasma, experiments are carried out in ADITYA-U tokamak located at the Institute for Plasma Research (IPR), Gandhinagar. The ADITYA-U tokamak is mid-sized tokamak having minor radii 0.25 m and major radii 0.75 m. It has a magnetic field of $\sim 0.75 - 1.5$ T. The chord averaged electron density is in the range of $2 - 3 \times 10^{19} \text{ m}^{-3}$. The plasma current and durations are $\sim 70 - 150$ kA and $\sim 70 - 200$ ms respectively. The spectroscopic instruments used in this study include various spectrometers and PMTs. Many front-end optics and optomechanical components required for investigating the plasma via various lines of sight (LOS) are developed during the course of this work.

During this study, a high-resolution spectrometer was set up to measure the radial profiles of neutral and impurity ions. This setup was made adaptable to measure the plasma inboard and outboard emissions simultaneously using eight LOS through the development of a large rectangular viewport, which can view the entire outboard and most of the inboard regions of the plasma-poloidal cross-section at one toroidal location. The system has a spectral resolution

in terms of $\Delta\lambda_{FWHM}$ of 0.032 nm at 650 nm. Initially, C^+ ion temperature was estimated from the apparent broadening of C^+ line spectra caused due to temperatures (Doppler broadening). The measured ion temperature was found to be $T_{C^+} \sim 30 - 60$ eV at various radial locations of plasma. The temperature measurements were very surprising knowing the fact that they are higher than the ionization potential of C^+ ions which are ~ 24 eV. The anomaly present in the temperature estimation is then corrected through the modelling of line-shapes by the inclusion of the Zeeman components along with the Doppler broadening. Including the line-shape broadening originating from the Zeeman splitting of the spectral line due to the magnetic field present at that location of the plasma, the corrected temperature of C^+ ion comes out to be ~ 10 eV. This is a clear demonstration of how crucial to the inclusion of the Zeeman Effect is in the estimation of ion/neutral temperatures from the spectral line-broadening measurements.

Then the radial profiles of C^+ and O^{4+} impurity ion temperatures were obtained by employing the Able-like matrix inversion technique. The temperature of C^+ and O^{4+} ions at different radial locations are found to be in the range of $\sim 2 - 15$ eV and $\sim 10 - 30$ eV respectively. The ion temperatures are found to be higher at the extreme edge ($\rho = 0.86$). This is due to the thermalization time at the extreme edge being lower as compared to the ionization time at the same location, however, in the inner plasma region, the ions become ionize quickly to a higher stage before thermalization occurs resulting in lower C^+ ion temperature as compared to the extreme edge of the plasma. Another crucial finding of this study is the observation of sudden peaking of temperatures of these ions at around $r = 0.12 - 0.15$ m ($\rho = 0.5 - 0.6$) of plasma radii. Detailed investigation revealed that this peaking of temperature is related to the existence of $m = 2$ MHD mode present at that radial location of ADITYA-U and there the increase in the ion temperatures may be occurring due to the reduced plasma transport inside the island associated with $m = 2$ mode.

Similarly, the neutral temperature has been estimated using H_α spectral line shapes. It was found that the measured line-shapes of hydrogen-neutrals could not be fitted even properly including Zeeman and Doppler broadened single Gaussians having a single temperature. Hence two Doppler broadened components with respective Zeeman splitting were considered for fitting. The two temperature components are found to be warm and hot, having temperatures of $1 - 10$ eV and more than 10 eV respectively. Both temperature components are in the range of $T_{H_\alpha|HOT} \sim 15 - 30$ eV and $T_{H_\alpha|WARM} \sim 3 - 5$ eV for various plasma radial locations. The warm component of temperatures is mainly due to molecular dissociation, dissociative ionization, and Franck–Condon dissociation processes and the hot temperature component is

coming from the charge-exchange process. These observations are also supported by modelling of spectral line profiles using the neutral transport code DEGAS2. After obtaining the radial profile using Abel inversion, the neutral warm temperature shows a significant rise at $\rho = 0.6$. However, neutral warm temperature components show a rise in temperature at $\rho = 0.6$, similar to the case of ion temperatures as described earlier.

As the magnetic field is higher (HFS) on the inboard side than the outboard (LFS), several differences in plasma transport and asymmetry ion temperatures between the two sides have been observed in several tokamaks. However, neutral temperature and their asymmetries are not explored. In ADITYA-U tokamak, the spatial profile of neutral temperature has been measured from both low and high field sides simultaneously. In ADITYA-U tokamak, the poloidal asymmetry in neutral temperatures is observed for the first time in tokamak history. The temperatures of the warm component of neutral are ~ 2 eV and $4 - 5$ eV in the low and high field sides of the plasma, respectively. This may be related to the poloidal asymmetry in impurity ion temperature observed in many tokamaks as the neutral gain temperature from the ions.

Disruption mitigation is important to prevent bulk PWI and protect the material surfaces. In this direction, the experiments were carried out at ADITYA-U tokamak by launching the Li_2TiO_3 pellet using an inductively driven pellet injection technique to maximize the radiation during a disruption event. The neutral Li emissions were measured using high-resolution spectroscopic diagnostics to understand the power loss occurring in the plasma due to the pellet. In Lii emission line at 670.8 nm, a dip in the spectral line profile is observed immediately after the pellet injection. Analyzing the spectrum further, it was found that the dip in the line-shape is due to the presence of a self-absorption phenomenon happening because of high Li density. This is for the first time that the self-absorption phenomenon is a non-intrinsic impurity has been reported in a tokamak. The opacity analysis of this observed spectral line provides the lithium density, n_{Li} of $\sim 2 \times 10^{22} \text{ m}^{-3}$, and the estimated power loss is ~ 148 kW. This is more than 60% of input power which is radiated due to the pellet causing the sudden disruption of plasma and enable us to understand the physics behind developing the technique for disruption mitigation.

Finally, through this line profiles modelling work, a code by the inclusion of different broadening mechanisms, i.e., Gaussian broadening due to temperature, instrumental broadening due to spectrometer, Zeeman broadening with different energy level split for different neutral

and ions and self-absorption has been developed as a part of this thesis work and now readily available to study the ADITYA-U tokamak plasma.

A detailed investigation on plasma influx measurement and recycling was carried out for different surfaces (graphite limiter and SS wall) with and without wall conditioning, i.e., with and without lithium coating. For this purpose, PMT based diagnostic setup having interference filters with a center wavelength corresponding to the wavelength H_{α} (656.28 nm), O^+ (441.5 nm) and C^{2+} (464.7 nm) are used. Particle confinement time \sim 5 to 25 ms for ADITYA-U tokamak was estimated by measuring the fuel particle influxes from the wall and the limiter. It has been observed that the particle confinement time increases with the reduction of particle recycling. The recycling coefficients during the plasma current flat top phase also were estimated for many discharges. It was found that at the beginning of any campaign when the machine walls were clean or uncontaminated by hydrogen, the wall acted as a sink to the plasma. However, after a few days, the wall started acting as the source of the plasma.

With normal GDC cleaning, hydrogen integrated influx from the limiter and wall were almost similar ($\sim 10 - 24 \times 10^{20} \text{ sec}^{-1}$). For O^+ influx measurement, it is found that the limiter surface contributes moderately higher oxygen impurity influxes than that from the wall. Contribution from C^{2+} is almost similar to both LOS terminating on the wall and limiter. This is occurring due to C^{2+} has ionization energy and resides relatively at a higher temperature region in the plasma edge hence it is being affected by plasma transport and then influxes from both LOS become similar. In addition to this, it may be also related to the migration of carbon to the wall from the graphite tiles of the limiter. The total oxygen impurity (integrated over plasma exposed surfaces) to fuel hydrogen ratio is $\sim 4\%$ for limiter terminating LOS and 2% for wall terminating LOS and the ratio of carbon to hydrogen becomes 2% for limiter terminating LOS and 4 – 6% for wall terminating LOS. When lithium coating was done along with GDC, the influx measurements show a reduction in the emissions, including H_{α} , O^+ and C^{2+} . However, the percentage of emission reduction differs for species, as lithium has a remarkable affinity toward oxygen, the oxygen emission is reduced by 50% from the wall and 80% from the limiter surface with increased Li emissions. Then hydrogen emission reduces by 30% from the wall and 60% from the limiter surface. The carbon emission shows an equal reduction from both surfaces by 50%.

The neutral and impurity transport modelling in ADITYA-U tokamak has been carried to understand the contribution of molecular processes in the particle influx measurement and to understand the mass dependency of impurity transport, respectively.

The radial profile of visible spectral lines and signal chord measurement of VUV spectral lines from various charge states of impurities have been measured to study the mass dependency of impurity transport. The radial profiles of visible emission from C²⁺ at 464.7 nm, O⁴⁺ at 650 nm, Ne⁺ at 371.8 nm and Ar⁺ at 476.4 nm and VUV emission of Fe¹⁴⁺ at 28.4 nm and Fe¹⁵⁺ at 33.5 nm were used for transport studies. The radial profile of emissivity obtained in the visible range for C, O, Ne, and Ar was modelled using an impurity transport code to obtain diffusivity (D) and convective velocity (v). In the case of Fe, VUV spectral lines from two charge states and their ratios were modelled to find the iron impurity transport. It was found that the diffusion coefficient decreases with increasing atomic number and correspondingly with atomic masses of impurities. However, the convection velocity does not have any dependencies with the increasing mass of impurities.

The molecular contribution to particle influx at the tokamak plasma edge region is investigated. Individual S/XB values for atomic H, molecular H₂, and H₂₊ ions in H emission are determined. The radial profile of H α emissivity is first simulated using the neutral particle transport DEGAS2 code to quantify molecular H₂, and H₂₊ ions for estimating particle influxes from the molecule by comparing the simulated data with measurements taken along two viewing chords that pass through the entire and only edge region of ADITYA plasma, respectively. The particle influxes for ADITYA-U tokamak plasma are also estimated for various edge electron temperatures. It has been discovered that edge T_e \sim 10 eV, molecular contribution to particle influx is not significant. Total influxes are calculated to be $4.09 \times 10^{16} \text{ cm}^{-2} \text{ s}^{-1}$ with only atomic processes considered and $3.88 \times 10^{16} \text{ cm}^{-2} \text{ s}^{-1}$ when both atomic and molecular processes are considered. However, the effect of molecular contribution is more noticeable when measured through a viewing chord that passes only through the plasma edge and not the entire plasma. When the edge-chord measurement is considered, the molecular contribution to the total influx rises to 6 – 10%. When the edge/SOL temperature falls below 5 eV, as in detached divertor plasmas, the contribution from molecular processes increases significantly.

The last chapter of the thesis is the founding stone for characterizing divertor plasma of ADITYA-U tokamak by developing a proper methodology to find the gas temperature. The

experiments were carried out on a linear plasma device for developing tungsten coating for the limiter tiles of ADITYA-U tokamak. In this study, the neutral gas temperatures have been measured through N₂ molecular bands. Furthermore, the contribution of other molecular bands contaminating the N₂ molecular bands are identified. After correcting the intensity contribution from other bands in the N₂ molecular band the corrected vibrational temperatures are estimated. The visible spectrum was recorded using a survey spectrometer in the wavelength range of 350 – 900 nm. The nitrogen molecular band of the first positive B³Π_g – A³Σ_u⁺ was observed with Δv = 4, 3 and 2 presented in the 560 to 800 nm wavelength range. Along with these bands, the hydrogen atomic lines and second positive system of N₂ molecular bands are also visible in the spectrum. Here, two techniques are developed to measure the gas temperature, one is fitting the experimental data to be used for the Boltzmann plot method and the other is simulating whole spectral data of all three molecular band N₂ first positive using the known values of different constants and parameters. After thorough analysis, it was found that there has been a discrepancy in the temperature estimated form bands between Δv = 4 and Δv = 2, 3 bands using the experimental Boltzmann plot method. Also, in the simulated method, the experimental data for Δv = 2 band can be fitted well with the simulated band, whereas the simulation does not fit well the measured spectra of Δv = 4 and 3 bands. This analysis result demonstrates that Δv = 4 and Δv = 3 bands are contaminated by other atomic lines or molecular bands. Detailed investigation revealed that the presence of H₂ - Fulcher bands affect mostly the Δv = 4 N₂ band and partially Δv = 3 band, the temperature estimation from these bands may not be accurate. This ambiguity present in measurement was corrected by subtracting the Fulcher band 600 – 650 nm from the spectrum in both methods. The measured corrected temperature hence comes out to be ~ 0.60 – 0.68 eV, which is similar to those estimated from uncontaminated bands.

Overall, this thesis presents the rigorous work on edge plasma characterization of the tokamak ADITYA-U carried out using spectroscopic diagnostic. It deals with various studies using plasma spectroscopy via several spectroscopic instruments in the visible range (Spectrometers and PMTs) and their corresponding optics. On the developmental side, all the spectrometer and PMT systems along with their light collection optics are designed and installed. Several experiments were planned and carried out by carefully guiding the discharges according to the experimental requirements. On the computational side, the DEGAS2 and STRAHL codes have been used to model the experimental emissivity profile. The analysis part is mostly done with MATLAB and Origin was used for plotting the data. The thesis deals with fuel and non-fuel neutrals H_α, Li_α and intrinsic and non-intrinsic impurity

emissions C^+ , C^{2+} , O^+ and O^{4+} . Most of them are dominated in the edge region because of their low Z values. The radial profile of neutral and impurity ion temperature measured in this work and the poloidal asymmetries in neutral temperature were found for the first time in tokamak history. The Spectral line shape modelling of the self-absorbed Li spectral line observed during the IPI experiment gives the opacity measurement in the tokamak plasma. The details study of particle and impurity influxes shows the importance of the wall for understanding the tokamak edge plasma as the wall contributes significantly to the integrated influx to the plasma. Not only that, Here the role of molecular processes in particle influx estimation has been investigated through the estimation of direct contribution H_α emission from hydrogen molecules and molecular ions using the modelling of radial profile H_α using DEGAS2 code. Spectral emission in visible and VUV from several medium and high-Z impurities (Ar, Ne, Fe) have been modelled using an impurity transport code. STRAHL investigated the mass dependency on impurity transport and it was found that diffusivity decreases with increasing impurity mass. The result presented in the thesis will be very helpful to understand neutral and impurity ion dynamics in the edge plasma region of ADITYA-U tokamak.

7.1. Future scope

In future work, the following studies can be taken

1. The line shape modelling work can be extended to measure accurate core ion temperature using CX produced line. It can be further utilized to develop Zeeman polarization spectroscopy to find out the safety factor profile in the plasma edge region to study the plasma stability.
2. Furthermore, as there exists high electric fields in the edge region, the Stark broadening due to electric field needs to be included in the spectral line shape regeneration model along with pressure broadening in some experiments.
3. The influx and particle recycling are here studied for GDC and lithium coated wall conditioned plasmas, it can be further extended to several other coatings as well as with impurity-seeded plasmas and also in divertor regions. The contribution of molecular processes in the influx coming out from the divertor region can be quantified by doing the upcoming divertor operation of ADITYA-U.
4. Not only that, the radial profile of H_α emission can be used to investigate the role of radial variation of neutral atom in generating the additional radial electric field and

radial electric field shear near the separatrix of ADITYA-U tokamak during it divertor operation.

5. The radial profile of H_{α} emission measurement can be utilized to understand how the change in neutral fraction inside the plasma influences the plasma confinement via ionization in the particle balance equation, by modifying the parallel and poloidal ion flow and flow shear and modifying the radial electric field through the transport of toroidal angular momentum. The impurity transport study can be extended to understand the role of various micro-instability in the higher diffusivity for low Z impurities.
6. The vibrational temperature measurements in the tokamak edge during nitrogen seeding also remain in the future scope of this thesis work. The measurements of vibrational temperature will throw light on molecular dynamics occurring in the extreme edge region of a tokamak.

APPENDIX: A

Mathematical explanation for Zeeman Polarization components

The transition probability of Zeeman interaction is given by dipole approximation of quantum mechanics. It is described by the following proportional relation,

$$W_{ab} \propto |e \cdot r_{ab}|^2$$

Here, e is the unit vector in the polarization direction and $r_{ab} \equiv \langle b | r | a \rangle$. Try to understand this from figure 1. Here e_p and e_s are the polarization vectors and k is unit length wavevector. In Cartesian coordinate system these quantities are represented as,

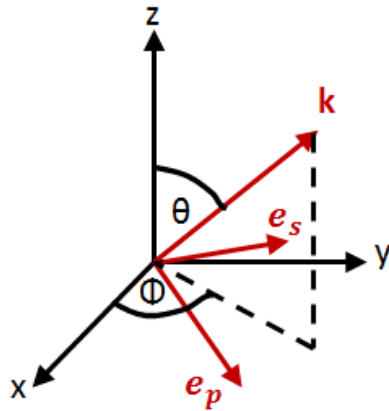


Figure 1. Understanding of polarization through cartesian coordinate system

$$k = (\sin\theta \cos\phi, \sin\theta \sin\phi, \cos\theta);$$

$$e_p = (\cos\theta \cos\phi, \cos\theta \sin\phi, -\sin\theta);$$

$$e_s = (-\sin\phi, \cos\phi, 0)$$

$$e \cdot r_{ab} = e_1(r_{ab})_1 + e_0(r_{ab})_0 + e_{-1}(r_{ab})_{-1} \quad (a)$$

The spherical component of vector e ,

$$e_1 = -\frac{1}{\sqrt{2}}(v_x + iv_y) \quad ; \quad e_0 = v_z \quad ; \quad e_{-1} = \frac{1}{\sqrt{2}}(v_x - iv_y)$$

$$(e_p)_1 e_p = -\frac{1}{\sqrt{2}} \cos\theta e^{i\phi} \quad ; \quad (e_s)_1 e_s = \frac{ie^{i\phi}}{\sqrt{2}}$$

$$(e_p)_0 e_p = -\sin\theta \quad ; \quad (e_s)_0 e_s = 0$$

$$(e_p)_{-1} e_p = -\frac{1}{\sqrt{2}} \cos \theta e^{-i\phi} \quad ; \quad (e_s)_{-1} e_s = \frac{i e^{-i\phi}}{\sqrt{2}}$$

1. $\Delta m_j = 1$, $e_1(r_{ab})_1$ will survive from equation (a) and the transition probability is

$$W_{ab} \propto \left| (e_p)_1 e_p + (e_s)_1 e_s \right|^2 \propto \frac{1}{2} (1 + \cos^2 \theta) |e^{i\phi}|^2$$

- B_{\perp} : If $\theta = \frac{\pi}{2}$, $\cos \theta = 0$ then, $W_{ab} \propto \frac{1}{2} |e^{i\phi}|^2$

- $B_{||}$: If $\theta = 0$, $\cos \theta = 1$ then, $W_{ab} \propto |e^{i\phi}|^2$

Hence in both cases (parallel and perpendicular magnetic fields), σ_+ component will be non-zero and it is visible.

2. $\Delta m_j = 0$, $e_0(r_{ab})_0$ will survive from equation (a) and the transition probability is

$$W_{ab} \propto \left| (e_p)_0 e_p + (e_s)_0 e_s \right|^2 W_{ab} \propto \sin^2 \theta$$

- B_{\perp} : If $\theta = \frac{\pi}{2}$, $\sin^2 \theta = 1$ then, $W_{ab} \propto 1$

- $B_{||}$: If $\theta = 0$, $\sin^2 \theta = 0$ then, $W_{ab} \propto 0$

The above equation states that when the magnetic field is parallel to the viewing direction, the π component becomes zero and hence it is not visible. However, when magnetic field is perpendicular to the viewing direction, the π component is non-zero and it is visible.

3. $\Delta m_j = -1$, $e_{-1}(r_{ab})_{-1}$ will survive from equation (a) and the transition probability is

$$W_{ab} \propto \left| (e_p)_1 e_p + (e_s)_1 e_s \right|^2 \propto \frac{1}{2} (1 + \cos^2 \theta) |e^{-i\phi}|^2$$

- B_{\perp} : If $\theta = \frac{\pi}{2}$, $\cos \theta = 0$ then, $W_{ab} \propto \frac{1}{2} |e^{-i\phi}|^2$

- $B_{||}$: If $\theta = 0$, $\cos \theta = 1$ then, $W_{ab} \propto |e^{-i\phi}|^2$

Hence in both cases (parallel and perpendicular magnetic fields), σ_- component will be non-zero and it is visible.

In summary, with mathematical explanation it authenticated that,

(a) Magnetic field is parallel to LOS: σ_+, σ_- components are visible and π is not visible.

(b) Magnetic field is perpendicular to LOS: σ_+, σ_- and π all components are visible

APPENDIX: B

List of Abbreviates

AAPPS	ADITYA Pulsed Power System
AC	Alternating Current
ADAS	Atomic Data and Analysis Structure
AXUV	Absolute eXtreme Ultra Violet
BCC	Black Correction Coil
CCD	Charge Coupled Detector
CCP	Capacitively Coupled Plasma
CE	Coronal Equilibrium
CF	Conflat
CMOS	Complementary Metal-Oxide Semiconductor
CRE	Collision Radiative Equilibrium
DAQ	Data Acquisition
DC	Direct Current
DMS	Disruption Mitigation System
ECR	Electron Cyclotron Resonance
EIR	Electron-Ion Recombination
ELM	Edge Localised Modes
EM	Electromagnetic
FFB	Fast Feedback Coil
FLP	Flush Langmuir Probe
FWHM	Full Width Half Maxima
GDC	Glow Discharge Cleaning
GLP	Garland Langmuir Probe
HFS	High Field Side
HXR	Hard-Xray
ICF	Inertial Confinement Fusion
ICP	Inductively Coupled Plasma
IE	Ionization Energy
IF	Interference Filter
IOC	Improved Ohmic Confinement

IPI	Inductively driven Particle accelerator and Injector
ITG	Ion Temperature Gradient
LCFS	Last Closed Flux Surface
LFS	Low Field Side
LHEP	Laser Heated Emissive Probe
LO	Local Oscillator
LP	Langmuir Probe
LTE	Local Thermodynamic Equilibrium
MAI	Molecular Activated Ionization
MAR	Molecular Activated Recombination
MCF	Magnetic Confinement Fusion
MGI	Massive Gas Injection
MHD	Magneto Hydrodynamic
MTS	Multi-Track Spectrometer
NIR	Near Infra-Red
NIST	National Institute of Standards and Technology
PDC	Pulse Discharge Cleaning
PF	Poloidal Field
PFC	Plasma Facing Component
P-GDC	Pulsed Glow Discharge Cleaning
PMT	Photo Multiplier Tube
PWI	Plasma Wall Interaction
PWC	Plasma Wall Components
QMA	Quadrupole Mass Analyser
RE	Runaway Electron
RF	Radio Frequency
RITE	Radial Impurity Transport Equation
SITA	Semi-Implicit Transport code for ADITYA-U
SMA	Sub Miniature A
SOL	Scrape Off Layer
SPI	Shattered Pellet Injection
SS	Stainless Steel
SXR	Soft X-Ray
TEM	Trapped Electron Mode

TESPEL	Tracer Encapsulated Solid Pellet
TF	Toroidal Field
TQ	Thermal Quench
TR	Transformer
TTL	Transistor Transistor Logic
UHV	Ultra High Vacuum
VCB	Vacuum Circuit Breaker
VF	Vertical Field
VUV	Vacuum Ultra Violet
XUV	eXtreme Ultra Violet

List of standard symbols used

Plasma major radius	R
Plasma minor radius	a
Magnetic field strength	B
Toroidal magnetic field	B_T
Vertical magnetic field	B_v
Loop voltage	V_{loop}
Plasma current	I_P
Normalized plasma radius = r/a	ρ
Electron density	n_e
Ion density	n_i
Lithium density	n_{Li}
Density of neutral atom	n_n
Mass of electron	m_e
Mass of ion	m_i
Temperature	T
Electron temperature	T_e
Ion temperature	T_i
Carbon ion temperature	T_{C+}
Oxygen ion temperature	T_{O4+}
Neutral gas temperature	T_n
Vibrational temperature	T_{vib}
Gas temperature	T_g
Particle confinement time	τ_p
Electron ion thermalization time	τ_{th}
Electron impact ionization time	τ_{ion}
Ion saturation current	I_{sat}
Poloidal beta	β_P
Permittivity in vacuum	ϵ_0
Velocity of light in vacuum	c
Planck's constant	\hbar
Electron charge	e

Larmor radius	ρ_L
Cyclotron frequency	ω_c
Velocity in the perpendicular direction	v_\perp
Emissivity	E_{ji}
Vibrational energy	E_{vib}
Hamiltonian	H
Hamiltonian of Zeeman	H_Z
Unperturbed Hamiltonian	H_0
Spin orbit Hamiltonian	H_{SO}
External magnetic field perturbation Hamiltonian	H_{mag}
Critical field	B_C
Bohr's magneton	μ_B
Emission coefficient	ε
Transition probability	A
Total angular momentum quantum numbers	j
Angular momentum quantum numbers	l
Spin momentum quantum numbers	s
Absorption coefficient	κ
Opacity	τ
Oscillator strength	f
Profile function (Gaussian, Lorentzian and Voigt)	$f(\nu)$
Lorentzian FWHM	$\Delta\lambda_1^L$
Gaussian FWHM	$\Delta\lambda_1^G$
Total FWHM	$\Delta\lambda$
Instrumental FWHM	$\Delta\lambda_I$
Doppler FWHM	$\Delta\lambda_D$
Doppler FWHM due to Zeeman components	$\Delta\lambda_D^Z$
Total experimental FWHM	$\Delta\lambda_D^{Exp}$
Total simulated FWHM	$\Delta\lambda_D^{Simu}$
Ionization rate coefficient	$<\sigma\nu>_{ion}$
Coulomb logarithm	$ln\Lambda$
Radiative cooling rate coefficient	L_{LI}

APPENDIX: B

Recycling coefficient	R
Fuelling efficiency	η
Particle flux	Γ
Carbon influx from SS wall	$\Gamma_{C,W}$
Oxygen influx from SS wall	$\Gamma_{O,W}$
Hydrogen influx from SS wall	$\Gamma_{H,W}$
Carbon influx from graphite limiter	$\Gamma_{C,L}$
Oxygen influx from graphite limiter	$\Gamma_{O,L}$
Hydrogen influx from graphite limiter	$\Gamma_{H,L}$
Source rate	Q
Diffusion coefficient	D
Convective drift velocity	V
Collision frequency	ν
Absolute intensity	I_{abs}
Total particle influx	$\Gamma_{particle}$
Effective ionization rate coefficient	S
Effective excitation rate coefficient	X
Branching ratio	B
Ionization per photon	$\frac{S}{XB}$
Reaction rate coefficient	R_H
Total outflux	Γ_{out}
Radial velocity	v_r

APPENDIX: C

List of Indian tokamaks discussed in this thesis

Tokamak	ADITYA-U	ADITYA	SST-1 (Steady-state Superconducting Tokamak)
Year of Operations	2017	1989-2014	2013
Configuration	Double null divertor	Circular Limiter	Double-null Divertor
Major radius(m)	0.75	0.75	1.10
minor radius(m)	0.18 to 0.22	0.25	0.20
TF (T)	1.5	1.5	3.0
IP (KA)	0.15	0.25	0.220

List of worldwide tokamaks discussed in this thesis

(Nick Balshaw)

Tokamak	Country	Year Of Operations	Configuratio n	Major Radius (M)	Minor Radius (M)	TF (T)	IP (Ka)
ALCATOR A (ALto CAmpo TORu)	USA	1969 - 1982	Circular Limiter	0.54	0.10	10	0.3
ALCATOR C (ALto CAmpo TORus)	USA	1978 – 1987	Circular Limiter	0.64	0.16	12	0.9
ALCATOR C- Mod (ALto CAmpo TORus)	USA	1993 – 2016	D-shape Divertor (single or double null)	0.67	0.22	8	2
ASDEX upgrade	Germany	1991	D-shape Divertor	1.65	0.5-0.8	3.9	1.4
ASDEX (Axially Symmetric Divertor EXperiment)	Germany	1980 - 1990	Circular Divertor (double null)	1.54	0.40	2.6	0.5
ATC	USA	1972 - 1976		0.88	0.11	2	0.05

APPENDIX: C

COMPASS	Czech Republic	2008	D-shape Divertor	0.56	0.21	2.1	0.32
D III-D	USA	1986	D-shape Divertor (double null)	1.66	0.67	2.2	3
EAST (Experimental Advanced Superconducting Tokamak) (HT- 7U)	China	2006	D-shape Divertor (single or double) and limiter	1.75	0.43	5 SC	0.5
HT-7	China	1993 – 2013	Circular Limiter	1.22	0.35	3 SC	0.4
ISX-A (Impurity Study eXperiment - A)	USA	1977-1978	Circular Limiter	0.92	0.26	1.8	0.22
ISX-B (Impurity Study eXperiment - B)	USA	1978 to 1984	Non-circular Limiter	0.93	0.27	1.8	0.24
ITER	France	2025	D-shape Divertor	6.20	2.00	5.3 SC	15 (17)
JET (Joint European Torus) (divertor config.)	EU	1992	D-shape Divertor	2.96	0.96	4	6
JET(Joint European Torus)(origin	EU	1983 - 1992	D-shape Limiter	3.00	1.25- 2.1	3.45	7
JT-60 SA	Japan	2019	D-shape Divertor (double null)	3.16	1.02	2.7 SC	5.5
JT-60 (lower divertor configuration)	Japan	1987 - 1989	Lower Divertor / Limiter	3.00	0.70	4.5	LD2.2 /L3.2
JT-60 (outer divertor configuration)	Japan	1985 - 1987	Outer Divertor / Circular Limiter	3.00	1.00	4.5	D2.1 /L2.7

JT-60U	Japan	1991 - 2010	D-shape Divertor	3.40	1.00	4.2	5
PLT (Princeton Large Torus)	USA	1975 – 1986	Circular Limiter	1.32	0.40	4	0.7 (1)
TCV (Tokamak a Configuration Variable)	Switzerlan d	1992	Variable config. (elongation)	0.88	0.25- 0.7	1.4	1.2
TEXTOR	Germany	1981 (1994) – 2013	Circular Limiter / Dynamic Ergodic Divertor	1.75	0.47	2.8	0.800
TRIAM-1M (Tokamak of Research Institute for Applied Mechanics)	Japan	1986 - 2005	D-shape Limiter, with divertor added later	0.80	0.12 - 0.18	8 SC	0.42

BIBLIOGRAPHY

- Achenbach, Joel, and Evan Halper. "U.S. Announces Milestone on Fusion Energy, Sparking Hopes for Clean Power." *Washington Post*, 17 Dec. 2022, <https://www.washingtonpost.com/business/2022/12/13/fusion-energy-biden-climate/>.
- Afonin, K. Yu., and V. G. Petrov. "Influence of High-Temperature Effects on Interpretation of Probing Wave Time Delay in the ITER Refractometry Measurements." *Plasma Physics Reports*, vol. 47, no. 4, Apr. 2021, pp. 337–44. Springer Link, <https://doi.org/10.1134/S1063780X21040012>.
- Ambulkar, K. K., et al. "Measurement of LHCD Antenna Position in Aditya Tokamak." *Journal of Physics: Conference Series*, vol. 208, no. 1, Feb. 2010, p. 012025. Institute of Physics, <https://doi.org/10.1088/1742-6596/208/1/012025>.
- Angioni, C., et al. "Off-Diagonal Particle and Toroidal Momentum Transport: A Survey of Experimental, Theoretical and Modelling Aspects." *Nuclear Fusion*, vol. 52, no. 11, Oct. 2012, p. 114003. Institute of Physics, <https://doi.org/10.1088/0029-5515/52/11/114003>.
- Arambhadiya, Bharat, et al. "Automation of Aditya Tokamak Plasma Position Control DC Power Supply." *Fusion Engineering and Design*, vol. 112, Nov. 2016, pp. 714–17. ScienceDirect, <https://doi.org/10.1016/j.fusengdes.2016.06.032>.
- Artsimovich, L. A. "Tokamak Devices." *Nuclear Fusion*, vol. 12, no. 2, Mar. 1972, pp. 215–52. Institute of Physics, <https://doi.org/10.1088/0029-5515/12/2/012>.
- ASDEX Team. "The H-Mode of ASDEX." *Nuclear Fusion*, vol. 29, no. 11, Nov. 1989, p. 1959. Institute of Physics, <https://doi.org/10.1088/0029-5515/29/11/010>.
- Atrey, P. K., et al. "Design, Development, and Operation of Seven Channels' 100-GHz Interferometer for Plasma Density Measurement." *IEEE Transactions on Plasma Science*, vol. 47, no. 2, Feb. 2019, pp. 1316–21. IEEE Xplore, <https://doi.org/10.1109/TPS.2018.2890307>.

BIBLIOGRAPHY

- Bandyopadhyay, I., et al. “Modelling of Ohmic Discharges in ADITYA Tokamak Using the Tokamak Simulation Code.” *Plasma Physics and Controlled Fusion*, vol. 46, no. 9, Sept. 2004, pp. 1443–53, <https://doi.org/10.1088/0741-3335/46/9/007>.
- Banerjee, Santanu, Joydeep GHOSH, et al. “Observations of H α Emission Profiles in Aditya Tokamak.” *J. Plasma Fusion Res.*, vol. 9, 2010, pp. 29–32, https://www.academia.edu/16904929/Observations_of_H%CE%B1_emission_profiles_in_Aditya_tokamak.
- Banerjee, Santanu, Vinay Kumar, et al. “Space- and Time-Resolved Visible-Emission Spectroscopy of Aditya-Tokamak Discharges Using Multi-Track Spectrometer.” *Measurement Science and Technology*, vol. 19, no. 4, Apr. 2008, p. 045603, <https://doi.org/10.1088/0957-0233/19/4/045603>.
- Barnes, M. *A Pulsed RF Discharge for a Caesium Free H⁻ Ion Source - ProQuest*. University of Liverpool, 30 Sept. 2018. [liverpository.liverpool.ac.uk](https://liverpository.liverpool.ac.uk/handle/8355ed7101b5fd65b510b8b84e45c2c1/1?pq-origsite=gscholar&cbl=44156), <https://www.proquest.com/openview/8355ed7101b5fd65b510b8b84e45c2c1/1?pq-origsite=gscholar&cbl=44156>.
- Bauer, W. “Surface Processes in Plasma Wall Interactions.” *Journal of Nuclear Materials*, vol. 76–77, Sept. 1978, pp. 3–15. *ScienceDirect*, [https://doi.org/10.1016/0022-3115\(78\)90114-9](https://doi.org/10.1016/0022-3115(78)90114-9).
- Baylor, L. R., et al. “Pellet Injection Technology and Applications on ITER.” *2015 IEEE 26th Symposium on Fusion Engineering (SOFE)*, 2015, pp. 1–8. *IEEE Xplore*, <https://doi.org/10.1109/SOFE.2015.7482362>.
- Bedoya, F., et al. “Initial Studies of Plasma Facing Component Surface Conditioning in the National Spherical Tokamak Experiment Upgrade with the Materials Analysis Particle Probe.” *Nuclear Materials and Energy*, vol. 12, Aug. 2017, pp. 1248–52. *ScienceDirect*, <https://doi.org/10.1016/j.nme.2017.03.035>.
- Behringer, K. *Description of the Impurity Transport Code “STRAHL.”* JET-R--87-08, 1987, https://inis.iaea.org/search/search.aspx?orig_q=RN:19047926.
- Behringer, K., and U. Fantz. “The Influence of Opacity on Hydrogen Excited-State Population and Applications to Low-Temperature Plasmas.” *New Journal of Physics*, vol. 2, Sept. 2000, pp. 23–23, <https://doi.org/10.1088/1367-2630/2/1/323>.

- Behringer, K. H., et al. "Impurity and Radiation Studies during the JET Ohmic Heating Phase." *Nuclear Fusion*, vol. 26, no. 6, June 1986, pp. 751–68, <https://doi.org/10.1088/0029-5515/26/6/004>.
- Behringer, K. H. "Spectroscopic Studies of Plasma-Wall Interaction and Impurity Behaviour in Tokamaks." *Journal of Nuclear Materials*, vol. 145–147, Feb. 1987, pp. 145–53. *ScienceDirect*, [https://doi.org/10.1016/0022-3115\(87\)90319-9](https://doi.org/10.1016/0022-3115(87)90319-9).
- Bell, Ronald E. "Inversion Technique to Obtain an Emissivity Profile from Tangential Line-integrated Hard X-ray Measurements." *Review of Scientific Instruments*, vol. 66, no. 1, Jan. 1995, pp. 558–60. *aip.scitation.org*, <https://doi.org/10.1063/1.1146350>.
- Bethe, Hans A., and Edwin E. Salpeter. *Quantum Mechanics of One-and Two-Electron Atoms*. Springer Science & Business Media, 2012.
- Bhatt, S B, et al. "Aditya: The First Indian Tokamak." *Indian Journal of Pure and Applied Physics*, vol. 27, Jan. 1989, p. 710.
- Bhatt, S. B., et al. "Different Types of Lithium Coating in Tokamak ADITYA." *IEEE Transactions on Plasma Science*, vol. 40, no. 6, June 2012, pp. 1773–77. *IEEE Xplore*, <https://doi.org/10.1109/TPS.2012.2193421>.
- Bhattacharya, Amrita, Joydeep Ghosh, Malay B. Chowdhuri, et al. "A Study of the O⁴⁺ Emissivity Profiles with Two Separate Photon Emissivity Coefficient Databases and a Comparison of the Impurity Diffusion Coefficients in the Aditya Tokamak." *Plasma and Fusion Research*, vol. 14, no. 0, Oct. 2019, pp. 1403155–1403155, <https://doi.org/10.1585/pfr.14.1403155>.
- Bhattacharya, Amrita, Prabhat Munshi, et al. "A Study of the von Neumann Stability Analysis of a Semi-Implicit Numerical Method Applied Over the Radial Impurity Transport Equation in Tokamak Plasma." *Journal of Fusion Energy*, vol. 37, 2018, pp. 211–37, <https://doi.org/10.1007/s10894-018-0188-8>.
- Bhattacharya, Amrita, Joydeep Ghosh, M. B. Chowdhuri, and Ashoke De. "Generalization of the Stability Condition for the Semi-Implicit Formulation of the Radial Impurity Transport Equation in Tokamak Plasma in Terms of the Magnetic Flux Surface Coordinate." *Journal of Fusion Energy*, vol. 40, no. 2, Aug. 2021, p. 20. *Springer Link*, <https://doi.org/10.1007/s10894-021-00308-2>.

BIBLIOGRAPHY

- Bhattacharya, Amrita, Joydeep Ghosh, M. B. Chowdhuri, and Prabhat Munshi. "Numerical Estimation of the Oxygen Impurity Transport in the Aditya Tokamak." *Physics of Plasmas*, vol. 27, no. 2, Feb. 2020, p. 023303, <https://doi.org/10.1063/1.5115230>.
- Biel, W., et al. "Diagnostics for Plasma Control – From ITER to DEMO." *Fusion Engineering and Design*, vol. 146, Sept. 2019, pp. 465–72, <https://doi.org/10.1016/j.fusengdes.2018.12.092>.
- Biel, W, et al. *Investigation of Argon Impurity Transport at TEXTOR-94*. 1999, p. 4.
- Bisai, N., M. B. Chowdhuri, et al. "Dynamics of Neon Ions after Neon Gas Seeding into Tokamak Plasma." *Nuclear Fusion*, vol. 59, no. 12, Dec. 2019, p. 126013, <https://doi.org/10.1088/1741-4326/ab3d31>.
- Bisai, N., R. Jha, et al. "Role of Neutral Gas in Scrape-off Layer Tokamak Plasma." *Physics of Plasmas*, vol. 22, no. 2, Feb. 2015, p. 022517. [aip.scitation.org](https://aip.scitation.org/10.1063/1.4913429), <https://doi.org/10.1063/1.4913429>.
- Bisai, N., R. Singh, et al. "Scrape-off Layer Tokamak Plasma Turbulence." *Physics of Plasmas*, vol. 19, no. 5, May 2012, p. 052509. [aip.scitation.org](https://aip.scitation.org/10.1063/1.4718714), <https://doi.org/10.1063/1.4718714>.
- Boehm, Sophie, and Clea Schumer. *10 Big Findings from the 2023 IPCC Report on Climate Change*. Mar. 2023. [www.wri.org](https://www.wri.org/insights/2023-ipcc-ar6-synthesis-report-climate-change-findings), <https://www.wri.org/insights/2023-ipcc-ar6-synthesis-report-climate-change-findings>.
- Bosch, H. S., and G. M. Hale. "Improved Formulas for Fusion Cross-Sections and Thermal Reactivities." *Nuclear Fusion*, vol. 32, no. 4, Apr. 1992, p. 611. *Institute of Physics*, <https://doi.org/10.1088/0029-5515/32/4/I07>.
- Bransden B.H.H and Joachain C.J. *The Physics of Atoms and Molecules (1983).Pdf*. Prentice Hall (Pearson Prentice Hall (Pearson Education Ltd), 1983. [www.academia.edu](https://www.academia.edu/38360213/Bransden_B_H_H_Joachain_C_J_The_Physics_of_Atoms_and_Molecules_1983_pdf), https://www.academia.edu/38360213/Bransden_B_H_H_Joachain_C_J_The_Physics_of_Atoms_and_Molecules_1983_pdf.
- Bransden, Brian Harold, et al. *Physics of Atoms and Molecules*. Pearson Education India, 2003.

- Brault, C., et al. “Experimental Study of a Drifting Low Temperature Plasma Extracted from a Magnetized Plasma Column.” *Physics Letters A*, vol. 360, no. 2, Dec. 2006, pp. 299–303. *ScienceDirect*, <https://doi.org/10.1016/j.physleta.2006.08.018>.
- Brezinsek, S., et al. “Characterization of the Deuterium Recycling Flux in Front of a Graphite Surface in the TEXTOR Tokamak.” *Plasma Physics and Controlled Fusion*, vol. 47, no. 4, Mar. 2005, pp. 615–34. *Institute of Physics*, <https://doi.org/10.1088/0741-3335/47/4/003>.
- Brooks, J. N., et al. “Plasma–Surface Interaction Issues of an All-Metal ITER.” *Nuclear Fusion*, vol. 49, no. 3, Mar. 2009, p. 035007, <https://doi.org/10.1088/0029-5515/49/3/035007>.
- Bruhn, C., et al. “A Novel Method of Studying the Core Boron Transport at ASDEX Upgrade.” *Plasma Physics and Controlled Fusion*, vol. 60, no. 8, June 2018, p. 085011. *Institute of Physics*, <https://doi.org/10.1088/1361-6587/aac870>.
- Brunner, S., et al. “Global Approach to the Spectral Problem of Microinstabilities in Tokamak Plasmas Using a Gyrokinetic Model.” *Physics of Plasmas*, vol. 5, no. 11, Oct. 1998, p. 3929. *world, aip.scitation.org*, <https://doi.org/10.1063/1.873113>.
- Buzi, Luxherta, et al. “Influence of Particle Flux Density and Temperature on Surface Modifications of Tungsten and Deuterium Retention.” *Journal of Nuclear Materials*, vol. 455, no. 1, Dec. 2014, pp. 316–19. *ScienceDirect*, <https://doi.org/10.1016/j.jnucmat.2014.06.059>.
- Čadež, Iztok, et al. “Processes with Neutral Hydrogen and Deuterium Molecules Relevant to Edge Plasma in Tokamaks.” *Journal of Physics: Conference Series*, vol. 133, IOP Publishing, 2008, p. 012029.
- Chakraborty Thakur, Saikat, et al. “Suppression of Drift Wave Turbulence and Zonal Flow Formation by Changing Axial Boundary Conditions in a Cylindrical Magnetized Plasma Device.” *Physics of Plasmas*, vol. 20, no. 1, Jan. 2013, p. 012304, <https://doi.org/10.1063/1.4775775>.
- Chapman, Brian and J. L. Vossen. “Glow Discharge Processes: Sputtering and Plasma Etching | Wiley.” *Physics Today*, vol. 62, 1981, <https://www.wiley.com/en-us/Glow+Discharge+Processes%3A+Sputtering+and+Plasma+Etching-p-9780471078289>.

BIBLIOGRAPHY

- Chattopadhyay, Asim Kumar, et al. “Second-Harmonic Ion Cyclotron Resonance Heating Scenarios of Aditya Tokamak Plasma.” *Pramana*, vol. 85, no. 4, Oct. 2015, pp. 713–21. [link.springer.com](https://link.springer.com/10.1007/s12043-014-0908-1), <https://doi.org/10.1007/s12043-014-0908-1>.
- Chen, Francis F. *Introduction to Plasma Physics*. Springer Science & Business Media, 2012.
- Chen, H., et al. “Poloidally Asymmetric Distribution of Impurities in Joint European Torus Plasmas.” *Physics of Plasmas*, vol. 7, no. 11, 2000, pp. 4567–72.
- Chowdhuri, M. B., R. Manchanda, J. Ghosh, N. Yadava, et al. “A Diagnostic for Measuring Radial Profile of Visible Continuum Radiation from ADITYA-U Tokamak Plasmas.” *Fusion Engineering and Design*, vol. 173, Dec. 2021, p. 112884. *ScienceDirect*, <https://doi.org/10.1016/j.fusengdes.2021.112884>.
- Chowdhuri, M. B., R. Manchanda, J. Ghosh, S. B. Bhatt, et al. “Improvement of Plasma Performance with Lithium Wall Conditioning in Aditya Tokamak.” *Plasma Science and Technology*, vol. 15, no. 2, Feb. 2013, pp. 123–28, <https://doi.org/10.1088/1009-0630/15/2/09>.
- Chowdhuri, M. B., J. Ghosh, et al. “Investigation of Oxygen Impurity Transport Using the O⁴⁺ Visible Spectral Line in the Aditya Tokamak.” *Nuclear Fusion*, vol. 53, no. 2, 2013, p. 023006.
- Chowdhuri, Malay Bikas, et al. “NEON GAS SEEDED RADIATIVE IMPROVED MODE IN ADITYA-U TOKAMAK.” *IAEA-CN-258*, 2018.
- Churchill, R. M., et al. “In–out Impurity Density Asymmetry in the Pedestal Region of Alcator C-Mod.” *Nuclear Fusion*, vol. 53, no. 12, 2013, p. 122002.
- Coda, S., et al. “Electron Cyclotron Current Drive and Suprathermal Electron Dynamics in the TCV Tokamak.” *Nuclear Fusion*, vol. 43, no. 11, Nov. 2003, p. 1361. *Institute of Physics*, <https://doi.org/10.1088/0029-5515/43/11/008>.
- Condrea, I., et al. “Local Poloidal and Toroidal Plasma Rotation Velocities and Ion Temperature in a Tokamak Plasma Obtained with a Matrix Inversion Method Considering Asymmetries.” *Physics of Plasmas*, vol. 7, no. 9, Sept. 2000, pp. 3641–53. [aip.scitation.org](https://aip.scitation.org/10.1063/1.1287417), <https://doi.org/10.1063/1.1287417>.

- D E Post, et al. “Steady-State Radiative Cooling Rates for Low-Density, High-Temperature Plasmas.” *Atomic Data and Nuclear Data Tables*, vol. 20, no. 5, Nov. 1977, pp. 397–439. www.sciencedirect.com, [https://doi.org/10.1016/0092-640X\(77\)90026-2](https://doi.org/10.1016/0092-640X(77)90026-2).
- Davison, Lee, and Yasuyuki Horie, editors. *High-Energy-Density Physics*. Springer Berlin Heidelberg, 2006, <https://doi.org/10.1007/3-540-29315-9>.
- Deeba, F., et al. *Optical Emission Spectroscopy of 2.45 Ghz Microwave Induced Plasma*. 2015.
- Dey, Ritu, M. B. Chowdhuri, Joydeep Ghosh, R. Manchanda, Nandini Yadava, et al. “Investigation of Atomic and Molecular Processes in H α Emission through Modelling of Measured H α Emissivity Profile Using DEGAS2 in the ADITYA Tokamak.” *Nuclear Fusion*, vol. 59, no. 7, May 2019, p. 076005. *Institute of Physics*, <https://doi.org/10.1088/1741-4326/ab0f01>.
- Dey, Ritu, Joydeep Ghosh, et al. “Investigation of Neutral Particle Dynamics in Aditya Tokamak Plasma with DEGAS2 Code.” *Nuclear Fusion*, vol. 57, no. 8, 2017, p. 086003.
- Dey, Ritu, M. B. Chowdhuri, Joydeep Ghosh, Ranjana Manchanda, Nandini Yadava, et al. “Modeling of the H α Emission from ADITYA Tokamak Plasmas.” *Atoms*, vol. 7, no. 4, 4, Dec. 2019, p. 95. www.mdpi.com, <https://doi.org/10.3390/atoms7040095>.
- Dhyani, Pravesh, J. Ghosh, et al. “A Novel Approach for Mitigating Disruptions Using Biased Electrode in Aditya Tokamak.” *Nuclear Fusion*, vol. 54, no. 8, June 2014, p. 083023. *Institute of Physics*, <https://doi.org/10.1088/0029-5515/54/8/083023>.
- Dhyani, Pravesh, Joydeep Ghosh, et al. “A Set-up for a Biased Electrode Experiment in ADITYA Tokamak.” *Measurement Science and Technology*, vol. 25, no. 10, Sept. 2014, p. 105903. *Institute of Physics*, <https://doi.org/10.1088/0957-0233/25/10/105903>.
- Dimitrova, M., et al. “Effect of the Gas Puff Location on the Divertor Plasma Properties in COMPASS Tokamak.” *Journal of Physics: Conference Series*, vol. 1492, no. 1, Mar. 2020, p. 012003, <https://doi.org/10.1088/1742-6596/1492/1/012003>.
- Dux R. *STRAHL User Manual*. 10/20, Max Planck Institute for Plasma Physics, Germany, 2006.

BIBLIOGRAPHY

- Dux, R., et al. “Z Dependence of the Core Impurity Transport in ASDEX Upgrade H Mode Discharges.” *Nuclear Fusion*, vol. 39, no. 11, Nov. 1999, pp. 1509–22. *Institute of Physics*, <https://doi.org/10.1088/0029-5515/39/11/302>.
- Dux, R., and A. G. Peeters. “Neoclassical Impurity Transport in the Core of an Ignited Tokamak Plasma.” *Nuclear Fusion*, vol. 40, no. 10, Oct. 2000, p. 1721. *Institute of Physics*, <https://doi.org/10.1088/0029-5515/40/10/304>.
- Edappala, Praveenlal, et al. “Multi-Channel Control Circuit for Real-Time Control of Events in Aditya Tokamak.” *Fusion Engineering and Design*, vol. 112, Nov. 2016, pp. 678–82. *ScienceDirect*, <https://doi.org/10.1016/j.fusengdes.2016.05.030>.
- EG&G JUDSON. *HUV1100BQ Datasheet & Application Notes - Datasheet Archive*. 2009, <https://www.datasheetarchive.com/HUV1100BQ-datasheet.html>.
- Eidietis, N. W., et al. “The ITPA Disruption Database.” *Nuclear Fusion*, vol. 55, no. 6, May 2015, p. 063030. *Institute of Physics*, <https://doi.org/10.1088/0029-5515/55/6/063030>.
- Eni Staff. “Tokamak, the Promise of Magnetic Fusion.” *Eni.Com*, 2022, <https://www.eni.com/en-IT/scientific-research/tokamak-promise-magnetic-fusion.html>.
- Equipe TFR. “Tokamak Plasma Diagnostics.” *Nuclear Fusion*, vol. 18, no. 5, May 1978, pp. 647–731, <https://doi.org/10.1088/0029-5515/18/5/004>.
- Escarguel, A., B. Pégourié, et al. “Atomic and Molecular Deuterium Edge Density Evaluation from Spectral Analysis of the D α Line Shape.” *Plasma Physics and Controlled Fusion*, vol. 43, no. 12, Nov. 2001, pp. 1733–46. *Institute of Physics*, <https://doi.org/10.1088/0741-3335/43/12/307>.
- Escarguel, A., R. Guirlet, et al. “Spectral Profile Analysis of the D α Line in the Divertor Region of Tore-Supra.” *Journal of Nuclear Materials*, vol. 290–293, Mar. 2001, pp. 854–58. *ScienceDirect*, [https://doi.org/10.1016/S0022-3115\(00\)00650-4](https://doi.org/10.1016/S0022-3115(00)00650-4).
- Eubank, A., and E. Sindoni. “Course on Plasma Diagnostics and Data Acquisition Systems, Varenna, Italy, September 3-11, 1975, Proceedings.” *Course on Plasma Diagnostics and Data Acquisition Systems, 1975. NASA ADS*, <https://ui.adsabs.harvard.edu/abs/1975pdda.proc.....E>.

EUROfusion. *History of Fusion*. 2022 2014, <https://www.euro-fusion.org/fusion/history-of-fusion/>.

Fantz, U., et al. “Hydrogen Molecules in the Divertor of ASDEX Upgrade.” *Journal of Nuclear Materials*, vol. 290–293, Mar. 2001, pp. 367–73. *ScienceDirect*, [https://doi.org/10.1016/S0022-3115\(00\)00638-3](https://doi.org/10.1016/S0022-3115(00)00638-3).

Farley, D. R., et al. “Modeling of Hydrogen Ground State Rotational and Vibrational Temperatures in Kinetic Plasmas.” *Journal of Quantitative Spectroscopy and Radiative Transfer*, vol. 112, no. 5, Mar. 2011, pp. 800–19. *ScienceDirect*, <https://doi.org/10.1016/j.jqsrt.2010.10.015>.

Federici, G., et al. “Assessment of Erosion of the ITER Divertor Targets during Type I ELMs.” *Plasma Physics and Controlled Fusion*, vol. 45, no. 9, Aug. 2003, p. 1523. *Institute of Physics*, <https://doi.org/10.1088/0741-3335/45/9/301>.

Federici, G. “Plasma Wall Interactions in ITER.” *Physica Scripta*, vol. 2006, no. T124, Apr. 2006, p. 1. *Institute of Physics*, <https://doi.org/10.1088/0031-8949/2006/T124/001>.

Foster, A. R., et al. “Erosion and Transport of Sn and In in the SOL of MAST Plasmas.” *Journal of Nuclear Materials*, vol. 363–365, June 2007, pp. 152–56. *ScienceDirect*, <https://doi.org/10.1016/j.jnucmat.2007.01.056>.

Freidberg, Jeffrey P. *Plasma Physics and Fusion Energy*. Cambridge university press, 2008.

Fujita, Keiji, et al. “Global Calculation of Neoclassical Impurity Transport Including the Variation of Electrostatic Potential.” *Journal of Plasma Physics*, vol. 86, no. 3, June 2020, p. 905860319. *Cambridge University Press*, <https://doi.org/10.1017/S0022377820000598>.

Furth, H. P. “Tokamak Research.” *Nuclear Fusion*, vol. 15, no. 3, June 1975, pp. 487–534, <https://doi.org/10.1088/0029-5515/15/3/014>.

Fussmann, G., et al. “Impurity Transport and Neoclassical Predictions.” *Plasma Physics and Controlled Fusion*, vol. 33, no. 13, Nov. 1991, p. 1677. *Institute of Physics*, <https://doi.org/10.1088/0741-3335/33/13/013>.

Gao, Wei, Juan Huang, Jianxun Su, et al. “Analysis of Asymmetry of the D α Emission Spectra under the Zeeman Effect in Boundary Region for D–D Experiment on EAST

BIBLIOGRAPHY

- Tokamak.” *Chinese Physics B*, vol. 30, no. 2, Feb. 2021, p. 025201. *Institute of Physics*, <https://doi.org/10.1088/1674-1056/abc162>.
- Gao, Wei, Juan Huang, Chengrui Wu, et al. “Analysis of the Zeeman Effect on D α Spectra on the EAST Tokamak.” *Chinese Physics B*, vol. 26, Apr. 2017, p. 045203. *ResearchGate*, <https://doi.org/10.1088/1674-1056/26/4/045203>.
- Ghosh, J, R. L. Tanna, et al. “Upgradation of Aditya Tokamak with Limiter Configuration to Aditya Upgrade Tokamak with Divertor Configuration.” *IAEA-CN-234*, 2018, p. 8.
- Ghosh, Joydeep, H. R. Griem, et al. “Measurements of Ion and Neutral Atom Flows and Temperatures in the Inner and Outer Midplane Scrape-off Layers of the Alcator C-Mod Tokamak.” *Physics of Plasmas*, vol. 11, no. 3, 2004, pp. 1033–42.
- Ghosh, Joydeep, Sambaran PAHARI, et al. “Novel Concept for Disruption Mitigation in the ADITYA - U Tokamak by Fast Time Response Electromagnetic Driven Pellet Impurity Injector.” *IAEA-CN-286*, 2021.
- Ghosh, Soumen, K. K. Barada, et al. “Resolving an Anomaly in Electron Temperature Measurement Using Double and Triple Langmuir Probes.” *Plasma Sources Science and Technology*, vol. 24, no. 1, Dec. 2014, p. 015017. *Institute of Physics*, <https://doi.org/10.1088/0963-0252/24/1/015017>.
- Gibney, Elizabeth. “Nuclear-Fusion Reactor Smashes Energy Record.” *Nature*, vol. 602, no. 7897, Feb. 2022, pp. 371–371. www.nature.com, <https://doi.org/10.1038/d41586-022-00391-1>.
- Gilmore, Forrest R., et al. “Franck–Condon Factors, r -Centroids, Electronic Transition Moments, and Einstein Coefficients for Many Nitrogen and Oxygen Band Systems.” *Journal of Physical and Chemical Reference Data*, vol. 21, no. 5, Sept. 1992, pp. 1005–107, <https://doi.org/10.1063/1.555910>.
- Glöggler, Stephan. *Experimental and Numerical Investigation of Neon-Seeded High Radiation Discharges at the JET Tokamak*.

- Goswami, Mayank, et al. “Plasma Diagnostics at Aditya Tokamak by Two Views Visible Light Tomography.” *Fusion Engineering and Design*, vol. 89, no. 11, Nov. 2014, pp. 2659–65. *ScienceDirect*, <https://doi.org/10.1016/j.fusengdes.2014.07.003>.
- Goswami, Rajiv. “Influence of Plasma Surface Interactions on Tokamak Startup.” *Physics of Plasmas*, vol. 20, no. 8, Aug. 2013, p. 082516, <https://doi.org/10.1063/1.4818988>.
- Goswami, Rajiv, and Jean-François Artaud. “An Enhanced Tokamak Startup Model.” *Physics of Plasmas*, vol. 24, no. 1, Jan. 2017, p. 012508. *aip.scitation.org*, <https://doi.org/10.1063/1.4973826>.
- Goto, M., and S. Morita. “Determination of the Line Emission Locations in a Large Helical Device on the Basis of the Zeeman Effect.” *Physical Review E*, vol. 65, no. 2, Jan. 2002, p. 026401. *APS*, <https://doi.org/10.1103/PhysRevE.65.026401>.
- Goto, Motoshi, and Shigeru Morita. “Poloidal Distribution Measurement of Inward Neutral Flux in LHD.” *Plasma and Fusion Research*, vol. 2, 2007, pp. S1053–S1053, <https://doi.org/10.1585/pfr.2.S1053>.
- Gravier, E., et al. “Low-Frequency Instabilities in a Laboratory Magnetized Plasma Column.” *Physics of Plasmas*, vol. 11, no. 2, Feb. 2004, pp. 529–37. *aip.scitation.org*, <https://doi.org/10.1063/1.1636479>.
- Greenwald, M., et al. “H Mode Confinement in Alcator C-Mod.” *Nuclear Fusion*, vol. 37, no. 6, June 1997, p. 793. *Institute of Physics*, <https://doi.org/10.1088/0029-5515/37/6/I07>.
- Griem, H. R. “Principles of Plasma Spectroscopy.” *Fast Electrical and Optical Measurements: Volume I—Current and Voltage Measurements / Volume II—Optical Measurements*, edited by James E. Thompson and Lawrence H. Luessen, Springer Netherlands, 1986, pp. 885–910. *Springer Link*, https://doi.org/10.1007/978-94-017-0445-8_34.
- Groebner, R. J., et al. “The Role of Neutrals in High-Mode (H-Mode) Pedestal Formation.” *Physics of Plasmas*, vol. 9, no. 5, May 2002, pp. 2134–40, <https://doi.org/10.1063/1.1462032>.
- Groth, M., et al. “EDGE2D-EIRENE Predictions of Molecular Emission in DIII-D High-Recycling Divertor Plasmas.” *Nuclear Materials and Energy*, vol. 19, May 2019, pp. 211–17. *ScienceDirect*, <https://doi.org/10.1016/j.nme.2019.02.035>.

BIBLIOGRAPHY

- Gupta, C. N., et al. “Recent High Current Plasma Discharges Operations with Booster Power Supply Assisted Vertical Magnetic Field in Aditya Tokamak.” *2015 IEEE 26th Symposium on Fusion Engineering (SOFE)*, 2015, pp. 1–4. *IEEE Xplore*, <https://doi.org/10.1109/SOFE.2015.7482398>.
- Haas, G., et al. “Recycling Studies in the ASDEX Divertor with Pellet or Gas Puff Refuelling.” *Journal of Nuclear Materials*, vol. 145–147, Feb. 1987, pp. 519–22. *ScienceDirect*, [https://doi.org/10.1016/0022-3115\(87\)90392-8](https://doi.org/10.1016/0022-3115(87)90392-8).
- Hanada, K., et al. “Particle Balance Investigation with the Combination of the Hydrogen Barrier Model and Rate Equations of Hydrogen State in Long Duration Discharges on an All-Metal Plasma Facing Wall in QUEST.” *Nuclear Fusion*, vol. 59, no. 7, July 2019, p. 076007, <https://doi.org/10.1088/1741-4326/ab1858>.
- Hartwig, Zachary Seth. *An In-Situ Accelerator-Based Diagnostic for Plasma-Material Interactions Science in Magnetic Fusion Devices*. MASSACHUSETTS INSTITUTE OF TECHNOLOGY, 2014.
- Hassanein, A. M. “Stability and Erosion of Melt Layers Formed During Plasma Disruptions.” *Fusion Technology*, vol. 15, no. 2P2A, Mar. 1989, pp. 513–21. *Taylor and Francis+NEJM*, <https://doi.org/10.13182/FST89-A39751>.
- Hayashi, Y., et al. “Plasma Detachment Study of High Density Helium Plasmas in the Pilot-PSI Device.” *Nuclear Fusion*, vol. 56, no. 12, Sept. 2016, p. 126006. *Institute of Physics*, <https://doi.org/10.1088/0029-5515/56/12/126006>.
- Heald, Mark A., and C. B. Wharton. *Plasma Diagnostics with Microwaves*. Wiley, 1965.
- Hender, T. C., et al. “Chapter 3: MHD Stability, Operational Limits and Disruptions.” *Nuclear Fusion*, vol. 47, no. 6, June 2007, pp. S128–202. *Eindhoven University of Technology research portal*, <https://doi.org/10.1088/0029-5515/47/6/S03>.
- Henderson, S. S., et al. “Neoclassical and Gyrokinetic Analysis of Time-Dependent Helium Transport Experiments on MAST.” *Nuclear Fusion*, vol. 54, no. 9, Sept. 2014, p. 093013, <https://doi.org/10.1088/0029-5515/54/9/093013>.

- Herman, Robin. *Fusion : The Search for Endless Energy*. Cambridge [England] ; New York : Cambridge University Press, 1990. Internet Archive, <http://archive.org/details/fusionsearchfore00herm>.
- Herzberg, Gerhard. “Molecular Spectra and Molecular Structure. I. Spectra of Diatomic Molecules.” *American Journal of Physics*, vol. 19, no. 6, Sept. 1951, pp. 390–91. [aip.scitation.org](https://doi.org/10.1119/1.1932852), <https://doi.org/10.1119/1.1932852>.
- Hey, J. D., C. C. Chu, Ph Mertens, et al. “Atomic Collision Processes with Ions at the Edge of Magnetically Confined Fusion Plasmas.” *Journal of Physics B: Atomic, Molecular and Optical Physics*, vol. 37, no. 12, June 2004, pp. 2543–67. *Institute of Physics*, <https://doi.org/10.1088/0953-4075/37/12/010>.
- Hey, J. D., Y. T. Lie, D. Rusbüldt, et al. “Doppler Broadening and Magnetic Field Effects on Some Ion Impurity Spectra Emitted in the Boundary Layer of a Tokamak Plasma.” *Contributions To Plasma Physics*, vol. 34, no. 6, 1994, pp. 725–47.
- Hey, J. D., M. Korten, Y. T. Lie, et al. “Doppler Broadening and Magnetic Field Effects on the Balmer Lines Emitted at the Edge of a Tokamak Plasma.” *Contributions to Plasma Physics*, vol. 36, no. 5, 1996, pp. 583–604.
- Hey, J. D., C. C. Chu, and E. Hintz. “On a Heating Mechanism for Cold Hydrogen and Deuterium Atoms Produced at the Edge of a Tokamak Plasma.” *Journal of Physics B: Atomic, Molecular and Optical Physics*, vol. 32, no. 14, July 1999, pp. 3555–73. *Institute of Physics*, <https://doi.org/10.1088/0953-4075/32/14/321>.
- Hey, J D, C. C. Chu, S. Brezinsek, et al. “Oxygen Ion Impurity in the TEXTOR Tokamak Boundary Plasma Observed and Analysed by Zeeman Spectroscopy.” *Journal of Physics B: Atomic, Molecular and Optical Physics*, vol. 35, no. 6, Mar. 2002, pp. 1525–53, <https://doi.org/10.1088/0953-4075/35/6/309>.
- Hinton, F. L., and Richard D. Hazeltine. “Theory of Plasma Transport in Toroidal Confinement Systems.” *Reviews of Modern Physics*, vol. 48, no. 2, 1976, p. 239.
- Hirai, Takeshi, et al. “ITER Relevant High Heat Flux Testing on Plasma Facing Surfaces.” *MATERIALS TRANSACTIONS*, vol. 46, no. 3, 2005, pp. 412–24, <https://doi.org/10.2320/matertrans.46.412>.

BIBLIOGRAPHY

Hirooka, Y., et al. “A New Plasma-surface Interactions Research Facility: PISCES-B and First Materials Erosion Experiments on Bulk-boronized Graphite.” *Journal of Vacuum Science & Technology A*, vol. 8, no. 3, May 1990, pp. 1790–97. *aip.scitation.org*, <https://doi.org/10.1116/1.576805>.

Hirooka, Yoshi, et al. “Modeling of Global Particle Balance in Steady-State Magnetic Fusion Devices – Analysis of the Recent Data from the TRIAM-1M Tokamak.” *Journal of Nuclear Materials*, vol. 313–316, Mar. 2003, pp. 588–94. *ScienceDirect*, [https://doi.org/10.1016/S0022-3115\(02\)01419-8](https://doi.org/10.1016/S0022-3115(02)01419-8).

Hollmann, E. M., S. Brezinsek, et al. “Spectroscopic Measurement of Atomic and Molecular Deuterium Fluxes in the DIII-D Plasma Edge.” *Plasma Physics and Controlled Fusion*, vol. 48, no. 8, July 2006, pp. 1165–80. *Institute of Physics*, <https://doi.org/10.1088/0741-3335/48/8/009>.

Hollmann, E. M., P. B. Aleynikov, et al. “Status of Research toward the ITER Disruption Mitigation System.” *Physics of Plasmas*, vol. 22, no. 2, Feb. 2015, p. 021802. *aip.scitation.org*, <https://doi.org/10.1063/1.4901251>.

Horton, W., et al. “Vorticity Probes and the Characterization of Vortices in the Kelvin–Helmholtz Instability in the Large Plasma Device Experiment.” *Physics of Plasmas*, vol. 12, no. 2, Jan. 2005, p. 022303, <https://doi.org/10.1063/1.1830489>.

Houlberg, W. A., et al. “Bootstrap Current and Neoclassical Transport in Tokamaks of Arbitrary Collisionality and Aspect Ratio.” *Physics of Plasmas*, vol. 4, no. 9, Sept. 1997, pp. 3230–42. *Silverchair*, <https://doi.org/10.1063/1.872465>.

Houtte, D. van, et al. “Recent Fully Non-Inductive Operation Results in Tore Supra with 6 Min, 1 GJ Plasma Discharges.” *Nuclear Fusion*, vol. 44, no. 5, May 2004, pp. L11–15. *Institute of Physics*, <https://doi.org/10.1088/0029-5515/44/5/L01>.

<http://www.iter.org/sci/fusion>. “Advantages of Fusion.” *ITER*, 7 Sept. 2022, <http://www.iter.org/sci/fusion>.

Huber, Klaus-Peter, and Gerhard Herzberg, editors. *Molecular Spectra and Molecular Structure. 4: Constants of Diatomic Molecules*. van Nostrand Reinhold Comp, 1979.

- Huddlestone, Richard H., and Stanley L. Leonard, editors. *Plasma Diagnostic Techniques*. Academic Press, 1965.
- Hutchinson, Ian H. *Principles of Plasma Diagnostics*. 2. ed, Cambridge Univ. Press, 2002.
- Isler, R. C., K. Behringer, et al. "Impurity Fluxes and Concentrations in the ISX-B Beryllium Limiter Experiment." *Nuclear Fusion*, vol. 25, no. 11, Nov. 1985, pp. 1635–55, <https://doi.org/10.1088/0029-5515/25/11/009>.
- Isler, R. C. "Profiles and polarizations of the Balmer- α line from high-temperature hydrogen atoms in strong magnetic fields." *Physical Review A*, vol. 14, no. 3, Sept. 1976, pp. 1015–19. *APS*, <https://doi.org/10.1103/PhysRevA.14.1015>.
- Isler, R. C., G. R. McKee, et al. "Signatures of Deuterium Recombination in the DIII-D Divertor." *Physics of Plasmas*, vol. 4, no. 8, Aug. 1997, pp. 2989–96. *aip.scitation.org*, <https://doi.org/10.1063/1.872432>.
- Isler, R. C., N. H. Brooks, et al. "Spectroscopic Analysis of Normal and Reversed Ion Flows in the DIII-D Divertor." *Physics of Plasmas*, vol. 6, no. 2, Feb. 1999, pp. 541–49. *aip.scitation.org*, <https://doi.org/10.1063/1.873198>.
- Isler, R. C., R. W. Wood, et al. "Spectroscopic Characterization of the DIII-D Divertor." *Physics of Plasmas*, vol. 4, no. 2, 1997, pp. 355–68.
- Iwamae, Atsushi, et al. "Polarization Resolved H α Spectra from the Large Helical Device: Emission Location, Temperature, and Inward Flux of Neutral Hydrogen." *Physics of Plasmas*, vol. 12, no. 4, 2005, p. 042501.
- Jackson, G. L., et al. "Enhanced Confinement Discharges in DIII-D with Neon and Argon Induced Radiation." *Journal of Nuclear Materials*, vol. 266–269, Mar. 1999, pp. 380–85. *ScienceDirect*, [https://doi.org/10.1016/S0022-3115\(98\)00653-9](https://doi.org/10.1016/S0022-3115(98)00653-9).
- Jadeja, K., et al. *ADITYA Upgrade Vacuum Vessel: Design, Construction, Testing, Installation and Operation*. 2017. Semantic Scholar, <https://doi.org/10.1016/J.FUSENGDES.2017.03.148>.
- Jadeja, K. A., et al. "Lithium Wall Conditioning Techniques in ADITYA-U Tokamak for Impurity and Fuel Control." *Nuclear Fusion*, vol. 62, no. 1, Dec. 2021, p. 016003. *iopscience.iop.org*, <https://doi.org/10.1088/1741-4326/ac35a0>.

BIBLIOGRAPHY

- Jadeja, K.A., et al. “Novel Approach of Pulsed-Glow Discharge Wall Conditioning in the ADITYA Upgrade Tokamak.” *Nuclear Fusion*, vol. 59, no. 8, Aug. 2019, p. 086005, <https://doi.org/10.1088/1741-4326/ab1ab6>.
- Jadeja, K. A., and S. B. Bhatt. “Study of Hydrogen Pumping through Condensed Argon in Cryogenic Pump.” *Journal of Physics: Conference Series*, vol. 390, no. 1, Nov. 2012, p. 012028. *Institute of Physics*, <https://doi.org/10.1088/1742-6596/390/1/012028>.
- Jaeger, S., et al. “Direct Observation of a Cross-Field Current-Carrying Plasma Rotating around an Unstable Magnetized Plasma Column.” *Physics of Plasmas*, vol. 16, no. 2, Feb. 2009, p. 022304. *aip.scitation.org*, <https://doi.org/10.1063/1.3076931>.
- Jahoda, F. C., et al. “Continuum Radiation in the X Ray and Visible Regions from a Magnetically Compressed Plasma (Scylla).” *Physical Review*, vol. 119, no. 3, Aug. 1960, p. 843. *journals.aps.org*, <https://doi.org/10.1103/PhysRev.119.843>.
- Janev, R. K., D. Reiter, et al. *Collision Processes in Low-Temperature Hydrogen Plasmas*. JUEL--4105, Forschungszentrum Juelich GmbH (Germany). Inst. fuer Plasmaphysik, 2003. *inis.iaea.org*, http://inis.iaea.org/Search/search.aspx?orig_q=RN:35040310.
- Janev, R. K., D. E. Post, et al. “Survey of Atomic Processes in Edge Plasmas.” *Journal of Nuclear Materials*, vol. 121, May 1984, pp. 10–16. *ScienceDirect*, [https://doi.org/10.1016/0022-3115\(84\)90096-5](https://doi.org/10.1016/0022-3115(84)90096-5).
- Janev Ratko, et al. *Elementary Processes in Hydrogen-Helium Plasmas: Cross Sections and Reaction*. Springer, 1987, <https://link.springer.com/book/10.1007/978-3-642-71935-6>.
- Jenkins, Francis Arthur, and Harvey Elliott White. *Fundamentals of Optics*. McGraw-Hill, 1976.
- JET Team. “Fusion Energy Production from a Deuterium-Tritium Plasma in the JET Tokamak.” *Nuclear Fusion*, vol. 32, no. 2, Feb. 1992, pp. 187–203, <https://doi.org/10.1088/0029-5515/32/2/I01>.
- Jha, R., et al. “Investigation of Gas Puff Induced Fluctuation Suppression in ADITYA Tokamak.” *Plasma Physics and Controlled Fusion*, vol. 51, no. 9, Sept. 2009, p. 095010, <https://doi.org/10.1088/0741-3335/51/9/095010>.

- JT-60 Team, et al. “Reduction of Ion Thermal Diffusivity Inside a Magnetic Island in JT-60U Tokamak Plasma.” *Physical Review Letters*, vol. 109, no. 6, Aug. 2012, p. 065001. *APS*, <https://doi.org/10.1103/PhysRevLett.109.065001>.
- Juan, Huang, et al. “Wall Recycling in Long Duration Discharges on the HT-7 Tokamak.” *Plasma Science and Technology*, vol. 7, no. 4, Aug. 2005, pp. 2911–14. *Institute of Physics*, <https://doi.org/10.1088/1009-0630/7/4/006>.
- Kaw, P. K. “Tokamak in India.” *Science*, vol. 270, 1995, p. 1918, <https://www.science.org/doi/10.1126/science.273.5277.861.c>.
- Kim, Young-Cheol, et al. “Correlation between Vibrational Temperature of N₂ and Plasma Parameters in Inductively Coupled Ar/N₂ Plasmas.” *Physics of Plasmas*, vol. 22, no. 8, Aug. 2015, p. 083512. *Silverchair*, <https://doi.org/10.1063/1.4928907>.
- Kodarkar, Nakul M., et al. “Analysis of Limiters for ADITYA Tokamak.” *International Journal of Mechanical and Industrial Engineering*, vol. 2, no. 1, Sept. 2020, <https://doi.org/10.47893/IJMIE.2012.1064>.
- Koepke, Mark E. “Interrelationship between Lab, Space, Astrophysical, Magnetic Fusion, and Inertial Fusion Plasma Experiments.” *Atoms*, vol. 7, no. 1, 1, Mar. 2019, p. 35. *www.mdpi.com*, <https://doi.org/10.3390/atoms7010035>.
- Kramida, Alexander, and Yuri Ralchenko. *NIST Atomic Spectra Database, NIST Standard Reference Database 78*. National Institute of Standards and Technology, 1999. *DOI.org (Datacite)*, <https://doi.org/10.18434/T4W30F>.
- Krasheninnikov, S. I., and A. S. Kukushkin. “Physics of Ultimate Detachment of a Tokamak Divertor Plasma.” *Journal of Plasma Physics*, vol. 83, no. 5, Oct. 2017, p. 155830501, <https://doi.org/10.1017/S0022377817000654>.
- Kremeyer, Thierry, et al. “Analysis of Hydrogen Fueling, Recycling, and Confinement at Wendelstein 7-X via a Single-Reservoir Particle Balance.” *Nuclear Fusion*, vol. 62, no. 3, Mar. 2022, p. 036023. *Institute of Physics*, <https://doi.org/10.1088/1741-4326/ac4acb>.

BIBLIOGRAPHY

- Kubo, H., et al. “The Spectral Profile of the Line Emitted from the Divertor Region of JT-60U.” *Plasma Physics and Controlled Fusion*, vol. 40, no. 6, June 1998, pp. 1115–26, <https://doi.org/10.1088/0741-3335/40/6/017>.
- Kumagai, A., et al. “Spatial variation of D α line spectral profile and emission process in the divertor region of JT-60U.” *Plasma Physics and Controlled Fusion*, vol. 42, no. 5, May 2000, pp. 529–43. *Institute of Physics*, <https://doi.org/10.1088/0741-3335/42/5/304>.
- Kumar, Pramod. “The Future of Energy Consumption, Security and Natural Gas: LNG in Baltic Sea Region.” *Strategic Analysis*, vol. 46, no. 5, Sept. 2022, pp. 553–54. *Taylor and Francis+NEJM*, <https://doi.org/10.1080/09700161.2022.2115230>.
- Kumar, Rohit, J. Ghosh, et al. “Characterisation of Induced Vessel Current during Mirnov Probe Calibration Experiment in ADITYA-U Tokamak.” *Fusion Engineering and Design*, vol. 166, May 2021, p. 112320. *ScienceDirect*, <https://doi.org/10.1016/j.fusengdes.2021.112320>.
- Kumar, Rohit, Suman Aich, et al. “Optimization of the Metallic Vessel-Wall Effect on the Magnetic Diagnostics Calibration in ADITYA-U Tokamak.” *Fusion Engineering and Design*, vol. 167, June 2021, p. 112339. *ScienceDirect*, <https://doi.org/10.1016/j.fusengdes.2021.112339>.
- Kumar, Rohit, Pramila Gautam, et al. “Real-Time Feedback Control System for ADITYA-U Horizontal Plasma Position Stabilisation.” *Fusion Engineering and Design*, vol. 165, Apr. 2021, p. 112218. *ScienceDirect*, <https://doi.org/10.1016/j.fusengdes.2020.112218>.
- Kumar, S. Sasanka, M. K. Jayaraj, et al. “Development of In Situ Laser Blow Off Cleaning Setup for ADITYA Tokamak Window.” *Fusion Science and Technology*, vol. 64, no. 1, July 2013, pp. 54–62. *Taylor and Francis+NEJM*, <https://doi.org/10.13182/FST13-A17047>.
- Kumar, Sameer, Ratneshwar Jha, et al. “Diamagnetic Flux Measurement in Aditya Tokamak.” *Review of Scientific Instruments*, vol. 81, no. 12, Dec. 2010, p. 123505. *aip.scitation.org*, <https://doi.org/10.1063/1.3514092>.

- Kunze, Hans-Joachim. *Introduction to Plasma Spectroscopy*. Springer Science & Business Media, 2009.
- Lackner, K., et al. "Control of Particle and Energy Transport across the Boundary of a Tokamak Plasma." *Plasma Physics and Controlled Fusion*, vol. 26, no. 1A, Jan. 1984, pp. 105–15, <https://doi.org/10.1088/0741-3335/26/1A/328>.
- Lawson, J. D. "Some Criteria for a Power Producing Thermonuclear Reactor." *Proceedings of the Physical Society. Section B*, vol. 70, no. 1, Jan. 1957, pp. 6–10. *Institute of Physics*, <https://doi.org/10.1088/0370-1301/70/1/303>.
- Lehnen, M., et al. "Disruptions in ITER and Strategies for Their Control and Mitigation." *Journal of Nuclear Materials*, vol. 463, Aug. 2015, pp. 39–48. *ScienceDirect*, <https://doi.org/10.1016/j.jnucmat.2014.10.075>.
- Leonard, A. W. "Plasma Detachment in Divertor Tokamaks." *Plasma Physics and Controlled Fusion*, vol. 60, no. 4, Apr. 2018, p. 044001, <https://doi.org/10.1088/1361-6587/aaa7a9>.
- Leonard, A. W., et al. "The Impact of ELMs on the ITER Divertor." *Journal of Nuclear Materials*, vol. 266–269, Mar. 1999, pp. 109–17. *ScienceDirect*, [https://doi.org/10.1016/S0022-3115\(98\)00522-4](https://doi.org/10.1016/S0022-3115(98)00522-4).
- Levinson, S. J., et al. "Space/Time Statistics of the Turbulence in a Tokamak Edge Plasma." *Nuclear Fusion*, vol. 24, no. 5, May 1984, pp. 527–39. *Institute of Physics*, <https://doi.org/10.1088/0029-5515/24/5/001>.
- Light, A. D., et al. "Direct Extraction of Coherent Mode Properties from Imaging Measurements in a Linear Plasma Column." *Physics of Plasmas*, vol. 20, no. 8, Aug. 2013, p. 082120, <https://doi.org/10.1063/1.4818148>.
- Lipschultz, B., et al. "Marfe: An Edge Plasma Phenomenon." *Nuclear Fusion*, vol. 24, no. 8, Aug. 1984, p. 977. *Institute of Physics*, <https://doi.org/10.1088/0029-5515/24/8/002>.
- Loarte, Alberto. "Effects of Divertor Geometry on Tokamak Plasmas." *Plasma Physics and Controlled Fusion*, vol. 43, no. 6, June 2001, pp. R183–224, <https://doi.org/10.1088/0741-3335/43/6/201>.

BIBLIOGRAPHY

Lopez, Jose L. *Low –Temperature Plasmas Technologies*. SULI Introductory Course in Plasma Physics.

Loudon, Rodney. “One-Dimensional Hydrogen Atom.” *American Journal of Physics*, vol. 27, no. 9, Dec. 1959, pp. 649–55. *aip.scitation.org*, <https://doi.org/10.1119/1.1934950>.

Lukash, V. E., et al. “Modeling of Major Disruption Mitigation by Fast Injection of Massive Li Pellets in ITER Like Tokamak-Reactor.” *IAEA-FEC-124*, 2010.

Luxon, J. L. “A Design Retrospective of the DIII-D Tokamak.” *Nuclear Fusion*, vol. 42, no. 5, May 2002, p. 614. *Institute of Physics*, <https://doi.org/10.1088/0029-5515/42/5/313>.

Macwan, Tanmay, et al. “Gas-Puff Induced Cold Pulse Propagation in ADITYA-U Tokamak.” *Nuclear Fusion*, vol. 61, no. 9, Aug. 2021, p. 096029. *Institute of Physics*, <https://doi.org/10.1088/1741-4326/ac189b>.

Makwana, Bhumika, et al. “Emission Profile Reconstruction of Edge Plasma of Aditya Tokamak.” *2013 International Conference on Communication and Signal Processing*, 2013, pp. 519–23. *IEEE Xplore*, <https://doi.org/10.1109/iccsp.2013.6577108>.

Manchanda, R., et al. “Drift-Alfven Waves Induced Optical Emission Fluctuations in Aditya Tokamak.” *Physics of Plasmas*, vol. 17, no. 7, July 2010. *pubs.aip.org*, <https://doi.org/10.1063/1.3461165>.

Manchanda, R., M. B. Chowdhuri, et al. “Physics Studies of ADITYA & ADITYA-U Tokamak Plasmas Using Spectroscopic Diagnostics.” *Nuclear Fusion*, vol. 62, no. 4, Feb. 2022, p. 042014. *Institute of Physics*, <https://doi.org/10.1088/1741-4326/ac2cf6>.

Manchanda, R., et al. “Vacuum Coupling of Photo Multiplier Tube with Monochromator for Improved Monitoring of VUV Emission from Aditya Tokamak.” *APPL PHYS*, vol. 51, 2013.

Maqueda, R. J., et al. “Gas Puff Imaging of Edge Turbulence (Invited).” *Review of Scientific Instruments*, vol. 74, no. 3, Mar. 2003, pp. 2020–26. *aip.scitation.org*, <https://doi.org/10.1063/1.1535249>.

Mattioli, M., C. De Michelis, et al. “Behaviour of Intrinsic Carbon and Laser Blow-off Injected Nickel in Tore Supra during Ergodic Divertor Activation.” *Nuclear Fusion*, vol. 35,

- no. 7, July 1995, pp. 807–25. *Institute of Physics*, <https://doi.org/10.1088/0029-5515/35/7/I05>.
- Mattioli, M., M. Erba, et al. “Enhanced Transport of Impurity Ions and Electron Heat in Tore Supra Ohmic Discharges Following Nickel Laser Blow-off Injection.” *Nuclear Fusion*, vol. 38, no. 2, Feb. 1998, pp. 189–206. *Institute of Physics*, <https://doi.org/10.1088/0029-5515/38/2/304>.
- Mattioli, M., K. B. Fournier, et al. “Experimental and Simulated Neon Spectra in the 10-Nm Wavelength Region from Tokamak and Reversed Field Pinch Plasmas.” *Physical Review E*, vol. 60, no. 4, Oct. 1999, pp. 4760–69. *APS*, <https://doi.org/10.1103/PhysRevE.60.4760>.
- McCcone, John, et al. *Carbon Transport in MAST*. 2010.
- McCracken, G. M., et al. “Impurity Screening in Ohmic and High Confinement (H-Mode) Plasmas in the Alcator C-Mod Tokamak.” *Physics of Plasmas*, vol. 4, no. 5, May 1997, pp. 1681–89. *aip.scitation.org*, <https://doi.org/10.1063/1.872365>.
- McCracken, Garry, and Peter Stott. “Chapter 3 - Fusion in the Sun and Stars.” *Fusion*, edited by Garry McCracken and Peter Stott, Academic Press, 2005, pp. 17–32. *ScienceDirect*, <https://doi.org/10.1016/B978-012481851-4/50005-6>.
- McNeill, D. H. “H-Alpha Photon Yield in Fuelling of Tokamaks.” *Journal of Nuclear Materials*, vol. 162–164, Apr. 1989, pp. 476–81. *ScienceDirect*, [https://doi.org/10.1016/0022-3115\(89\)90315-2](https://doi.org/10.1016/0022-3115(89)90315-2).
- Michelis, C. De, and M. Mattioli. “Spectroscopy and Impurity Behaviour in Fusion Plasmas - IOPscience.” *Reports on Progress in Physics*, vol. 47, no. 10, Oct. 1984, p. 1233, <https://doi.org/10.1088/0034-4885/47/10/001>.
- Mishra, Kishore, et al. “Direct Electron Heating Experiment on the Aditya Tokamak Using Fast Waves in the Ion Cyclotron Resonance Frequency Range.” *Plasma Physics and Controlled Fusion*, vol. 53, no. 9, Aug. 2011, p. 095011. *Institute of Physics*, <https://doi.org/10.1088/0741-3335/53/9/095011>.
- Miyamoto, K. *Plasma Physics for Nuclear Fusion*. Jan. 1980. *www.osti.gov*, <https://www.osti.gov/biblio/5540319>.

BIBLIOGRAPHY

- Morgan, T. W., et al. “A High-Repetition Rate Edge Localised Mode Replication System for the Magnum-PSI and Pilot-PSI Linear Devices.” *Plasma Physics and Controlled Fusion*, vol. 56, no. 9, July 2014, p. 095004. *Institute of Physics*, <https://doi.org/10.1088/0741-3335/56/9/095004>.
- Mori, M., et al. “Achievement of High Fusion Triple Product in the JT-60U High \dot{p} / H Mode.” *Nuclear Fusion*, vol. 34, no. 7, July 1994, pp. 1045–53. *Institute of Physics*, <https://doi.org/10.1088/0029-5515/34/7/I09>.
- Morita, Shigeru, et al. “Spectroscopic Studies on Impurity Transport of Core and Edge Plasmas in LHD.” *Plasma Science and Technology*, vol. 8, no. 1, Jan. 2006, pp. 55–60, <https://doi.org/10.1088/1009-0630/8/1/13>.
- Muhammad Fahad, Sajjad Ali, Khizar Hussain Shah, Asim Shahzad, and Muhammad Abrar. “Quantitative Elemental Analysis of High Silica Bauxite Using Calibration-Free Laser-Induced Breakdown Spectroscopy.” *Applied Optics*, vol. 58, no. 27, 2019, pp. 7588–96, <https://doi.org/10.1364/AO.58.007588>.
- Mukhovatov, V. S., and V. D. Shafranov. “Plasma Equilibrium in a Tokamak.” *Nuclear Fusion*, vol. 11, no. 6, Dec. 1971, p. 605. *Institute of Physics*, <https://doi.org/10.1088/0029-5515/11/6/005>.
- Mulliken, Robert S. “The Interpretation of Band Spectra Part III. Electron Quantum Numbers and States of Molecules and Their Atoms.” *Reviews of Modern Physics*, vol. 4, no. 1, Jan. 1932, pp. 1–86. *APS*, <https://doi.org/10.1103/RevModPhys.4.1>.
- Nagora, U., et al. “Design & Development of 140 GHz D-Band Phase Locked Heterodyne Interferometer System for Real-Time Density Measurement.” *Journal of Instrumentation*, vol. 15, no. 11, Nov. 2020, p. P11011. *iopscience.iop.org*, <https://doi.org/10.1088/1748-0221/15/11/P11011>.
- Nakashima, Y., et al. “Progress of Divertor Simulation Research toward the Realization of Detached Plasma Using a Large Tandem Mirror Device.” *Journal of Nuclear Materials*, vol. 463, Aug. 2015, pp. 537–40. *ScienceDirect*, <https://doi.org/10.1016/j.jnucmat.2014.12.063>.

- Namioka, T. "Theory of the Concave Grating. I*†." *JOSA*, vol. 49, no. 5, May 1959, pp. 446–60. *opg.optica.org*, <https://doi.org/10.1364/JOSA.49.000446>.
- Nassar, H., et al. "N₂⁺/N₂ Ratio and Temperature Measurements Based on the First Negative N₂⁺ and Second Positive N₂ Overlapped Molecular Emission Spectra." *Journal of Physics D: Applied Physics*, vol. 37, no. 14, July 2004, pp. 1904–16, <https://doi.org/10.1088/0022-3727/37/14/005>.
- Nick Balshaw. *All-the-Worlds-Tokamaks*. 2018, <http://www.tokamak.info/>.
- Nishizawa, T., et al. "Non-Parametric Inference of Impurity Transport Coefficients in the ASDEX Upgrade Tokamak." *Nuclear Fusion*, vol. 62, no. 7, May 2022, p. 076021. *Institute of Physics*, <https://doi.org/10.1088/1741-4326/ac60e8>.
- Ohno, N. "Plasma Detachment in Linear Devices." *Plasma Physics and Controlled Fusion*, vol. 59, no. 3, Feb. 2017, p. 034007. *Institute of Physics*, <https://doi.org/10.1088/1361-6587/aa5394>.
- Ongena, J., and A. M. Messiaen. "Heating, Confinement and Extrapolation to Reactors." *Fusion Science and Technology*, vol. 53, no. 2T, Feb. 2008, pp. 443–58. *Taylor and Francis+NEJM*, <https://doi.org/10.13182/FST08-A1730>.
- Pandya, H. K. B., et al. "Thermal Electron Cyclotron Emission Measurement on the Aditya Tokamak by Radiometers." *Plasma Physics and Controlled Fusion*, vol. 49, no. 11, Oct. 2007, p. 1809. *Institute of Physics*, <https://doi.org/10.1088/0741-3335/49/11/005>.
- Pandya, Santosh P., Kumar Ajay, et al. "Core-Ion Temperature Measurement of the ADITYA Tokamak Using Passive Charge Exchange Neutral Particle Energy Analyzer." *The Review of Scientific Instruments*, vol. 84, no. 2, Feb. 2013, p. 023503. *PubMed*, <https://doi.org/10.1063/1.4791998>.
- Pandya, Santosh P., Shwetang N. Pandya, et al. "Development of Infrared Imaging Video Bolometer for the ADITYA Tokamak." *Plasma and Fusion Research*, vol. 7, 2012, pp. 2402089–2402089. *J-Stage*, <https://doi.org/10.1585/pfr.7.2402089>.
- Paradkar, Bhooshan, et al. "Runaway-Loss Induced Negative and Positive Loop Voltage Spikes in the Aditya Tokamak." *Physics of Plasmas*, vol. 17, no. 9, Sept. 2010, p. 092504. *aip.scitation.org*, <https://doi.org/10.1063/1.3474949>.

BIBLIOGRAPHY

- Park, Jae Sun, et al. "Atomic Processes Leading to Asymmetric Divertor Detachment in KSTAR L-Mode Plasmas." *Nuclear Fusion*, vol. 58, no. 12, Nov. 2018, p. 126033. *Institute of Physics*, <https://doi.org/10.1088/1741-4326/aae865>.
- Patel, Jatinkumar J., et al. "PXIE Based Data Acquisition and Control System for ECRH Systems on SST-1 and Aditya Tokamak." *Fusion Engineering and Design*, vol. 112, Nov. 2016, pp. 919–23. *ScienceDirect*, <https://doi.org/10.1016/j.fusengdes.2016.05.014>.
- Patel, K. M., et al. *Limiter and Divertor of ADITYA-U Tokamak*. Institute for Plasma Research, 2020.
- Patel, Kiran, Vishal Pillai, et al. "GPIB Based Instrumentation and Control System for ADITYA Thomson Scattering Diagnostic." *Fusion Engineering and Design*, vol. 112, Nov. 2016, pp. 860–64. *ScienceDirect*, <https://doi.org/10.1016/j.fusengdes.2016.06.021>.
- Patel, Kiran, Umesh Nagora, et al. "LabVIEW-FPGA-Based Real-Time Data Acquisition System for ADITYA-U Heterodyne Interferometry." *IEEE Transactions on Plasma Science*, vol. 49, no. 6, June 2021, pp. 1891–97. *IEEE Xplore*, <https://doi.org/10.1109/TPS.2021.3082159>.
- Patel, Narendra, et al. "Programmable Pulse Generator for Aditya Gas Puffing System." *Journal of Physics: Conference Series*, vol. 390, Nov. 2012, p. 012012. *Institute of Physics*, <https://doi.org/10.1088/1742-6596/390/1/012012>.
- Patel, S., et al. "Study of Iron Impurity Behaviour in the ADITYA Tokamak." *Nuclear Fusion*, vol. 59, no. 8, June 2019, p. 086019. *Institute of Physics*, <https://doi.org/10.1088/1741-4326/ab1f12>.
- Peeters, A. G. "Reduced Charge State Equations That Describe Pfirsch Schlüter Impurity Transport in Tokamak Plasma." *Physics of Plasmas*, vol. 7, no. 1, Jan. 2000, pp. 268–75. *Silverchair*, <https://doi.org/10.1063/1.873812>.
- Peláez, R. J., et al. "Probing the Edge Ion Temperature by Passive Doppler Spectroscopy in the TJ-II Stellarator." *Journal of Physics B: Atomic, Molecular and Optical Physics*, vol. 43, no. 14, July 2010, p. 144016. *iopscience.iop.org*, <https://doi.org/10.1088/0953-4075/43/14/144016>.

- Photonics Hamamatsu. *Photomultiplier Tubes Hamamatsu*. 2000,
<https://hamamatsu.magnet.fsu.edu/articles/photomultipliers.html>.
- Pitts, R. A., et al. “Material Erosion and Migration in Tokamaks.” *Plasma Physics and Controlled Fusion*, vol. 47, no. 12B, Nov. 2005, p. B303. *Institute of Physics*, <https://doi.org/10.1088/0741-3335/47/12B/S22>.
- Pitts, R. A., and P. C. Stangeby. “Experimental Tests of Langmuir Probe Theory for Strong Magnetic Fields.” *Plasma Physics and Controlled Fusion*, vol. 32, no. 13, Dec. 1990, pp. 1237–48, <https://doi.org/10.1088/0741-3335/32/13/004>.
- Popov, Oleg A. *High Density Plasma Sources: Design, Physics and Performance*. Elsevier, 1996.
- Post, D. E. “A Review of Recent Developments in Atomic Processes for Divertors and Edge Plasmas.” *Journal of Nuclear Materials*, vol. 220–222, Apr. 1995, pp. 143–57. *ScienceDirect*, [https://doi.org/10.1016/0022-3115\(94\)00453-6](https://doi.org/10.1016/0022-3115(94)00453-6).
- Prakash, Ram, et al. “Calibration of a VUV Spectrograph by Collisional-Radiative Modelling of a Discharge Plasma.” *Journal of Physics B: Atomic, Molecular and Optical Physics*, vol. 43, no. 14, July 2010, p. 144012. *Institute of Physics*, <https://doi.org/10.1088/0953-4075/43/14/144012>.
- Psoda, M., et al. “Material Mixing on Plasma-Facing Components: Compound Formation.” *Journal of Nuclear Materials*, vol. 386–388, Apr. 2009, pp. 740–43. *ScienceDirect*, <https://doi.org/10.1016/j.jnucmat.2008.12.206>.
- Purohit, Shishir, et al. “Behavior of Non-Thermal Electrons during ECR Pre-Ionization at Aditya Tokamak.” *Plasma and Fusion Research*, vol. 12, no. specialissue1, 2017, pp. 24020021–25.
- R. W. Wood. “On a Remarkable Case of Uneven Distribution of Light in a Diffraction Grating Spectrum.” *The London, Edinburgh, and Dublin Philosophical Magazine and Journal of Science*, vol. 4, no. 21, <https://doi.org/10.1080/14786440209462857>. Accessed 2 July 2023.

BIBLIOGRAPHY

- Raj, Harshita, et al. “Generation and Transport of Runaway Electrons during Sawteeth Crash in the ADITYA Tokamak.” *Nuclear Fusion*, vol. 58, no. 7, May 2018, p. 076004. *Institute of Physics*, <https://doi.org/10.1088/1741-4326/aabdbf>.
- Rajpal, Rachana, et al. “Embedded Multi-Channel Data Acquisition System on FPGA for Aditya Tokamak.” *Fusion Engineering and Design*, vol. 112, Nov. 2016, pp. 964–68. *ScienceDirect*, <https://doi.org/10.1016/j.fusengdes.2016.03.068>.
- Ramaiya, N., et al. “Initial Results from Near-Infrared Spectroscopy on ADITYA-U Tokamak.” *Review of Scientific Instruments*, vol. 93, no. 11, Nov. 2022, p. 113552. *aip.scitation.org*, <https://doi.org/10.1063/5.0101850>.
- Raman, R., et al. “Fast Time Response Electromagnetic Disruption Mitigation Concept.” *Fusion Science and Technology*, Mar. 2017. world, www.tandfonline.com, <https://doi.org/10.13182/FST14-916>.
- Rathi, Dharmendra, et al. “Conceptual Design of Automation of ICRH Vacuum System on Aditya Tokamak.” *Journal of Physics: Conference Series*, vol. 208, no. 1, Feb. 2010, p. 012019. *Institute of Physics*, <https://doi.org/10.1088/1742-6596/208/1/012019>.
- Raulji, Vismaysinh D., et al. “Automation of Aditya Vacuum Control System Based on CODAC Core System.” *Fusion Engineering and Design*, vol. 112, Nov. 2016, pp. 910–14. *ScienceDirect*, <https://doi.org/10.1016/j.fusengdes.2016.05.032>.
- Reiter, Detlev, et al. “The EIRENE and B2-EIRENE Codes.” *Fusion Science and Technology*, vol. 47, no. 2, 2005, pp. 172–86.
- Rezaei, Fatemeh, and Tetsu Mieno. “Optically Thick Laser-Induced Plasmas in Spectroscopic Analysis.” *Plasma Science and Technology - Progress in Physical States and Chemical Reactions*, IntechOpen, 2016. www.intechopen.com, <https://doi.org/10.5772/61941>.
- Ribes, Andre, and Christian Caremoli. “Salomé Platform Component Model for Numerical Simulation.” *31st Annual International Computer Software and Applications Conference (COMPSAC 2007)*, vol. 2, 2007, pp. 553–64. *IEEE Xplore*, <https://doi.org/10.1109/COMPSAC.2007.185>.

- Rice, J. E., et al. “Understanding LOC/SOC Phenomenology in Tokamaks.” *Nuclear Fusion*, vol. 60, no. 10, Oct. 2020, p. 105001, <https://doi.org/10.1088/1741-4326/abac4b>.
- Rognlien, T. D., et al. *Users Manual for the UEDGE Edge-Plasma Transport Code*. UCRL-ID-137121, Lawrence Livermore National Lab., Livermore, CA (US), 10 Jan. 2000. www.osti.gov, <https://doi.org/10.2172/15007243>.
- Roseline, J. F. *PERFORMANCE EVALUATION OF ANN BASED PLASMA POSITION CONTROLLERS FOR ADITYA TOKAMAK*. 2013. *Semantic Scholar*, <https://www.semanticscholar.org/paper/PERFORMANCE-EVALUATION-OF-ANN-BASED-PLASMA-POSITION-Roseline/7405bc433edb72d9e83dd6ae2eb243b514ad5ead>.
- Roth, J., and G. Janeschitz. “Impurity Production and Transport in the Divertor Tokamak ASDEX.” *Nuclear Fusion*, vol. 29, no. 6, June 1989, pp. 915–35. *Institute of Physics*, <https://doi.org/10.1088/0029-5515/29/6/005>.
- Roux, F., and F. Michaud. “Investigation of the Rovibrational Levels of the $B^3\Pi_g$ State of $^{14}\text{N}_2$ Molecule above the Dissociation Limit $\text{N}(\ ^4S) + \text{N}(\ ^4S)$ by Fourier Transform Spectrometry.” *Canadian Journal of Physics*, vol. 68, no. 11, Nov. 1990, pp. 1257–61, <https://doi.org/10.1139/p90-181>.
- Rowan, W. L., et al. *GLOBAL PARTICLE CONFINEMENT IN THE TEXAS EXPERIMENTAL TOKAMAK*. 1987, p. 15.
- Rusbridge, M. G., et al. “Observations of the Interaction of a Plasma Stream with Neutral Gas: Evidence of Plasma Loss through Molecular-Activated Recombination.” *Plasma Physics and Controlled Fusion*, vol. 42, no. 5, May 2000, p. 579. *Institute of Physics*, <https://doi.org/10.1088/0741-3335/42/5/308>.
- Sahoo, Bibhu Prasad, et al. “Flow Structure and Shear Generation in the 3D SOL of a Circular Tokamak Plasma in Aditya.” *Nuclear Fusion*, vol. 55, June 2015, p. 063042. *NASA ADS*, <https://doi.org/10.1088/0029-5515/55/6/063042>.
- Sakamoto, M., et al. “Global Particle Balance and Wall Recycling Properties of Long Duration Discharges on TRIAM-1M.” *Nuclear Fusion*, vol. 44, no. 7, May 2004, pp. 693–98. *Institute of Physics*, <https://doi.org/10.1088/0029-5515/44/7/001>.

BIBLIOGRAPHY

- Sakharov, Andrei D. "Theory of the Magnetic Thermonuclear Reactor, Part II." *Soviet Physics Uspekhi*, vol. 34, no. 5, May 1991, p. 378. *iopscience.iop.org*, <https://doi.org/10.1070/PU1991v034n05ABEH002493>.
- Samm, U., et al. "Influence of Impurity Radiation Losses on Plasma Edge Properties in TEXTOR." *Journal of Nuclear Materials*, vol. 176–177, Dec. 1990, pp. 273–77. *ScienceDirect*, [https://doi.org/10.1016/0022-3115\(90\)90059-V](https://doi.org/10.1016/0022-3115(90)90059-V).
- Sangwan, Deepak, Ratneshwar Jha, Jana Brotankova, and M. V. Gopalkrishna. "Modification of Plasma Flows with Gas Puff in the Scrape-off Layer of ADITYA Tokamak." *Physics of Plasmas*, vol. 20, no. 6, June 2013, p. 062503. *Semantic Scholar*, <https://doi.org/10.1063/1.4811476>.
- Sangwan, Deepak, Ratneshwar Jha, and Rakesh L. Tanna. "Multidirectional Plasma Flow Measurement by Gundestrup Probe in Scrape-off Layer of ADITYA Tokamak." *Physics of Plasmas*, vol. 22, no. 11, Nov. 2015, p. 112501. *aip.scitation.org*, <https://doi.org/10.1063/1.4935292>.
- Sangwan, Deepak, Ratneshwar Jha, Jana Brotankova, and M. V. Gopalakrishna. "Transport Driven Plasma Flows in the Scrape-off Layer of ADITYA Tokamak in Different Orientations of Magnetic Field." *Physics of Plasmas*, vol. 21, no. 6, June 2014, p. 062512, <https://doi.org/10.1063/1.4885108>.
- Sawyer, Ralph A. "Experimental Spectroscopy." *American Journal of Physics*, vol. 19, Dec. 1951, pp. 567–68. *NASA ADS*, <https://doi.org/10.1119/1.1933090>.
- Schenkel, T., et al. "Investigation of Light Ion Fusion Reactions with Plasma Discharges." *Journal of Applied Physics*, vol. 126, no. 20, Nov. 2019, p. 203302. *aip.scitation.org*, <https://doi.org/10.1063/1.5109445>.
- Schmitz, L., R. Lehmer, et al. "Experimental Simulation of the Gaseous Divertor Concept in PISCES-A." *Journal of Nuclear Materials*, vol. 176–177, Dec. 1990, pp. 522–27. *ScienceDirect*, [https://doi.org/10.1016/0022-3115\(90\)90100-2](https://doi.org/10.1016/0022-3115(90)90100-2).
- Schmitz, L., B. Merriman, et al. "Plasma and Neutral Dynamics in a Simulated Tokamak Gas Target Divertor: Physics of Plasmas: Vol 2, No 8." *Physics of Plasmas*, vol. 2, no. 8, Aug. 1995, pp. 3081–94, <https://doi.org/10.1063/1.871206>.

- Sciortino, Francesco, et al. “Investigation of Core Impurity Transport in DIII-D Diverted Negative Triangularity Plasmas.” *Plasma Physics and Controlled Fusion*, 2022. *Institute of Physics*, <https://doi.org/10.1088/1361-6587/ac94f6>.
- Sertoli, M., et al. “Measuring the Plasma Composition in Tokamaks with Metallic Plasma-Facing Components.” *Journal of Plasma Physics*, vol. 85, no. 5, Oct. 2019. *Cambridge University Press*, <https://doi.org/10.1017/S0022377819000618>.
- Shah, K., et al. “Observations of Visible Argon Line Emissions and Its Spatial Profile from Aditya-U Tokamak Plasma.” *Review of Scientific Instruments*, vol. 92, no. 5, May 2021, p. 053548. *aip.scitation.org (Atypon)*, <https://doi.org/10.1063/5.0043877>.
- Shaing, K. C., et al. “Neoclassical Plasma Viscosity and Transport Processes in Non-Axisymmetric Tori.” *Nuclear Fusion*, vol. 55, no. 12, Nov. 2015, p. 125001, <https://doi.org/10.1088/0029-5515/55/12/125001>.
- Sharma, Devendra, et al. “3-D Simulations of Plasma Transport in the Ring Limiter Scrape-off Layer of Tokamak Aditya.” *Journal of Nuclear Materials*, vol. 438, July 2013, pp. S554–58. *ScienceDirect*, <https://doi.org/10.1016/j.jnucmat.2013.01.115>.
- Shikama, T., S. Kado, H. Zushi, A. Iwamae, et al. “Application of the Zeeman Patterns in O γ and H α Spectra to the Local Plasma Diagnostics of the TRIAM-1M Tokamak.” *Physics of Plasmas*, vol. 11, no. 10, 2004, pp. 4701–08.
- Shikama, T., S. Kado, H. Zushi, M. Sakamoto, et al. “Application of the Zeeman Patterns to the Measurement of Local Neutral Behaviour in the Edge Plasma of TRIAM-1M Tokamak.” *Plasma Physics and Controlled Fusion*, vol. 48, no. 8, 2006, p. 1125.
- Shukla, B. K., D Bora, et al. “42GHz 0.5MW ECRH System for Tokamaks SST-1 and Aditya.” *IEEE Transactions on Plasma Science*, vol. 40, no. 4, 2012, pp. 1234–38, <https://doi.org/10.1109/TPS.2019.29321>.
- Shukla, B. K., D. Bora, et al. “Operation and Control of High Power Gyrotrons for ECRH Systems in SST-1 and Aditya.” *Fusion Engineering and Design*, vol. 112, Nov. 2016, pp. 673–77. *ScienceDirect*, <https://doi.org/10.1016/j.fusengdes.2016.05.031>.

BIBLIOGRAPHY

- Shunji Tsuji. “Experimental Scaling of Particle Confinement in Tokamaks.” *Fusion Engineering and Design*, vol. 15, no. 4, Jan. 1991, pp. 311–24. www.sciencedirect.com, [https://doi.org/10.1016/0920-3796\(92\)90017-X](https://doi.org/10.1016/0920-3796(92)90017-X).
- Smeulders, P. “Tomography of Quasi-Static Deformations of Constant-Emission Surfaces of High-Beta Plasmas in ASDEX.” *Nuclear Fusion*, vol. 26, no. 3, 1986, p. 267.
- Strangeby, P. C. *The Plasma Boundary of Magnetic Fusion Devices*. 1st ed., Taylor, 2000, <https://www.taylorfrancis.com/books/mono/10.1201/9780367801489/plasma-boundary-magnetic-fusion-devices-strangeby>.
- Strangeby, P. C., and G. M. McCracken. “Plasma Boundary Phenomena in Tokamaks.” *Nuclear Fusion*, vol. 30, no. 7, 1990, p. 1225.
- Stephens, H. D., et al. “Electron Thermal Transport within Magnetic Islands in the Reversed-Field Pincha....” *Physics of Plasmas*, vol. 17, 2010, p. 056115(1-10).
- Stotler, D. P., F. Scotti, et al. “Midplane Neutral Density Profiles in the National Spherical Torus Experiment.” *Physics of Plasmas*, vol. 22, no. 8, Aug. 2015, p. 082506. aip.scitation.org/10.1063/1.4928372.
- Stotler, D. P., B. LaBombard, et al. “Neutral Transport Simulations of Gas Puff Imaging Experiments.” *Journal of Nuclear Materials*, vol. 313–316, Mar. 2003, pp. 1066–70. *ScienceDirect*, [https://doi.org/10.1016/S0022-3115\(02\)01495-2](https://doi.org/10.1016/S0022-3115(02)01495-2).
- Stott, P. E., et al. “Control of Re-Cycling and Impurities in the ATC Tokamak by Means of Gettered Surfaces.” *Nuclear Fusion*, vol. 15, no. 3, June 1975, pp. 431–39, <https://doi.org/10.1088/0029-5515/15/3/009>.
- Strait, E. J., et al. “Progress in Disruption Prevention for ITER.” *Nuclear Fusion*, vol. 59, no. 11, June 2019, p. 112012. *iopscience.iop.org*, <https://doi.org/10.1088/1741-4326/ab15de>.
- Stroke, George W. “Diffraction Gratings.” *Optische Instrumente / Optical Instruments*, edited by S. Flügge, Springer, 1967, pp. 426–754. *Springer Link*, https://doi.org/10.1007/978-3-642-46077-7_8.

- Sudit, Isaac D., and R. Claude Woods. "A Study of the Accuracy of Various Langmuir Probe Theories." *Journal of Applied Physics*, vol. 76, no. 8, Oct. 1994, pp. 4488–98, <https://doi.org/10.1063/1.357280>.
- Sudo, Shigeru. "A Review of Impurity Transport Characteristics in the LHD." *Plasma Physics and Controlled Fusion*, vol. 58, no. 4, Apr. 2016, p. 043001, <https://doi.org/10.1088/0741-3335/58/4/043001>.
- Sudo, Shigeru, Naoki Tamura, Chihiro Suzuki, et al. "Multiple-Tracer TESPEL Injection for Studying Impurity Behaviour in a Magnetically Confined Plasma." *Nuclear Fusion*, vol. 52, no. 6, Apr. 2012, p. 063012. *Institute of Physics*, <https://doi.org/10.1088/0029-5515/52/6/063012>.
- Sudo, Shigeru, Naoki Tamura, Sadatsugu Muto, et al. "Transport Characteristics of Tracer and Intrinsic Impurities Depending on the Density of LHD Plasmas." *Plasma Physics and Controlled Fusion*, vol. 55, no. 9, Aug. 2013, p. 095014. *Institute of Physics*, <https://doi.org/10.1088/0741-3335/55/9/095014>.
- Sudo, Shigeru, and Naoki Tamura. "Tracer-Encapsulated Solid Pellet Injection System." *The Review of Scientific Instruments*, vol. 83, no. 2, Feb. 2012, p. 023503. *PubMed*, <https://doi.org/10.1063/1.3681447>.
- Summers, H. P. "The ADAS User Manual, Version 2.6." *Http://Www.Adas.Ac.Uk/*, 2004. *cir.nii.ac.jp*, <https://cir.nii.ac.jp/crid/1573668925563490688>.
- Suratia, Pooja, et al. "FPGA Based Fuzzy Logic Controller for Plasma Position Control in ADITYA Tokamak." *Fusion Engineering and Design*, vol. 87, no. 11, Nov. 2012, pp. 1866–71, <https://doi.org/10.1016/j.fusengdes.2012.09.004>.
- Tahiliani, Kumudni, Ratneshwar Jha, and Prabhat Kumar. "Estimation of Effective Responsivity of AXUV Bolometer in ADITYA Tokamak by Spectrally Resolved Radiation Power Measurement." *Plasma and Fusion Research*, vol. 8, Jan. 2013, pp. 2402124–2402124. *NASA ADS*, <https://doi.org/10.1585/pfr.8.2402124>.
- Tahiliani, Kumudni, Ratneshwar Jha, M. V. Gopalkrishana, et al. "Radiation Power Measurement on the ADITYA Tokamak." *Plasma Physics and Controlled Fusion*, vol. 51, no. 8, July 2009, p. 085004. *Institute of Physics*, <https://doi.org/10.1088/0741-3335/51/8/085004>.

BIBLIOGRAPHY

- Takenaga, H., et al. “Study of Global Wall Saturation Mechanisms in Long-Pulse ELMy H-Mode Discharges on JT-60U.” *Nuclear Fusion*, vol. 46, no. 3, Mar. 2006, pp. S39–48, <https://doi.org/10.1088/0029-5515/46/3/S06>.
- Tang, W. M., et al. *Microinstabilities in Weak Density Gradient Tokamak Systems*. no. 11, 1986, pp. 3715–18.
- Tanna, R L, K. A. Jadeja, et al. “Influence of Wall Conditioning on ADITYA Plasma Discharges.” *Journal of Physics: Conference Series*, vol. 390, Nov. 2012, p. 012044, <https://doi.org/10.1088/1742-6596/390/1/012044>.
- Tanna, R. L., J. Ghosh, P. K. Chattopadhyay, et al. “Novel Approaches for Mitigating Runaway Electrons and Plasma Disruptions in ADITYA Tokamak.” *Nuclear Fusion*, vol. 55, no. 6, May 2015, p. 063010. *Institute of Physics*, <https://doi.org/10.1088/0029-5515/55/6/063010>.
- Tanna, R L, Harshita Raj, Joydeep Ghosh, et al. “Overview of Operation and Experiments in the ADITYA – U Tokamak.” *Nuclear Fusion*, Feb. 2019. *Crossref*, <https://doi.org/10.1088/1741-4326/ab0a9e>.
- Tanna, R. L., Tanmay Macwan, J. Ghosh, et al. “Overview of Recent Experimental Results from the ADITYA-U Tokamak.” *Nuclear Fusion*, vol. 62, no. 4, Feb. 2022, p. 042017. *Institute of Physics*, <https://doi.org/10.1088/1741-4326/ac31db>.
- Tanna, R. L., J. Ghosh, Harshita Raj, et al. “Plasma Production and Preliminary Results from the ADITYA Upgrade Tokamak.” *Plasma Science and Technology*, vol. 20, no. 7, May 2018, p. 074002. *Institute of Physics*, <https://doi.org/10.1088/2058-6272/aabb4f>.
- Terry, J. L., et al. “Volume Recombination and Opacity in Alcator C-Mod Divertor Plasmas.” *Physics of Plasmas*, vol. 5, no. 5, May 1998, pp. 1759–66, <https://doi.org/10.1063/1.872845>.
- The ASDEX Team and The NI Team, et al. “Effects of Edge Conditions on Plasma Confinement in ASDEX.” *Journal of Nuclear Materials*, vol. 176–177, Dec. 1990, pp. 89–101. *ScienceDirect*, [https://doi.org/10.1016/0022-3115\(90\)90031-H](https://doi.org/10.1016/0022-3115(90)90031-H).
- Thomas Morgan. *Measurement of MAST Edge Ion Temperatures and Velocities*. 2011, <https://etheses.whiterose.ac.uk/2098/>.

- Tynan, G. R., P. H. Diamond, et al. “Nonlinear Dynamics of Shear Flows and Plasma Rotation in a Simple Laboratory Plasma System.” *Plasma Physics and Controlled Fusion*, vol. 51, no. 12, Nov. 2009, p. 124055. *Institute of Physics*, <https://doi.org/10.1088/0741-3335/51/12/124055>.
- Tynan, G. R., L. Schmitz, et al. “Turbulent Edge Transport in the Princeton Beta Experiment-Modified High Confinement Mode.” *Physics of Plasmas*, vol. 1, no. 10, Oct. 1994, pp. 3301–07. *aip.scitation.org*, <https://doi.org/10.1063/1.870916>.
- Unterberg, E. A., et al. “Experimental Comparison of Recycling and Pumping Changes during Resonant Magnetic Perturbation Experiments at Low and High Collisionality in DIII-D.” *Journal of Nuclear Materials*, vol. 390–391, June 2009, pp. 486–89. *ScienceDirect*, <https://doi.org/10.1016/j.jnucmat.2009.01.052>.
- UVP. *UVP Pen-Ray Light Sources*. 1997, <https://www.uvp.com/products/ultraviolet-products/uvp-pen-ray-light-sources>.
- V. Philipps, et al. “Deposition and Qualification of Tungsten Coatings Produced by Plasma Deposition in WF₆precursor Gas.” *Physica Scripta*, vol. T145, Dec. 2011, p. 014030. *Institute of Physics*, <https://doi.org/10.1088/0031-8949/2011/T145/014030>.
- V. Philipps. “Plasma Wall Interaction and Its Control by Wall Conditioning.” *Fusion Technology*, vol. 33, no. 2T, Mar. 1998, pp. 261–72. *Taylor and Francis+NEJM*, <https://doi.org/10.13182/FST98-A11947017>.
- Vincent van Gogh. “The Starry Night.” *Google Arts & Culture*, 1988, <https://artsandculture.google.com/asset/starry-night/uQE3XORhSK37Dw>.
- Vries, P. C. De, et al. “Density Profile Peaking inside m/N=2/1 Magnetic Islands in TEXTOR-94.” *Nuclear Fusion*, vol. 37, no. 11, Nov. 1997, p. 1641. *Institute of Physics*, <https://doi.org/10.1088/0029-5515/37/11/I13>.
- Wagner, F. *Investigation of Limiter Recycling in the Divertor Tokamak ASDEX*. 1981.
- Wan, Baonian, et al. “PSI Issues toward Steady State Plasmas in the HT-7 Tokamak.” *Journal of Nuclear Materials*, vol. 313–316, Mar. 2003, pp. 127–34. *ScienceDirect*, [https://doi.org/10.1016/S0022-3115\(02\)01389-2](https://doi.org/10.1016/S0022-3115(02)01389-2).

BIBLIOGRAPHY

- Weaver, J. L., et al. “Localization of Emission through Interpretation of Observed Zeeman Pattern.” *Review of Scientific Instruments*, vol. 71, no. 4, Apr. 2000, pp. 1664–70. *aip.scitation.org*, <https://doi.org/10.1063/1.1150516>.
- Welch, B. L., et al. “Neutral Atom Temperature and Flow Measurements in the Edge Region of the Alcator C-Mod Tokamak.” *Physics of Plasmas*, vol. 8, no. 4, Apr. 2001, pp. 1253–62. *aip.scitation.org*, <https://doi.org/10.1063/1.1355025>.
- Wenzel, U., et al. “Volume Recombination in Divertor I of ASDEX Upgrade.” *Nuclear Fusion*, vol. 39, no. 7, July 1999, pp. 873–82. *Institute of Physics*, <https://doi.org/10.1088/0029-5515/39/7/304>.
- Wesson, John, and D. J. Campbell. *Tokamaks*. OUP Oxford, 2011.
- Weynants, R. R., et al. “Confinement and Profile Changes Induced by the Presence of Positive or Negative Radial Electric Fields in the Edge of the TEXTOR Tokamak.” *Nuclear Fusion*, vol. 32, no. 5, May 1992, pp. 837–53, <https://doi.org/10.1088/0029-5515/32/5/I10>.
- White, Harvey Elliott. *Introduction To Atomic Spectra*. McGraw Hill Kogakusha Limited, 1939.
- Whyte, D. G., J. P. Coad, et al. “Similarities in Divertor Erosion/Redeposition and Deuterium Retention Patterns between the Tokamaks ASDEX Upgrade, DIII-D and JET.” *Nuclear Fusion*, vol. 39, no. 8, Aug. 1999, p. 1025. *Institute of Physics*, <https://doi.org/10.1088/0029-5515/39/8/306>.
- Whyte, D. G., B. L. Lipschultz, et al. “The Magnitude of Plasma Flux to the Main-Wall in the DIII-D Tokamak.” *Plasma Physics and Controlled Fusion*, vol. 47, no. 10, Sept. 2005, pp. 1579–607. *Institute of Physics*, <https://doi.org/10.1088/0741-3335/47/10/002>.
- Wienhold, P., et al. “In Situ Measurement of the Hydrogen Recycling Constant of the Textor Liner.” *Journal of Nuclear Materials*, vol. 123, no. 1–3, May 1984, pp. 1180–86, [https://doi.org/10.1016/0022-3115\(84\)90238-1](https://doi.org/10.1016/0022-3115(84)90238-1).
- Wigner, Eugene. “Phys. Rev. 73, 1002 (1948) - On the Behavior of Cross Sections Near Thresholds.” *Physical Review*, vol. 73, no. 9, 1948, p. 1002, <https://journals.aps.org/pr/abstract/10.1103/PhysRev.73.1002>.

- Willett, Hannah Victoria. *Applications of Linear Plasma Device Studies to the Improvement of Power Injection and Handling in Tokamaks*. University of York, 2018, https://etheses.whiterose.ac.uk/21925/1/Willett2018_PhDthesis.pdf.
- Williams, Mark C., et al. “The U.S. Department of Energy, Office of Fossil Energy Stationary Fuel Cell Program.” *Journal of Power Sources*, vol. 143, no. 1, Apr. 2005, pp. 191–96. *ScienceDirect*, <https://doi.org/10.1016/j.jpowsour.2004.12.003>.
- Winter, J., H. G. Esser, et al. “Boronization in Textor.” *Journal of Nuclear Materials*, vol. 162–164, Apr. 1989, pp. 713–23. *ScienceDirect*, [https://doi.org/10.1016/0022-3115\(89\)90352-8](https://doi.org/10.1016/0022-3115(89)90352-8).
- Winter, J., F. G. Waelbroeck, et al. “Characterization of the First Wall of TEXTOR with Respect to Hydrogen Recycling.” *Journal of Vacuum Science & Technology A: Vacuum, Surfaces, and Films*, vol. 2, no. 2, Apr. 1984, pp. 679–85, <https://doi.org/10.1116/1.572427>.
- Winter, J. “Tokamak Wall Coatings.” *Plasma Physics and Controlled Fusion*, vol. 36, no. 12B, Dec. 1994, pp. B263–76, <https://doi.org/10.1088/0741-3335/36/12B/022>.
- Wolf, N. S., et al. “Role of Neutrals in Core Fueling and Pedestal Structure in H-Mode DIII-D Discharges.” *Journal of Nuclear Materials*, vol. 313–316, Mar. 2003, pp. 564–67. *ScienceDirect*, [https://doi.org/10.1016/S0022-3115\(02\)01406-X](https://doi.org/10.1016/S0022-3115(02)01406-X).
- Wootton, A. J., et al. “Fluctuations and Anomalous Transport in Tokamaks.” *Physics of Fluids B: Plasma Physics*, vol. 2, no. 12, Dec. 1990, pp. 2879–903, <https://doi.org/10.1063/1.859358>.
- Wu, Songtao. “An Overview of the EAST Project.” *Fusion Engineering and Design*, vol. 82, no. 5, Oct. 2007, pp. 463–71. *ScienceDirect*, <https://doi.org/10.1016/j.fusengdes.2007.03.012>.
- Yadava, Nandini, Joydeep Ghosh, Malay Chowdhuri, Ashoke de, Amrita Bhattacharya, et al. *Investigation of Charge Dependency in Impurity Transport in Aditya-U Tokamak*. Jan. 2021, p. CO07.004. NASA ADS, <https://ui.adsabs.harvard.edu/abs/2021APS..DPPCO7004Y>.

BIBLIOGRAPHY

- YADAVA, Nandini, et al. "Investigation of Recycling and Impurities Influxes in ADITYA-U Tokamak Plasmas." *Plasma and Fusion Research*, vol. 16, 2021, pp. 2402055–2402055, <https://doi.org/10.1585/pfr.16.2402055>.
- Yadava, Nandini. "Investigation of Self-Absorbed Lithium Spectral Line Emissions During Li₂TiO₃ Injection In Aditya-U Tokamak." *IAEA-CN-286*, 2021, p. 1.
- Yadava, Nandini, Joydeep Ghosh, Malay Bikas Chowdhuri, Ranjana Manchanda, Ritu Dey, et al. "Observation of Poloidal Asymmetry in Measured Neutral Temperatures in Aditya-U Tokamak Plasma." *Nuclear Fusion*, 2019.
- Yadava, Nandini, Joydeep Ghosh, Malay Bikas Chowdhuri, Ranjana Manchanda, Sripathi Punchithaya K, et al. "Spatial Profile of Neutral Temperature Measurement in Aditya-U Tokamak Plasmas." *Atoms*, vol. 7, no. 3, 3, Sept. 2019, p. 87. www.mdpi.com, <https://doi.org/10.3390/atoms7030087>.
- Yadava, Nandini, Sachin S. Chouhan, Amulya Sanyasi, Uttam Sharma, Jayashree Sharma, et al. "Vibrational Temperature Estimation of Nitrogen Molecules in Radio-Frequency (RF) Produced Plasma." *Plasma and Fusion Research*, vol. 17, Aug. 2022, pp. 2401095–2401095. www.jstage.jst.go.jp, <https://doi.org/10.1585/pfr.17.2401095>.
- Yamada, K., et al. "A Study of Particle Confinement Properties in Ohmically and Neutral Beam Heated Hydrogen Plasmas in the JT-60 Tokamak." *Nuclear Fusion*, vol. 27, no. 8, Aug. 1987, pp. 1203–11, <https://doi.org/10.1088/0029-5515/27/8/001>.
- Zeeman, P. "On the Influence of Magnetism on the Nature of the Light Emitted by a Substance." *The Astrophysical Journal*, vol. 5, May 1897, p. 332. NASA ADS, <https://doi.org/10.1086/140355>.
- Zhang, Xin-Rong, and Trygve Magne Eikevik. *CO₂ Refrigeration Cycle and Systems*. Springer link, 2023, <https://link.springer.com/book/10.1007/978-3-031-22512-3>.
- Zhuravlev, D. A. "E. G. Loewen and E. Popov Diffraction Gratings and Their Applications (Marcel Dekker, New York, 1997)." *Optics and Spectroscopy*, vol. 88, no. 1, Jan. 2000, pp. 143–44. Springer Link, <https://doi.org/10.1134/1.626762>.

- Zylstra, A. B., et al. "Publisher Correction: Burning Plasma Achieved in Inertial Fusion." *Nature*, vol. 603, no. 7903, Mar. 2022, pp. E34–E34, <https://doi.org/10.1038/s41586-022-04607-2>.

LIST OF PUBLICATIONS

Publications during Ph.D. period [2020-2023]

1. [Computational and Experimental Study of Nonequilibrium Flow in Plasma Wind Tunnel](#), Unnikrishnan, Vinay, **Nandini Yadava**, et al. *Journal of Thermophysics and Heat Transfer* (**2023**): 1-14.
2. [Initial results from near-infrared spectroscopy on ADITYA-U tokamak](#), N. Ramaiya, R. Manchanda, M. B. Chowdhuri, **Nandini Yadava** et al., *Review of Scientific Instruments*, 93(11), (**2022**) p.113552.
3. [Vibrational Temperature Estimation of Nitrogen Molecules in Radio-Frequency \(RF\) Produced Plasma](#), **Nandini Yadava**, et al. *Plasma and Fusion Research* 17 (**2022**), 2401095-2401095.
4. [Impurity Behaviour in High Performance ADITYA Tokamak Plasmas](#), Malay Bikas Chowdhuri, Ranjana Manchanda, Joydeep Ghosh, **Nandini Yadava** et al. *Plasma and Fusion Research* 17 (**2022**): 2402011-2402011.
5. [Physics studies of ADITYA and ADITYA-U tokamak plasmas using spectroscopic diagnostics](#). Ranjana Manchanda, Malay Bikas Chowdhuri, Joydeep Ghosh, Nilam Ramaiya, **Nandini Yadava** et al. (**2022**). *Nuclear Fusion* 62, 042014
6. [A diagnostic for measuring radial profile of visible continuum radiation from ADITYA-U Tokamak Plasmas](#), Malay Bikas Chowdhuri, Ranjana Manchanda, Joydeep Ghosh, **Nandini Yadava** et al. et al. (**2021**). *Fusion Engineering and Design*, 173, 112884.
7. [Lithium wall conditioning techniques in ADITYA-U tokamak for impurity and fuel control](#). Kumarpal Jadeja, Joydeep Ghosh, **Nandini Yadava**, et al. (**2021**) *Nuclear Fusion* 62, no. 1 016003.
8. [Observations of visible argon line emissions and its spatial profile from Aditya-U tokamak plasma](#). Kajal Shah, Joydeep Ghosh, Gaurav Shukla, Malay Bikas Chowdhuri, Ranjana Manchanda, **Nandini Yadava** et al. (**2021**). *Review of Scientific Instruments*, 92(5), 053548.
9. [Gas-puff induced cold pulse propagation in ADITYA-U tokamak](#). Tanmay Macwan, Harshita Raj, **Nandini Yadava** et al. (**2021**) *Nuclear Fusion*, 61(9), 096029, 2021.

LIST OF PUBLICATIONS

10. [Overview of recent experimental results from the ADITYA-U Tokamak.](#) R L Tanna, Tanmay Macwan, ... **Nandini Yadava**, et al. (2021). Nuclear Fusion
11. [Investigation of Recycling and Impurities Influxes in ADITYA-U Tokamak Plasmas,](#) **Nandini Yadava**, et al. *Plasma and Fusion Research* 16 (2021): 2402055-2402055.
12. [Real-time feedback control system for ADITYA-U horizontal plasma position stabilization,](#) Kumar, Rohit, ... **Nandini Yadava** et al. *Fusion Engineering and Design* 165 (2021): 112218.

Other publications [2018-2020]

13. [Spatial Profile of Neutral Temperature Measurement in Aditya-U Tokamak Plasmas,](#) **Nandini Yadava**, et al. *Atoms* 7, no. 3 (2019): 87.
14. [Observation of Poloidal Asymmetry in Measured Neutral Temperatures in Aditya-U Tokamak Plasma,](#) **Nandini Yadava**, et al. *Nuclear Fusion* 59 (2019), no 10, 106003.
15. [Poloidal rotation and edge ion temperature measurements using spectroscopy diagnostic on Aditya-U tokamak,](#) Gaurav Shukla, ..., **Nandini Yadava**, et al., *Atoms* 7, no. 3 (2019): 93.
16. [Modelling of the H \$\alpha\$ emission from ADITYA tokamak plasmas,](#) Ritu Dey, ..., **Nandini Yadava**, et al. *Atoms* 7, no. 4 (2019): 95.
17. [Evaluation of Oxygen Transport Coefficient in Aditya Tokamak using Radial Profile of O \$4+\$ Emissivity and Importance of Atomic Data Used therein,](#) M. B. Chowdhuri, ..., **Nandini Yadava**, et al., *Atoms* 7, no. 3 (2019): 90.
18. [Investigation of atomic and molecular processes in H \$\alpha\$ emission through modelling of measured H \$\alpha\$ emissivity profile using DEGAS2 in the ADITYA tokamak,](#) Ritu Dey, ..., **Nandini Yadava** et al. (2019) *Nuclear Fusion* 59, no.7: 076005.
19. [Overview of operation and experiments in the ADITYA-U tokamak,](#) R.L. Tanna, ..., **Nandini Yadava** et al. (2019) *Nuclear Fusion* 59, no. 11: 112006.
20. [Development of RF Based capacitively coupled plasma system for tungsten nano deposition on graphite,](#) Sachin S Chauhan,, **Nandini Yadava** et al. (2018) *Material Research Express* 5, no 11, 115020.

Under review:

1. Quantification of molecular contribution in particle influx estimation using S/XB calculations of H α emission in tokamaks, Ritu Dey and Nandini Yadava et al.,
2. Removal of an Anomaly in Edge Ion Temperature Estimation Using Spectroscopy in ADITYA-U Tokamak Nandini Yadava, J. Ghosh, M. B. Chowdhuri et al.
3. Investigation of Self-absorbed Lithium Spectral Line Emissions during Li₂TiO₃ Injection in Aditya-U tokamak Nandini Yadava, J. Ghosh, M. B. Chowdhuri et al.

Paper under preparation:

4. Study on mass dependency on diffusion coefficient in Aditya-U tokamak. Nandini Yadava, J. Ghosh, M. B. Chowdhuri, Ashoke De et al.

Conference proceedings (International):

1. Vibrational Temperature Estimation of Nitrogen Molecules in Radio-Frequency (RF) Produced Plasma, Nandini Yadava, et al., The 30th International Toki Conference **2020**, Online conference, Toki, Japan. (virtual).
2. Investigation of Charge Dependency in impurity transport in Aditya-U tokamak, Nandini Yadava et al. 29th APPS Division of Plasma Physics Meeting **2021** (virtual).
3. Investigation of Self-Absorbed Lithium Spectral Line Emissions during Li₂TiO₃ Injection in ADITYA-U tokamak, Nandini Yadava et al, 28th Fusion Energy Conference **2021** (virtual).
4. A Diagnostic for Measurement of Radial Profile of Visible Bremsstrahlung for determining Z_{eff} in ADITYA-U Tokamak Plasmas, M. B. Chowdhuri, ..., N. Yadava, et al. High Temperature Plasma Diagnostic Conference **2020**, Online conference, LANL, New Mexico, US. (virtual)
5. Observation of spatially resolved Argon line emissions in ADITYA-U tokamak using high resolution spectroscopic diagnostic, K. Shah, ..., N. Yadava, et al. High Temperature Plasma Diagnostic Conference **2020**, Online conference, LANL, New Mexico, US. (virtual)
6. Investigation of Recycling and Impurities Influxes in ADITYA-U Tokamak Plasmas, Nandini Yadava, et al. 29th International Toki Conference **2020**, Online conference, Toki, Japan. (virtual)

Oral presentation (International):

7. Investigation of Charge Dependency in impurity transport in Aditya-U tokamak. Nandini Yadava et al., 63rd Annual Meeting of the APS Division of Plasma Physics **2021**; Pittsburgh, PA (virtual)
8. Vibrational temperature estimation of nitrogen molecules in radio-frequency (RF) produced plasma, Nandini Yadava, et al. 30th International Toki Conference on Plasma and Fusion Research **2021** (virtual)
9. Behaviour of hydrogen and impurities in ADITYA-U tokamak plasmas after lithium coating, Nandini Yadava et al, V International Summer School on the Physics of Plasma-Surface Interactions **2021**, Moscow, MEPhI, (virtual)

Oral presentation (National):

10. **BUTI Young Scientist Award:** Understanding the Physical Processes Prevailing in the Edge Plasma Region of ADITYA-U Tokamak using Spectroscopic Measurements, Nandini Yadava et al. 37th National Symposium on Plasma Science and Technology **2022**, IIT-Jodhpur, Rajasthan.
11. Spectroscopic Plasma Diagnostic Technique to Estimate Temperature from Lines Emissions Influenced by Magnetic Field, Nandini Yadava et al. 8th PSSI Plasma Scholars Colloquium (PSC-**2020**, Kalinga Institute of Industrial Technology (KIIT). (virtual)

Poster presentations (International):

12. Global Particle Balance and Recycling Properties in Aditya-U Tokamak Plasmas, Nandini Yadava, et al., 5th Asia-Pacific Conference on Plasma Physics **2021**. (virtual)
13. Investigation of Self-Absorbed Lithium Spectral Line Emissions during Li₂TiO₃ Injection in ADITYA-U tokamak, Nandini Yadava, et al., 28th Fusion Energy Conference **2021**. (virtual)

Poster presentations (National):

14. Impurity Transport in Aditya-U Tokamak with Indigenously Developed Semi-Implicit Impurity Transport Code, Nandini Yadava, et al. 34th National Symposium on Plasma Science and Technology **2021**, Birla Institute of Technology (BIT), Mesra, Jaipur. (virtual)

- 15.** Neutral and impurity influx measurement from limiter and wall of Aditya-U Tokamak **Nandini Yadava**, et al. 8th Topical conference (TC-2020) on Atomic and Molecular Collisions for Plasma Applications **2020**, IIT-Roorkee.
- 16.** Investigation of Neutral Recycling and Ion Temperature of Various Plasma Species in ADITYA and ADITYA-U Tokamak, **Nandini Yadava**, et al. National Symposium for Commemorating 30-years of ADITYA Tokamak **2020**, Entrepreneurship Development Institute of India, Ahmedabad.

School:

- 17.** Participated in **V International Summer School on the Physics of Plasma-Surface Interactions** organized online during July 05 – 09, **2021**, Moscow, MEPhI, presented work entitled, “Behaviour of hydrogen and impurities in ADITYA-U tokamak plasmas after lithium coating” (virtual)